Engineering the Ceramic-Polymer Interface for Advanced Ballistic Protection

T. Commins, Magdalen College, University of Oxford

Submitted for the degree of D. Phil., Hilary 2023

Abstract

Ballistic impact on body armour is a complex phenomenon involving sophisticated materials and multiple interactions. The armours of interest to this study are polymer-backed ceramic plate composites, which are standard amongst military personnel. The composite nature adds complexity to the armour because of the interaction between the ceramic and polymer, which is thought to play a significant role in the armour performance; however, despite this importance, this interplay is relatively poorly understood. The research in this thesis aims to explore the effect of the interface and polymer backing on armour performance. A methodical study into the fundamental behaviour of armour using simplified materials and interactions has been performed. Two commercially available polyurethanes (PUs) were selected, and these were first characterised to find the effect of loading rate and temperature on the mechanical response. Interfaces between these polymers and the chosen ceramic (alumina) were also characterised with respect to rate and temperature using a variety of surface modifications. These characterisation experiments were used to model behaviour of simplified armours, which were also impacted over a range of speeds in a series of experiments in which the influence of the backing and interfacial properties on overall armour response was recorded. The model armour was designed to be quasi-1D to allow the fracture pathways and failure, which would otherwise be obscured by the geometry of the material, to be visually investigated. The polymer and interfacial characteristics influenced the observed fracture pathways of the model armour under quasi-static and impact loading which affected the energy absorptive

capabilities of the armour. This behaviour was further predicted from independently calibrated FEA simulations.

Acknowledgements

I cannot thank my supervisor, Prof. Clive Siviour, enough for his support, guidance, and patience throughout this DPhil. Without him, this project would not have been completed and I owe it all to him. Thanks must also be extended to those who supported my research at the university: Igor Dyson for this experimental assistance and thorough machine training, Nick Hawkins for his commitment and experimental interpretation, and Peter Walters. I must also thank those in the machine workshop who were pivotal in ensuring my experimental designs became reality, in particular to Andy Bateman and Neil Warland for their hard work and welcoming atmosphere. I also have to thank my family, my partner, Natalie, and my friends for putting up with me during this time. Thanks in particular to my friends/colleagues, Aaron Graham and Isabella Mendoza, without whom this work would have been completed twice as fast.

I would also like to thank Magdalen College for their financial support of me during this DPhil and to Dstl for their financial and intellectual support of this work under contract number DSTLX1000128371. In particular, Rebecca Livesey and Neil Middleton for their support and stimulating discussions.

Table of Contents

Acknowledgements ..... **ii**

Table of Contents ..... **iii**

List of Figures ..... **vii**

List of Tables ..... **xiv**

1 Introduction **1**

1.1 Motivation 1

1.2 Aims 2

1.3 Thesis Structure 3

2 Background **5**

2.1 Armour 5

2.1.1 Background 5

2.1.2 Interface 10

2.2 Polymer 11

2.2.1 Structure 11

2.2.2 Time Temperature Superposition 14

2.2.3 Modelling 16

2.2.4 Prony Series Fitting 19

2.3 Fracture Mechanics 20

2.3.1 Fracture Mechanics Basics 20

2.3.2 J-integral 22

2.3.3 Modelling 23

2.4 Experimental Techniques 25

2.4.1 Thermomechanical Characterisation 25

2.4.2 Quasi-static Strain rate 29

2.4.3 Dynamic Strain Rate 31

2.4.4 Digital Image Correlation 35

2.5 References 37

3 Stress relaxation after low and high-rate deformation of polyurethanes **46**

3.1 Chapter Introduction 46

3.2 Abstract....47
3.3 Introduction....48
3.4 Materials....50
3.5 Experimental Procedure....50
3.5.1 DMA....51
3.5.2 Compression....52
3.5.3 Relaxation....53
3.6 Modelling....55
3.6.1 Prony Series Representation....55
3.6.2 Low-Rate Stress Relaxation Modelling....56
3.6.3 High-Rate Relaxation Modelling....57
3.7 Results and Discussion....58
3.7.1 DMA....58
3.7.2 Large Strain Compression....62
3.7.3 Low Rate Relaxation Response....67
3.7.4 High Rate Relaxation Response....73
3.8 Discussion....80
3.9 Conclusions....81
3.10 Acknowledgements....82
3.11 Appendix....83
3.11.1 DSC Data....83
3.11.2 DMA data from single cantilever bend....84
3.11.3 Task 3 Prony Series Values....86
3.11.4 Task 11 Prony Series Values....89
3.12 References....92
4 The Use of Time-Temperature Superposition for Interface Characterisation using the J-Integral....94
4.1 Chapter Introduction....94
4.2 Abstract....95
4.3 Introduction....96
4.4 Materials and Specimen Preparation....98
4.4.1 Materials....98
4.4.2 Specimen Preparation....99

4.5 Experimental Overview....100
4.6 Polymer Properties....101
4.7 Analytical Procedure and FEA....103
4.7.1 Procedure Pipeline....103
4.7.2 Dynamic Influence....104
4.8 Results and Discussion....108
4.8.1 Analytical Procedure.... 108
4.8.2 Quasi-static Results....112
4.8.3 Dynamic Results....117
4.9 Discussion....120
4.10 Conclusions....123
4.11 Acknowledgements....125
4.12 References....126
5 Quasi-1D Model Armour under Impact and Quasi-static Loading 130
5.1 Chapter Introduction....130
5.2 Abstract....131
5.3 Introduction....132
5.4 Materials and Specimen Preparation....134
5.4.1 Materials....134
5.4.2 Specimen Preparation....134
5.5 Experimental Overview....136
5.5.1 Quasi-static Beam Bend....136
5.5.2 Impact Beam Bend....136
5.6 Polymer Properties....138
5.6.1 Stiffness....138
5.6.2 Modelling....140
5.7 Results and Discussion....141
5.7.1 Quasi-static Beam Bend....141
5.7.2 Impact Beam Bend....157
5.8 FEA Results....165
5.8.1 Material Models....165
5.8.2 Quasi-static FEA response....172

5.8.3 Impact FEA Comparison....175
5.9 Conclusions....177
5.10 Acknowledgements....179
5.11 Appendix....179
5.11.1 DSC Data....179
5.11.2 GFPC DMA data....180
5.11.3 DIC parameters....181
5.11.4 Task 3 and Task 11 Prony series parameters....182
5.12 References....183
6 Conclusion....186
6.1 Thesis Aims....186
6.2 Accomplishments and Future Work....187
6.2.1 Polymer characterisation and stress relaxation....187
6.2.2 Quasi-static and Dynamic Properties of the Ceramic-Polymer Interface....188
6.2.3 Quasi-static and Impact Performance of Quasi-1D Model Armour....189
6.3 Concluding Remarks....191

List of Figures

Chapter 2

Figure 1 - Common armour materials plotted with lines of constant Cunniff velocity [9]. A high Cunniff velocity represents a more effective armour....6

Figure 2 - Typical stages of ballistic impact [29]....9

Figure 3 -Monomer and polymer of ethene and repeat unit of polyethylene....12

Figure 4 - Synthesis of Polyurethane [42]....12

Figure 5 – Schematic of typical variation of modulus with temperature (or loading time). Approximate values of the modulus are marked on the y-axis and the alpha, beta and gamma transitions. Figure has been adapted from [47]....13

Figure 6 - Example of TTS shift using dynamic mechanical analysis (DMA) data for rubber to create a mastercurve for a 25 °C reference temperature. Figure adapted from [49]....15

Figure 7 - Standard linear model in either the Maxwell or in the Kelvin-Voigt representation....17

Figure 8 - Spring dashpot representation of a generalised Maxwell model....18

Figure 9 - Example mastercurve with Prony series fit....19

Figure 10 - Crack modes of loading....20

Figure 11 - Example TSL response....24

Figure 12A - Storage and loss modulus....27

Figure 13 - Example DSC results for two polyurethanes. These materials were heated at a rate of 3 °C min^{-1} from - 90 °C to 120 °C....28

Figure 14 - Schematic of three-point bend loading....30

Figure 15 - Schematic of the Hopkinson bar experiment....32

Figure 16 - Projectile and sabot used for impact experiments....35

Figure 17 - Schematic for the experimental set up for impact loading experiments....35

Figure 18 - Example speckle pattern used for DIC with subset tracking from initial position, 1, to final deformed position, 2....36

Chapter 3

FIGURE 1 - SPRING-DASHPOT REPRESENTATION OF A K-BRANCH PRONY SERIES.....55

FIGURE 2 - BOUNDARY CONDITIONS FOR LOADING AND RELAXATION FOR A K-BRNAHCED PRONY SERIES UNDER QUASI-STATIC LOADING.....57

FIGURE 3 - BOUNDARY CONDITIONS FOR LOADING AND RELAXATION FOR A K-BRNAHCED PRONY SERIES UNDER DYNAMIC LOADING 58

FIGURE 4 - RELAXATION DMA DATA. THE REFERENCE TEMPERATURE, 20 °C HAS BEEN PRESENTED BY A DASHED LINE.....59

FIGURE 5 - SHIFT FACTORS USED TO PRODUCE RELAXATION MASTERCURVE AT 20 °C.....60

FIGURE 6 - COMPARISON OF 20 °C MASTERCURVES PRODUCED USING RELAXATION DATA IN THE THREE POINT BEND CONFIGURATION OR OSCILLATORY IN SINGLE CANTILEVER (SC) CONFIGURATION.....60

FIGURE 7 - MASTERCURVES FOR 'TASK 11' AND 'TASK 3' FOR A 20 °C REFERENCE TEMPERATURE FROM THREE-POINT BEND DMA COMPARED TO THE PRONY FIT TO THESE CURVES USING BRANCHES WITH RELAXATION TIMES SPACED ONE PER DECADE.....61

FIGURE 8 - STRESS-STRAIN CURVES FROM LOW AND HIGH RATE CHARACTERISATION AT ROOM TEMPERATURE. IN ALL CASES, THE END OF THE CURVE REPRESENTS THE END OF LOADING, THE SPECIMENS DID NOT FAIL.....62

FIGURE 9 - STRESS-STRAIN RESPONSE OF BOTH POLYMERS IN COMPRESSION AT SUB-AMBIENT TEMPERATURES AND 10^{-3} s^{-1}.....63

FIGURE 10 – YIELD STRESS OF TASK 3 WITH VARYING LOADING TIME.....64

FIGURE 11 – VARIATION OF STRESS OF TASK 11 AT 4% STRAIN WITH LOADING TIME. NOTE THIS POLYMER DOES NOT HAVE A YIELD POINT.....64

FIGURE 12 – YIELD STRENGTH OF TASK 3 WITH VARYING TEMPERATURE.....64

FIGURE 13 – VARIATION OF STRESS OF TASK 11 AT 4% STRAIN WITH TEMPERATURE.....64

FIGURE 14 -COMPARISON OF STRESS STRAIN CURVES FOR TASK 3 AT LOW STRAIN RATES AND TASK 11 AT HIGH RATES. THESE TWO DIFFERENT POLYMERS EXHIBIT SIMILAR BEHAVIOURS WHEN THE ALPHA MOTIONS (WHICH GOVERN THE GLASS TRANSITION) ARE RESTRICTED.....65

FIGURE 15 - COMPARISON BETWEEN HIGH RATE EXPERIMENTS PERFORMED UNDER AMBIENT CONDITIONS AND LOW RATE (10^{-3} s^{-1}) EXPERIMENTS PERFORMED AT SUB-AMBIENT TEMPERATURES.....67

FIGURE 16 - STRESS-TIME RELAXATION RESPONSE FOR TASK 3 AND 11.....68

FIGURE 17 – STRESS-TIME RELAXATION RESPONSE FOR TASK 3 AND 11. THE RESPONSE HAS BEEN NORMALISED TO THE PEAK STRESS OBSERVED AT EACH CONDITION....68
FIGURE 18 - STRESS-STRAIN RELAXATION RESPONSE FOR TASK 3 AND 11....69
FIGURE 19 – LOW TEMPERATURE RELAXATION DATA OVERLAIN ON THE POLYMER MASTERCURVES GENERATED FROM DMA EXPERIMENTS IN THREE POINT BEND AND SINGLE CANTILEVER. THE LOW TEMPERATURE CURVES HAVE BEEN SHIFTED BY THEIR CORRESPONDING SHIFT FACTORS....69
FIGURE 20 - STRESS-TIME BEHAVIOUR FOR TASK 3 AND TASK 11. SPECIMENS WERE NOW LOADED TO LARGER STRAINS BEFORE RELAXATION....72
FIGURE 21 - STRESS-STRAIN RESPONSE FOR TASK 3 AND TASK 11....73
FIGURE 22 - STRESS-TIME DYNAMIC RELAXATION RESPONSE OF 10 MM DIAMETER SPECIMENS. THE MODEL WAS LOADED USING THE STRESS-TIME PROFILE FROM THE EXPERIMENT. RELAXATION WAS ALLOWED TO OCCUR UNDER THE CONFINING FORCE OF TWO DASHPOTS....75
FIGURE 23 - STRAIN-TIME DYNAMIC RELAXATION RESPONSE OF 10 MM DIAMETER SPECIMENS....75
FIGURE 24 - STRESS-STRAIN RESPONSE OF 10 MM DIAMETER SPECIMENS....76
FIGURE 25 - MODELLED STRESS-TIME RESPONSE DURING RELAXATION WITH VARIOUS BOUNDARY CONDITIONS APPLIED....76
FIGURE 26 - STRESS-TIME DYNAMIC RELAXATION RESPONSE OF 6 MM DIAMETER SPECIMENS....77
FIGURE 27 - STRAIN-TIME DYNAMIC RELAXATION RESPONSE OF 6 MM DIAMETER SPECIMENS....78
FIGURE 28 - STRESS-STRAIN RESPONSE OF TASK 3 AND TASK 11 AT HIGH RATE WITH 6 MM GEOMETRY....78
FIGURE 29 - STRESS-TIME RESPONSE COMPARING INDIVIDUAL 10 MM AND 6 MM HIGH RATE RELAXATION SPECIMENS FOR TASK 3 AND TASK 11. THE STRESS HAS BEEN NORMALISED TO THE STRESS AT THE ONSET OF RELAXATION....80
FIGURE 30 - MODIFIED POLYMER MODEL TO ACCOUNT FOR LOW AND HIGH RATE NON-LINEARITIES....81
FIGURE 31 - DSC RESULTS FOR TASK 3 AND TASK 11....83
FIGURE 32 – SEPARATED RAW DMA DATA FROM OSCILLATORY SINGLE CANTILEVER CONFIGURATION....84
FIGURE 33 – SHIFT FACTORS FOR SINGLE CANTILEVER DMA....84
FIGURE 34 – STORAGE MODULUS VARIATION WITH LOADING DURATION....85
FIGURE 35 – THERMAL VARIATION OF STORAGE MODULUS AT A SINGLE FREQUENCY, 1 HZ....85

Chapter 4

FIGURE 1 - DIMENSIONS OF WEDGE TEST SPECIMEN. THE SURFACE HAS BEEN PAINTED WITH A SPECKLE PATTERN TO ALLOW DIGITAL IMAGE CORRELATION (DIC) TO BE USED TO ANALYSE THE RESULTING DISPLACEMENT FIELD DURING LOADING. SPECIMENS WERE 20 MM WIDE.....99

FIGURE 2 - EXPERIMENTAL SET UP FOR DYNAMIC WEDGE TEST.....101

FIGURE 3 - STIFFNESS MASTERCURVE FOR TASK 3 AND TASK 11. MASTERCURVES WERE CREATED FROM ISOTHERMAL STRESS RELAXATION EXPERIMENTS USING DMA APPARATUS IN A 3-POINT BEND CONFIGURATION.....102

FIGURE 4 - SCHEMATIC OF FEA WEDGE EXPERIMENT. THE DEFORMATION HAS BEEN GREATLY EXAGGERATED.....105

FIGURE 5 - FEA OUTPUT RESULTS COMPARING THE EFFECTS OF INERTIA, DIC PROCESSING SETTINGS AND IMAGE NOISE ON THE J-INTEGRAL, K_1 AND K_{11}.....106

FIGURE 6 - KINETIC AND STRAIN ENERGY CONTRIBUTIONS TO TOTAL ENERGY IN THE SIMULATED WEDGE EXPERIMENT USING ALUMINA WITH REPRESENTATIVE (3000 KG M^{-3}) AND ARTIFICIALLY LOW (3 KG M^{-3}) DENSITIES.....108

FIGURE 7 - TYPICAL EXPERIMENTAL IMAGE UNDER QUASI-STATIC LOADING.....108

FIGURE 8 – TYPICAL EXPERIMENTAL IMAGE UNDER DYNAMIC LOADING.....109

FIGURE 9 - CORRELATION COEFFICIENT MAP FOR DYNAMICALLY LOADED WEDGE SPECIMEN. THE HIGHLIGHTED REGION PROVIDES EVIDENCE FOR THE ONSET OF FRACTURE.....110

FIGURE 10 - INTERFACE SEPARATION AS A FUNCTION OF POSITION FOR EACH IMAGE. THE IMAGE ORIGIN WAS ON THE LEFT OF EACH IMAGE. THE DASHED LINES ARE THE SEPARATION DATA, AND THE SOLID LINES ARE A FOURTH-ORDER POLYNOMIAL FIT TO THESE DATA. POINTS HIGHLIGHTED IN RED ARE THE POSITIONS AT WHICH CRACK FAILURE HAS OCCURRED.....111

FIGURE 11 - TYPICAL CRACK POSITION AS A FUNCTION OF TIME FOR TASK 3 PRIMER SPECIMENS. CRACK LENGTH INCREASES FROM 25 MM UNTIL FRAME EXIT. THE RED CIRCLE HIGHLIGHTS THE INFLUENCE OF PERIODIC NOISE IN THE CAMERA EVERY 10^{TH} FRAME.....112

FIGURE 12 – K_1 VS TIME OR CRACK LENGTH FOR QUASI-STATIC WEDGE EXPERIMENT. ERROR BARS ON THE RIGHT DEMOTE THE MEAN AND ONE STANDARD DEVIATION. P REPRESENTS PRIMER SURFACE PRE-TREATMENT AND NP REPRESENTS NON-PRIMER. TWO EXPERIMENTS WERE PERFORMED FOR EACH SPECIMEN TYPE, LABELLED AS 1 AND 2.....113

FIGURE 13 – K_{11} VS TIME OR CRACK LENGTH FOR QUASI-STATIC WEDGE EXPERIMENT. ERROR BARS ON THE RIGHT DEMOTE THE MEAN AND ONE STANDARD DEVIATION. P REPRESENTS PRIMER SURFACE PRE-TREATMENT AND NP REPRESENTS NON-PRIMER. 114

Figure 14 – J Integral vs time or crack length for quasi-static wedge experiment for Task 11. Error bars on the right demote the mean and one standard deviation. P represents primer surface pre-treatment and NP represents non-primer.....115
Figure 15 - J Integral vs time or crack length for quasi-static wedge experiment for Task 3. Error bars on the right demote the mean and one standard deviation. P represents primer surface pre-treatment and NP represents non-primer.....115
Figure 16 - J integral vs crack length and time for the dynamic wedge experiment. Error bars on the right demote the mean and one standard deviation. P represents primer surface pre-treatment and NP represents non-primer.....117
Figure 17 - K1 vs crack length and time for the dynamic wedge experiment. Error bars on the right demote the mean and one standard deviation. P represents primer surface pre-treatment and NP represents non-primer. 118
Figure 18 – K_{11} vs crack length and time for the dynamic wedge experiment. Error bars on the right demote the mean and one standard deviation. P represents primer surface pre-treatment and NP represents non-primer. 118
Figure 19 - K1 stress intensity factor for Task 3 non-primer at room temperature.....121

Chapter 5

Figure 1 - Beam bend specimen schematic. Specimens were 5 mm thick.....135
Figure 2 – Schematic of the gas gun used to investigate the impact behaviour of specimens under beam bend.....137
Figure 3 – Projectile and sabot used for impact beam bend.....138
Figure 4 - Three-point bend DMA stiffness mastercurve for Task 3 and Task 11.....139
Figure 5 - Schematic representation of a Prony series.....140
Figure 6 - Force vs. displacement for unbacked ceramic.....142
Figure 7 - Force vs. displacement for unbacked ceramic normalised by Young's Modulus and second moment of area of each specimen to account for geometric effects.....142
Figure 8 - Weibull plot for unpacked ceramic loaded under three-point bend.....143
Figure 9 - Schematics of Type 1 and Type 2 failure.....144

Figure 10 - Typical Force-displacement curves for Type 1 (Interfacial failure) and Type 2 (central failure). The shaded areas represent the additional load carrying capacity from each failure type.....145
Figure 11 – Type 1- Interfacial failure of a composite bend specimen. Specimens have been painted to allow DIC to be performed.....147
Figure 12 – Type 2 - Central failure of a composite bend specimen. Specimens have been painted to allow DIC to be performed.....147
Figure 13 – Type 1 (interfacial failure) of a composite bend specimen using DIC to calculate the correlation coefficient map. The crack has propagated along the interface of the specimen from the right.....148
Figure 14 – Early stages of Type 2 (central failure) of a composite bend specimen using DIC to calculate the correlation coefficient map.....148
Figure 15 - Force vs displacement response for Task 3 under quasi-static loading conditions split into the room temperature and low temperature experiments.....149
Figure 16 -Force vs displacement response for Task 11 under quasi-static loading conditions. Task 11 -36 °C and Task 3 room temperature share the same colour scheme (green) as these conditions were chosen to mimic each other.....149
Figure 17 - Comparison between Task 3 and low temperature Task 11. The temperature was chosen to give the similar polymer stiffness between the polymers.....151
Figure 18 - Breaking stress in the ceramic for ceramic bend specimens backed with Task 3. Diamonds denote Type 1 failure and stars, Type 2.....152
Figure 19 - Breaking stress in the ceramic for ceramic bend specimens backed with Task 11. Diamonds denote Type 1 failure and stars, Type 2.....152
Figure 20 - Energy absorbed during loading for Task 3. Diamonds denote Type 1 failure and stars, Type 2.....153
Figure 21 - Energy absorbed during loading for Task 11. Diamonds denote Type 1 failure and stars, Type 2.....153
Figure 22 – DIC vertical displacement map for Task 3 backed alumina for select images for the primer backed specimens. Failure from thermal contraction was observed.....155
Figure 23 - DIC vertical displacement map for Task 11 backed alumina for select images for the primer backed specimens. Failure from thermal contraction was observed.....156
Figure 24 - Incident vs. residual speed during impact for Task 3 and Task 11 with and without a primer pre-treatment. The line of y = x is shown for reference.....157

FIGURE 25 - TASK 3 BEAM BEND IMPACT AT 100 M/S WITH A PRIMER SURFACE PRE-TREATMENT. THE POLYMER-CERAMIC BOUNDARY IS SHOWN IN IMAGE 1 WITH THE CERAMIC AS THE STRIKE FACE. THE REGION CIRCLES IN RED SHOWS CRACK PROPOGATION ACROSS THE INTERFACE INTO THE POLYMER. IMAGE 1 IS AT THE MOMENT OF IMPACT AND SUBSEQUENT IMAGES ARE SHOWN EVERY 20 MS.....159

FIGURE 26 - TASK 3 BEAM BEND IMPACT AT 100 M/S WITHOUT A PRIMER SURFACE PRE-TREATMENT. THE POLYMER-CERAMIC BOUNDARY IS SHOWN IN IMAGE 1 WITH THE CERAMIC AS THE STRIKE FACE. IMAGE 1 IS AT THE MOMENT OF IMPACT AND SUBSEQUENT IMAGES ARE SHOWN EVERY 20 MS.....159

FIGURE 27 - TASK 11 BEAM BEND IMPACT AT 100 M/S WITH A PRIMER SURFACE PRE-TREATMENT. THE POLYMER-CERAMIC BOUNDARY IS SHOWN IN IMAGE 1 WITH THE CERAMIC AS THE STRIKE FACE. IMAGE 1 IS AT THE POINT OF IMPACT AND SUBSEQUENT IMAGES ARE SHOWN EVERY 20 MS.....160

FIGURE 28 - TASK 11 BEAM BEND IMPACT AT 100 M/S WITH A PRIMER SURFACE PRE-TREATMENT. THE POLYMER-CERAMIC BOUNDARY IS SHOWN IN IMAGE 1 WITH THE CERAMIC AS THE STRIKE FACE. IMAGE 1 IS AT THE POINT OF IMPACT AND SUBSEQUENT IMAGES ARE SHOWN EVERY 20 MS.....160

FIGURE 29 - MASS NORMALISED INCIDENT VS RESIDUAL SPEED FOR TASK 3 AND TASK 11 FOR PRIMER AND NON-PRIMER PRE-TREATMENT.....161

FIGURE 30 - TASK 11 AND TASK 3 RESIDUAL VS INCIDENT VELOCITIES UNDER PRIMER AND NON-PRIMER SURFACE PRE-TREATMENTS AND STRENGTHLESS INTERFACES.....162

FIGURE 31 - TASK 3 AND PC RESIDUAL VS INCIDENT VELOCITIES UNDER PRIMER, NON-PRIMER, STRENGTHLESS AND BONDED INTERFACIAL CONDITIONS. THE RESULTS FROM TASK 11 HAVE BEEN REMOVED FOR CLARITY.....163

FIGURE 32 - TASK 3 BONDED WITH DOWSIL 6-1104. IMPACT WAS AT 100 M/S AND EACH IMAGE IS SEPARATED BY 10 MS.....164

FIGURE 33 - GFPC BONDED WITH DOWSIL 6-1104. IMPACT WAS AT 100 M/S AND EACH IMAGE IS SEPARATED BY 10 MS.....164

FIGURE 34 - CERAMIC EXPERIMENT VS FEA UNDER QUASI-STATIC BEAM BEND.....166

FIGURE 35 - EXAMPLE TSL RESPONSE.....168

FIGURE 36 - COHESIVE REPRESENTATION AND TSL MODELLING OF THE PU-ALUMINA INTERFACE FOR TASK 3 AND TASK 11. THE SOLID LINES REPRESENT THE EXPERIMENTAL RESULTS AND THE DASHED, THE LINEAR TSL FIT.....169

FIGURE 37 - QUASI-STATIC BEAM BEND EXPERIMENTAL VS FEA RESULTS FOR TASK 3.....173

FIGURE 38 - TYPICAL SIMULATED FAILURE MODE FOR BEAM BEND LOADING FOR ALUMINA BACKED WITH TASK 3 AT AMBIENT AND SUB-AMBIENT CONDITIONS.....173

FIGURE 39 - QUASI-STATIC BEAM BEND EXPERIMENTAL VS FEA RESULTS FOR TASK 11.....174

Figure 40 - Failure modes of Task 11 at ambient and sub-ambient conditions.....175

Figure 41 - Incident vs residual speeds comparing experiment (solid) to simulation (dashed) for impact beam bend.

.....176

Figure 42 - DSC results for Task 3 and Task 11.....179

Figure 43 - Mastercurve of GFPC created using oscillatory single cantilever DMA.....180

Figure 44 - Shift factors used to generate the mastercurve for GFPC.....180

List of Tables

Chapter 3

Table 1 - Experimental conditions for low rate compression.....52

Table 2 - Low rate stress relaxation experimental conditions for T11.....54

Table 3 - Low rate stress relaxation experimental conditions for T3.....54

Table 4 - Task 3 20 °C and 0° C Prony values for ABAQUS.....86

Table 5 - Task 3 -20 °C and -40° C Prony values for ABAQUS.....87

Table 6 - Task 3 -60° C Prony values for ABAQUS.....88

Table 7 - Task 11 20 °C and 0° C Prony values for ABAQUS.....89

Table 8 - Task 11 -20 °C and -40° C Prony values for ABAQUS.....90

Table 9 - Task 11 -60 °C Prony values for ABAQUS.....91

Chapter 4

Table 1 - Camera properties and DIC Processing settings.....100

Table 2 - Material properties and mesh parameters used for the wedge experiment FEA simulation.....106

Table 3 - Mean and standard deviation for the critical J-integral, K_1 and K_{11} for quasi-static wedge experiments.

.....116

Table 4 - Critical J-integral, K_1 and K_{11} results for the dynamic wedge experiment.....119

Table 5 - Average J integral for all loading conditions.....123

Table 6 - Average K_1 for all loading conditions.....123

TABLE 7 - AVERAGE K_{11} FOR ALL LOADING CONDITIONS.....123

Chapter 5

TABLE 1 - QUASI-STATIC SPECIMEN TYPE AND ENVIRONMENTAL TESTING CONDITIONS.....136

TABLE 2- EXPERIMENTAL SPECIMEN VARIATION FOR IMPACT BEAM BEND EXPERIMENT.....137

TABLE 3 - ENERGY ABSORBED FOR EACH LOADING CONDITION.....153

TABLE 4 - SIMULATION PARAMETERS TO MODEL THE RESPONSE OF STEEL.....165

TABLE 5 – SIMULATION PARAMETERS TO MODEL THE RESPONSE OF ALUMINA.....166

TABLE 6 - TSL PARAMETER DEFINITIONS.....169

TABLE 7 – SIMULATION PARAMETERS TO MODEL THE RESPONSE OF TASK 3 AND TASK 11 FOR A STATIC GENERAL SIMULATION...171

TABLE 8 - SIMULATION PARAMETERS TO MODEL THE RESPONSE OF TASK 3 AND TASK 11 FOR A DYNAMIC EXPLICIT SIMULATION.

.....171

TABLE 9 - CAMERA PROPERTIES AND DIC PROCESSING SETTINGS.....181

TABLE 10 – PRONY SERIES VALUES FOR TASK 3 AND TASK 11 AT 20 °C.....182

1 Introduction

1.1 Motivation

This thesis describes a fundamental methodical study on model composite armours, which aims to explore the influence of the ceramic-polymer interface on overall performance.

Armour protection is an important and complex problem that has existed for as long as there has been warfare. Throughout the ages, there has been an arms race between armours and the projectiles they seek to arrest. Modern armours of interest to this project are composite structures comprising of a ceramic strike face with a ductile polymer backing. These types of armours aim to arrest higher kinetic energy density projectiles, such as those classified as armour piercing. Structurally, the ceramic strike face deforms and disrupts incoming projectiles whilst the polymer backing limits the fragmentation of the ceramic, catches low energy projectile fragments that have penetrated the ceramic layer, as well deforming itself. All these processes are designed to be as energy dispersive as possible, and the interaction between the two materials is thought to be of paramount importance for the overall armour performance.

Ballistic loading is inherently complex due to the dynamic nature of the loading and stress wave generation under impact. This is furthered by the sophisticated materials used. For example, an armour system might consist of Boron Carbide, which is designed to commutate under impact, bonded to UHMWPE, comprising of uni-directional plies in a matrix and designed to be very stiff. The heterogeneity of these materials, coupled with the impedance mismatch at the ceramic-polymer interface, creates a highly complex stress wave loading state.

Significant research has been conducted to understand and develop armours; however, because it is such a complex problem, progress is challenging. This thesis aims to approach this issue from a fundamental standpoint and to reduce the complexity as much as possible to allow the fundamentals of ballistic engineering to be addressed. A methodical study built from base material characterisation with emphasis on the interfacial influence on the overall model armour performance has been proposed and implemented.

1.2 Aims and Overview

This thesis aims to investigate a novel method of measuring model armour performance supported by thorough material and interface characterisation and FEA simulations. The methodology presented in this research allows further insight to be gathered into the fundamental behaviour of armour and could be developed to support industrial armour development and assist the screening of potential armour materials in a quicker and cheaper way than by conventional means.

In this research, these specimens were designed to be as simple as possible to allow the fundamental properties of the material and interface to be reflected in the model armour performance. Specimens were quasi-1D in nature, consisting of strips of ceramic backed with a polymer; variations in the backing and interfacial properties were investigated.

Two urethane-based polymers were chosen for their distinct mechanical differences whilst retaining the same chemical backbone. Further interfacial modifications were made from the presence or absence of a primer surface pre-treatment. The polymers and interfaces used were fully characterised to rate and temperature. Broadly, the research was performed in three sections:

- A thermomechanical analysis of the polymers.
- Characterisation of the interfaces at different rates and temperatures.
- Investigation of model armour specimens under quasi-static and impact loading (up to around 300 m s^{-1}).

All sections are supported with FEA simulations populated using data from characterisation experiments.

1.3 Thesis Structure

Chapter 2 outlines the background literature required to understand the subsequent research. An overview is given on the role and dynamics of armours, alongside the mechanics of the materials used, with an emphasis on the polymers and interface behaviour. Experimental techniques to characterise these are further discussed.

Chapter 3 discusses the thermomechanical characterisation of the two polyurethanes involved in this project. Compression experiments were conducted alongside dynamic mechanical analysis (DMA) experiments, where the latter were used to populate a Prony series to capture the polymer behaviour. Emphasis was placed on the stress relaxation behaviour of the polymer in timescales associated with quasi-static and dynamic loading; this was thought to be influential due to its energy dispersive nature. A novel methodology recently reported in the literature was further developed to determine this material response.

Chapter 4 presents the characterisation of the ceramic-polymer interface and populates a cohesive element material model to be used in FEA simulations presented in chapter 5. Within this chapter, pairs of ceramic strips are bonded with both previously mentioned polyurethanes with and without a primer surface pre-treatment and loaded under a wedge

test configuration at quasi-static and dynamic loading conditions. A further aspect of this chapter was to investigate the use of time-temperature superposition to allow the dynamic behaviour of the interface to be inferred from quasi-static experiments at sub-ambient temperatures.

Chapter 5 develops quasi-1D ceramic strips with polymer backings loaded under quasi-static and impact conditions. When analysing the data obtained, the results of the previously investigated characterisation experiments were considered. Further FEA simulations were conducted predicting the experimental response of these specimens, and these models were populated using data extracted from previous characterisation experiments.

Chapter 6 draws together the different strands of the work, presents more general conclusions and allows for discussion of the potential development of this subject in the future.

2 Background

2.1 Armour

2.1.1 Background

For the duration of warfare, there has been a continuous race between armour and the arms they seek to arrest, which likely began with the advent of clothing [1]. Beginning as hardened leather, armour progressed to chainmail and plate as weapons developed. Metal plate armour reached its peak in the 15th and 16th centuries. However, as gunpowder and small arms developed through the later centuries, this armour was made obsolete, and its use declined. In the 20th century, there was a resurgence in armour development [2] with a focus on ceramic composite armours, for which the earliest evidence was recorded from 1918 [3]. However, a significant focus on ceramic armour development began in the 1960s with pioneering work from Wilkins [4]–[6] and Cook [7] before being employed for the first time in combat in the Vietnam war. This armour was used for flooring for helicopter pilot protection and, between the years of 1968-70, it was estimated the rates of non-fatal and fatal wounds dropped by 27 % and 53 %, respectively, as a result of this protection [3].

For a material to be a good armour material, it must display a specific set of properties: broadly, it must be stiff, strong and lightweight. This can be neatly captured in the material's Cunniff velocity, c^* [8], defined as

$$c^{¿} = \left(\frac{\sigma\varepsilon}{2\rho} \sqrt{\frac{E}{\rho}} \right)^{\frac{1}{3}} \quad (1)$$

Here, σ and ε are the ultimate tensile stress and strain in the material, ρ is its density and E is Young's Modulus. A closer examination of c^*, reveals that it is the product of a specific

strain energy, $\frac{\sigma\varepsilon}{2\rho}$, which is the energy required per unit mass to deform a material to a particular stress, and the longitudinal wave speed $\sqrt{\frac{E}{\rho}}$. These two groups represent two fundamental parameters in armour systems: the ability to absorb energy and the ability to rapidly delocalise stress away from the site of impact, thus utilising a larger proportion of the armour. Therefore, a higher Cunniff velocity broadly represents a better armour material. Plotting these two parameters for a range of materials, Figure 1, gives an initial view of what would make good armour materials.

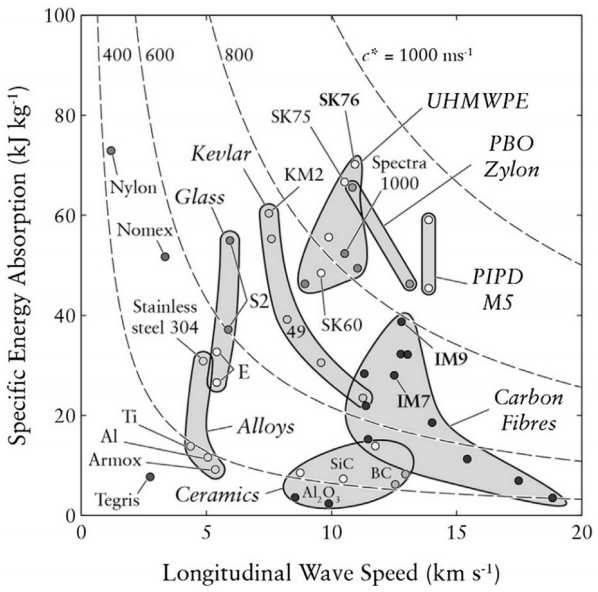


Figure 1 - Common armour materials plotted with lines of constant Cunniff velocity [9]. *A high Cunniff velocity represents a more effective armour for certain ballistic threats.*

Metals are good armour materials, as evidenced by their historic use; however, when specific properties are taken into account, as the Cunniff velocity does, they are greatly inferior to polymers. Polymers, such as Kevlar, have found widespread use, although when used in isolation are known as ‘soft’ armours and are only able to withstand some types of

small arms fire because they lack the hardness to arrest high kinetic energy density munitions [10]. This highlights a limitation of the Cunniff analysis: it cannot capture the full complexity of the interaction; however, it does give a good initial idea of materials of interest for certain ballistic threats.

When considering high energy projectiles such as those classified as armour piercing (AP) [11], no one material has been found that can arrest these munitions at an acceptable mass for body armour. Generally, polymers lack hardness, ceramics are too brittle, and metals are too dense for body armour use. This led to the development of ceramic composite armours. Armours used in military applications consist of a ceramic plate, such as boron carbide, bonded to the polymer backing, typically fibres of ultra-high molecular weight polyethylene (UHMWPE), where brands such as Spectra or Dyneema are common [12]–[15]. Other polymers such as M5 or Zylon, despite displaying excellent potential [16], [17], have not been widely used due to difficulties such as environmental degradation [17]–[19].

The ceramic and polymer plates in composite armours play specific roles: the ceramic strike face behaves as a ‘disrupter’ and the polymer backing as an ‘absorber’ [11], [20]. It is the role of the disrupter to disturb the path of the projectile as much as possible by erosion and fragmentation of the projectile. These are significant energy absorption mechanisms, approximately 40 % of the total [11], and can cause the projectile fragments to disperse over a greater area, reducing the incident kinetic area density. The absorber absorbs the incident energy via deformation and acts to convert this energy into heat. A secondary purpose of the absorber is to delay and limit the failure of the disrupter because, although energy is absorbed during fracture, for ceramics, which have a low fracture surface energy, this is only approximately 5 % of the total energy absorbed [21]. If ceramic fragmentation is

limited, then the multi-hit capacity is improved as the areas compromised will be smaller [22], although mosaic designed armour can be implemented to assist this [23], [24].

Ballistic impact on ceramic composite armours creates stress waves which cause fracture in the ceramic in a conical pattern. A typical impact is shown in Figure 2. The cracks propagate along lines of maximum tensile stress [25] and have been observed experimentally [26]–[28]. These cracks propagate outwards in a conical pattern, which acts to distribute the incident load over a larger area on the backing of the armour, thus significantly aiding projectile defeat. Immediately under the projector tip the ceramic is crushed and pulverises. These fragments can comminute and interlock to further resist the projectile motion, especially if these fragments are still radially confined by the surrounding material. This emphasises the importance of the backing's role in limiting bulk fragmentation of the ceramic. However, of possibly greater importance, is the role of the interface as this determines how these two materials interact and allows them to behave as a composite.

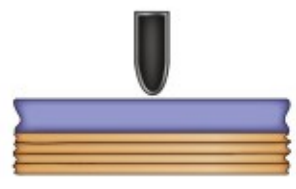
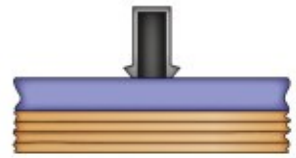
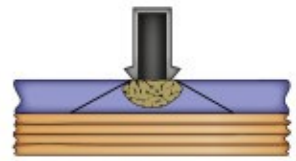
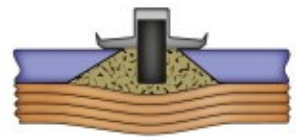
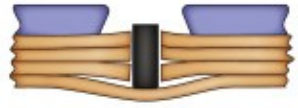
	1. **Starting Position:** Normal impact from hard-cored copper-jacketed small arms bullet.
	2. **Dwell Period:** Jacket starts to get stripped away from the impact zone (and ignored) and the tip of the core gets eroded. The core loses mass and becomes more blunt.
	3. **Cone Formation:** Hertzian cracks initiate around the point of impact, and conoidal fracture follows.
	4. **Core penetrates rubble:** eroded core penetrates commuted areas and continues to erode. The backing material starts to bulge under pressure from the core.
	5. **Through-thickness compression of backing material:** The eroded, blunt core exerts TT compression in the backing material which starts to delaminate.
	6. **Ejection of fractured ceramic:** As the shortened core comes to rest in the rear layers of the backing material, most of the fractured ceramic from the point of impact gets ejected and removes energy from the impact site.

Figure 2 - Typical stages of ballistic impact. Figure modified from [29].

2.1.2 Interface

The interface is highly important in composite body armour because it influences how the two distinct materials interact. Upon impact, stress waves are generated at the point of impact. Generalised, once these reach the interface between two homogenous materials, denoted 1 and 2 below, a portion of this incident energy is transmitted, *T*, and the other reflected, *R*, where the resulting wave amplitudes in the materials, depending upon the relative impedances, *Z*, are defined as,

$$R=\frac{Z_2-Z_1}{Z_1+Z_2} \qquad T=\frac{2Z_2}{Z_1+Z_2} \tag{2) (3}$$

where,

$$Z=\sqrt{\rho E} \tag{4}$$

Therefore, in ceramic-polymer armours, where the ceramic has a high impedance and the polymer a low, a significant proportion of the incident compression wave will be reflected as a tensile wave. Ceramics have notoriously poor tensile strength; therefore, this tensile wave can cause significant fragmentation. It is desirable to limit this fragmentation because this increases the fragmentation and erosion of the projectile, which are significant energy absorption mechanisms, as previously described. Therefore, typical polymer backings possess high stiffness to limit the reflected tensile energy.

Frequently, in composite armours the ceramic and polymer plates are adhered together, which adds further complexity to the interface and stress wave behaviour. The choice of adhesive and thickness strongly influences ballistic performance where, typically, a stiffer adhesive allows for a greater proportion of stress wave transmission into the polymer; however, these adhesives tend to have a smaller failure strain. If the failure strain is too low,

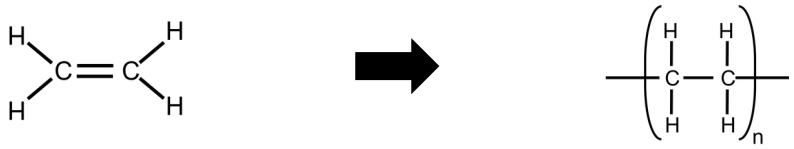
the ceramic and polymer will lose adhesion and the armour performance falls significantly [30]–[35]. Further, because adhesion consists of both chemical and mechanical constituents, the performance of the armour can be influenced by the chemical composition of the surface and its wettability [36], [37]. For these reasons and the high complexity of armours, this thesis presents a methodical study in which quasi-1D geometries are investigated, allowing the fracture paths to be visually observed, and only polymers of the same chemical bases were considered.

2.2 Polymer

2.2.1 Structure

A significant focus of this research will be on the effect of the polymer backing on the interface and overall model armour behaviour.

To understand the behaviour of polymers, it is beneficial to understand the fundamental microstructure because this, ultimately, governs the macroscopic response. Polymers are long chain organic molecules, synthesised from the combination of a very large number of monomers. These monomers react, typically by an addition or condensation reaction, see [38], to create polymer chains that consist of approximately 10^5 – 10^7 repeating units. These can be relatively simple, in the case of polyethylene, Figure 3, or more complex, such as polyurethane, Figure 4, which is the polymer of interest to this project. Polyurethanes are produced by a reaction between a diol and a diisocyanate and, depending upon the constituent materials, can possess a wide range of properties with numerous applications [39]–[41].



Monomer **Repeat unit**

Figure 3 - Monomer and polymer of ethene and repeat unit of polyethylene.

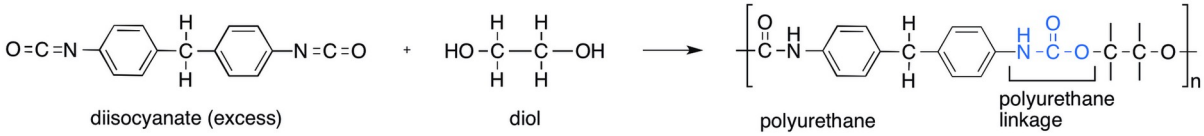


Figure 4 - Synthesis of Polyurethane [42].

Whilst there are strong, covalent bonds between the atoms along each polymer chain, the interaction between molecules comprises weaker Van der Waals forces, although covalent bonds can exist between chains, known as crosslinking. Depending upon the nature of the polymer and the side groups, the polymers can be fully amorphous or local regions of order can emerge as semi-crystallinity.

Due to the relative weakness of the intermolecular forces between polymer chains, the process of reptation can occur [43]–[46]. Broadly, this is the relative movement of polymer chains past one another in a snakelike manner from the motion of kinks. This process is thermally activated and hence, the probability that a segment of a chain has sufficient energy to overcome an activation barrier to motion is dependent upon the temperature. Polymers display an enormous range of stiffnesses from the MPa to the GPa range owing to this phenomenon. If there is insufficient energy for motion, the polymer chains are effectively frozen in place, leading to a stiff polymer response to applied load; this state is known as glassy. If there is sufficient energy, reptation can occur freely and the polymer will deform with little resistance; this state is known as rubbery. The temperature at which the

transition between behaviours occurs is known as the glass or alpha transition temperature although, in reality, this change in behaviour happens over a range of temperatures, whose width depends upon the polymer structure.

The glass transition describes changes in the motion of the main polymer backbone and leads to a substantial change in stiffness (of orders of magnitude). However, polymers often possess further transitions associated with degrees of freedom with lower activation energies, such as the motion of branches or other groups. These transitions typically have less of an effect on the polymer stiffness compared to the glass transition; each transition proceeding downwards in temperature from the glass transition is sequentially known as the beta or gamma transition etc. An overview of the influence these transitions have on the modulus is presented in Figure 5, which also indicates the effect of molecular weight or degree of crystallinity etc.

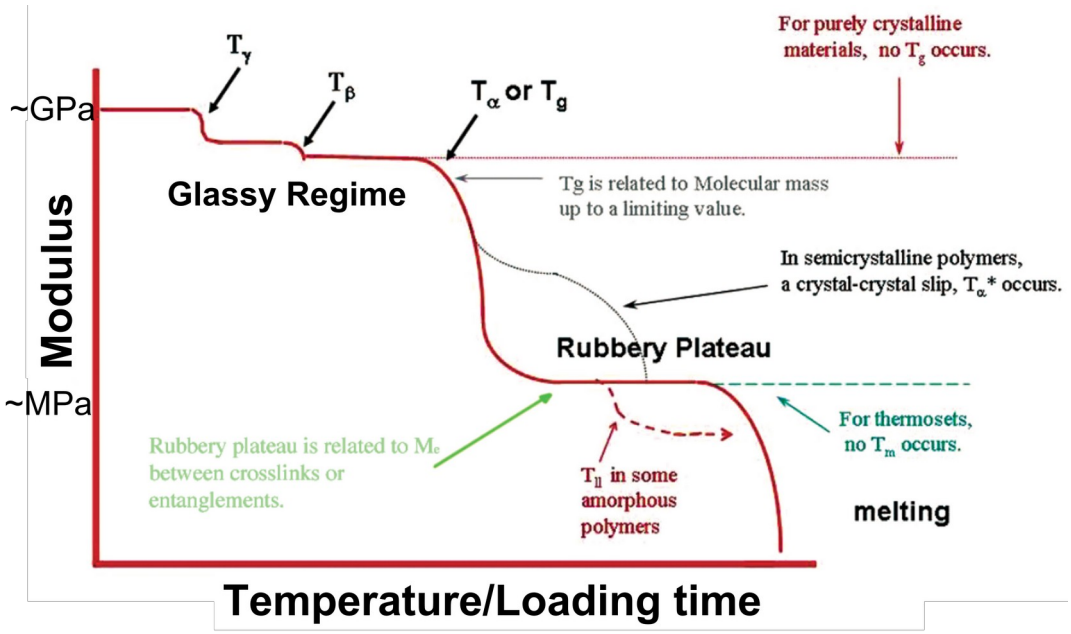


Figure 5 – Schematic of typical variation of modulus with temperature (or loading time). Approximate values of the modulus are marked on the y-axis and the alpha, beta and gamma transitions. The figure has been adapted from [47].

2.2.2 Time Temperature Superposition

As previously discussed, reptation of polymer chains is a process in which an energy barrier must be overcome. As well as being influenced by the temperature, this thermally activated process is also influenced by the time scale over which the polymer is deformed; therefore, an equivalence has been observed between the influence of temperature and time on the polymer [48]; this phenomenon is named the principle of time-temperature superposition (TTS). This principle is extremely useful in polymer engineering because it allows investigations to be conducted into the behaviour under very fast or very slow loading, which can be challenging to measure experimentally, by manipulation of the temperature. Practically, this equivalence of time and temperature dictates that, when plotting a graph of log(modulus) vs log(loading time) of a polymer, temperature manipulation translates into a horizontal shifting of the plot. To make use of this principle a series of experiments, described later, may be performed where the modulus of the polymer is determined, generally, at time scales of around 1 - 100 s, and this is repeated at a range of temperatures. The TTS principle is applied to horizontally shift each isothermal modulus-time curve until they all collapse onto one mastercurve at a chosen reference temperature: this process is demonstrated in Figure 6.

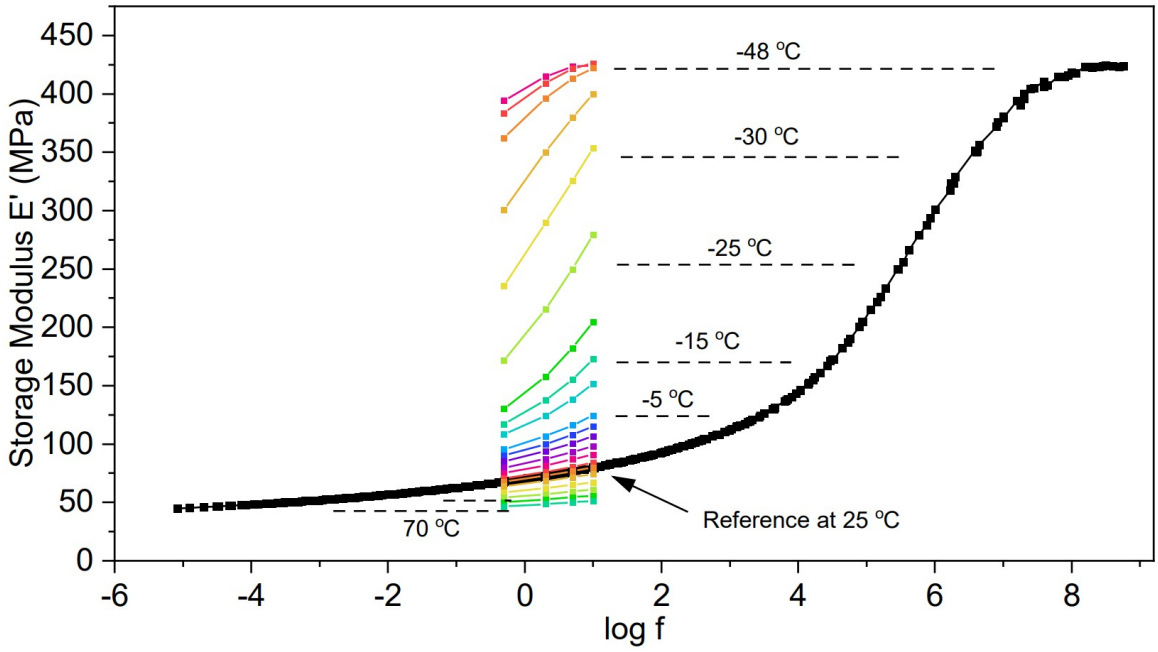


Figure 6 - Example of TTS shift using dynamic mechanical analysis (DMA) data for rubber to create a mastercurve for a 25 °C reference temperature. Figure adapted from [49]

The amount of horizontal shift for each isothermal curve is quantified by the parameter $\log(a_{Ti})$. Williams, Landel and Ferry [50] observed that this parameter varies with temperature according to the relationship

$$\log a_T = \frac{-C_1(T - T_{ref})}{C_2 + (T - T_{ref})}, \tag{5}$$

where C_1 and C_2 are constants and T_{ref} is the chosen reference temperature. Known as the WLF relationship, this is valid around the glass transition temperature, but deviates as the temperature moves away from T_g.

As with all methodologies, there are several limitations to this method. Firstly, mastercurves are created from the horizontal shifting and overlapping of many isotherms. Therefore, errors will accumulate in this shifting process and, as such, the predicted moduli will be less accurate further from the isotherm of the reference temperature. Secondly, this technique assumes that the polymer is behaving as a linear viscoelastic material, so the TTS

mastercurve could be poor at capturing large strain behaviour. Finally, a TTS mastercurve might predict the modulus at a chosen timescale, but inherent differences may still be present between the predicted and experimental behaviour e.g., stress wave propagation in high strain rate experiments. Despite these limitations, TTS is a powerful tool in polymer mechanics and has been well documented [38], [60]–[63].

2.2.3 Modelling

This internal motion of molecular chains is the cause of the time-dependent behaviour exhibited in polymers. Under an applied load or displacement, the polymer chains can rearrange in response to this applied boundary condition and stress relaxation or creep can be observed. This time-dependent nature of the polymer's response causes polymers to be classified as viscoelastic materials [64].

To capture this viscoelasticity, many polymer material models are assembled from series and parallel combinations of springs and dashpots. These springs, which exhibit purely elastic behaviour, can combine with dashpots, which are purely viscous, to model viscoelastic response. Mathematically, the behaviours are expressed as

$$\sigma = E\varepsilon \quad (6) \qquad \sigma = \mu\dot{\varepsilon} \quad (7)$$



Spring



Dashpot

where E is the characteristic stiffness of the spring and μ the viscosity of the dashpot. The simplest models are simply a series or parallel spring-dashpot pairings, known as the Maxwell or Kelvin-Voigt elements respectively. Each captures elements of polymer

behaviour such as stress relaxation in the Maxwell element or creep in the Kelvin-Voigt element. True polymers exhibit both these behaviours, therefore, the models are combined in the form of the standard linear solid (SLS), Figure 7, often known as the Zener model. The model can take either the Maxwell or the Kelvin-Voigt representation, but the fundamental behaviour captured is the same.

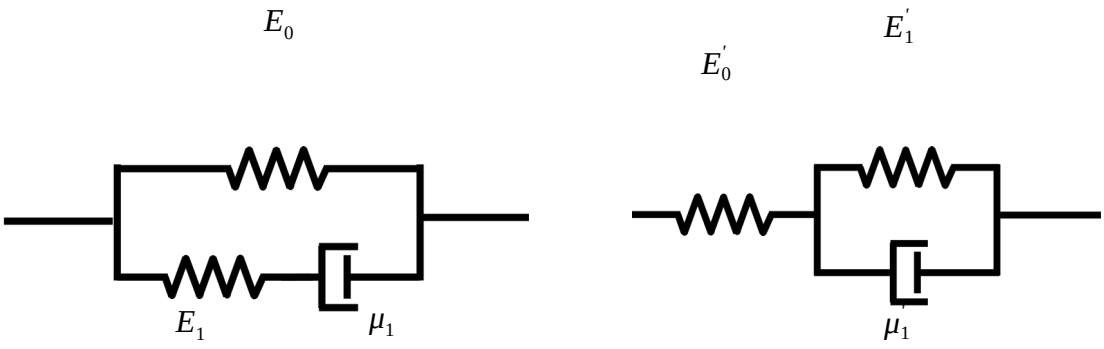


Figure 7 - Standard linear model in either the Maxwell or the Kelvin-Voigt representation.

Mathematically, the Maxwell model can be described by the differential equation

$$\sigma+\frac{\mu_1^{'}}{E_1^{'}}\dot{\sigma}=E_0^{'}\varepsilon+\frac{(E_1^{'}+E_0^{'})\mu_1^{'}}{E_1^{'}}\dot{\varepsilon}, \tag{8}$$

and the Kelvin-Voigt model by

$$\sigma+\frac{\mu_1}{E_0+E_1}\dot{\sigma}=\frac{E_0E_1}{E_0+E_1}\varepsilon+\frac{E_1\mu_1}{E_0+E_1}\dot{\varepsilon}. \tag{9}$$

These can be solved by taking Laplace transforms [38], [63]. The SLS model is able to capture the most fundamental polymer behaviour, but in order to capture the increased complexity of real polymers, multiple SLS elements can be stacked into a generalised Maxwell or Kelvin-Voight model. For this research, the generalised Maxwell model is used, Figure 8. This consists of multiple Maxwell elements, constructed in parallel, for as many branches, *k*, as required to capture the full polymer behaviour.

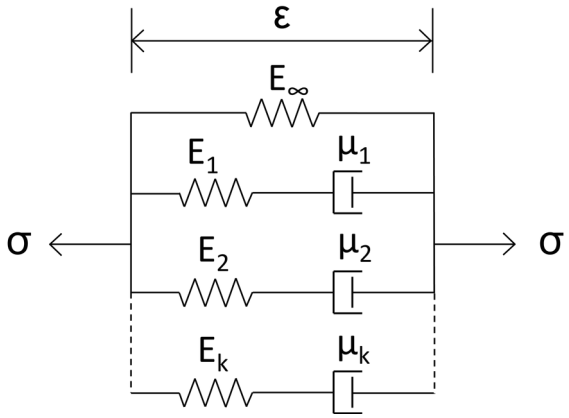


Figure 8 - Spring dashpot representation of a generalised Maxwell model.

For this model, the stress relaxation behaviour, which is of interest to this project, can be captured by equation (10), known as a Prony series. Under a step strain input of magnitude ε_0, the modulus of the material can be represented by,

$$\frac{\sigma(t)}{\varepsilon_0} = E(t) = E_\infty + \sum_{n=1}^{k} E_n e^{\frac{-t}{\tau_n}} \qquad (10)$$

where, $\tau_n = \frac{\mu_n}{E_n}$ (11)

For more general loading cases, the complexity increases because relaxation begins as soon as the loading starts. Therefore, for a general case the stress is calculated from the strain history as

$$\sigma(t) = \varepsilon ¿ \tag{12}$$

where *s* is a dummy variable representing time.

2.2.4 Prony Series Fitting

To model a polymer using a Prony series, values must be assigned to all springs and dashpots. This is achieved by characterising the polymer stiffness over the timescales of interest (either directly or using TTS) and fitting equation (10) to the data. A TTS mastercurve with the assigned Prony fit is presented in Figure 9.

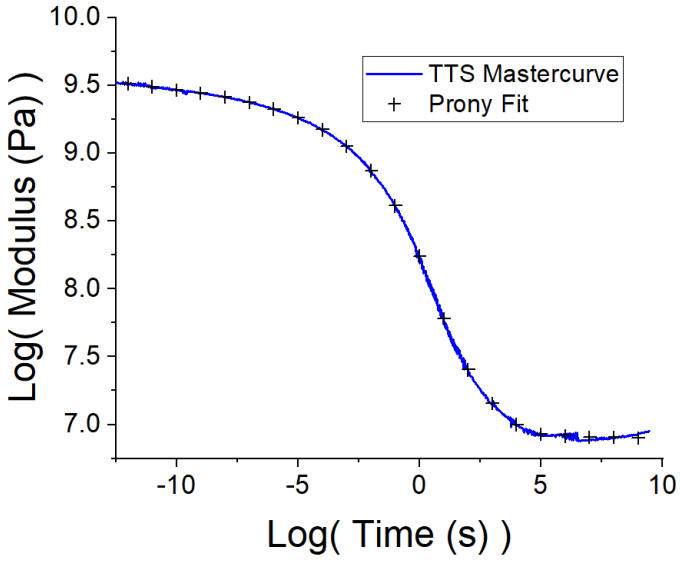


Figure 9 - Example mastercurve with Prony series fit.

The Prony series was fitted using the curve fitting tool in Matlab®. Each branch of the Prony series has a characteristic time constant, equation (11), and in this case these were defined to be spaced by one decade. The determined Prony series was implemented into Abaqus

2021, a commercially available finite element software, to model the behaviour of the polymer under various loading conditions.

2.3 Fracture Mechanics

2.3.1 Fracture Mechanics Basics

To understand how the polymers influence the interfacial behaviour, it is necessary to understand how interfaces fracture and fail.

All materials contain cracks. Cracks are able to propagate under applied loading of sufficient magnitude, and this can occur in a stable or unstable manner. Unstable propagation, known as fast fracture, can be incredibly costly to human life and the economy [65].

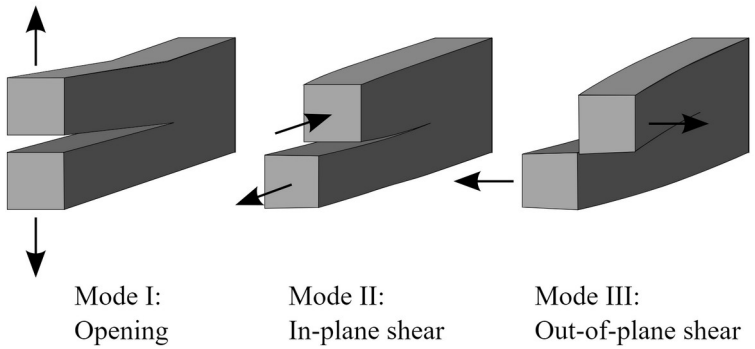


Figure 10 - Crack modes of loading.

Cracks propagate in one of three failure modes, Figure 10. To characterise these cracks and to determine when they will become unstable, there are two widely used methods. The first, the energy release rate, can be thought of as the energy available to the crack for propagation. Proposed by Griffith in 1920 and building upon the work of Inglis [66], this considers a balance between the energy required to create two new fracture surfaces and

the energy stored in the system as elastic energy [67] and released as the crack propagates. Griffith derived the energy release rate as a crack propagates, *G*, as,

$$G = \frac{\sigma^2 \pi a}{E} \tag{13}$$

where σ is the applied stress, a is the crack length, and E is the Young's modulus. Once it becomes energetically favourable for the crack to propagate, it will do so, and this occurs when the combination of crack length and applied stress cause G to exceed the critical energy release rate, G_c, which is itself a property of the material or system [68].

The second method, the stress intensity factor (SIF), is a measure of the stress field around a crack tip. This was proposed by Irwin in 1957 [69], who built upon the work of Westergaard's analytical solution of the stress field surrounding a crack tip [70] to produce a more useable approximate solution valid in the near tip vicinity. This can be generalised as,

$$\sigma_{ij}(r,\theta) = \frac{K}{\sqrt{2\pi r}} f_{ij}(\theta) \tag{14}$$

where,

$$K = \sigma_\infty \sqrt{\pi a} \tag{15}$$

Here, σ_∞ is the tensile stress applied to the bulk material, a is the ellipse half width, r and θ are the radial distance and angle from the crack tip, respectively, and f is the function that the θ term follows; this is dependent upon geometric properties and loading. This approach describes the stress field around a crack tip and once this stress state reaches a critical value described by the critical stress intensity factor, K_c, the crack will propagate.

These two methods, the energy release rate and the stress intensity factor describe the same phenomenon and have been shown to be equivalent. There is a relationship between them described as

$$G=\frac{K_1^2}{E'}+\frac{K_{11}^2}{E'} \tag{16}$$

where E' = E for plane stress and $E^{'}=\frac{E}{1-\nu^2}$ for plane strain conditions. Mode 3 loading has been ignored. These approaches were initially derived using assumptions for perfectly brittle materials, but in reality, there will likely be some plasticity present at the crack tip and modifications can be applied to account for this [69]–[75].

2.3.2 J-integral

The main measurement used to characterise crack growth in this project is the J-integral, which is an extension of the energy release rate described above [76], [77]. The J-integral can account for non-linear fracture mechanics, which G cannot. In addition to this, the stress intensity factors will also be calculated. Both the J-integral, J, and the stress intensity factor, K_1 and K_{11}, approaches describe the same phenomena, and they follow the same equivalence as equation (16). The J-integral for a crack is calculated by taking a path integral that encapsulates the crack tip and begins and ends on the free surfaces of the crack. If this is the case, then the J-integral is equal to the energy available for crack growth. The J-integral is calculated using,

$$J=\int_{\Gamma} W d x_2-t.\frac{\partial u_i}{\partial x_1} d s \tag{17}$$

where Γ is the path contour encircling the crack tip, W is the strain energy density, u is the displacement vector, and x_1 and x_2 are coordinate directions parallel and perpendicular to the direction of crack propagation. The traction vector is $\boldsymbol{t}$, defined as $t = \sigma n$ where $\boldsymbol{n}$ is the unit normal vector at each increment of arc length ds. For the strain energy density, W, the stress strain response does not have to be linear. One assumption made in the J-integral derivation is that all the stored strain energy is available for crack growth. This is not true for plasticity but can be considered valid for monotonically increasing loading. In practice, it is difficult to use a path integral, so Green's theorem can be applied to convert it to an area integral [78] which can be better implemented into FE software.

To determine the J-integral experimentally, the displacement around the crack tip is required. In this study, digital image correlation, a non-contact displacement measurement technique as will be described later, was used. This technique was able to calculate the desired crack time and the field was subsequently inputted into Abaqus to calculate the J-integral. See Marrow and Barhli [79] or Chapter 4 for a detailed description of this method.

2.3.3 Modelling

The J-integral was used to characterise the crack at many points during loading. This behaviour can be implemented into finite element simulations, and this was performed using a traction separation law (TSL). These results were then used to populate cohesive elements in Abaqus. To be able to model a propagating crack, the TSL makes use of the relation,

$$\sigma(\Delta) = \frac{dJ}{d\Delta} \tag{18}$$

where Δ is the opening displacement at the crack tip, σ is the traction normal to the crack and J represents the J-integral [76], [77]. Therefore, if the evolution of the J-integral with tip opening displacement is known, then the behaviour of the crack can be modelled from the gradient of this relationship [80]. An idealised J-integral vs tip opening relation would start from zero, where the crack is fully closed, before rising to a critical steady state value where the crack is propagating; see [81] for a detailed description. Therefore, the gradient of this curve would rise to a peak before reducing, and this can be approximately represented by the relationship in Figure 11. The behaviour of the element beyond δ^*, where the onset of damage begins, can take a variety of shapes; however, for this study, a linear damage evolution model was chosen.

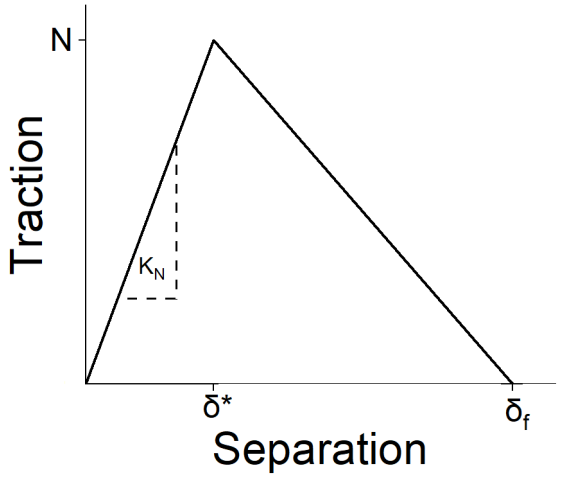


Figure 11 - Example TSL response.

2.4 Experimental Techniques

2.4.1 Thermomechanical Characterisation

2.4.1.1 Dynamic Mechanical Analysis

In this study, a variety of methods has been used to characterise the polymer, interface and armour response. Initially, polymer characterisation was performed using dynamic mechanical analysis (DMA).

Polymers are viscoelastic materials whose mechanical properties have a heavy dependence upon rate and temperature. These loading and environmental conditions affect not only the modulus but also the proportion of the response governed by elastic and viscous processes. This response is commonly characterised by DMA [82]–[85]. Here, polymer samples are loaded at a range of temperatures in configurations such as tension, single/dual cantilever, three/four point bend, torsion etc. Two testing procedures were used in this project: stress relaxation and oscillatory loading.

For stress relaxation experiments, specimens are loaded to a given displacement and the force required to maintain this displacement is recorded over a period of time. This relaxation is governed by the viscous component of the polymer response. For oscillatory experiments, a sinusoidal stress is applied and the force-displacement response is determined. Depending upon the observed phase difference between the applied force and resulting displacement, the polymer response can be deconstructed into its viscous and

elastic components. If the loading is perfectly in phase with the displacement, the material is purely elastic; if there is a 90° phase difference between them, the material is purely viscous. A polymer, due to its viscoelastic nature, will typically lie in between these extremes, but the nature of the response will change with temperature and strain rate. Typically, polymers are loaded at frequencies, *f*, between 10^{-2} – 10 Hz and the applied strain rate, $\dot{\varepsilon}$, can be approximated by the Cox-Merz rule: $\dot{\varepsilon} = 2\pi f$ [86].

A typical output from a DMA experiment is presented in the form of a complex modulus, E^*, which comprises of the storage modulus, E', and the loss modulus, E'':

$$E^{*} = E' + iE'', \tag{19}$$

with a further definition of the loss tangent, or tan delta, defined as

$$\tan(\delta) = \frac{E''}{E'}. \tag{20}$$

Here, the storage modulus captures the elastic proportion of the material response whilst the loss modulus captures the viscous component and tan delta defines the ratio of the two, and hence the phase difference between force and deformation. Tan delta is frequently used as a means to locate transitions, such as the glass transition, in the polymer because a peak is observed in this parameter as the polymer passes through the transition. An example of a typical DMA output for natural rubber is presented in Figure 12 [87], and this clearly displays the frequency and temperature dependence of the polymer.

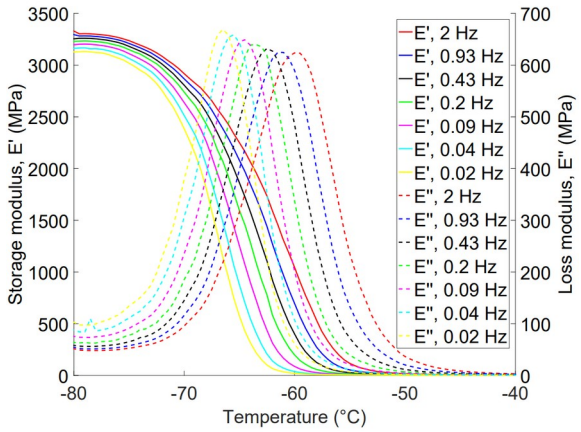


Figure 12A - Storage and loss modulus

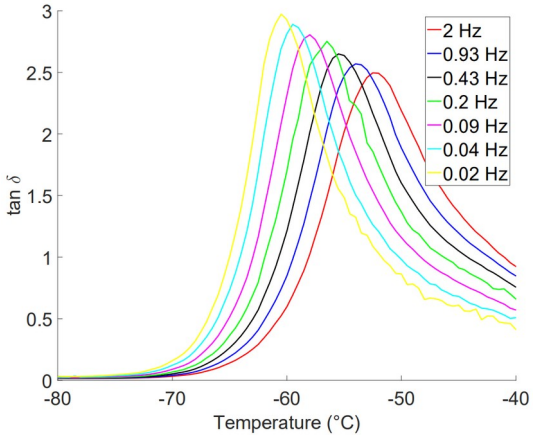


Figure 12B – Tan delta

Figure 12 – Typical DMA response curve. This is example data performed on natural rubber [87].

Whilst DMA is a powerful tool for polymer characterisation and is frequently used to provide the base data for time-temperature superposition, it is not without limitations. Most notably, the material response is dependent upon the configuration, tension/single cantilever etc., as well as specimen geometry and clamping pressure, with each option for these presenting particular merits and drawbacks [52]–[59]. Additionally, data collection can become more difficult for certain loading configurations, such as three-point bend, above the glass transition temperature because of the very low specimen stiffnesses. Therefore, care should be taken upon selection of the loading configuration and temperature range of interest.

2.4.1.2 Differential Scanning Calorimetry

Polymers can be further characterised by the method of differential scanning calorimetry (DSC). This is concerned with the heat flux required to heat or cool a known sample along a temperature ramp. The energy required to change the temperature is a function of the heat capacity of the material as well as contributions from any endothermic or exothermic

processes. Therefore, by comparing the sample to an inert reference, it is possible to relate changes in heat flow to energetic changes. In a polymer, these changes can be caused by transitions, recrystallisation, melting, etc. [88], [89]. Example results are presented in Figure 13; here, two polyurethanes were heated from -90 °C to 120 °C at a rate of 3 °C min^{-1}. The behaviour of these polymers is relatively simple with one main transition, the glass transition, at approximately 15 °C (blue) and 50 °C (red).

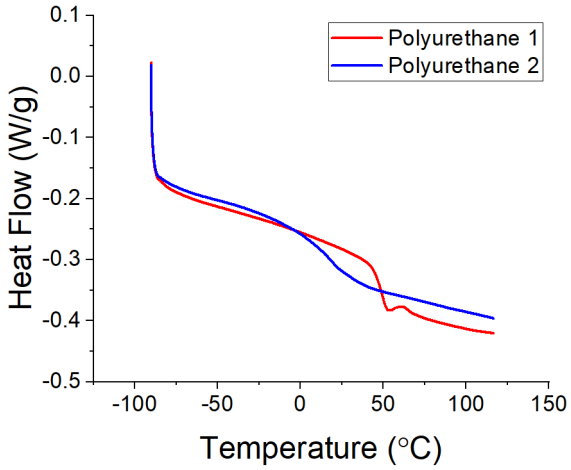


Figure 13 - Example DSC results for two polyurethanes. These materials were heated at a rate of 3 °C min^{-1} from -90 °C to 120 °C.

The polymers used in this study had relatively straightforward responses over the temperature range of interest. However, when there are multiple overlapping processes, it can be challenging to discern them, which is a limit to the DSC technique. In this case, modulated DSC (MDSC) can be used in which a sinusoidal oscillation is superposed on the heating ramp, allowing the separation of reversing and kinetic components of the heat capacity [90].

2.4.2 Quasi-static Strain rates

The quasi-static mechanical behaviour, 10^{-3} - 10^{-1} s^{-1}, of the polymers is of interest to this project. To achieve these strain rates, an Instron 3400 Series screw driven compression frame was used. The force-displacement output from this machine was used to calculate the stress-strain response. An environmental chamber was used in combination with liquid nitrogen to perform experiments at sub-ambient conditions, down to -60 °C.

Specimens were compressed between two hardened steel plattens. The displacement was recorded either through the position of the crosshead or via an extensometer clipped to the plattens, and the force was measured using the in-built load cell. To minimise barrelling of the specimens, the platten faces were lubricated using Vaseline® at ambient conditions and AEROSPEC 201 Graphited grease at sub-ambient conditions.

2.4.2.1 Analysis

From the force-displacement relationship of the specimens, the stress-strain response can be determined. The nominal strain, ε_N, and nominal stress, σ_N, of the material can be calculated using the relations,

$$\varepsilon_N = \frac{L_0 - L}{L_0} \quad (21) \qquad \sigma_N = \frac{F}{A_0} \quad (22)$$

where, F is the measured force, L and A are the lengths and cross-sectional area of the specimen and the subscript 0 denotes the initial configuration. In order to calculate the true strain rate, conservation of volume was assumed so that $AL = A_0 L_0$, and the true strain, ε_T, and true stress σ_T, can be calculated as,

$$\varepsilon_T = -\log\left(1 - \varepsilon_N\right) \quad (23) \qquad \sigma_T = \sigma_N\left(1 - \varepsilon_N\right) \quad (24)$$

Here, compressive stress and strain have been defined to be positive, and this will be the convention for this research unless otherwise stated.

2.4.2.2 Three-Point Bend

One geometry of particular interest to this project was three-point bend loading, in which a rectangular prismatic specimen is simply supported at the two ends and loaded by a point load at the centre, Figure 14. The load was applied quasi-statically using the screw driven apparatus, and the force and displacement were measured. Using this, the maximum breaking stress of the material can be determined using the beam-bend relationship:

$$\sigma = \frac{M y_{max}}{I} \tag{25}$$

where, M is the applied moment, defined as $\frac{FL}{4}$ for a centrally loaded beam where F is the applied force and L is the span of the supports. The maximum distance from the neutral axis is denoted y_{max}, which is half the specimen height, and I is the second moment of area. Only rectangular beams are of interest so the second moment of area is defined as,

$$I = \frac{b h^3}{12} \tag{26}$$

where b is the width of the specimen and h is the height.

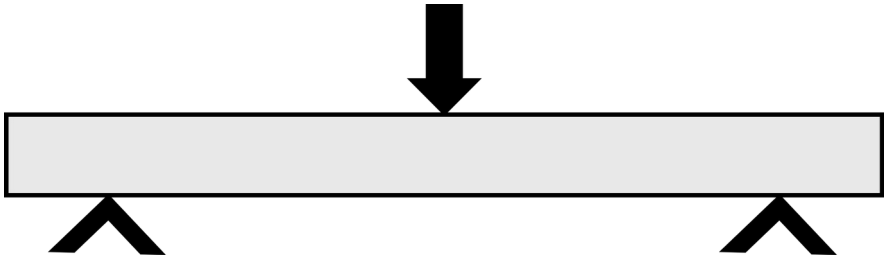


Figure 14 - Schematic of three-point bend loading.

2.4.3 Dynamic Strain Rates

2.4.3.1 Split Hopkinson Pressure bar

Material characterisation becomes more difficult under dynamic conditions, i.e. strain rates of order 1000 s^{-1} or above, because the loading timescales of interest are now comparable to the natural frequency of the specimen. Therefore, care must be taken to ensure a state of static equilibrium is achieved within the material to minimise the effects of inertia. A number of techniques for high strain rate characterisation are described in the literature, such as the Taylor impact test [91], the plate impact test [92], [93] or the modified drop weight [94]. However, the technique of interest to this project was the Split Hopkinson Pressure Bar (SHPB). Since its development [95], [96], the Hopkinson bar has become a widely used apparatus to investigate the dynamic properties of materials and is capable of a wide range of materials including soft materials, such as polymers, which are of particular interest to this research. Loading can be performed in compression, tension and torsion with many thorough reviews present in the literature [97]–[103].

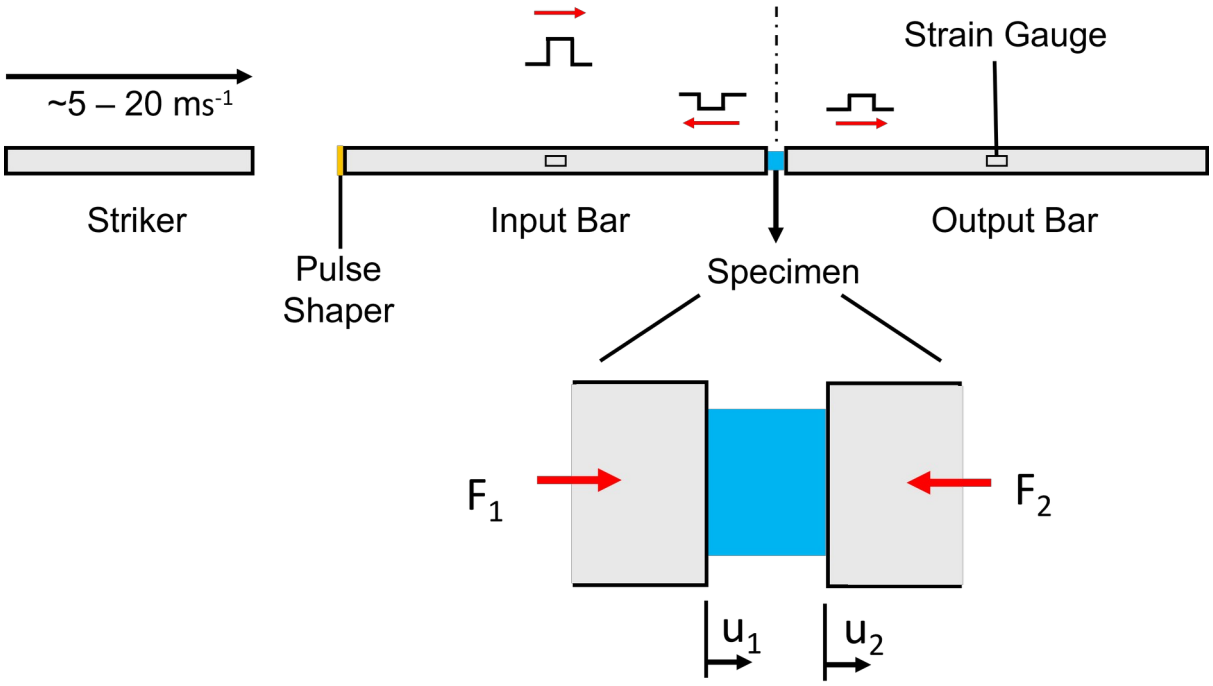


Figure 15 - Schematic of the Hopkinson bar experiment.

A schematic of this technique is presented in Figure 15, where the apparatus comprises of a striker bar, an input bar and an output bar. Typically the input and output bars are on the order of 1 m long, although very long versions are found which can achieve large strains at intermediate loading speeds [104]. The striker is significantly shorter, and its length governs the duration of loading of the specimen. This striker bar is fired using pressurised gas and impacts the input bar in a planar impact at approximately 10-20 m s^{-1}. This impact creates a stress wave in the input bar, ideally as a square wave, where the maximum stress, σ, is proportional to the density, ρ, longitudinal wave speed, c, and particle velocity, v, in the bar, as,

$$\sigma = \frac{\rho c v}{2} \tag{27}$$

This stress pulse propagates along the bar and interacts with the specimen. Upon its interaction, reflected and transmitted stress waves are generated, which can be used to

calculate the stress and strain in the material being characterised. Strain gauges are frequently used to measure these stress waves, although alternate measurement systems are available, e.g. piezoelectric gauges [105], [106]. The stress and strains in the specimen can be calculated through the relations,

$$\varepsilon_s = 2\frac{c_b}{L_s}\int_0^t \varepsilon_R\, dt \quad (28) \qquad \sigma_s = \frac{E_b A_b}{A_s}\varepsilon_T \quad (29)$$

where *c* is the wave speed in the bar, *L* is the length of the specimen, *A* is the cross-sectional area and *E* is the Young's modulus. The subscripts *b* and *s* denote the bar and specimen, respectively. The strains from the transmitted signal, ε_T, and the reflected signal, ε_R, are found from the strain gauges on the input and output bars. For these equations to be valid, the specimen must be in a state of dynamic equilibrium, which is to say the force exerted on the specimen from the input bar is equal to that exerted by the output bar and thus, the relation $F_T = F_I + F_R$ is valid.

The requirement for the specimen to be in a state of dynamic equilibrium demonstrates one of the limitations of the Hopkinson bar apparatus. A general rule of thumb is that dynamic equilibrium is achieved after the time for the stress wave within the specimen to propagate along the length of this specimen three times; however, for soft materials such as polymers, this can be a significant duration of loading. A further issue arises when using soft materials because there is often a significant impedance mismatch between the input bar and specimen. This would cause a significant proportion of the incident signal to be reflected with a small proportion transmitted, which means the signal to noise ratio would be poor in the output bar [107]. To mitigate these effects, the impedance of the bar must be suitably chosen depending on the specimen. This can be accounted for by reducing the cross-

sectional area of the bars, using a hollow geometry or using polymers or low density metals [99], [107]–[112].

Another challenge of the Hopkinson bar apparatus is the influence of specimen inertia because it can be challenging to separate this from the material response. Pulse shaping, by means of adding a small deformable insert between the striker and the input bar, is often used to reduce the high frequency components of the input pulse. This reduces early rapid loading of the specimen and also allows for a more constant loading rate. A constant strain rate is particularly important for polymers because the material properties are often highly strain rate dependent. The choice of the specimen geometry is influential on the inertial effects [113] and geometries are often limited to ratios of 1:1 to 1:2 [114]; however, it is possible to approximate these effects [115].

2.4.3.2 Impact

Impact experiments were performed using the same geometry as the previously discussed quasi-static three-point bend specimens; however, loading was now performed under dynamic impact loading conditions. Specimens were impacted with 30 mm EN16 steel projectiles of 8 mm diameter and the specimens had a cylindrically rounded tip of 4 mm radius, Figure 16. This projectile was fired using compressed Nitrogen at speeds ranging from 50 – 100 m s^{-1}. Before impact, the sabot was stripped using a sabot stripper and then a light gate was used to determine the impact speed. Specimens were imaged from the side using a Photron Fastcam SA-Z high speed camera at frame rates up to 100,000 fps.

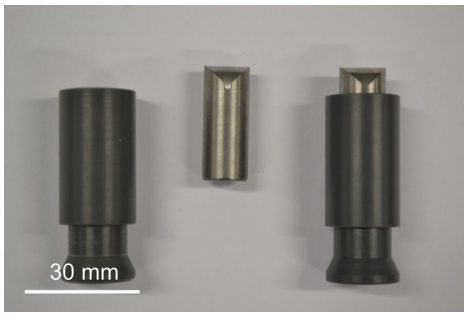


Figure 16 - Projectile and sabot used for impact experiments.

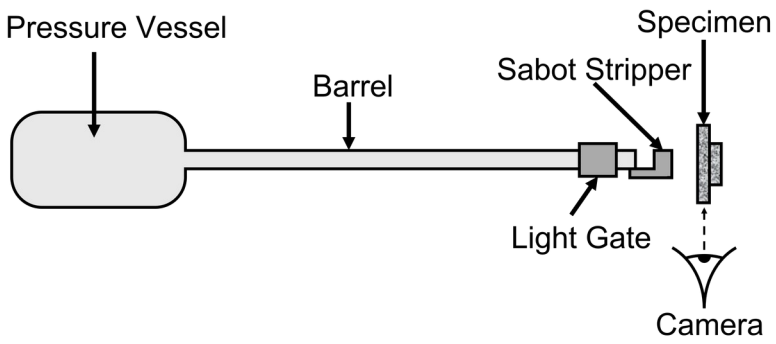


Figure 17 - Schematic for the experimental set up for impact loading experiments.

2.4.4 Digital Image Correlation

Digital image correlation (DIC) is a non-contact imaging technique that is used to determine the displacement across a surface. Introduced in the 1980s [116]–[120], this technique has great advantages over conventional displacement measurement methods because it allows the generation of a full field displacement map, as opposed to the single data points at each strain gauge location for example. Other full field optical techniques exist [121]–[123], although DIC is the most commonly used.

In general, a specimen is imaged during deformation and this method works to compare images between the undeformed and deformed state and uses the differences to calculate the displacement field. To enable tracking between images, the specimen surface is given a randomised texture which can be grouped into unique subsets. Frequently this is achieved

using speckles of black and white paint. However, any surface modification that would produce an observable randomised pattern could be used. The pattern is split into unique subsets of a user-defined number of pixels in area. Each subset is tracked between images through the optimisation of a cross correlation criteria [124]–[126] and can allow first and second order deformations of each subset to be measured [127], the specifics of which are user defined depending on the level of accuracy desired. A displacement map consisting of the deformation and motion of these subsets can be generated and from this stress and strain fields can be determined. The DIC methodology can allow for sub-pixel accuracy in these measured displacements [128]. For further details see [124], [129], [130], although many comprehensive reviews are available.

Whilst not of direct interest to his study, many extensions have been made to this methodology. For example, multiple cameras can be introduced to allow for 3D-DIC on curved surfaces or for 2D surfaces with excessive out-of-plane deformation [131], [132] or, if there are suitable internal features to track, X-rays can be used to record and track internal volumes known as digital volume correlation (DVC) [133], [134].

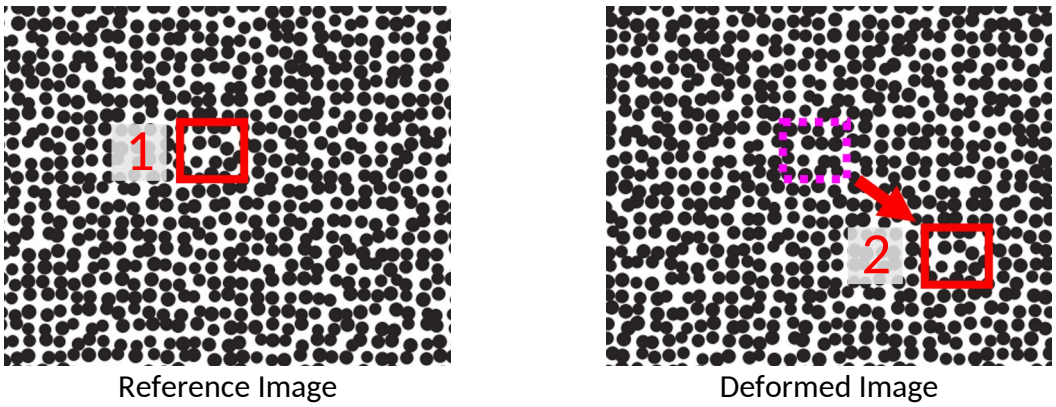


Figure 18 - Example speckle pattern used for DIC with subset tracking from initial position, 1, to final deformed position, 2.

2.5 References

[1] R. Laible, *Ballistic materials and penetration mechanics*, vol. 5. Elsevier, 2012.

[2] R. Shephard and M. Helliker, “The Development of UK Body Armour and Helmets from WWII to the end of the 20 th Century,” 2014.

[3] S. Dunstan, *Flak jackets: 20th century military body armour*, no. 157. Osprey publishing, 1984.

[4] M. Wilkins, C. Honodel, and D. Sawle, “APPROACH TO THE STUDY OF LIGHT ARMOR.,” California Univ., Livermore. Lawrence Radiation Lab., 1967.

[5] M. Wilkins, “Second progress report of light armor program,” Lawrence Livermore National Lab.(LLNL), Livermore, CA (United States), 1967.

[6] M. L. Wilkins, “Third progress report of light armor program,” CALIFORNIA UNIV BERKELEY BERKELEY United States, 1968.

[7] R. L. Cook, “Hard faced ceramic and plastic armour,” *US 350983 Goodyear Aerospace*, 1970.

[8] P. M. Cunniff, “Dimensionless parameters for optimization of textile-based body armor systems,” in *Proceedings of the 18th international symposium on ballistics*, 1999, vol. 2, pp. 1303–1310.

[9] K. Karthikeyan, B. P. Russell, N. A. Fleck, H. N. G. Wadley, and V. S. Deshpande, “The effect of shear strength on the ballistic response of laminated composite plates,” *European Journal of Mechanics-A/Solids*, vol. 42, pp. 35–53, 2013.

[10] “Ballistic Resistance of Body Armor NIJ Standard-0101.0.”

[11] P. J. Hazell, *Armour: materials, theory, and design*. CRC press, 2022.

[12] Honeywell Spectra, “https://industrial.honeywell.com/us/en/applications/armor-ballistic-protection.”

[13] DSM Dyneema, “https://www.dsm.com/dyneema/en_GB/our-products/dyneema-fiber.html.”

[14] B. P. Russell, K. Karthikeyan, V. S. Deshpande, and N. A. Fleck, “The high strain rate response of ultra high molecular-weight polyethylene: from fibre to laminate,” *Int J Impact Eng*, vol. 60, pp. 1–9, 2013.

[15] D. Zhang, *Advances in filament yarn spinning of textiles and polymers*. Elsevier, 2014.

[16] O. C. van der Jagt and A. Beukers, “The potential of a new rigid-rod polymer fibre (M5’) in advanced composite structures,” *Polymer (Guildf)*, vol. 40, no. 4, pp. 1035–1044, 1999.

[17] P. M. Cunniff, M. A. Auerbach, E. Vetter, and D. J. Sikkema, “High performance ‘M5’ fiber for ballistics/structural composites,” in *23rd. Army science conference*, 2002, p. 1e8.

[18] X. Chen and Y. Zhou, “6 - Technical textiles for ballistic protection,” in *Handbook of Technical Textiles (Second Edition)*, A. R. Horrocks and S. C. Anand, Eds. Woodhead Publishing, 2016, pp. 169–192. doi: https://doi.org/10.1016/B978-1-78242-465-9.00006-9.

[19] Environmental degradation causes recall of Zylon-based Armour, “http://www.cnn.com/2005/US/06/22/body.armor.defects/index.html.”

[20] W. A. Gooch, “2011 OVERVIEW OF THE DEVELOPMENT OF CERAMIC ARMOUR TECHNOLOGY: PAST, PRESENT AND THE FUTURE,” in *Ceramic Engineering and Science Proceedings*, 2011, vol. 32, no. 5, pp. 195–213.

[21] P. C. Reijer, “Impact on ceramic faced armour PhD thesis,” *Technical University Delft, Delft, The Netherlands*, 1991.

[22] K. Akella and N. K. Naik, “Composite armour—A review,” *J Indian Inst Sci*, vol. 95, no. 3, pp. 297–312, 2015.

[23] B. James, “Practical issues in ceramic armour design,” *Ceramic transactions*, vol. 134, pp. 33–44, 2002.

[24] D. Hu, Y. Zhang, Z. Shen, and Q. Cai, “Investigation on the ballistic behavior of mosaic SiC/UHMWPE composite armor systems,” *Ceram Int*, vol. 43, no. 13, pp. 10368–10376, Sep. 2017, doi: 10.1016/J.CERAMINT.2017.05.071.

[25] H. Hertz, “On the contact of elastic solids,” *Z. Reine Angew. Mathematik*, vol. 92, pp. 156–171, 1881.

[26] M. M. Chaudhri and S. M. Walley, “Damage to glass surfaces by the impact of small glass and steel spheres,” *Philosophical Magazine A*, vol. 37, no. 2, pp. 153–165, 1978.

[27] J. C. LaSalvia *et al.*, “Shear localization in a sphere-impacted armor-grade boron carbide,” in *23rd International Symposium on Ballistics Tarragona, Spain*, 2007, pp. 1329–1337.

[28] J. C. LaSalvia, M. J. Normandia, H. T. Miller, and D. E. MacKenzie, “Sphere Impact Induced Damage in Ceramics: I. Armor-Grade SiC and TiB2,” in *Advances in Ceramic Armor: A Collection of Papers Presented at the 29th International Conference on Advanced Ceramics and Composites, January 23-28, 2005, Cocoa Beach, Florida, Ceramic Engineering and Science Proceedings*, 2005, vol. 26, pp. 170–181.

[29] I. G. Crouch, G. v Franks, C. Tallon, S. Thomas, and M. Naebe, “7 - Glasses and ceramics,” in *The Science of Armour Materials*, I. G. Crouch, Ed. Woodhead Publishing, 2017, pp. 331–393. doi: https://doi.org/10.1016/B978-0-08-100704-4.00007-4.

[30] R. Zaera, S. Sánchez-Sáez, J. L. Pérez-Castellanos, and C. Navarro, “Modelling of the adhesive layer in mixed ceramic/metal armours subjected to impact,” *Compos Part A Appl Sci Manuf*, vol. 31, no. 8, pp. 823–833, 2000.

[31] W. Seifert, E. Strassburger, S. Grefen, and S. Schaare, “Experimental study about the influence of adhesive stiffness to the bonding strengths of adhesives for ceramic/metal targets,” *Defence technology*, vol. 12, no. 2, pp. 188–200, 2016.

[32] A. Prakash, J. Rajasankar, N. Anandavalli, M. Verma, and N. R. Iyer, “Influence of adhesive thickness on high velocity impact performance of ceramic/metal composite targets,” *Int J Adhes Adhes*, vol. 41, pp. 186–197, 2013.

[33] J. López-Puente, A. Arias, R. Zaera, and C. Navarro, “The effect of the thickness of the adhesive layer on the ballistic limit of ceramic/metal armours. An experimental and numerical study,” *Int J Impact Eng*, vol. 32, no. 1–4, pp. 321–336, 2005.

[34] M. F. Buchely, J. D. Acuna, and A. Maranon, “Effect of the bonding layer on ballistic performance of personal protective plate armor,” in *ECCM 2012-Compos. Venice, Proc. 15th Eur. Conf. Compos. Mater*, 2012, pp. 24–28.

[35] Y. Gao, W. Zhang, P. Xu, X. Cai, and Z. Fan, “Influence of epoxy adhesive layer on impact performance of TiB2-B4C composites armor backed by aluminum plate,” *Int J Impact Eng*, vol. 122, pp. 60–72, 2018.

[36] A. Harris, B. Vaughan, J. Yeomans, P. Smith, and S. Burnage, “Ballistic testing of surface-treated alumina and silicon carbide with improved adhesive bond strength,” *Int J Appl Ceram Technol*, vol. 14, no. 3, pp. 323–330, May 2017, doi: 10.1111/ijac.12668.

[37] A. J. Harris, B. Vaughan, J. A. Yeomans, P. A. Smith, and S. T. Burnage, “Surface preparation of silicon carbide for improved adhesive bond strength in armour applications,” *J Eur Ceram Soc*, vol. 33, no. 15–16, pp. 2925–2934, Dec. 2013, doi: 10.1016/j.jeurceramsoc.2013.05.026.

[38] N. G. McCrum, C. P. Buckley, C. P. Buckley, and C. B. Bucknall, *Principles of polymer engineering*. Oxford University Press, USA, 1997.

[39] A. Reghunadhan and S. Thomas, “Polyurethanes: structure, properties, synthesis, characterization, and applications,” in *Polyurethane polymers*, Elsevier, 2017, pp. 1–16.

[40] M. Szycher, *Polyurethanes*. CRC press Boca Raton, 2013.

[41] R. S. F. N. Hirzin, A. D. Azzahari, R. Yahya, A. Hassan, and H. Tahir, “The behavior of semi-rigid polyurethane film based on functionalized rubber by one-shot and two-shot method preparation,” *J Mater Sci*, vol. 53, no. 18, pp. 13280–13290, 2018.

[42] “RLM0518, CC BY-SA 3.0 <https://creativecommons.org/licenses/by-sa/3.0>, via Wikimedia Commons.”

[43] P.-G. de Gennes and P.-G. Gennes, *Scaling concepts in polymer physics*. Cornell university press, 1979.

[44] M. Doi, S. F. Edwards, and S. F. Edwards, *The theory of polymer dynamics*, vol. 73. oxford university press, 1988.

[45] M. Doi and S. F. Edwards, “Dynamics of concentrated polymer systems. Part 1.—Brownian motion in the equilibrium state,” *Journal of the Chemical Society, Faraday Transactions 2: Molecular and Chemical Physics*, vol. 74, pp. 1789–1801, 1978.

[46] P.-G. de Gennes, “Reptation of a polymer chain in the presence of fixed obstacles,” *J Chem Phys*, vol. 55, no. 2, pp. 572–579, 1971.

[47] I. PerkinElmer, “Dynamic Mechanical Analysis (DMA)-A Beginner’s Guide,” *Introduction to DMA*, pp. 1–23, 2008.

[48] A. v Tobolsky, “Elastoviscous properties of polyisobutylene. VI. Relation between stress relaxation modulus and dynamic modulus,” *J Am Chem Soc*, vol. 74, no. 15, pp. 3786–3788, 1952.

[49] H. Chen, “Thermomechanical behaviours of unfilled/filled thermoplastic polyurethane,” University of Oxford, 2021.

[50] M. L. Williams, R. F. Landel, and J. D. Ferry, “The temperature dependence of relaxation mechanisms in amorphous polymers and other glass-forming liquids,” *J Am Chem Soc*, vol. 77, no. 14, pp. 3701–3707, 1955.

[51] H. Eyring, “Viscosity, plasticity, and diffusion as examples of absolute reaction rates,” *J Chem Phys*, vol. 4, no. 4, pp. 283–291, 1936.

[52] S. Deng, M. Hou, and L. Ye, “Temperature-dependent elastic moduli of epoxies measured by DMA and their correlations to mechanical testing data,” *Polym Test*, vol. 26, no. 6, pp. 803–813, Sep. 2007, doi: 10.1016/j.polymertesting.2007.05.003.

[53] I. R. Henriques, L. A. Borges, M. F. Costa, B. G. Soares, and D. A. Castello, “Comparisons of complex modulus provided by different DMA,” *Polym Test*, vol. 72, pp. 394–406, 2018.

[54] I. M. McAninch, G. R. Palmese, J. L. Lenhart, and J. J. la Scala, “DMA testing of epoxy resins: The importance of dimensions,” *Polym Eng Sci*, vol. 55, no. 12, pp. 2761–2774, 2015.

[55] J. Duncan, “Principles and applications of mechanical thermal analysis,” *Principles and applications of thermal analysis*, vol. 2, pp. 119–163, 2008.

[56] G. W. Ehrenstein, G. Riedel, and P. Trawiel, “Dynamic Mechanical Analysis (DMA),” in *Thermal Analysis of Plastics*, Carl Hanser Verlag GmbH & Co. KG, 2004, pp. 236–299. doi: doi:10.3139/9783446434141.006.

[57] P. Lee-Sullivan and D. Dykeman, “Guidelines for performing storage modulus measurements using the TA Instruments DMA 2980 three-point bend mode: I. Amplitude effects,” *Polym Test*, vol. 19, no. 2, pp. 155–164, 2000.

[58] R. Kazakevičiūtė-Makovska, S. Mogharebi, H. Steeb, G. Eggeler, and K. Neuking, “A critical assessment of experimental methods for determining the dynamic mechanical characteristics of shape memory polymers,” *Adv Eng Mater*, vol. 15, no. 8, pp. 732–739, 2013.

[59] N. M. Alves, J. F. Mano, and J. L. G. Ribelles, “Analysis of the thermal environment inside the furnace of a dynamic mechanical analyser,” *Polym Test*, vol. 22, no. 4, pp. 471–481, 2003.

[60] E. Tombari and G. P. Johari, “Endothermic effects on heating physically aged sucrose glasses and the Clausius theorem violation in glass thermodynamics,” *J Phys Chem B*, vol. 124, no. 10, pp. 2017–2028, 2020.

[61] K. S. Cho, “Time-Temperature Superposition,” in *Viscoelasticity of Polymers*, Springer, 2016, pp. 437–457.

[62] J. D. Ferry, *Viscoelastic properties of polymers*. John Wiley & Sons, 1980.

[63] A. S. Wineman and K. R. Rajagopal, *Mechanical response of polymers*. Cambridge: Cambridge University Press, 2000.

[64] N. W. Tschoegl, *The phenomenological theory of linear viscoelastic behavior: an introduction*. Springer Science & Business Media, 2012.

[65] R. P. Reed, "The Economic effects of fracture in the United States. Washington, D.C.," *U.S. Dept. of Commerce, National Bureau of Standards*, 1983.

[66] C. E. Inglis, "Stresses in a plate due to the presence of cracks and sharp corners," *Trans Inst Naval Archit*, vol. 55, pp. 219–241, 1913.

[67] A. A. Griffith, "VI. The phenomena of rupture and flow in solids," *Philosophical transactions of the royal society of london. Series A, containing papers of a mathematical or physical character*, vol. 221, no. 582–593, pp. 163–198, 1921.

[68] G. R. Irwin, "Onset of fast crack propagation in high strength steel and aluminum alloys," Naval Research Lab Washington DC, 1956.

[69] B. G. R Irwin, "Analysis of Stresses and Strains Near the End of a Crack Traversing a Plate," 1957. [Online]. Available: http://asmedigitalcollection.asme.org/appliedmechanics/article-pdf/24/3/361/6750462/361_1.pdf

[70] H. M. Westergaard, "Bearing pressures and cracks: Bearing pressures through a slightly waved surface or through a nearly flat part of a cylinder, and related problems of cracks," 1939.

[71] M. L. Williams, "On the stress distribution at the base of a stationary crack," 1957.

[72] G. I. Barenblatt, "The mathematical theory of equilibrium cracks in brittle fracture," *Advances in applied mechanics*, vol. 7, pp. 55–129, 1962.

[73] D. S. Dugdale, "Yielding of steel sheets containing slits," *J Mech Phys Solids*, vol. 8, no. 2, pp. 100–104, 1960.

[74] E. Orowan, "Fracture and strength of solids," *Reports on progress in physics*, vol. 12, no. 1, p. 185, 1949.

[75] G. R. Irwin, "Fracture dynamics," *Fracturing of metals*, 1947.

[76] J. R. Rice, "A Path Independent Integral and the Approximate Analysis of Strain Concentration by Notches and Cracks," 1968. [Online]. Available: http://asmedigitalcollection.asme.org/appliedmechanics/article-pdf/35/2/379/5449160/379_1.pdf

[77] G. P. Cherepanov, "The propagation of cracks in a continuous medium," *Journal of Applied Mathematics and Mechanics*, vol. 31, no. 3, pp. 503–512, 1967.

[78] F. Z. Li, C. F. Shih, and A. Needleman, "A comparison of methods for calculating energy release rates," *Eng Fract Mech*, vol. 21, no. 2, pp. 405–421, 1985.

[79] S. M. Barhli, M. Mostafavi, A. F. Cinar, D. Hollis, and T. J. Marrow, "J-Integral Calculation by Finite Element Processing of Measured Full-Field Surface Displacements," *Exp Mech*, vol. 57, no. 6, pp. 997–1009, Jul. 2017, doi: 10.1007/s11340-017-0275-1.

[80] F. Sun and B. R. K. Blackman, “A DIC method to determine the Mode I energy release rate G, the J-integral and the traction-separation law simultaneously for adhesive joints,” *Eng Fract Mech*, vol. 234, p. 107097, 2020.

[81] T. L. Anderson, *Fracture mechanics: fundamentals and applications*. CRC press, 2017.

[82] K. P. Menard and N. R. Menard, *Dynamic mechanical analysis*. CRC press, 2020.

[83] M. Sepe, *Dynamic mechanical analysis for plastics engineering*. William Andrew, 1998.

[84] T. Murayama, *Dynamic mechanical analysis of polymeric material*. Elsevier Scientific Pub. Co., 1978.

[85] B. E. Read and G. D. Dean, *The determination of dynamic properties of polymers and composites*. John Wiley & Sons, 1978.

[86] W. P. Cox and E. H. Merz, “Correlation of dynamic and steady flow viscosities,” *Journal of Polymer Science*, vol. 28, no. 118, pp. 619–622, 1958.

[87] A. Trivedi, “High rate properties of particulate composites,” University of Oxford, 2020.

[88] G. Höhne, J. L. McNaughton, W. Hemminger, H.-J. Flammersheim, and H.-J. Flammersheim, *Differential scanning calorimetry*. Springer Science & Business Media, 2003.

[89] J. Drzeżdżon, D. Jacewicz, A. Sielicka, and L. Chmurzyński, “Characterization of polymers based on differential scanning calorimetry based techniques,” *TrAC Trends in Analytical Chemistry*, vol. 110, pp. 51–56, 2019.

[90] M. Reading, A. Luget, and R. Wilson, “Modulated differential scanning calorimetry,” *Thermochim Acta*, vol. 238, pp. 295–307, 1994, doi: https://doi.org/10.1016/S0040-6031(94)85215-4.

[91] G. I. Taylor, “The testing of materials at high rates of loading,” *J. Inst. Civil Eng*, vol. 26, no. 8, pp. 487–501, 1946.

[92] K. J. Frutschy and R. J. Clifton, “High-temperature pressure-shear plate impact experiments using pure tungsten carbide impactors,” *Exp Mech*, vol. 38, no. 2, pp. 116–125, 1998.

[93] G. F. Raiser, J. L. Wise, R. J. Clifton, D. E. Grady, and D. E. Cox, “Plate impact response of ceramics and glasses,” *J Appl Phys*, vol. 75, no. 8, pp. 3862–3869, 1994.

[94] P. H. Mott, J. N. Twigg, D. F. Roland, H. S. Schrader, J. A. Pathak, and C. M. Roland, “High-speed tensile test instrument,” *Review of scientific instruments*, vol. 78, no. 4, p. 045105, 2007.

[95] H. Kolsky, “An investigation of the mechanical properties of materials at very high rates of loading,” *Proceedings of the physical society. Section B*, vol. 62, no. 11, p. 676, 1949.

[96] B. Hopkinson, “X. A method of measuring the pressure produced in the detonation of high, explosives or by the impact of bullets,” *Philosophical Transactions of the Royal Society of London. Series A, Containing Papers of a Mathematical or Physical Character*, vol. 213, no. 497–508, pp. 437–456, 1914.

[97] K. T. Ramesh, “Springer handbook of experimental solid mechanics,” *New York: Springer Science*, pp. 929–960, 2008.

[98] W. W. Chen and B. Song, *Split Hopkinson (Kolsky) bar: design, testing and applications*. Springer Science & Business Media, 2010.

[99] G. T. Gray III and W. R. Blumenthal, “Split-Hopkinson pressure bar testing of soft materials,” *ASM handbook*, vol. 8, pp. 488–496, 2000.

[100] G. T. GRAY III, “Classic split Hopkinson pressure bar testing,” *ASM handbook*, vol. 8, pp. 462–476, 2000.

[101] C. R. Siviour, “High strain rate characterization of polymers,” in *AIP Conference Proceedings*, 2017, vol. 1793, no. 1, p. 060029.

[102] R. Othman, *The Kolsky-Hopkinson bar machine: selected topics*. Springer, 2018.

[103] W. Chen, F. Lu, D. J. Frew, and M. J. Forrestal, “Dynamic compression testing of soft materials,” *J. Appl. Mech.*, vol. 69, no. 3, pp. 214–223, 2002.

[104] B. Song, W. W. Chen, and W.-Y. Lu, “Mechanical characterization at intermediate strain rates for rate effects on an epoxy syntactic foam,” *Int J Mech Sci*, vol. 49, no. 12, pp. 1336–1343, 2007.

[105] H. Chen, L. R. Hart, W. Hayes, and C. R. Siviour, “Mechanical characterisation and modelling of a thermoreversible superamolecular polyurethane over a wide range of rates,” *Polymer (Guildf)*, vol. 221, p. 123607, 2021.

[106] M. J. Kendall, D. R. Drodge, R. F. Froud, and C. R. Siviour, “Stress gage system for measuring very soft materials under high rates of deformation,” *Meas Sci Technol*, vol. 25, no. 7, p. 075603, 2014.

[107] W. Chen, F. Lu, and B. Zhou, “A quartz-crystal-embedded split Hopkinson pressure bar for soft materials,” *Exp Mech*, vol. 40, no. 1, pp. 1–6, 2000.

[108] W. Chen, B. Zhang, and M. J. Forrestal, “A split Hopkinson bar technique for low-impedance materials,” *Exp Mech*, vol. 39, no. 2, pp. 81–85, 1999.

[109] W. Chen, F. Lu, and M. Cheng, “Tension and compression tests of two polymers under quasi-static and dynamic loading,” *Polym Test*, vol. 21, no. 2, pp. 113–121, 2002.

[110] J. J. Harrigan, B. Ahonsi, E. Palamidi, and S. R. Reid, “Experimental and numerical investigations on the use of polymer Hopkinson pressure bars,” *Philosophical Transactions of the Royal Society A: Mathematical, Physical and Engineering Sciences*, vol. 372, no. 2023, p. 20130201, 2014.

[111] R. Gerlach, C. Kettenbeil, and N. Petrinic, “A new split Hopkinson tensile bar design,” *Int J Impact Eng*, vol. 50, pp. 63–67, 2012.

[112] T. J. Cloete, A. van der Westhuizen, S. Kok, and G. N. Nurick, “A tapered striker pulse shaping technique for uniform strain rate dynamic compression of bovine bone,” *EDP Sciences*, vol. 1, pp. 901–907, 2009.

[113] B. Song, Y. Ge, W. W. Chen, and T. Weerasooriya, “Radial inertia effects in Kolsky bar testing of extra-soft specimens,” *Exp Mech*, vol. 47, no. 5, pp. 659–670, 2007.

[114] D. A. Gorham, “The effect of specimen dimensions on high strain rate compression measurements of copper,” *J Phys D Appl Phys*, vol. 24, no. 8, p. 1489, 1991.

[115] C. R. Siviour and S. M. Walley, “Inertial and frictional effects in dynamic compression testing,” in *The Kolsky-Hopkinson bar machine*, Springer, 2018, pp. 205–247.

[116] W. H. Peters, W. F. Ranson, M. A. Sutton, T. C. Chu, and J. Anderson, “Application of digital correlation methods to rigid body mechanics,” *Optical Engineering*, vol. 22, no. 6, pp. 738–742, 1983.

[117] T. C. Chu, W. F. Ranson, and M. A. Sutton, “Applications of digital-image-correlation techniques to experimental mechanics,” *Exp Mech*, vol. 25, no. 3, pp. 232–244, 1985.

[118] T. C. Chu, W. F. Ranson, and M. A. Sutton, “Applications of digital-image-correlation techniques to experimental mechanics,” *Exp Mech*, vol. 25, no. 3, pp. 232–244, 1985.

[119] M. A. Sutton, W. J. Wolters, W. H. Peters, W. F. Ranson, and S. R. McNeill, “Determination of displacements using an improved digital correlation method,” *Image Vis Comput*, vol. 1, no. 3, pp. 133–139, 1983.

[120] W. H. Peters and W. F. Ranson, “Digital imaging techniques in experimental stress analysis,” *Optical engineering*, vol. 21, no. 3, pp. 427–431, 1982.

[121] H. T. Goldrein, S. J. P. Palmer, and J. M. Huntley, “Automated fine grid technique for measurement of large-strain deformation maps,” *Opt Lasers Eng*, vol. 23, no. 5, pp. 305–318, 1995.

[122] P. K. Rastogi, “Principles of holographic interferometry and speckle metrology,” *Photomechanics*, pp. 103–151, 2000.

[123] J. S. Sirkis and T. J. Lim, “Displacement and strain measurement with automated grid methods,” *Exp Mech*, vol. 31, no. 4, pp. 382–388, 1991.

[124] B. Pan, K. Qian, H. Xie, and A. Asundi, “Two-dimensional digital image correlation for in-plane displacement and strain measurement: a review,” *Meas Sci Technol*, vol. 20, no. 6, p. 062001, 2009.

[125] W. Tong, “An evaluation of digital image correlation criteria for strain mapping applications,” *Strain*, vol. 41, no. 4, pp. 167–175, 2005.

[126] A. Giachetti, “Matching techniques to compute image motion,” *Image Vis Comput*, vol. 18, no. 3, pp. 247–260, 2000.

[127] H. Lu and P. D. Cary, “Deformation measurements by digital image correlation: Implementation of a second-order displacement gradient,” *Exp Mech*, vol. 40, no. 4, pp. 393–400, 2000.

[128] P. Bing, X. Hui-Min, X. Bo-Qin, and D. Fu-Long, “Performance of sub-pixel registration algorithms in digital image correlation,” *Meas Sci Technol*, vol. 17, no. 6, p. 1615, 2006.

[129] M. A. Sutton, J. J. Orteu, and H. Schreier, *Image correlation for shape, motion and deformation measurements: basic concepts, theory and applications*. Springer Science & Business Media, 2009.

[130] T. C. Chu, W. F. Ranson, and M. A. Sutton, “Applications of digital-image-correlation techniques to experimental mechanics,” *Exp Mech*, vol. 25, no. 3, pp. 232–244, 1985.

[131] M. A. Sutton, J. H. Yan, V. Tiwari, H. W. Schreier, and J.-J. Orteu, “The effect of out-of-plane motion on 2D and 3D digital image correlation measurements,” *Opt Lasers Eng*, vol. 46, no. 10, pp. 746–757, 2008.

[132] F. Yasmeen, S. Rajan, M. A. Sutton, and H. W. Schreier, “Experimental study of measurement errors in 3D-DIC due to out-of-plane specimen rotation,” in *International Digital Imaging Correlation Society*, Springer, 2017, pp. 211–215.

[133] B. K. Bay, T. S. Smith, D. P. Fyhrie, and M. Saad, “Digital volume correlation: three-dimensional strain mapping using X-ray tomography,” *Exp Mech*, vol. 39, no. 3, pp. 217–226, 1999.

[134] A. Koko, P. Earp, T. Wigger, J. Tong, and T. J. Marrow, “J-integral analysis: An EDXD and DIC comparative study for a fatigue crack,” *Int J Fatigue*, vol. 134, p. 105474, 2020.

3 Stress relaxation after low and high-rate deformation of polyurethanes

This chapter comprises an introduction, then a paper submitted for publication to Proceedings of the Royal Society A.

3.1 Chapter Introduction

For this thesis, the polymers were of significant interest, so these were characterised for rate and temperature dependence under monotonic loading and stress relaxation. A Prony series material model was calibrated to each polymer and verified to predict the polymer response. Emphasis was placed on the ability of the model to capture the stress relaxation behaviour of the polymer because, due to its inherent energy dispersive ability, this behaviour could be important for energy dispersive applications, such as ballistic impact. The presented dataset and model were used throughout the remainder of this thesis, particularly to populate FE simulations.

Cylindrical specimens were first characterised by a series of standard compression experiments under quasi-static loading, 10^{-3} to 10^{-1} s^{-1}, on a screw-driven compression machine, and dynamic loading, ~10^{3} s^{-1}, on a Hopkinson bar apparatus. Additional quasi-static compression experiments were conducted from -60 °C to 20 °C at 10^{-3} s^{-1}. The stress relaxation behaviour of the polymers was of particular interest, and this behaviour was compared to Prony model predicted, calibrated from DMA experiments. These relaxation experiments were performed under quasi-static conditions, 10^{-3} s^{-1}, at temperatures from -60 °C to 20 °C and dynamically, 10^{3} s^{-1}, at ambient temperature. Under both quasi-static

and dynamic loading a further investigation was conducted, under ambient conditions, where the final strain was varied. The Prony model compared well against experimental results, provided the correct boundary conditions were used and a recent novel analysis was furthered under dynamic conditions to determine this. The model was able to predict the experimental behaviour up to significant strain and through the glass transition; however, deviations occurred if irrecoverable deformation was observed in the polymer.

3.2 Abstract

Polymers possess a wide range of mechanical behaviours depending upon the temperature and loading rate. An often-overlooked aspect is relaxation, important because it acts over a wide range of time periods and begins as soon as the polymer is loaded. We have investigated the relaxation behaviour of two polyurethanes (PUs) following deformation at low-rate, 10^{-3} s^{-1}, and dynamic, 10^{3} s^{-1}, loading rates, with the former exploring temperatures from 20 °C to -60 °C. These are compared to a predictive Prony series model calibrated using data from dynamic mechanical analysis. For dynamic relaxation, a bespoke analysis was used to account for the movement of the bars during the relaxation. The model was able to predict the stress-time response after low-rate deformation to strains of 2 % at all temperatures. As the strains increased, irrecoverable deformation was observed and the model became less accurate. In the dynamic experiments, the model accurately predicted the early stages of relaxation for both PUs but deviated later on. A modification to the model was suggested to account for these observations. Further characterisation of the mechanical response under large strain compressive loading is also reported.

3.3 Introduction

Polymers are used in many applications that experience mechanical deformation over an extensive range of loading rates and temperatures, from quasi-static to ballistic impact [1]–[6]. The properties of most polymers vary significantly with loading rate and temperature, with variations of three orders of magnitude in stiffness not uncommon [7, 8]. Understanding the temperature and rate dependence of the polymer across relevant conditions is therefore essential. An often overlooked aspect of polymer behaviour is the relaxation, which acts over all time periods and begins as soon as the polymer is loaded. Therefore, it is particularly important to understand this behaviour, especially because it is inherently energy-dissipative and could be influential in energy absorptive applications.

In general, stress relaxation in polymers occurs through chemical and mechanical mechanisms, including chain scission, bond interchange, molecular entanglement, viscous flow and motion by reptation [9]–[13]. For the mechanical motion of polymer chains, there is an associated internal friction as the chains slide past each other. This drag force rises to a peak during the polymer's glass transition before decreasing. Additional smaller peaks in drag are observed at the secondary transitions [14]. Depending on the loading and environmental conditions, any combination of these mechanisms could be significant during relaxation. Phenomenologically, relaxation can be described in a model using a combination of elastic springs and viscous dashpots. In this research, a Prony series, an extension of the generalised Maxwell model [15]–[17] consisting of parallel branches of spring-dashpot pairs, is used.

To calibrate the model, dynamic mechanical analysis (DMA) is used. This experimental procedure measures the frequency and temperature dependence of the complex modulus

and the ratio of stored energy to dissipated internal energy (i.e. the loss tangent) in the polymer. For a comprehensive review, see [18]. The principle of time-temperature superposition can be applied to these results to create a mastercurve of stiffness at a single reference temperature [19] to which the Prony material model can be fitted. A limitation is that the DMA investigates only the small strain behaviour, and time-temperature superposition can only be used for this purpose in the linear-viscoelastic regime; therefore, other methods of measuring the large strain response are required.

To determine the large strain, high strain rate properties of polymers, a Split Hopkinson Pressure Bar (SHPB) can be used [20]–[24]. In conventional SHPB, a stress pulse is created from the impact of a striker on an input bar. This 'incident pulse' interacts with the specimen producing reflected and transmitted pulses that can be used to determine the stress-strain properties of the material. Of interest to this project is the period post-loading during which the specimen can relax [25].

The work reported in the current paper aims to determine the ability of the Prony series model, fitted using DMA data, to predict the relaxation behaviour of two polymers at microsecond and hundreds of second timescales. In order to achieve this, two representative polyurethane materials were obtained with different glass transition temperatures, one above (50 °C) and one below (15 °C) room temperature. The specimens were first characterised using DMA and large strain compression experiments at different strain rates and temperatures. Then, relaxation experiments were performed following low-rate and dynamic deformation. This allowed the performance of this model to be explored with variations in the temperature, strain rate and final strain, whilst at the same time considering both rubbery and glassy behaviours.

3.4 Materials

Two polyurethanes (PUs), commercially known as 'Task 3' and 'Task 11', were sourced from Bentley Advanced Materials [26]. The polymers were selected to have different glass transition temperatures whilst maintaining chemical similarity. Task 3 has a glass transition temperature of 55 °C; Task 11, 15 °C measured using differential scanning calorimetry (DSC) where the materials were heated from -90 °C to 120 °C at 3 °C min^{-1}, see Appendix. The PUs were obtained as two-part polymers and, once mixed and degassed, were cured in moulds to produce rectangular plates. The polymers were allowed to cure at room temperature for 24 hours before a final post-cure heat treatment at 65 °C for 4 hours per the manufacturer's instructions. Once cured, the polymer sheets were fly-cut flat to approximately 3.5 mm thickness, and circular specimens of either 6 or 10 mm diameter were cut from the sheets using a CNC mill.

3.5 Experimental Procedure

Three sets of experiments were performed:

Dynamic Mechanical Analysis - conducted as part of the thermomechanical analysis of the polymers of interest. A Prony series was fitted to these data.

Compression – Specimens were compressed at low and high strain rates. The low-rate experiments were conducted at ambient and sub-ambient temperatures. These were to characterise the polymer's response to rate and temperature.

Relaxation – Specimens were loaded to pre-determined strains or loads at low and high rates and allowed to relax. The low-rate relaxation experiments were conducted at ambient and sub-ambient conditions. These results were compared against Prony model predictions.

3.5.1 DMA

DMA was used to investigate the polymers' thermomechanical properties at low strains. Two configurations were used: single cantilever in oscillation different frequencies and temperatures, and three-point bend under isothermal relaxation.

For the single cantilever frequency sweeps, prismatic specimens of dimensions approximately 17.5 x 12.1 x 3.45 mm were oscillated with a 0.1 % strain amplitude at 0.1 Hz, 0.32 Hz, 1 Hz, 3.16 Hz and 10 Hz. This was performed isothermally at temperatures from -70 °C to +70 °C in 2.5 °C intervals. Specimens were held at each temperature interval for 5 minutes before loading to ensure isothermal conditions.

For the relaxation experiments, prismatic specimens of approximately 55 x 12.1 x 3.3 mm were loaded in a 3-point bend configuration. A stress relaxation testing procedure was used. Here, specimens were loaded slowly in 3-point bend to 0.1 % strain. They were then held for 10 minutes, during which time the required force was recorded. The polymer was then allowed to recover, unloaded, for 20 minutes before repeating the experiment at a new temperature. Measurements were made from -85 °C to +55 °C in 5 °C intervals.

From these data, time-temperature superposition was used to create a mastercurve, which describes the storage modulus of the polymer over a far greater time range than can be tested experimentally. This mastercurve was used to calibrate a Prony series using the procedure described in section 3.7.1.

3.5.2 Compression

3.5.2.1 Low-Rate Compression

The low-rate response of the polymers was investigated using a commercial screw-driven testing machine (Instron 3400 Series), instrumented with a contacting extensometer attached to the loading platens close to the specimen. To reduce friction between the specimen and platen faces, AEROSPEC 201 Graphited grease was used. This screw-driven apparatus was used to compress cylindrical specimens of 10 mm diameter and 3.5 mm height to 50 % true strain. Experiments were performed over a range of strain rates at room temperature and at a range of temperatures at 10^{-2} s^{-1}, Table 1.

	Strain Rate	Final True Strain	Temperature
Varying Strain Rate	10^{-1}, 10^{-2}, 10^{-3}	0.5	20 °C
Varying Temperature	10^{-3}	0.5	- 60 °C, -40 °C, -20 °C, 0 °C, 20 °C

Table 1 - Experimental conditions for low rate compression.

3.5.2.2 High-Rate Compression

To characterise the polymer response under high-rate loading, a Split Hopkinson Pressure Bar was used. In this project, the bars were made from a Titanium alloy (Ti6Al4V) and were 12.7 mm in diameter. The striker bar was 400 mm long, the input bar 1000 mm, and the output bar 500 mm long. Strain gauges were bonded to the input and output bars to measure the incident, transmitted and reflected waves. These data were then used to calculate the strain and stress in the specimen using the standard equations, see [21] for a

full analysis. The specimens were 6 mm in diameter and 3.5 mm thick. Vaseline was used to lubricate the contact between the polymer and bar faces.

3.5.3 Relaxation

3.5.3.1 Low-Rate Relaxation

Further experiments were conducted to investigate the stress relaxation of the polymer over 100s of seconds following low strain rate deformation. The specimens (3.5 mm height and 10 mm diameter) were first compressed in the screw-driven testing machine to a pre-determined force at a strain rate of 10^{-3} s^{-1}. Then, the crosshead was held in place for 600 s. The force supported by the specimen was recorded, allowing the specimen's relaxation behaviour to be measured under fixed boundary conditions. The force was chosen to be within the linear viscoelastic regime for each polymer and corresponded to 2 % strain, so it was therefore temperature-dependent. The experiment was performed from 20 °C to -60 °C in 20 °C intervals.

A further investigation was conducted into the relaxation behaviour at larger strains: 10 % and 15 % for Task 11; 4 % and 10 % for Task 3. Here, the specimen was loaded until the desired strain, chosen to match the final strains observed in the high-rate stress relaxation experiments. At the larger strains, non-linear effects such as plasticity were observed; therefore, a final load condition could not be used. For these experiments, a pre-load of 50 N was applied to the specimens before the experiment was conducted to remove end effects and ‘bedding in’ at the start of the experiment, allowing the specimens to be reliably loaded to a known strain.

This experimental procedure is summarised in Table 2 and Table 3.

	Varying Temperature				Varying Final Strain		
Temperature (°C)	-60	-40	-20	0	20	20	20
Loading Stress (MPa)	53	53	33	20	2.7	-	-
Loading Strain (%)	-	-	-	-	(6)	10	15

Table 2 - Low rate stress relaxation experimental conditions for T11.

	Varying Temperature				Varying Final Strain		
Temperature (°C)	-60	-40	-20	0	20	20	20
Loading Stress (MPa)	66	66	53	53	33	-	-
Loading Strain (%)	-	-	-	-	(2)	4	10

Table 3 - Low rate stress relaxation experimental conditions for T3.

3.5.3.2 High-Rate Relaxation

To investigate the microsecond timescale relaxation behaviour of the polymers, further SHPB experiments were performed. The experimental configuration was the same as described above; however, the striker bar was shortened to 250 mm to give a shorter loading duration. Thus, after the input pulse interacted with the specimen, there was a period of time in which the specimen could relax. This relaxation exerted a force on the confining input and output bars, measured using the strain gauges. Experiments were performed at 20 °C on specimens 3.5 mm in height and either 10 mm or 6 mm in diameter. Two specimen sizes were chosen to allow an investigation into the influence of the final loading strain on the subsequent relaxation behaviour to be conducted.

3.6 Modelling

3.6.1 Prony Series Representation

Polymers are viscoelastic materials; hence, they exhibit different behaviour depending upon the timescale over which the load is applied. Therefore, a material model that captures this time-dependent behaviour is required and, for this project, a Prony series was used. Represented schematically in Figure 1, a general k-branched Prony series consists of a number of branches in parallel, with each branch containing a spring-dashpot pair in series.

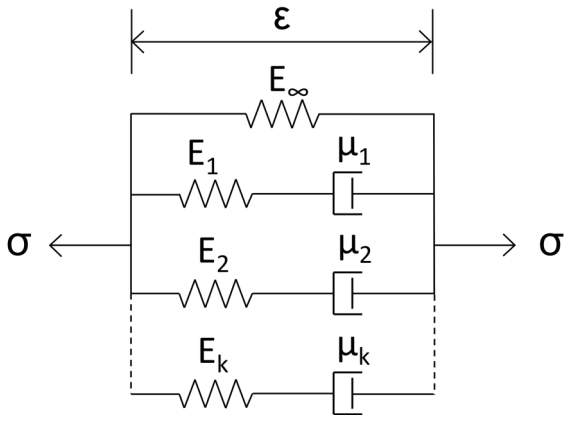


Figure 1 - Spring-dashpot representation of a k-branch Prony series.

The constitutive model for this Prony series representation can be derived initially through a force balance along each branch. A Laplace transform can then be taken, and the initial conditions applied. See [15], [27] for detailed descriptions. Under a step strain input, ε_0, the stress relaxation behaviour can be represented by

$$\frac{\sigma(t)}{\varepsilon_0} = E(t) = E_\infty + \sum_{n=1}^{k} E_n e^{\frac{-t}{\tau_n}} \qquad (1)$$

where, $\tau_n = \frac{\mu_n}{E_n}$ (2)

For more general loading cases, the complexity increases because relaxation of the model will begin as soon as the loading starts. Therefore, for a general case

$$\sigma(t) = \varepsilon ¿ \quad (3)$$

A single element model was created in ABAQUS to solve this equation during loading and relaxation. Relevant boundary conditions, described below, corresponding to the experiments performed, were applied to the model, and the stress response was calculated. The model was verified by initially considering an arbitrary two-branch Prony model whose solution can be determined by hand.

3.6.2 Low-Rate Stress Relaxation Modelling

The model boundary conditions were applied as follows (see also Figure 2). The model was deformed using the experimentally observed stress-time relationship until it achieved the peak stress measured in the experiments. Then the boundaries were fixed and the polymer was allowed to relax. The force at the boundaries was output from the model. The advantage of this method was that, experimentally, it is easier to measure the forces accurately than the specimen displacements, owing to compliance in the load frame and end effects on the specimen (e.g. non-parallel specimen faces, effects of the lubricant layer). At large deformations, if plasticity was observed in the experiment, it was assumed that the plastic deformation did not contribute to the subsequent relaxation – only the viscoelastic deformation relaxed. Hence, no plasticity model was required.

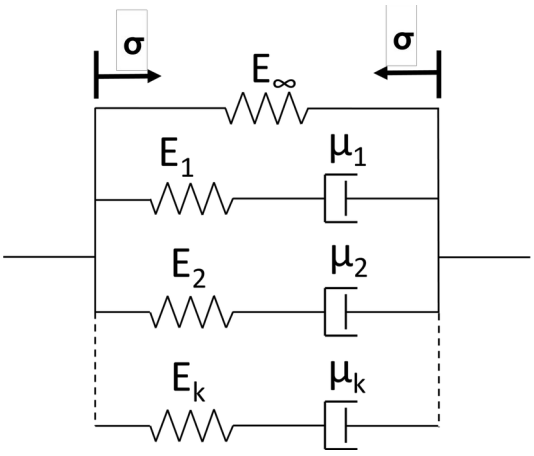


Figure 2a - Loading

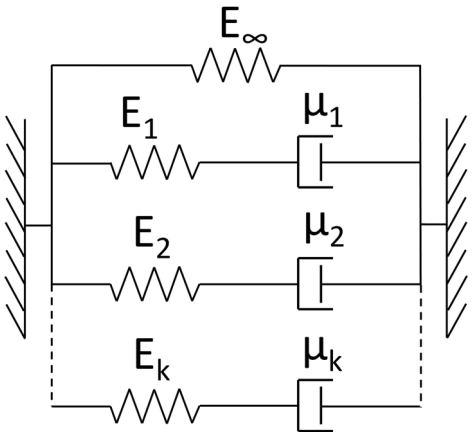


Figure 2b - Relaxation

Figure 2 - Boundary condition of the Prony model representation under low rate loading and relaxation. During loading, stress-time boundary conditions measured experimentally were applied to the model.

3.6.3 High-Rate Relaxation Modelling

For loading, the experimentally observed stress-time profile was again used as the models' boundary condition. Under relaxation, the analysis of Cloete *et al*. was used [25]. Here, the confining presence of the input and output bars can restrict, but not prevent, the expansion of the specimen during its relaxation. Because the bar movement is governed by wave propagation, the stress is proportional to the velocity. Hence, during relaxation, the specimen can be modelled as though the boundaries of this material are attached to two confining dashpots. The boundary conditions under loading and unloading are represented schematically in Figure 3a and Figure 3b. The dashpots have been shown to have a viscosity of

$$\mu_{SHB} = \frac{1}{2} L_s \frac{A_b}{A_s} \rho_b c_b \qquad (4)$$

where L_s is the length of the specimen, A_b and A_s are the area of the bar and specimen, respectively, and ρ_b and c_b are the bar's density and elastic wave speed, respectively [25].

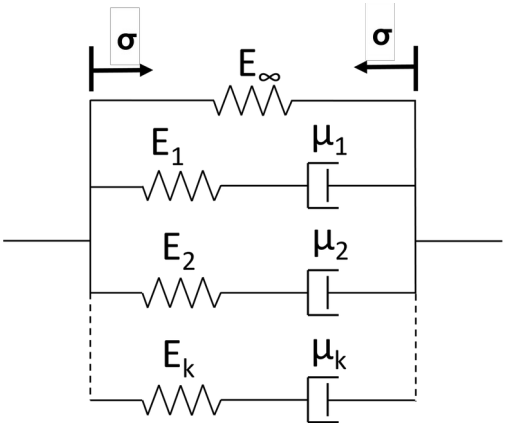


Figure 3a - Loading

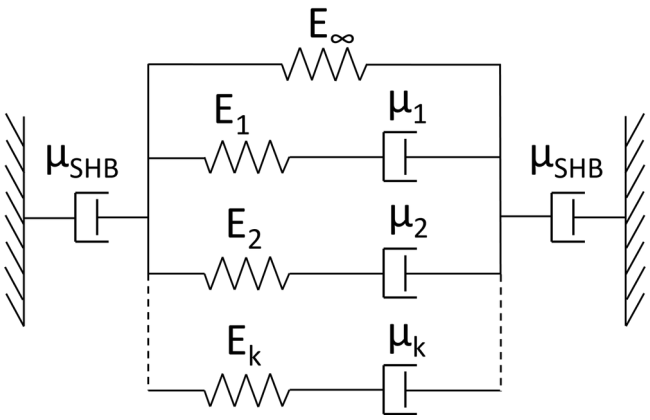


Figure 3b - Relaxation

Figure 3 - Boundary condition of a Prony model representation under high rate loading and relaxation. During loading, stress-time boundary conditions measured experimentally were applied to the model. During relaxation, the boundaries of the Prony model move as though limited by the action of two dashpots [24].

3.7 Results and Discussion

3.7.1 DMA

DMA was performed in two configurations: frequency sweeps on single cantilever specimens and stress-relaxation on three-point bend specimens. Mastercurves were produced using both sets of data. The full procedure is shown here for the stress relaxation data; however, an identical procedure was followed for single cantilever DMA, the results from which can be found in the Appendix.

The raw relaxation data for both polymers are displayed in Figure 4, where each line represents data obtained at a temperature between -85 °C and +55 °C, in 5 °C increments. At each temperature, the evolution of the relaxation modulus with time was measured and the temperatures of interest around the glass transition temperature have been marked. Away from these temperatures, where there was considerably less temperature dependency, significant grouping of the data was found. The principal of time-temperature

superposition was then implemented to produce a stiffness mastercurve [19]. To generate this mastercurve, all the curves for each temperature were horizontally shifted on the time axis to overlap with the data taken at a reference temperature, chosen here to be 20 °C. The magnitude of this shift was dependent upon the temperature and these shift factors required are presented in Figure 5. Once all the data were overlain, this produced the mastercurve in Figure 6. On this figure, both mastercurves from the single cantilever and three-point bend configurations are presented.

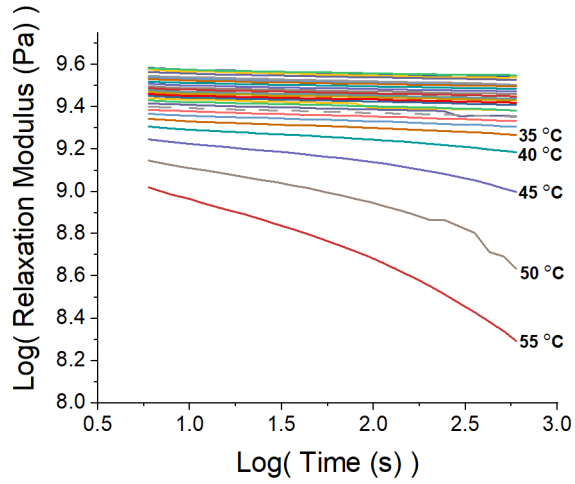


Figure 4a - Task 3

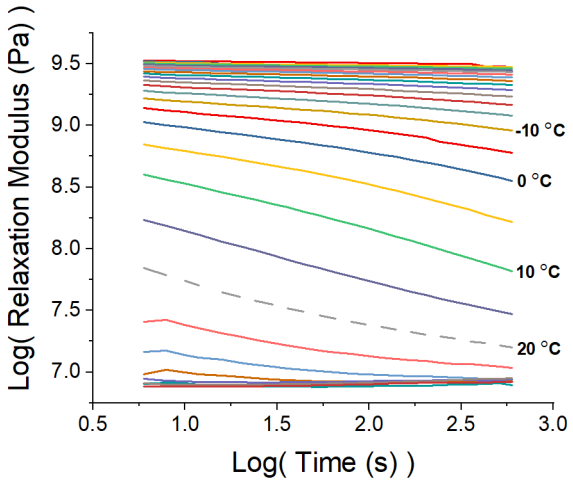
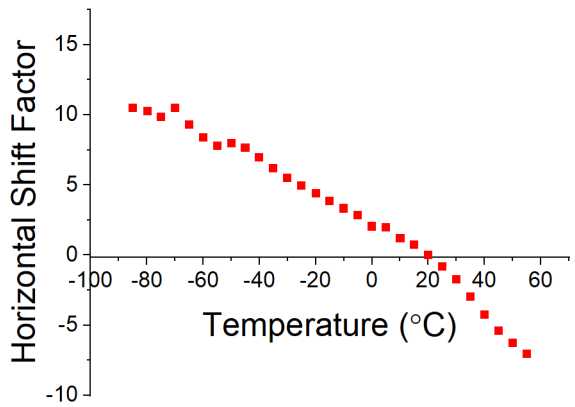


Figure 4b - Task 11

Figure 4 - Relaxation DMA data. The reference temperature, 20 °C has been presented by a dashed line.



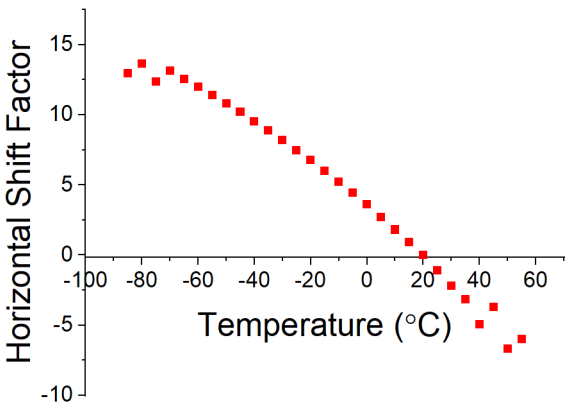
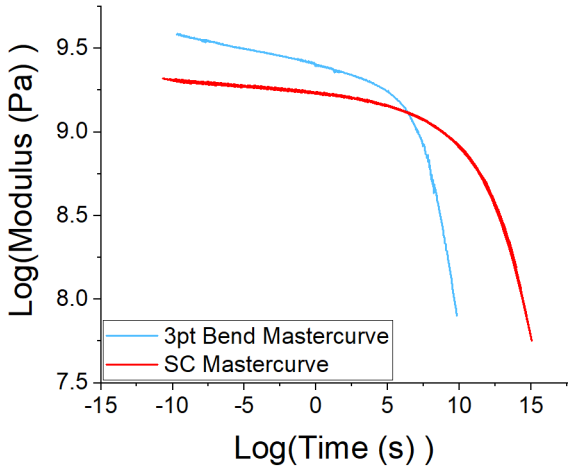


Figure 5a - Task 3

Figure 5b - Task 11

Figure 5 - Shift factors used to produce relaxation mastercurve at 20 ℃.



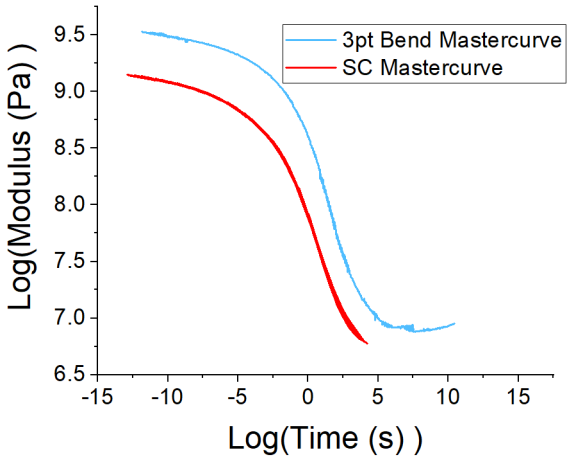


Figure 6a - Task 3

Figure 6b - Task 11

Figure 6 – Comparison of 20 ℃ mastercurves produced using relaxation data in the three point bend configuration or oscillatory in single cantilever (SC) configuration.

It is evident that there are significant differences in the mastercurves in Figure 6: the DMA configuration strongly influences the overall results. Broadly, it was observed that the single cantilever DMA produces a lower modulus than the three-point bend. Deng et al. [27] observed the same effect and found that the three-point bend DMA modulus agreed with moduli obtained from tensile experiments at various temperatures. For these reasons, data from the three-point bend configuration were used to calibrate the Prony model, Figure 7.

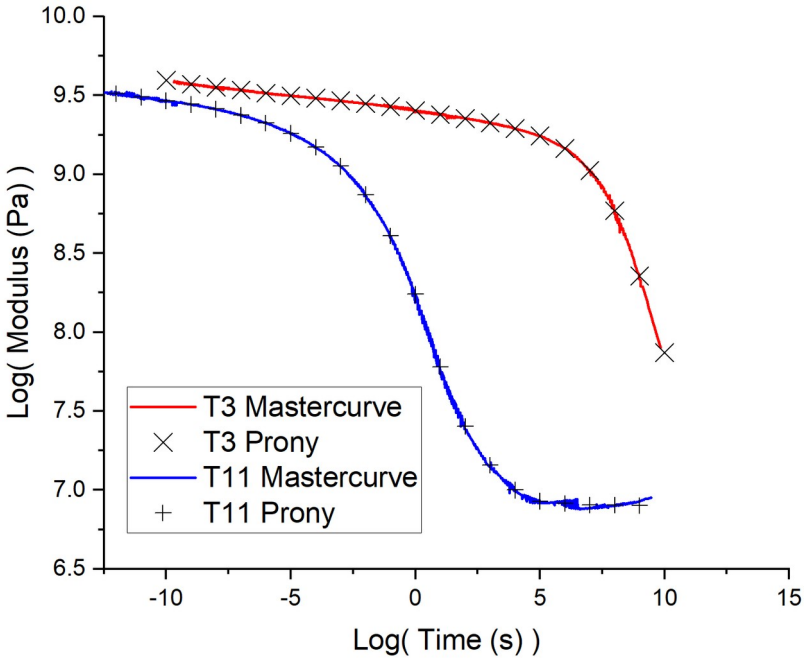


Figure 7 - Mastercurves for 'Task 11' and 'Task 3' for a 20 °C reference temperature from three-point bend DMA compared to the Prony fit to these curves using branches with relaxation times spaced one per decade.

The mastercurves for both polymers are shown in Figure 7 along with the Prony fits. Both polymers have similar overall behaviours, with the glass transition and no secondary transitions over the frequency range explored. At small relaxation times, i.e. below the glass transition, the stiffnesses of the polymers begin to converge, which is expected due to their

chemical similarity. It is also expected that the stiffnesses would converge at long relaxation times had suitable data been obtained; however, such data out of the scope of this project.

It is observed that Task 11 is the less stiff of the two polymers; at timescales on the order of seconds, it is within its glass transition and is highly rate-sensitive. At similar timescales, Task 3 is below its glass transition and is, therefore, stiffer and less rate-sensitive than Task 11.

To produce the Prony series representations equation (10) was fitted to the mastercurves using the curve fitting toolbox in Matlab®. The number of branches was set so that their characteristic times, as defined by equation (11), were spaced by one decade. Hence, a 22-branch and a 24-branch Prony series were fitted to Task 3 and Task 11, respectively; the predicted moduli at a number of frequencies are shown in Figure 7, whilst the Prony parameters alongside further material properties are presented in the Appendix.

3.7.2 Large Strain Compression

The low and high strain rate compression results obtained at 20 °C are shown in Figure 8. Low-rate results from experiments at sub-ambient temperatures are presented in Figure 9.

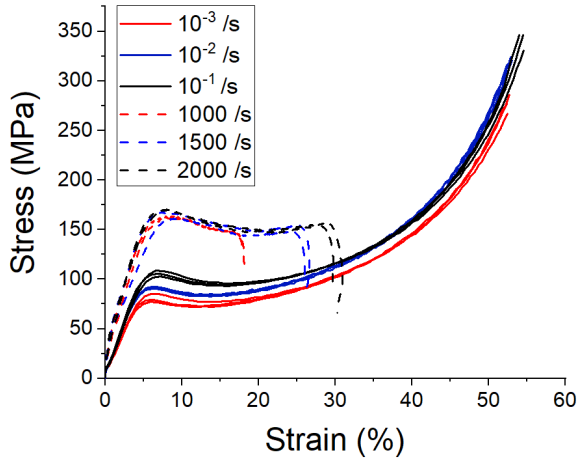


Figure 8a - Task 3

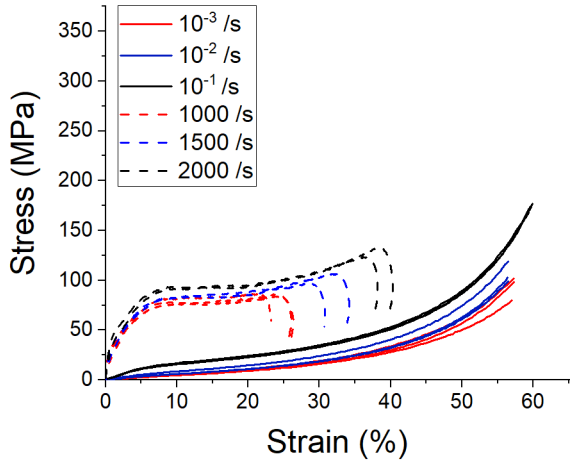


Figure 8b - Task 11

Figure 8 – Stress-strain curves from low and high rate characterisation at room temperature. In all cases, the end of the curve represents the end of loading, the specimens did not fail.

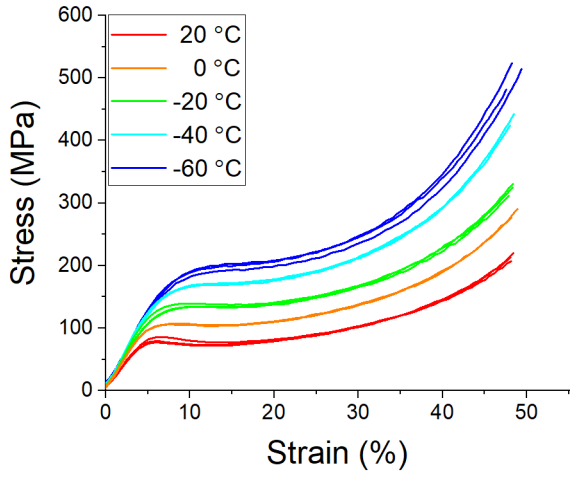


Figure 9a - Task 3

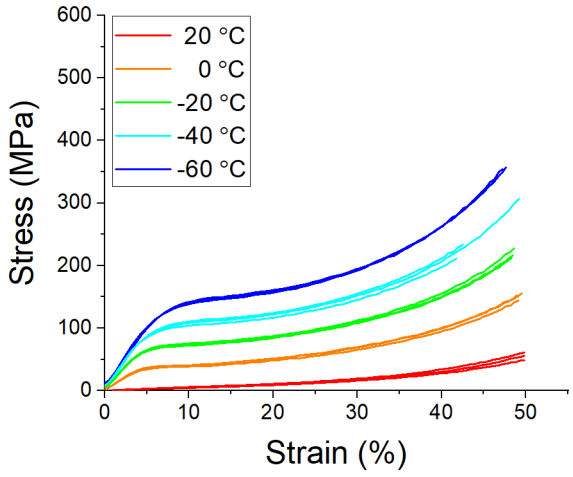


Figure 9b - Task 11

Figure 9 - Stress-strain response of both polymers in compression at sub-ambient temperatures and 10^{-3} s^{-1}.

There were distinctly different behaviours when comparing the low strain rate behaviour of the two polymers. The initial stiffness of Task 3, Figure 8a, was relatively rate insensitive, consistent with the DMA results. This polymer exhibited yielding, confirmed by measurement of permanent deformation of recovered specimens. This yield stress was rate sensitive and increased from around 80 to 110 MPa over the range of strain rates tested, Figure 10. For Task 11, significant rate sensitivity was observed, Figure 11, again consistent with the DMA data. However, no yielding was observed: the applied strain was fully recovered.

At sub-ambient temperatures, Task 3 exhibited minor sensitivity of initial stiffness but significant variation in yield stress, which increased from 80 MPa to 200 MPa over the temperature range explored, Figure 12. The post-yield behaviour also depended on temperature, with the amount of softening reducing as the temperature decreased. For

Task 11, there was significant temperature sensitivity, Figure 13: the stiffness increased by an order of magnitude over the temperature range explored and non-linear, but still fully recoverable, behaviour was observed. Note that the yield stress of Task 11 at the lowest temperature is similar to Task 3 at the highest temperature; this is consistent the DMA results that show the two polymers having similar behaviours below their glass transition.

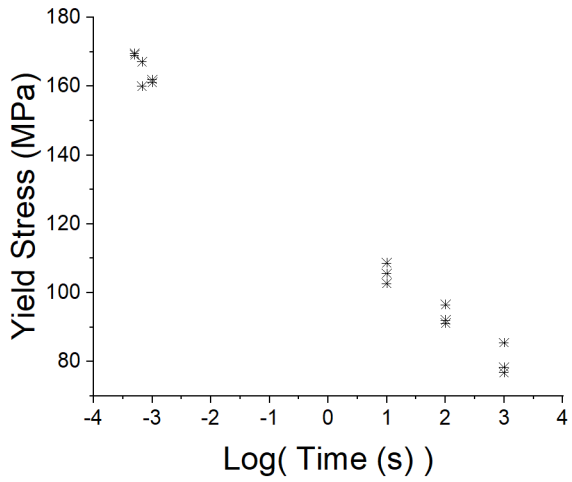


Figure 10 – Yield stress of Task 3 with varying loading time.

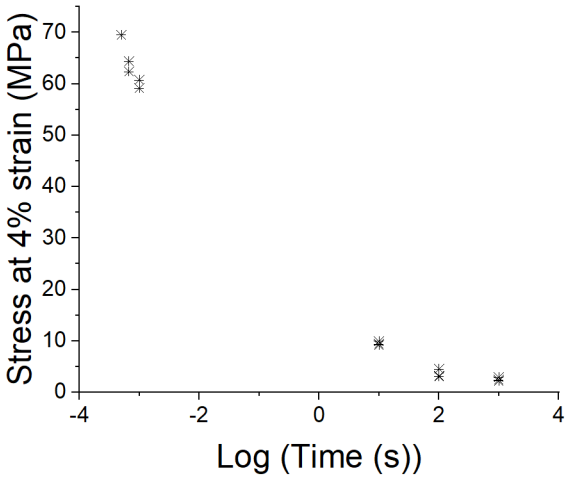


Figure 11 – Variation of stress of Task 11 at 4% strain with loading time. Note this polymer does not have a yield point.

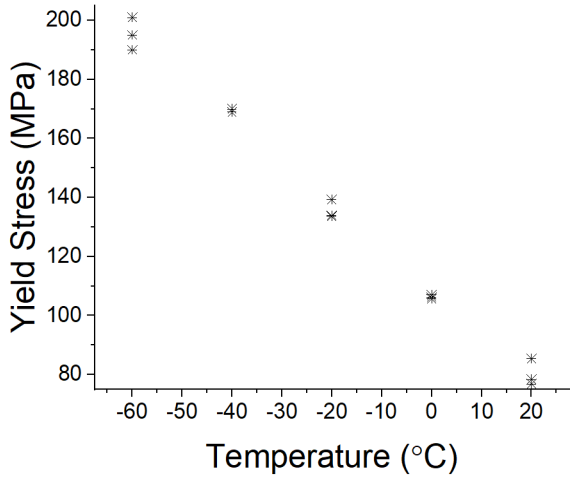


Figure 12 – Yield Strength of Task 3 with varying temperature.

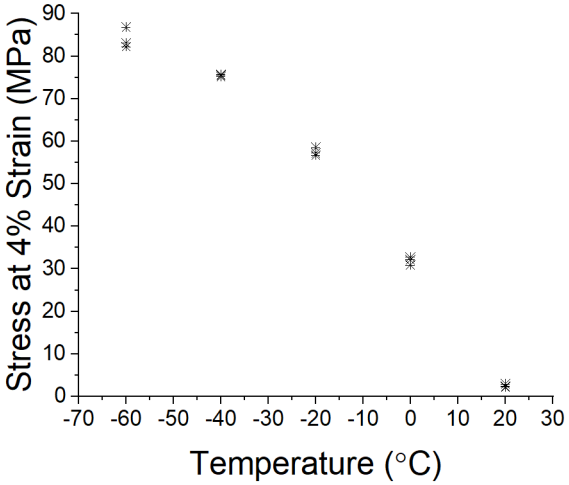


Figure 13 – Variation of stress of Task 11 at 4% strain with temperature.

Comparing the high strain rate response, Task 3 exhibited increased stiffness compared to that observed in the low rate experiment and yielded at a stress of approximately 160 MPa. Over the full range of strain rates tested, the yield stress appears to be approximately linear in log(strain rate). For Task 11, there was a significant increase in stiffness compared to the low rate experiments, as the polymer moved through the glass transition. Although the polymer displays non-linearity above a strain of approximately 5 %, the deformation remained fully recoverable, displaying behaviour akin to 'leathery' as described by Boyce [28].

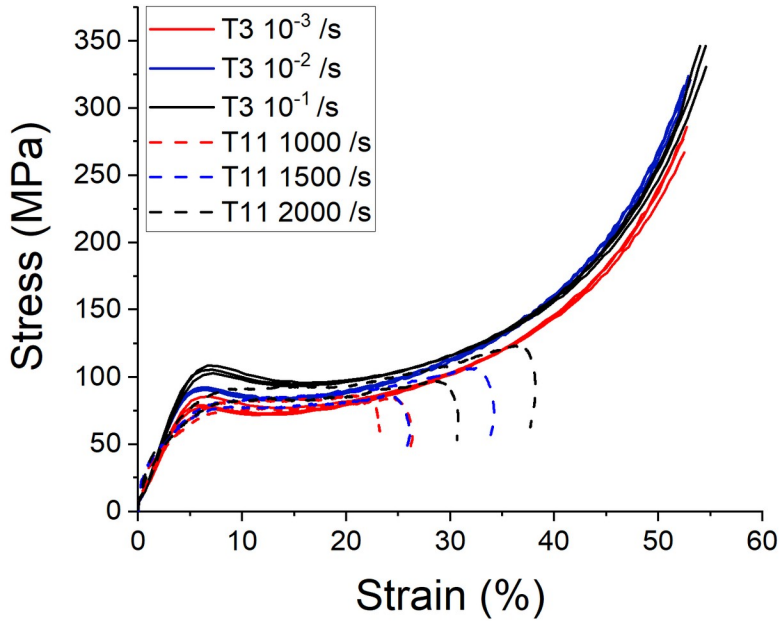


Figure 14 -Comparison of stress strain curves for Task 3 at low strain rates and Task 11 at high rates. These two different polymers exhibit similar behaviours when the alpha motions (which govern the glass transition) are restricted.

Interestingly, the low-rate experiments on Task 3, log(t) ~ 2, and the high-rate experiments on Task 11, log(t) ~ -6, correspond to similar positions for each polymer on their mastercurves, Figure 7. In both cases, the timescales are within the region of glassy

response, and, therefore, the polymers might be expected to exhibit similar behaviour. This is shown in Figure 14, where the stress-strain curves of the polymers are overlain. The main difference between the two is that Task 3 exhibits a peak (attributed to yielding) followed by strain softening, which is not seen in Task 11; it was also observed that Task 3 showed irrecoverable strain, whilst Task 11 did not. It must be noted that, in Task 11, *during the deformation*, structural relaxations associated with the glass transition cannot take place, but these relaxation can take place before and after the deformation. Hence, Task 11 starts and ends with its structure in a state of thermal equilibrium (because the room temperature is above the glass transition temperature), whereas Task 3 does not, because room temperature is below the glass transition and hence the structure is never in equilibrium.

A further comparison was performed between the low temperature and high strain rate behaviour of each polymer, Figure 15. As expected, the apparent stiffnesses and yield stresses agree at appropriate conditions. For Task 11, there is a good match for the whole of the stress-strain response, for Task 3 this is not the case, the curves obtained from the high-rate experiments soften considerably. One phenomenon of high strain rate testing is that the temperature in the specimen increases if mechanical work is converted to heat, because the heat does not have time to leave the specimen on the timescale of the loading. This would reduce the stress supported by the specimen. This may be the case in the Task 3 specimens and would be consistent with these specimens showing irrecoverable (plastic) deformation that is not observed in Task 11.

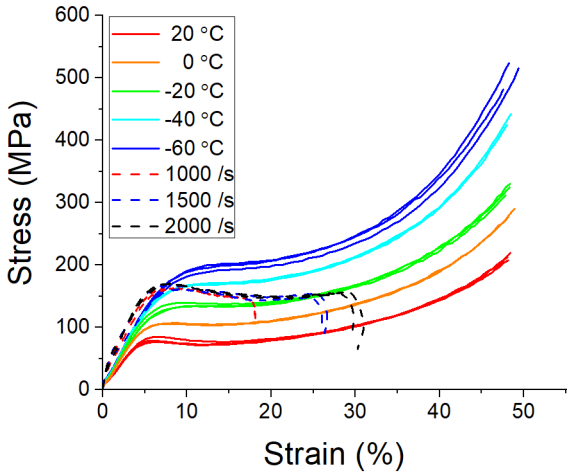


Figure 15a - Task 3

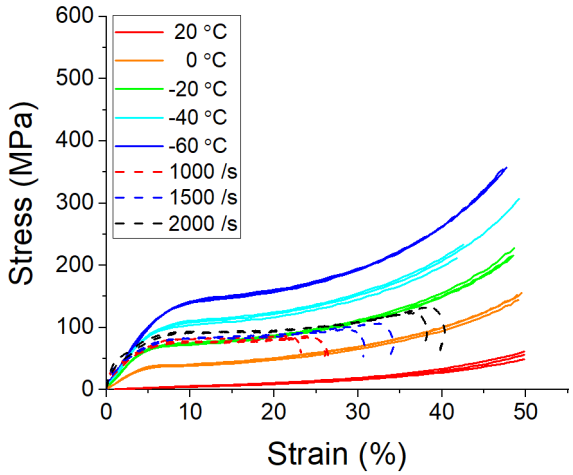


Figure 15b - Task 11

Figure 15 - Comparison between high rate experiments performed under ambient conditions and low rate (10^{-3} s^{-1}) experiments performed at sub-ambient temperatures.

3.7.3 Low Rate Relaxation Response

3.7.3.1 Low Temperature Small Strain Relaxation

The relaxation behaviour was measured at ambient and sub-ambient conditions and compared to predictions from the Prony model. Specimens were compressed to a pre-defined load, after which the crosshead was fixed in position, and the polymer was allowed to relax for 10 minutes. The load was selected, based on data in Figure 9, to ensure that the polymer did not yield.

The stress-time response for each polymer during loading and relaxation is presented in Figure 16a and Figure 16b. To enable comparisons, these data are normalised to the peak stress under each loading condition, Figure 17; the stress-strain response is shown in Figure 18. In all cases, the experimental data were compared to predictions from the Prony model.

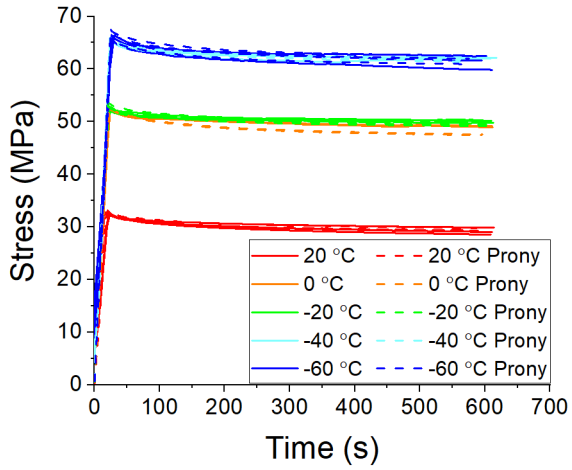


Figure 16a - T3 Stress-time

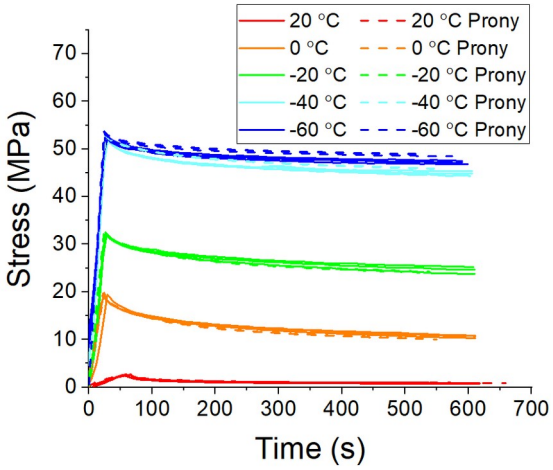


Figure 16b - T11 Stress-time

Figure 16 - Stress-time relaxation response for Task 3 and 11.

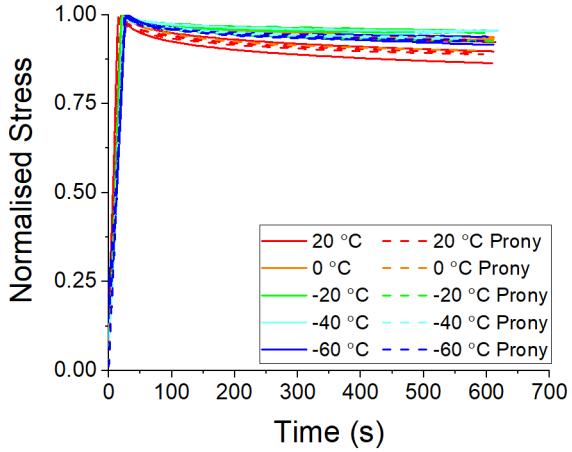


Figure 17a – Normalised T3 Stress-time

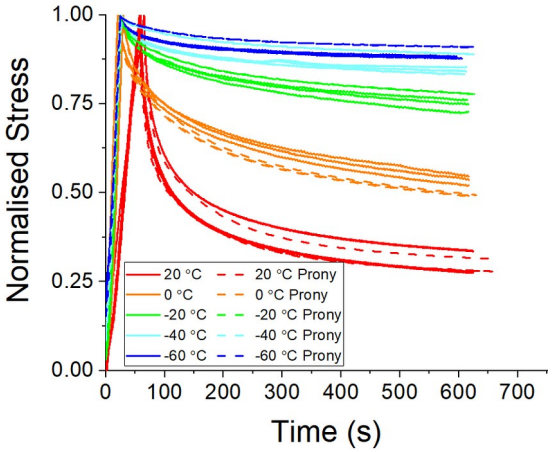


Figure 17b - Normalised T11 Stress-time

Figure 17 - Stress-time relaxation response for Task 3 and 11. The response has been normalised to the peak stress observed at each condition.

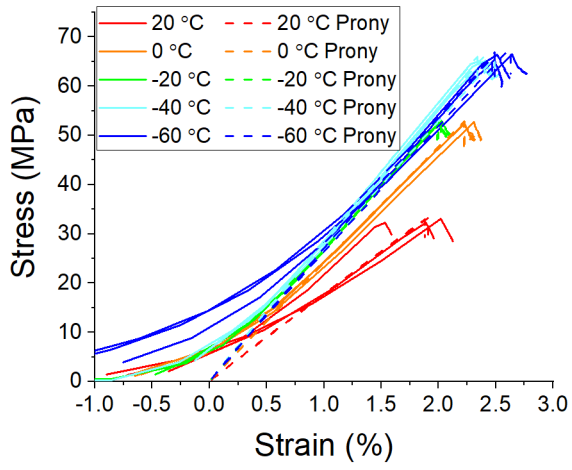


Figure 18a - T3 Stress-Strain

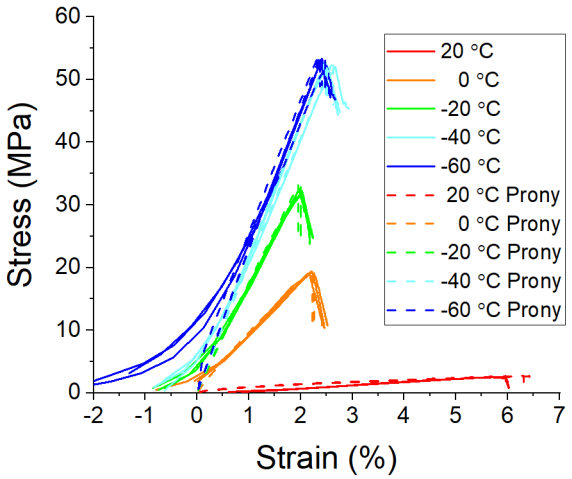


Figure 18b - T11 Stress-Strain

Figure 18 - Stress-strain relaxation response for Task 3 and 11.

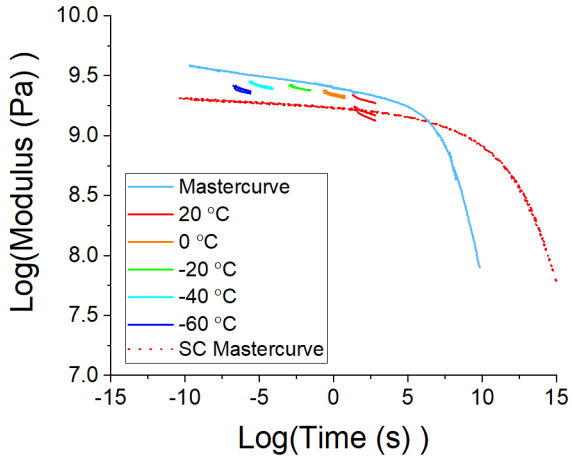


Figure 19a – Task 3

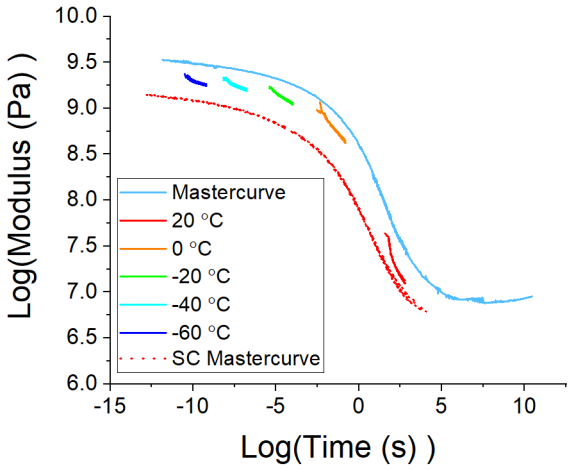


Figure 19b – Task 11

Figure 19 – Low temperature relaxation data overlain on the polymer mastercurves generated from DMA experiments in three point bend and single cantilever. The low temperature curves have been shifted by their corresponding shift factors.

For each of these experiments, the variation in modulus over time (defined as the stress divided by the strain) was calculated and compared to the mastercurves of each polymer, Figure 19. For each temperature, the previously calculated shift factors, derived using DMA and displayed in Figure 5, have been applied.

For the stress-time behaviour of Task 3, Figure 16a and Figure 15a, little relaxation was observed at all temperatures, and this appeared to be relatively temperature independent.

The polymer was above its glass transition at these temperatures, as shown in Figure 19a, so these results were expected. Conversely, Task 11 displayed a broad range of relaxation behaviour, Figure 16b and Figure 15b. This polymer moved through its glass transition, Figure 19b, so the behaviour is highly temperature dependent.

The model accurately predicts the stress-relaxation of both polymers under these conditions. There is a remarkably good fit for Task 11, particularly because this range of conditions captures the polymer's behaviour through the glass transition region and the relatively large relaxations. This is encouraging because the behaviour in this transition region is highly sensitive to the environmental conditions. The strain-strain behaviour, Figure 18, shows that the model gives a lower strain upon loading; however, because the model follows the experimental stress relaxation profile, this difference is simply a proportional factor in the modulus. It is well established that strains are difficult to measure in compression experiments, and that the measured values are typically too high because of end effects introduced by the lubricant layer and machining tolerances; one effect of this is the 'toeing in' at the start of each of the experimental curves. This justifies the use of force, rather than strain, targets in both the experiments and modelling. The difference in modulus is clear in Figure 19. Further, Figure 19 confirms the observation from [27] that the three-point bend mastercurve matched experimental data better than did the mastercurve from the single cantilever. Finally, taken as a whole, these data support this strategy for predicting relaxations from DMA experiments.

Finally, it can be observed that, during relaxation, the assumption that the boundaries remain fixed is not strictly true. Inspection of the stress-strain curves, for which strains are measured using contacting extensometers attached to the loading anvils close to the

specimen, reveal that the strain increased slightly. This was due to the compliance of the load chain, which expanded into the specimen as the load reduces, even if the crosshead was fixed. This effect will cause a slight increase in the observed stress during relaxation, which may further explain some of the discrepancies between the model and experimental results.

These results show that the Prony model can accurately capture the polymer stress relaxation behaviour under loading and relaxation. This is encouraging; however, only small strain behaviour has been examined. Therefore, an investigation was performed at higher strains, chosen to match the final strains in the high-rate relaxation experiments in Section 3.5.2.2.

3.7.3.2 Room Temperature Large Strain Response

Specimens were deformed to strains of 4 % and 10 % (Task 3) and 10 % and 15 % (Task 11) at ambient temperature. These strains were chosen to match those obtained in the interrupted Hopkinson bar experiments, described later, to allow comparison between low-rate and dynamic loading. In order to simulate these experiments, the boundary conditions for the model were modified to accommodate the non-linear (e.g. plastic) behaviour without having to produce a full viscoelastic-viscoplastic model. The model was again 'loaded' to the same stress as the experiment, before being allowed to relax with fixed boundaries. Effectively, the assumption was made that the total strain comprised of the sum of plastic and elastic strains, and it was the relaxation of the elastic component that governed the overall relaxation behaviour.

The stress-time behaviour of Task 3 loaded to three stresses before being allowed to relax is shown in Figure 20a. The relaxation behaviour of the polymer is dependent upon the

applied strain, with greater relaxation as the strain increases. Here, the Prony model can no longer accurately predict the relaxation, indicating that the assumptions above are not appropriate and that the onset of plasticity needs to be considered. The data for Task 11, Figure 20b, support this observation. Here, the Prony model can still accurately predict the polymer's relaxation response at strains two orders of magnitude greater than those used in the characterisation experiments from which it was derived.

The stress-strain behaviours of the Task 3 and Task 11 are shown in Figure 21a and Figure 21b, respectively. Due to the plasticity in Task 3, the model comparison to the experimental stress-strain response is highly inaccurate, whereas, for Task 11, the model can still predict the stress-strain response reasonably reliably.

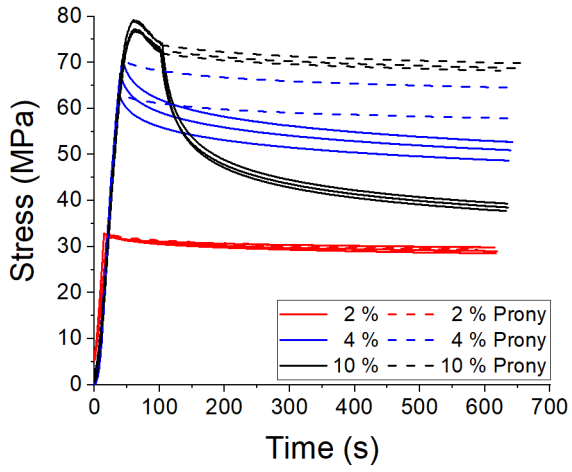


Figure 20a - T3 Stress-time

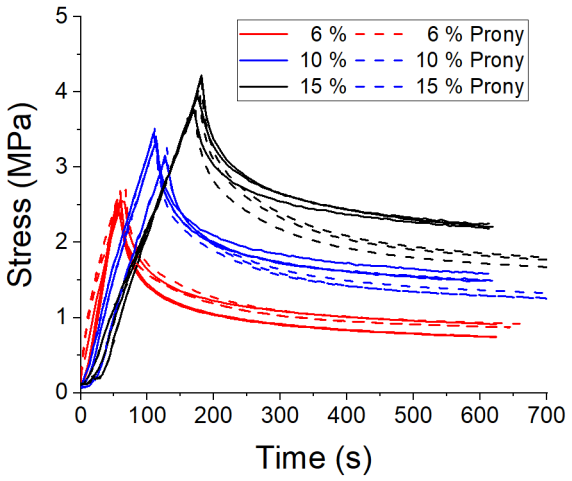


Figure 20b – T11 Stress-time

Figure 20 - Stress-time behaviour for Task 3 and Task 11. Specimens were now loaded to larger strains before relaxation.

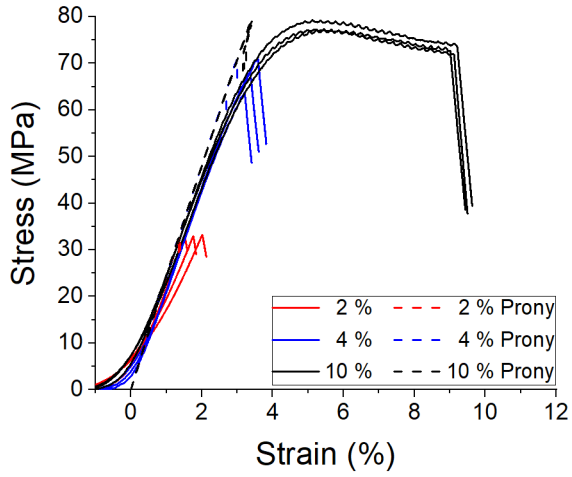


Figure 21a - T3 Stress-strain

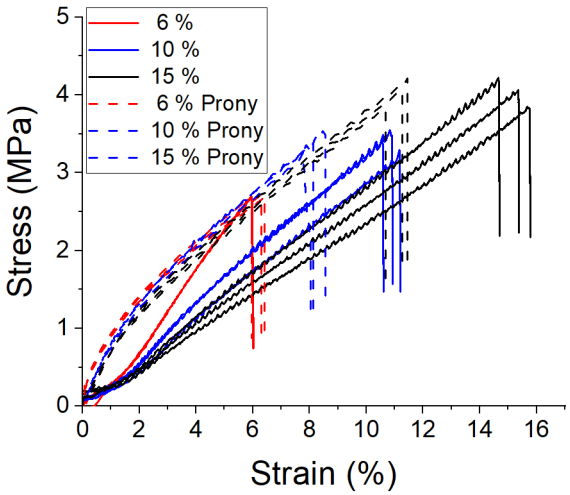


Figure 21b – T11 Stress-strain

Figure 21 – Stress-strain response for Task 3 and Task 11.

3.7.4 High Rate Relaxation Response

A Hopkinson bar was used to explore the relaxation of the polymer on microsecond timescales and to investigate the Prony model's ability to predict the behaviour. The same apparatus was used as the previous Hopkinson bar experiments; however, now a 250 mm striker bar was employed. This allowed a gap between wave oscillations in the system, giving a greater period of time to capture the dynamic relaxation response of the polymer. Two specimen geometries were used, both 3.5 mm long: 10 mm and 6 mm in diameter. The two sizes allowed an investigation into the effect of final strain to be conducted.

To model this experiment, the Prony series was loaded using the stress boundary conditions measured in the experiment and then allowed to expand as if they were restricted by two dashpots, as described in section 3.6.3. For comparison, model results were also obtained using fixed and free boundary conditions.

3.7.4.1 10 mm specimens

The 10 mm diameter specimen results are shown as stress-time, strain-time and stress-strain plots, and compared to the model predictions, in Figure 22 - Figure 24. For both polymers the Prony series representation was loaded using the measured stress-time boundary conditions. Once the peak stress was achieved, the model could relax under the confining force of two dashpots [25].

There are interesting comparisons that can be made between these materials. For Task 3, the model was able to predict accurately the measured relaxation behaviour. The model overpredicted the loading modulus slightly; this is consistent with the result previously observed in the sub-ambient relaxation experiments, Figure 19a. The effect of heating within the polymer during loading was also checked. Using a heat capacity of 1.38 J g^{-1} K^{-1} , taken from DSC experiments, the maximum temperature rise, if all applied work was converted to heat, was 2 °C. This heating was simulated; however, it was found to have a negligible effect on the response.

The model also captured the stress-time relaxation response of Task 11, but significantly underpredicted the strain. This observation of a modulus significantly greater than predicted agrees with the previously observed room temperature relaxation behaviour, Figure 19b. The model's ability to predict the stress-time response is encouraging because this suggests the Prony model can predict the stress relaxation response of the material well; however, there is a proportional offset in the stiffness which should be accounted for. Interestingly, from Figure 22b, there appears to be an emergence of a two phase-relaxation. The model can accurately predict the first phase of relaxation well but as the polymer relaxes further, there appears to be a step change in gradient and the polymer deviates from the model.

This is in contrast to the behaviour presented in Task 3, Figure 22a, in which no step change is observed and the model can accurately predict the polymer's stress behaviour under near full relaxation.

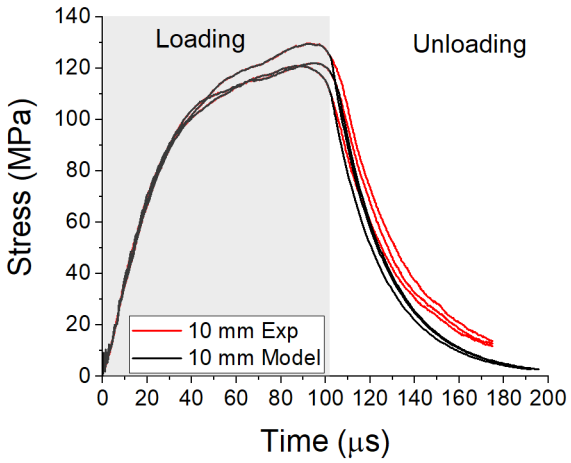


Figure 22a - Task 3

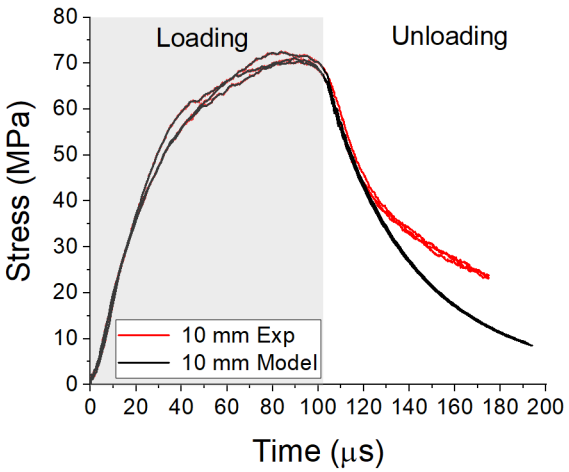


Figure 22b - Task 11

Figure 22 - Stress-time dynamic relaxation response of 10 mm diameter specimens. The model was loaded using the stress-time profile from the experiment. Relaxation was allowed to occur under the confining force of two dashpots.

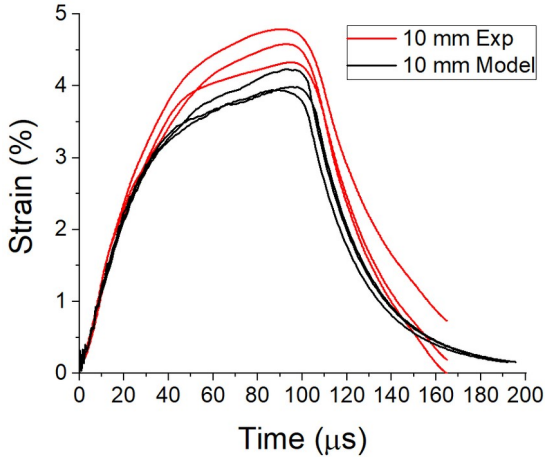


Figure 23a - Task 3

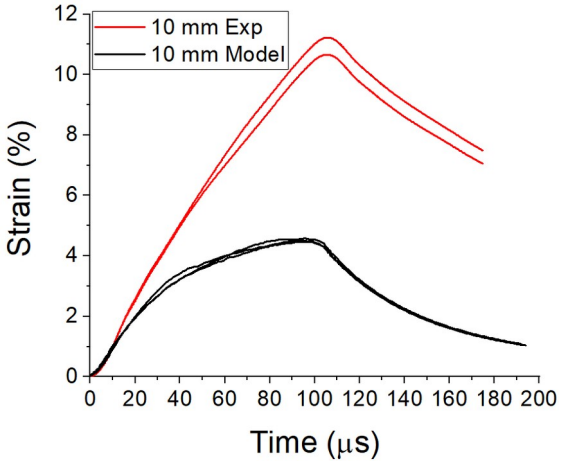


Figure 23b - Task 11

Figure 23 - Strain-time dynamic relaxation response of 10 mm diameter specimens.

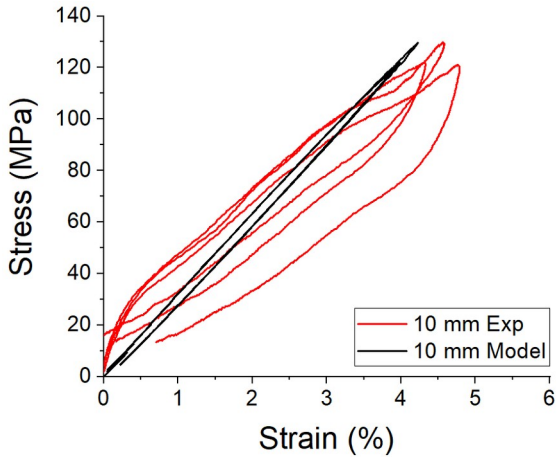


Figure 24a - Task 3

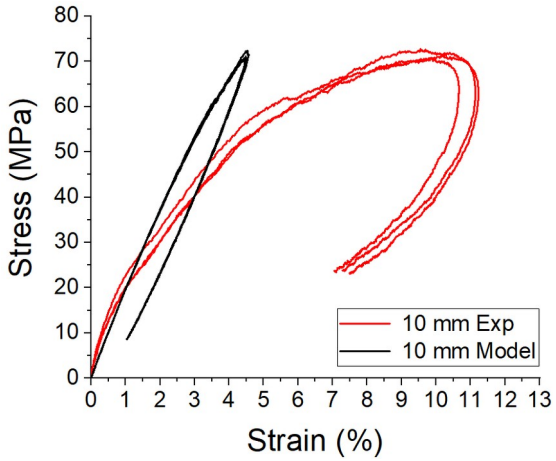


Figure 24b- Task 11

Figure 24 – Stress-strain response of 10 mm diameter specimens.

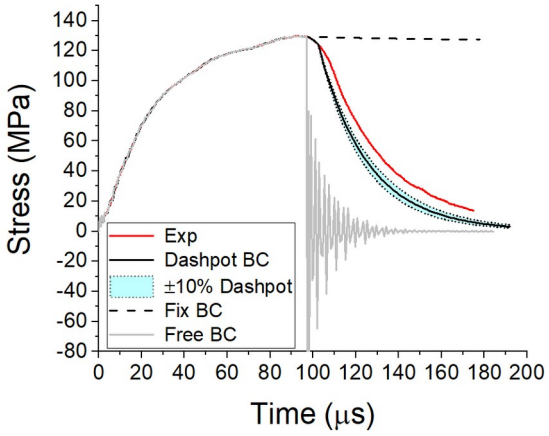


Figure 25a - Task 3

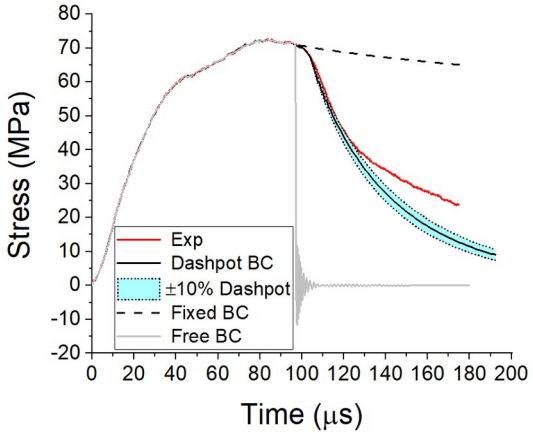


Figure 25b- Task 11

Figure 25 – Modelled stress-time response during relaxation with various boundary conditions applied.

A further investigation was conducted into the influence of the model's boundary conditions upon relaxation. The dashpot boundary conditions were applied to the model, calculated using the mechanical and geometric properties of the bar and specimens, as well as fixed and free boundary conditions. The results are presented in Figure 25. Under fixed boundary conditions, the model significantly overpredicts the stress. Interestingly, these boundaries cause a relaxation tangential to the stress-time curve at peak stress. This showed that as the confining bars change from loading to unloading the specimen, there is a finite period of time in which they do act as approximately immovable, and the polymer relaxes under fixed

conditions. Under free boundary conditions, the model relaxes nearly instantaneously, which because of the mass of the specimens causes the stress to oscillate around zero. A further investigation was conducted into the model's sensitivity to the value of the constraining dashpots' viscosity by varying this value by ± 10%. It was found that the variation of relaxation response (highlighted in blue) was relatively insensitive to variations in in this value.

3.7.4.2 6 mm specimens

The Hopkinson bar experiments were repeated using 6 mm diameter specimens, allowing the influence of larger strains to be investigated. The results are presented Figure 26 - Figure 28.

For Task 3, plasticity is now exhibited. The model can still predict the relaxation stress-time behaviour, Figure 26a, during the early phase of relaxation, but as the time increases, the polymer relaxed less than predicted. For Task 11 the model works well overall but appears to miss a high frequency component of the experimental relaxation. The strain was far greater than was expected as the experimental Task 11 had a greater modulus than expected, as observed before.

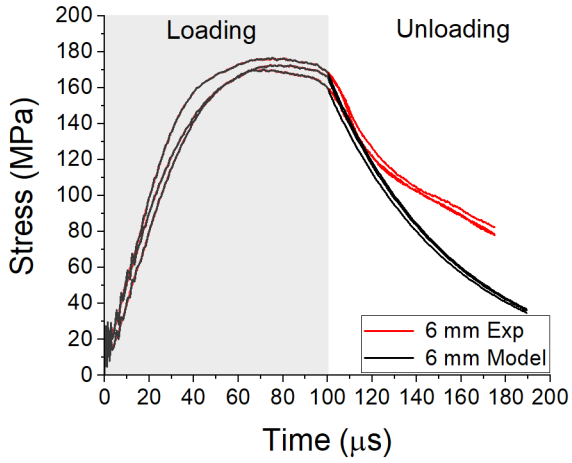


Figure 26a - Task 3

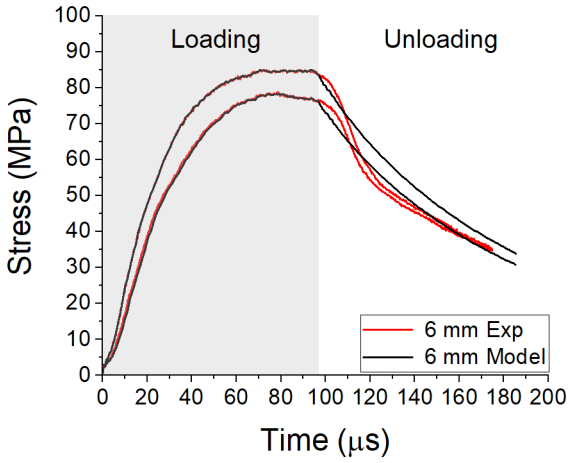


Figure 26b - Task 11

Figure 26 - Stress-time dynamic relaxation response of 6 mm diameter specimens.

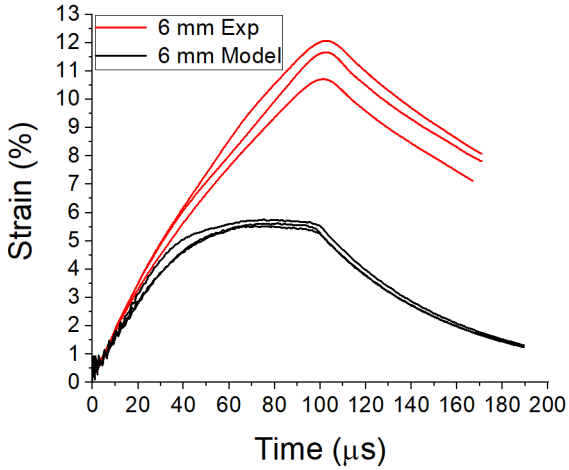


Figure 27a - Task 3

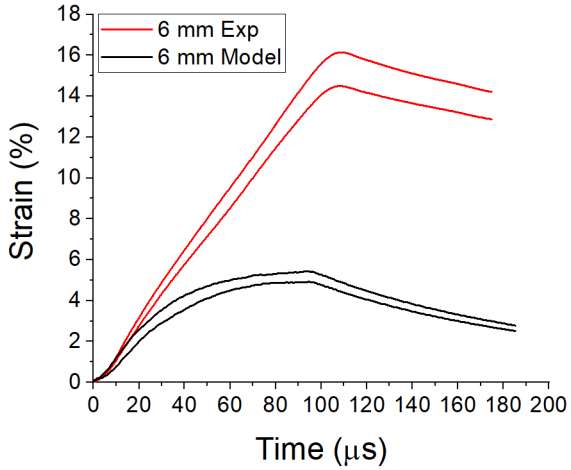


Figure 27b - Task 11

Figure 27 - Strain-time dynamic relaxation response of 6 mm diameter specimens.

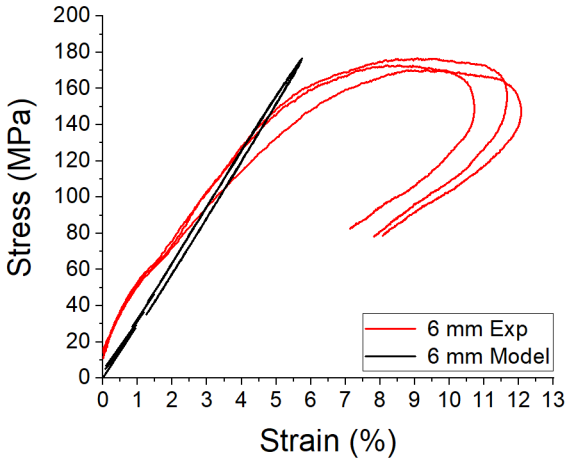


Figure 28a - Task 3

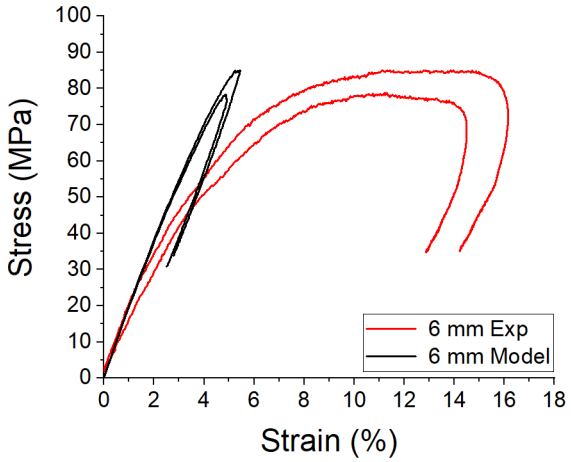


Figure 28b - Task 11

Figure 28 – Stress-strain response of Task 3 and Task 11 at high rate with 6 mm geometry.

Figure 29 displays overlain relaxation responses following high strain rate loading for both specimen geometries used. For comparison, the stress has been normalised to the value at the onset of relaxation. For both polymers, the relaxation for the 6 mm specimens, which were loaded to larger strains, is slower than for the 10 mm; the models capture this behaviour. Experimentally, the smaller area specimens exert less force on the confining bars, reducing their expansion and causing the specimen to relax more slowly. The model reflects this in the calculation of the viscosity of the confining dashpots.

As the relaxation progresses, there is evidence of a two-phase relaxation. In general, the model captured the initial phase of the relaxation well, indicating linear viscoelastic behaviour here. As the relaxation progressed, there was a rapid change in the experimental gradient, causing a divergence between experiment and model. Broadly, this two-phase response became more pronounced at greater strains. The change in relaxation response could be due to a boundary condition change or a deviation from linear viscoelasticity. The boundary conditions would have evolved during the experiment as the dimensions of the specimen changed. However, this would have been unlikely to produce a significant gradient step-change, as was observed here. Therefore, it is believed that a deviation from linear viscoelasticity took place at large strains.

For Task 3, these non-linear effects appear to become activated alongside plasticity because this phenomenon was not observed in the 10 mm specimen, which did not yield, but was present in the 6 mm. For Task 11, the effects are present in both specimens. Interestingly, the initial relaxation of this polymer is nearly independent of specimen diameter. Further, no yielding was observed in Task 11, therefore, it is thought that any non-linear processes which caused this effect were a function of increasing strain and included but were not limited to plasticity.

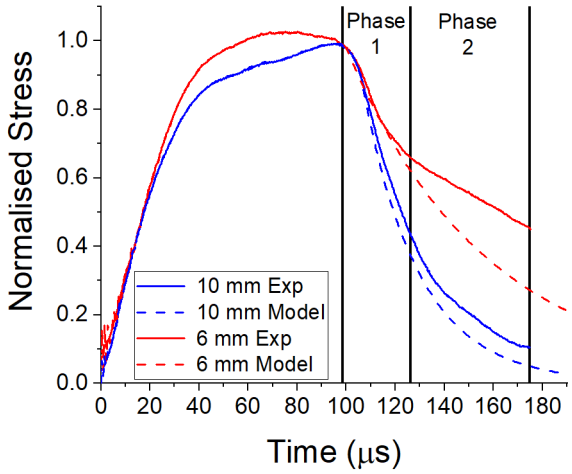


Figure 29a - Task 3

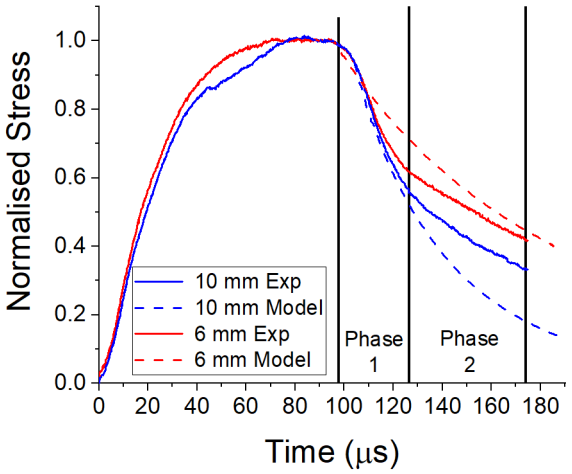


Figure 29b- Task 11

Figure 29 – Stress-time response comparing individual 10 mm and 6 mm high rate relaxation specimens for Task 3 and Task 11. The stress has been normalised to the stress at the onset of relaxation.

3.8 Discussion

The data above allow a range of comparisons to be made: between different materials; between different timescales; and between model and experiment. Broadly, the model was able to predict the relaxation behaviour of both polymers at low and high rates; however, when the polymer exhibited plasticity, the experiment and the model deviated.

Considering the relaxation of Task 3 following loading to larger strains, generally the model over-predicts the amount of relaxation in the high-rate experiments, and under-predicts at low rate, Figure 20. In particular, in the low rate as the strain increased and became closer to the yield point, the amount of stress relaxation increased significantly, and was far more than predicted. For Task 11, even at these increased strains, the ability of the model to capture the stress relaxation response was very good.

From these observations, modifications to the model are proposed, Figure 30, but were not implemented. These would take the form of a spring and dashpot pairing in series to the

original Prony model and the pairing would have a characteristic time constant between 100 μs and 100 s. The viscosity of the dashpot would be stress-dependent and would reduce at large stresses. At low rate, when the material model is relaxing under the restriction of fixed boundary conditions, this would allow the model to relax faster than the Prony series alone. At high rates, when the model is relaxing under the limitation of two external dashpots, this would act to reduce the stiffness of the combined model and thus slow the expansion. However, the exact formulation of this model is beyond the scope of this research.

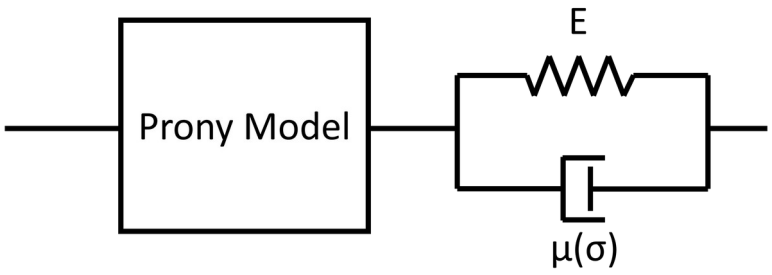


Figure 30 - Modified polymer model to account for low and high rate non-linearities.

3.9 Conclusions

In this study, the stress relaxation behaviour of two selected polyurethanes (PUs) was investigated following loading at low and high rates and modelled using a Prony series model calibrated using data from DMA experiments. Two geometries of DMA were used: single cantilever and three-point bend, the latter was found to produce modulus values closer to those determined in other experiments.

Monotonic compression and stress relaxation experiments were conducted at low rate over a range of temperatures. It was found that the Prony model accurately predicted the stress

relaxation behaviour, even through the glass transition. Further low-rate experiments were conducted at larger strains and the model was found to predict relaxation well provided the polymer did not yield. Once yielding occurred, the polymer relaxed more rapidly than predicted.

The monotonic compression experiments at different temperatures and strain rates showed well the equivalence of low temperature low rate experiments and ambient temperature dynamic experiments. They also showed the equivalence between the two polymers of similar structure but different glass transition temperatures, at appropriate combinations of temperature and rate.

Dynamic relaxation experiments were conducted on a Hopkinson bar. The model was able to capture the relaxation response of the PUs during the early phase of relaxation. The boundaries introduced by the Hopkinson bars during relaxation were successfully modelled using dashpots of appropriate viscosity; however, a sharp change in gradient observed during the relaxation was not predicted by the model. This change in gradient was exacerbated with increasing loading strain. It was suggested during early stages of relaxation, the material obeyed linear viscoelasticity with which the model was derived. However, various non-linear viscous processes in the material became activated during loading and became increasingly influential at larger strains. It may be possible to capture this behaviour in a nonlinear viscoelastic model by means of the addition of a parallel spring-dashpot pairing whose viscosity is stress dependent. However, the exact modifications are outside the scope of this research.

3.10 Acknowledgements

The authors would like to thank Dstl for their financial and intellectual support during this work under contract number DSTLX1000128371. Additionally, thanks must be extended to Igor Dyson and Nick Hawkins for their experimental and analytical assistance as well as Neil Warland and Andy Bateman for specimen manufacture.

For the purpose of Open Access, the author has applied a CC BY public copyright license to any Author Accepted Manuscript (AAM) version arising from this submission.

3.11 Appendix

3.11.1 DSC Data

Differential scanning calorimetry (DSC) was conducted on fully cured specimens of Task 3 and Task 11. The specimens were approximately 10 mg in weight and were heated from -90 to 120 °C at a rate of 3 °C per minute. The glass transition points were found to be at approximately 15 °C and 50 °C for Task 11 and Task 3 respectively, Figure 31.

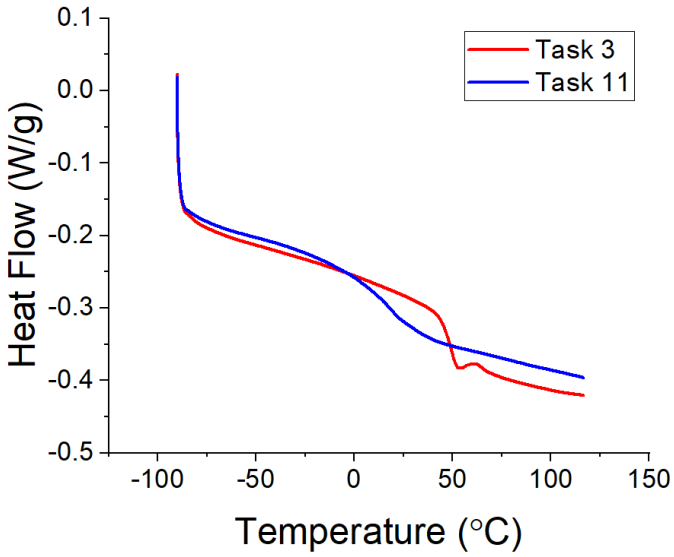


Figure 31 - DSC results for Task 3 and Task 11.

3.11.2 DMA data from single cantilever bend

The results obtained from single cantilever frequency sweeps are shown below. DMA results are displayed in Figure 32 and the shift factors used to create the subsequent mastercurves are presented in Figure 33 and Figure 34, respectively. Further, the variation of storage modulus with a single loading frequency, 1 Hz, is shown in Figure 35.

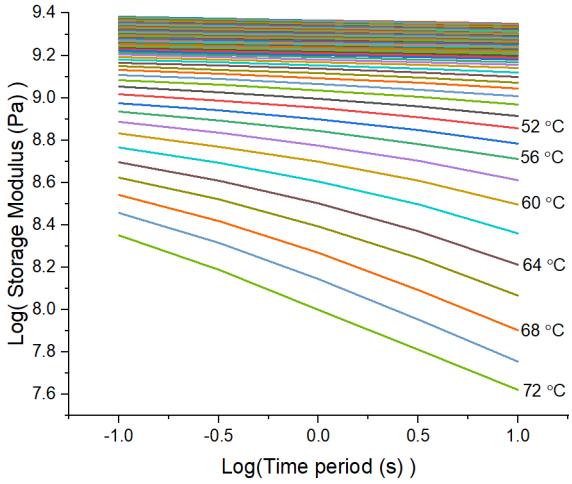


Figure 32a – Task 3

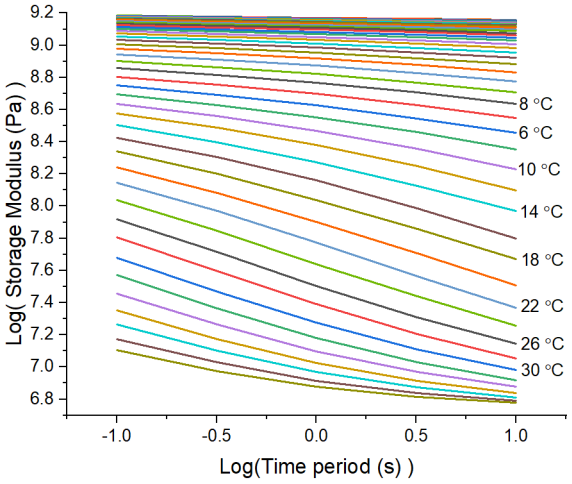


Figure 32b – Task 11

Figure 32 – Separated raw DMA data from oscillatory single cantilever configuration.

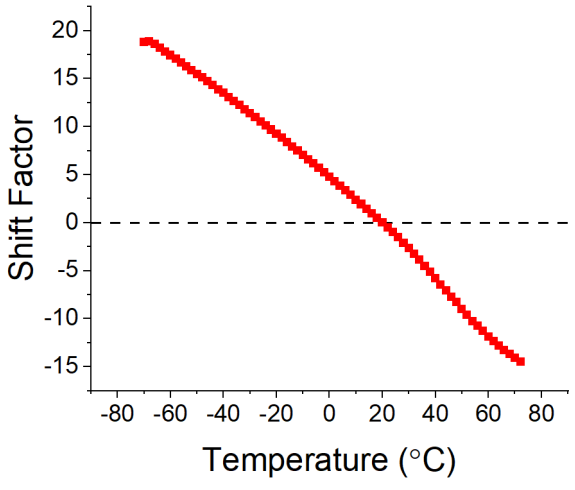


Figure 33a – Task 3

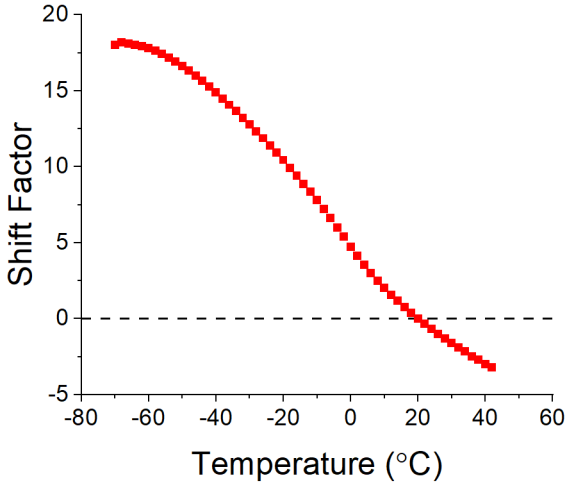


Figure 33b – Task 11

Figure 33 – Shift factors for single cantilever DMA.

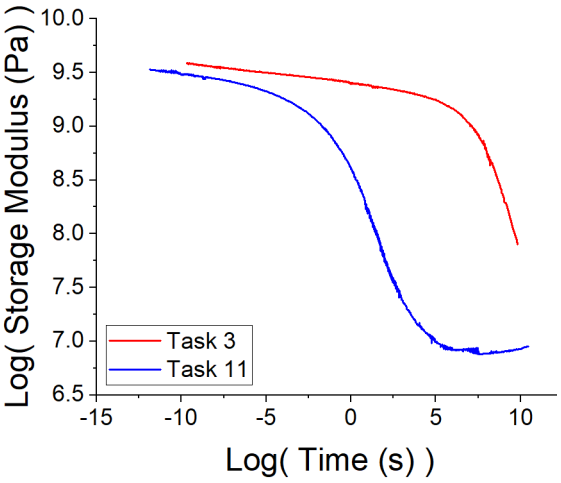


Figure 34 – Storage modulus variation with loading duration.

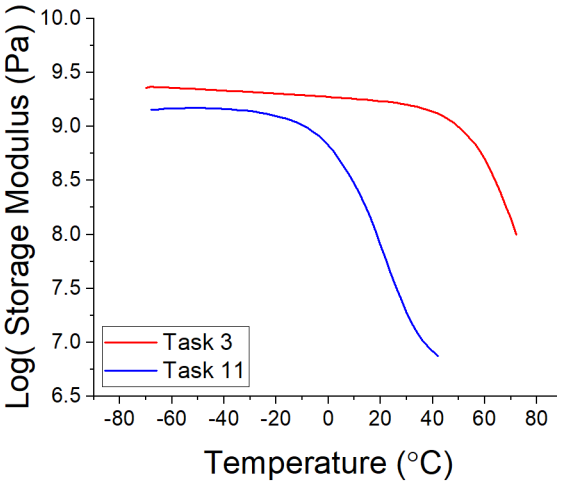


Figure 35 – Thermal variation of storage modulus at a single frequency, 1 Hz.

3.11.3 Task 3 Prony Series Values

Density = 1 kg/m^3

Poisson's ratio = 0.49

20 °C			0 °C		
E_0	6.335×10^9	(instantaneous)	E_0	6.394×10^9	(instantaneous)
log(τ)	g_i	k_i	log(τ)	g_i	k_i
-14	0.027024	0.027024	-14	0.088801	0.088801
-13	0.069250	0.069250	-13	0.001861	0.001861
-12	0.120835	0.120835	-12	0.052720	0.052720
-11	0.125524	0.125524	-11	0.025367	0.025367
-10	0.047087	0.047087	-10	0.124224	0.124224
-9	0.031334	0.031334	-9	0.048670	0.048670
-8	0.021768	0.021768	-8	0.052611	0.052611
-7	0.023346	0.023346	-7	0.030778	0.030778
-6	0.024357	0.024357	-6	0.022333	0.022333
-5	0.015738	0.015738	-5	0.022427	0.022427
-4	0.019053	0.019053	-4	0.024757	0.024757
-3	0.018074	0.018074	-3	0.015489	0.015489
-2	0.018484	0.018484	-2	0.018955	0.018955
-1	0.017316	0.017316	-1	0.017766	0.017766
0	0.027450	0.027450	0	0.018548	0.018548
1	0.021815	0.021815	1	0.016687	0.016687
2	0.018705	0.018705	2	0.027260	0.027260
3	0.023883	0.023883	3	0.021770	0.021770
4	0.026377	0.026377	4	0.018533	0.018533
5	0.032628	0.032628	5	0.023428	0.023428
6	0.050860	0.050860	6	0.026008	0.026008
7	0.069407	0.069407	7	0.031857	0.031857
8	0.082257	0.082257	8	0.049436	0.049436
9	0.048129	0.048129	9	0.067938	0.067938
10	0.011567	0.011567	10	0.081716	0.081716
11	0.002510	0.002510	11	0.049780	0.049780
			12	0.012906	0.012906
			13	0.001127	0.001127

Table 4 - Task 3 20 °C and 0° C Prony values for ABAQUS.

-20 ℃			-40 ℃		
E_0	$4.715x10^9$	(instantaneous)	E_0	$5.044x10^9$	(instantaneous)
log(τ)	g_i	k_i	log(τ)	g_i	k_i
-8	0.082657	0.082657	-5	0.096504	0.096504
-7	0.051266	0.051266	-4	0.086414	0.086414
-6	0.030586	0.030586	-3	0.052475	0.052475
-5	0.040597	0.040597	-2	0.039668	0.039668
-4	0.037924	0.037924	-1	0.026208	0.026208
-3	0.024668	0.024668	0	0.030371	0.030371
-2	0.037861	0.037861	1	0.029597	0.029597
-1	0.022165	0.022165	2	0.019983	0.019983
0	0.025113	0.025113	3	0.023809	0.023809
1	0.023735	0.023735	4	0.022897	0.022897
2	0.026343	0.026343	5	0.022798	0.022798
3	0.020371	0.020371	6	0.022540	0.022540
4	0.034934	0.034934	7	0.034256	0.034256
5	0.031646	0.031646	8	0.027199	0.027199
6	0.026216	0.026216	9	0.023531	0.023531
7	0.028846	0.028846	10	0.030291	0.030291
8	0.034509	0.034509	11	0.033364	0.033364
9	0.039261	0.039261	12	0.041651	0.041651
10	0.057162	0.057162	13	0.065321	0.065321
11	0.084184	0.084184	14	0.088436	0.088436
12	0.108067	0.108067	15	0.102768	0.102768
13	0.088426	0.088426	16	0.057133	0.057133
14	0.030013	0.030013	17	0.013593	0.013593
15	0.01345	0.01345			

Table 5 - Task 3 -20 ℃ and -40° C Prony values for ABAQUS.

-60 °C		
E_0	$6.355x10^9$	(instantaneous)
log(τ)	g_i	k_i
-3	0.128749	0.128749
-2	0.326827	0.326827
-1	0.024907	0.024907
0	0.025059	0.025059
1	0.015926	0.015926
2	0.024949	0.024949
3	0.014165	0.014165
4	0.016729	0.016729
5	0.01526	0.01526
6	0.017325	0.017325
7	0.013284	0.013284
8	0.022925	0.022925
9	0.020596	0.020596
10	0.017145	0.017145
11	0.018864	0.018864
12	0.022578	0.022578
13	0.025586	0.025586
14	0.037534	0.037534
15	0.055012	0.055012
16	0.070646	0.070646
17	0.057701	0.057701
18	0.019501	0.019501
19	0.008731	0.008731

Table 6 - Task 3 -60° C Prony values for ABAQUS.

3.11.4 Task 11 Prony Series Values

Density = 1 kg/m^3

Poisson's ratio = 0.49

20 °C			0 °C		
E_0	$4.058x10^9$	(instantaneous)	E_0	$3.978x10^9$	(instantaneous)
log(τ)	g_i	k_i	log(τ)	g_i	k_i
-14	0.099517	0.099517	-10	0.094606	0.094606
-13	0.018718	0.018718	-9	0.047466	0.047466
-12	0.062411	0.062411	-8	0.027102	0.027102
-11	0.023109	0.023109	-7	0.037913	0.037913
-10	0.049524	0.049524	-6	0.047844	0.047844
-9	0.03617	0.03617	-5	0.031778	0.031778
-8	0.034692	0.034692	-4	0.043167	0.043167
-7	0.049993	0.049993	-3	0.052595	0.052595
-6	0.055586	0.055586	-2	0.060942	0.060942
-5	0.064899	0.064899	-1	0.069566	0.069566
-4	0.075297	0.075297	0	0.081508	0.081508
-3	0.083994	0.083994	1	0.08734	0.08734
-2	0.092791	0.092791	2	0.101972	0.101972
-1	0.09826	0.09826	3	0.091388	0.091388
0	0.077958	0.077958	4	0.071652	0.071652
1	0.051643	0.051643	5	0.036279	0.036279
2	0.015981	0.015981	6	0.00977	0.00977
3	0.004859	0.004859	7	0.003485	0.003485
4	0.001534	0.001534	8	0.000534	0.000534
5	0.000939	0.000939	9	0.000668	0.000668
6	2.56E-05	2.56E-05	10	0.000297	0.000297
7	0.000113	0.000113	11	7.71E-05	7.71E-05
8	3.27E-06	3.27E-06	12	0.000154	0.000154
9	1.48E-06	1.48E-06	13	0.000227	0.000227
10	1.2E-05	1.2E-05	14	0.000626	0.000626
11	3.15E-05	3.15E-05	15	4.72E-06	4.72E-06
12	0.000527	0.000527			
13	7.43E-12	7.43E-12			
14	0.000666	0.000666			
15	0.000337	0.000337			

Table 7 - Task 11 20 °C and 0° C Prony values for ABAQUS.

-20 °C			-40 °C		
E_0	$4.85x10^9$	(Instantaneous)	E_0	$3.398x10^9$	(instantaneous)
log(τ)	g_i	k_i	log(τ)	g_i	k_i
-8	0.18032	0.18032	-3	0.029031	0.029031
-7	0.108316	0.108316	-2	0.047002	0.047002
-6	0.027754	0.027754	-1	0.054861	0.054861
-5	0.026579	0.026579	0	0.036907	0.036907
-4	0.040642	0.040642	1	0.0518	0.0518
-3	0.027383	0.027383	2	0.061954	0.061954
-2	0.032806	0.032806	3	0.072019	0.072019
-1	0.0426	0.0426	4	0.082114	0.082114
0	0.048642	0.048642	5	0.096124	0.096124
1	0.055797	0.055797	6	0.102098	0.102098
2	0.065571	0.065571	7	0.120081	0.120081
3	0.070623	0.070623	8	0.104953	0.104953
4	0.081654	0.081654	9	0.082409	0.082409
5	0.078314	0.078314	10	0.039733	0.039733
6	0.061591	0.061591	11	0.010595	0.010595
7	0.034971	0.034971	12	0.003473	0.003473
8	0.009889	0.009889	13	0.00138	0.00138
9	0.003128	0.003128	14	0.000577	0.000577
10	0.001088	0.001088	15	0.000463	0.000463
11	0.000585	0.000585	16	5.79E-05	5.79E-05
12	2.92E-05	2.92E-05			
13	5.74E-05	5.74E-05			
14	3.63E-10	3.63E-10			

Table 8 - Task 11 -20 °C and -40° C Prony values for ABAQUS.

-60 °C		
E_0	$4.972x10^9$	(instantaneous)
log(τ)	g_i	k_i
-3	0.108746	0.108746
-2	0.174955	0.174955
-1	0.047706	0.047706
0	0.01945	0.01945
1	0.040425	0.040425
2	0.029263	0.029263
3	0.028599	0.028599
4	0.040908	0.040908
5	0.045534	0.045534
6	0.053076	0.053076
7	0.061704	0.061704
8	0.068562	0.068562
9	0.076044	0.076044
10	0.079966	0.079966
11	0.063333	0.063333
12	0.041471	0.041471
13	0.012689	0.012689
14	0.00391	0.00391
15	0.001161	0.001161
16	0.000881	0.000881

Table 9 - Task 11 -60 °C Prony values for ABAQUS.

3.12 References

[1] N. M. Nurazzi *et al.*, “A review on natural fiber reinforced polymer composite for bullet proof and ballistic applications,” *Polymers (Basel)*, vol. 13, no. 4, pp. 1–42, Feb. 2021, doi: 10.3390/polym13040646.

[2] H. A. Aisyah *et al.*, “A comprehensive review on advanced sustainable woven natural fibre polymer composites,” *Polymers*, vol. 13, no. 3. MDPI AG, pp. 1–45, Feb. 01, 2021. doi: 10.3390/polym13030471.

[3] J. M. García, F. C. García, F. Serna, and J. L. de la Peña, “High-performance aromatic polyamides,” *Progress in Polymer Science (Oxford)*, vol. 35, no. 5. pp. 623–686, May 2010. doi: 10.1016/j.progpolymsci.2009.09.002.

[4] K. J. Groh *et al.*, “Overview of known plastic packaging-associated chemicals and their hazards,” *Science of the Total Environment*, vol. 651. Elsevier B.V., pp. 3253–3268, Feb. 15, 2019. doi: 10.1016/j.scitotenv.2018.10.015.

[5] E. Bugnicourt, P. Cinelli, A. Lazzeri, and V. Alvarez, “Polyhydroxyalkanoate (PHA): Review of synthesis, characteristics, processing and potential applications in packaging,” *Express Polym Lett*, vol. 8, no. 11, pp. 791–808, 2014, doi: 10.3144/expresspolymlett.2014.82.

[6] K. Akella and N. K. Naik, “Composite armour—A review,” *J Indian Inst Sci*, vol. 95, no. 3, pp. 297–312, 2015.

[7] M. I. Okereke, C. P. Buckley, and C. R. Siviour, “Compression of polypropylene across a wide range of strain rates,” *Mech Time Depend Mater*, vol. 16, no. 4, pp. 361–379, Nov. 2012, doi: 10.1007/s11043-012-9167-z.

[8] N. W. Tschoegl, W. G. Knauss, and I. Emri, “The effect of temperature and pressure on the mechanical properties of thermo- and/or piezorheologically simple polymeric materials in thermodynamic equilibrium - a critical review,” *Mechanics Time-Dependent Materials*, vol. 6, no. 1, pp. 53–99, 2002, doi: 10.1023/A:1014421519100.

[9] M. Doi *et al.*, “Molecular modelling of entanglement,” in *Philosophical Transactions of the Royal Society A: Mathematical, Physical and Engineering Sciences*, Apr. 2003, vol. 361, no. 1805, pp. 641–652. doi: 10.1098/rsta.2002.1168.

[10] C. Ortiz, R. Kim, E. Rodighiero, C. K. Ober, and E. J. Kramer, “Deformation of a Polydomain, Liquid Crystalline Epoxy-Based Thermoset,” 1998. [Online]. Available: https://pubs.acs.org/sharingguidelines

[11] N. v. David, X. L. Gao, and J. Q. Zheng, “Stress relaxation of a Twaron®/natural rubber composite,” *J Eng Mater Technol*, vol. 133, no. 1, 2011, doi: 10.1115/1.4002636.

[12] F. Björk and B. Stenberg, “Stress relaxation of a nitrile rubber surrounded by an oil that increases the network density,” *Polymer (Guildf)*, vol. 31, no. 9, pp. 1649–1657, 1990.

[13] L. H. Sperling, *Introduction to physical polymer science*. John Wiley & Sons, 2005.

[14] M. Arzhakov, *Relaxation in Physical and Mechanical Behavior of Polymers*. 2019. doi: 10.1201/9780429244520.

[15] A. S. Wineman and K. R. Rajagopal, *Mechanical response of polymers*. Cambridge: Cambridge University Press, 2000.

[16] R. L. Taylor, K. S. Pister, and G. L. Goudreau, “Thermomechanical analysis of viscoelastic solids,” *Int J Numer Methods Eng*, vol. 2, no. 1, pp. 45–59, 1970.

[17] S. W. Park and R. A. Schapery, “Methods of interconversion between linear viscoelastic material functions. Part I—a numerical method based on Prony series,” *Int J Solids Struct*, vol. 36, no. 11, pp. 1653–1675, 1999, doi: https://doi.org/10.1016/S0020-7683(98)00055-9.

[18] N. Saba, M. Jawaid, O. Y. Alothman, and M. T. Paridah, “A review on dynamic mechanical properties of natural fibre reinforced polymer composites,” *Construction and Building Materials*, vol. 106. Elsevier Ltd, pp. 149–159, Mar. 01, 2016. doi: 10.1016/j.conbuildmat.2015.12.075.

[19] M. L. Williams, R. F. Landel, and J. D. Ferry, “The temperature dependence of relaxation mechanisms in amorphous polymers and other glass-forming liquids,” *J Am Chem Soc*, vol. 77, no. 14, pp. 3701–3707, 1955.

[20] H. Kolsky, “An Investigation of the Mechanical Properties of Materials at very High Rates of Loading,” *Proceedings of the Physical Society. Section B*, vol. 62, no. 11, pp. 676–700, 1949, doi: 10.1088/0370-1301/62/11/302.

[21] G. Gray and W. R. Blumenthal, “Split-Hopkinson pressure bar testing of soft materials,” *Mechanical testing and evaluation*, vol. 8, pp. 1093–1114, Sep. 2000.

[22] J. E. Field, S. M. Walley, W. G. Proud, H. T. Goldrein, and C. R. Siviour, “Review of experimental techniques for high rate deformation and shock studies,” in *International Journal of Impact Engineering*, Aug. 2004, vol. 30, no. 7, pp. 725–775. doi: 10.1016/j.ijimpeng.2004.03.005.

[23] W. W. Chen and B. Song, *Split Hopkinson (Kolsky) bar: design, testing and applications*. Springer Science & Business Media, 2010.

[24] B. Song and W. Chen, “Split Hopkinson pressure bar techniques for characterizing soft materials,” *Latin American Journal of Solids and Structures*, vol. 2, no. 2, pp. 113–152, 2005.

[25] T. J. C. Loete, G. Paul, and E. B. Ismail, “A preliminary investigation of the dynamic viscoelastic relaxation of bovine cortical bone,” in *EPJ Web of Conferences*, Sep. 2015, vol. 94. doi: 10.1051/epjconf/20159403004.

[26] “Bentley Advanced Materials,” *https://www.benam.co.uk/products/plastic/task*.

[27] S. Deng, M. Hou, and L. Ye, “Temperature-dependent elastic moduli of epoxies measured by DMA and their correlations to mechanical testing data,” *Polym Test*, vol. 26, no. 6, pp. 803–813, Sep. 2007, doi: 10.1016/j.polymertesting.2007.05.003.

[28] J. Yi, M. C. Boyce, G. F. Lee, and E. Balizer, “Large deformation rate-dependent stress-strain behavior of polyurea and polyurethanes,” *Polymer (Guildf)*, vol. 47, no. 1, pp. 319–329, Jan. 2006, doi: 10.1016/j.polymer.2005.10.107.

4 The Use of Time-Temperature Superposition for Interface Characterisation using the J-Integral

This chapter comprises an introduction, then a paper submitted for publication to Strain.

4.1 Chapter Introduction

Of further interest to this thesis was the behaviour of the ceramic-polymer interface under a range of loading and environmental conditions. In this chapter, this interface is characterised, and the resulting data is used to populate FE simulations. Of particular interest was to investigate the use of TTS in predicting the dynamic behaviour of the interface through quasi-static experiments performed at sub-ambient conditions. After initially verifying, through FEA simulations, that the analysis pipeline was valid, ceramic-ceramic specimens, bonded with polymer, were loaded until interfacial failure, quasi-statically and dynamically. This was performed using a sharpened wedge on a screw-driven machine and a modified Hopkinson bar apparatus. Further quasi-static experiments were performed at sub-ambient conditions where the temperature was selected to mimic the polymer response observed under dynamic timescales. From these experiments, the J-integral and stress intensity factors were calculated with time and increasing crack length and used to characterise the interface. It was found that, in general, TTS was able to predict the dynamic behaviour well and could have potential in investigating the dynamic properties of an interface without the requirement for dynamic experiments. The observations made in

this chapter will be used to support quasi-static and impact observations made on model armour in Chapter 5.

4.2 Abstract

The management of interfaces and adhesives are highly important for the overall performance of a system, particularly under dynamic loading. However, the dynamic testing and analysis of interfaces can be very challenging. This is partly due to the inherent difficulties associated with dynamic experiments, such as the influence of stress wave oscillation and inertia. This could potentially be circumvented using the principle of time-temperature superposition, which allows the manipulation of temperature to mimic the response of polymers under dynamic loading conditions. In this paper, a polyurethane-alumina interface was investigated using a wedge test under quasi-static and dynamic loading conditions using a split Hopkinson pressure bar (SHPB). Two polyurethanes were investigated, and further surface modifications were applied by the addition of a primer surface pre-treatment to the ceramic. Quasi-static experiments were performed under ambient and sub-ambient environmental conditions with the low temperature chosen, using the principle of time-temperature superposition, to simulate the short timescale mechanical properties of the polymers. During loading, the displacement field was extracted using digital image correlation (DIC); this field was implemented as a boundary condition in an Abaqus simulation in order to calculate the J-integral and stress intensity factors were calculated. Additional finite element simulations were conducted to verify this analysis pipeline and investigate the influence of dynamic effects on the final results. It was found that good correlation was observed between the J-integrals calculated under dynamic-ambient and static-sub-ambient loading conditions for the polymers; this finding supports the use of time-temperature superposition for dynamic interface behaviour prediction. However, due to the non-separated approximation of the J-integral used here, this correlation was limited if there was excessive ductility in the polymer. Further limitations

were noted due to the influence of thermal strains across the interface and more complex interfaces, such as those with primer pre-treatments, causing weakening at sub-ambient temperatures.

4.3 Introduction

Fracture and unstable crack propagation under impact can be devastating and costly both in terms of human life and the economy [1]. Therefore, it is the role of the fracture mechanist to understand this behaviour and determine the consequences, which is particularly difficult because many materials and adhesives possess strong rate and temperature dependency [2]–[5].

There are several approaches to understanding fracture mechanics and the behaviour of cracks. In this paper, two are of interest. The first, pioneered by Irwin in 1957 [6], [7], who built upon the work of Westergaard [8], is the stress intensity factor, which is a measure of how the stress field in an extended body is affected by the crack tip. The second is the J-integral, which builds upon the idea of an energy balance as the crack increments [9], [10] and, for linear elastic materials, is equal to the energy release rate [11], [12]. Both the J-integral, J, and the stress intensity factor, K_1 and K_{11}, approaches describe the same phenomenon and there is an equivalence between the two in the form of

$$J=\frac{K_1^2}{E'}+\frac{K_{11}^2}{E'} \qquad (1)$$

where $E'=E$ for plane stress and $E'=\frac{E}{1-\upsilon^2}$ for plane strain. In this study, the main focus will be on the J-integral; however, K_1 and K_{11} will also be calculated.

The J-integral for a crack is calculated by taking a path integral that encapsulates the crack tip and begins and ends on the free surfaces of the crack:

$$J=\int_{\Gamma} W d x_2 - t \cdot \frac{\partial u_i}{\partial x_1} d s \qquad (2)$$

where Γ is the path contour encircling the crack tip, W is the strain energy density, u is the displacement vector, and x_1 and x_2 are coordinate directions parallel and perpendicular to the direction of crack propagation. The traction vector is $\boldsymbol{t}$, defined as $t=\sigma n$ where $\boldsymbol{n}$ is the unit normal vector at each increment of arc length ds. For the strain energy density, W, the stress strain response does not have to be linear. However, one assumption made in the J-integral derivation is that all the stored strain energy is available for crack growth. This is not true for plasticity but can be considered valid for monotonically increasing loading. In practice, it is difficult to use a path integral, so Green's theorem can be applied to convert it to an area integral [13] which can be better implemented into FE software.

Experimentally, under quasi-static loading, there are many methods and standards available to determine interfacial strength, such as the peel test [14], double cantilever beam (DCB) [15] and the end notched flexure (ENF) [16] to name but a few. However, these tests become more challenging under dynamic loading due to the inherent difficulties associated with dynamic experiments, such as the influence of stress wave oscillations and the rate of data acquisition as well as difficulties with the accurate application of dynamic loads to these experimental configurations. Various methods have been proposed, such as pendulum-based techniques [17], [18] or using a drop tower [19]–[22]. However, for this research, an apparatus based on a Hopkinson bar was used to investigate the dynamic response of an interface [23]–[31]. The interface was investigated by the insertion of a wedge between two ceramic strips bonded with the polymer of interest. Using this

configuration, loading can also be performed under both quasi-static and dynamic conditions [5], [32].

The behaviour of cracks is expected to differ under dynamic loading because many materials possess strain rate dependency as well as the influence of stress waves in the material. Hence, a dynamic J-integral was used to account for these effects [33]–[35]. However, taking into account inertial effects poses significant experimental challenges because extracting an accurate velocity field under dynamic loading rates is challenging, especially in the vicinity of a crack. Therefore, an aim of this paper is to use the principle of time-temperature superposition [36] to recreate the dynamic properties of a polymer adhesive under quasi-static loading. Polymers are highly rate and temperature dependent, and in the polymer chosen this is governed by a single thermally activated process, the glass transition. Hence, by a reduction of the temperature, the dynamic properties of the polymer can be mimicked under quasi-static conditions, see [37] for a detailed description.

In summary, in addition to characterising the static and dynamic performance of polyurethane-bonded alumina in a wedge configuration, this paper will further bridge the gap between the quasi-static and high speed experiments by temperature manipulations. Additionally, FEA simulations will be used to support these results to quantify the influence of the dynamic effects on the interface performance.

4.4 Materials and Specimen Preparation

4.4.1 Materials

Two polyurethanes (PU), commercially known as ‘Task 11’ and ‘Task 3’, were sourced from Bentley advanced polymers [38] and alumina (95 %), commercially known as Sintox FF, from Morgan Ceramics [39]. An extensive characterisation of the mechanical properties of the

polymers has been performed in Chapter 3 and is summarised in section 4.6. In addition to measuring the interfacial strength of bonds between these polymers and the ceramic, a further investigation was conducted into the influence of a primer pre-treatment applied to the ceramic service before bonding; the primer used was Sika 206 G + P [40]. In total, there were four types of specimens, using both types of PU with and without a primer surface pre-treatment.

4.4.2 Specimen Preparation

Specimens were prepared by sandwiching the polymer between two ceramic strips, Figure 1. The strips were sectioned from a larger tile and were of dimensions 100 x 20 x 8 mm. Before bonding, the ceramic surface was cleaned using isopropyl alcohol and water and then allowed to air dry. The PUs arrived as two-part polymers consisting of a diisocyanate and a diol. Each part was degassed, thoroughly mixed, then the mixtures were degassed again. The PU was then carefully poured onto the prepared ceramic surface before being sandwiched between this and the other ceramic strip. PTFE tape was used to define the bond thickness, which was limited to 0.5 ± 0.1 mm, as well as to define a 25 mm pre-crack. The specimens were left at room temperature for 24 hours to cure before a final 4-hour heat treatment at 65 °C, as per the manufacturer's instructions. Once cured, a razor blade was used to sharpen the pre-crack.

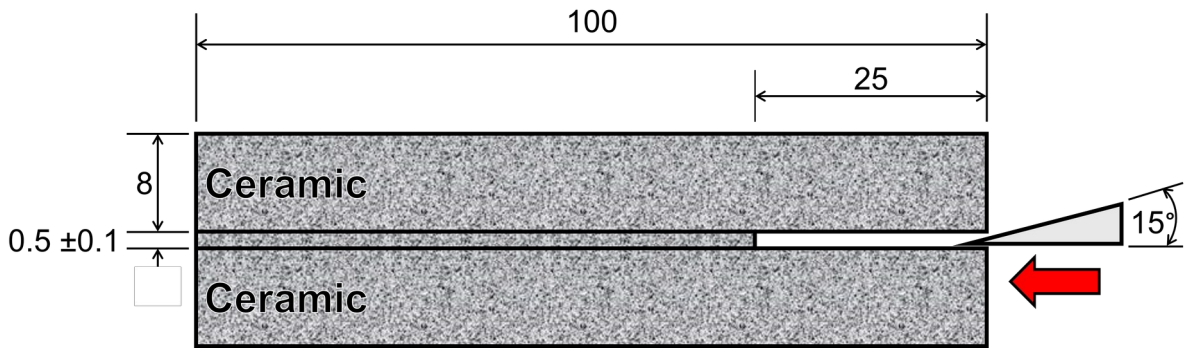


Figure 1 - Dimensions of wedge test specimen. Two ceramic strips have been bonded with a layer of polymer. The surface has been painted with a speckle pattern to allow digital image correlation (DIC) to be used to analyse the resulting displacement field during loading. Specimens were 20 mm wide.

The specimen's surface displacement field during loading was used in later calculations of the fracture toughness. To extract these displacements, the surface of the specimen was painted with a black and white speckle pattern using an airbrush, and the specimen was imaged during loading. Digital image correlation (DIC) was used to compare the images taken during loading to an unloaded reference. The minimum size of these speckles was determined by the resolution of the camera and larger speckles were required for the dynamic experiment. Full details of the DIC parameters are given in Table 1.

	Point Grey GS3-U3-41C6M-C Quasi-static	Specialised Imaging Kirana Dynamic
Camera Noise	0.9 %	1.9 %
Frame Rate	10 fps	(up to) 5 million fps
Exposure Time	50 ms	100 ns
Total number of frames	N/A	180
Field of View	2048 x 2048 pix	924 x 748 pix
DIC Software	MatchID.2021.2	MatchID.2021.2
Spatial Resolution	0.0457 pix	0.029 pix
Subset Size	25 pix	29 pix
Step Size	10 pix	5 pix
Pixel Size	0.0139 mm	0.0567 mm
Correlation Method	ZNSSD	ZNSSD
Image Prefilter	Gaussian, Kernel 5	Gaussian, Kernel 5

Interpolation	Bicubic Spline	Bicubic Spline
Shape Function	Quadratic	Quadratic

Table 1 - Camera properties and DIC Processing settings.

4.5 Experimental Overview

A 15° asymmetrical steel wedge was used to separate the two ceramic layers under quasi-static and dynamic conditions. Quasi-static loading was performed using a commercial screw-driven testing machine (Instron 3400 Series) at 0.05 mm s^{-1} at 20 °C, and dynamic loading was performed on an apparatus based on the Hopkinson pressure bar (SHPB), Figure 2. The wedge was formed on the end of a 400 mm long, 25.4 mm diameter steel bar, which was then hardened; a second bar of the same length was launched by a gas gun into the wedge bar. Impact speeds were of order 10 m s^{-1}. The specimen was imaged at quasi-static and dynamic timescales using a Point Grey GS3-U3-41C6M-C and a Specialised Imaging Kirana, respectively. The camera properties can be found in Table 1.

Further quasi-static experiments were performed at sub-ambient temperatures, allowing the principal of time-temperature superposition to be utilised. The temperature was chosen to be -40 °C and -22 °C for Task 3 and Task 11, respectively, at which the quasi-static mechanical properties are similar to those experienced under dynamic loading.

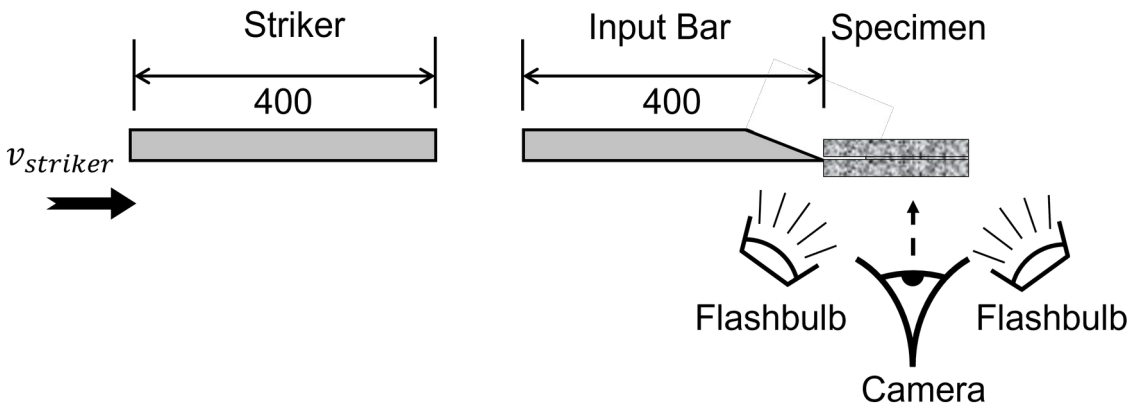


Figure 2 - Experimental set up for dynamic wedge test.

4.6 Polymer Properties

The PUs were chosen due to their combination of chemical similarity and different mechanical properties. This allowed an investigation into the mechanical influence of bonding with less concern about potential differences in chemical interactions across the interface because this has been shown to play a significant role [41], [42]. The modulus differed between polymers and is a function of time, as shown in Figure 3. The time scales of interest to this project are log(t) ~ 1 for the quasi-static experiment and log(t) ~ -5 for the dynamic.

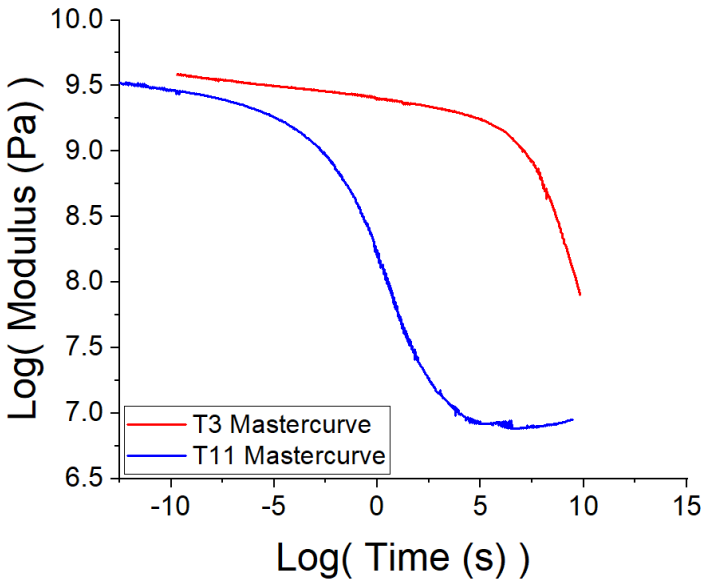


Figure 3 - Stiffness mastercurve for Task 3 and Task 11. Mastercurves were created from isothermal stress relaxation experiments using DMA apparatus in a 3-point bend configuration.

In order to obtain the data in Figure 3, DMA experiments were performed using a 3-point bend configuration and a stress relaxation testing procedure. Specimens were loaded slowly to 0.1 % strain, at which point the displacement was held constant and the force was recorded for 10 minutes as the specimens relaxed. Once loaded, the polymers were allowed to recover for a further 20 minutes. This was repeated at temperatures from -85 °C to +55 °C in 5 °C intervals. Time temperature-superposition [43] was then used to create the mastercurves shown in Figure 3, which describe the stiffness of the polymers over a very wide range of loading times. See Chapter 3 for a thermomechanical analysis of these polymers.

From Figure 3, both polymers displayed similar overall behaviour with a single transition, the glass transition, over the timescales measured. For each polymer, this transition was measured to be at 50 °C and 15 °C for Task 3 and Task 11, respectively. Under quasi-static loading, the appropriate timescales are log(t)~1; here, Task 3 is significantly stiffer than Task 11 and displays substantially less strain rate sensitivity. Under dynamic loading, log(t)~-5,

the stiffnesses and strain rate sensitivity of the polymers are similar. At very small timescales, the stiffness of both polymers appears to converge. This is also believed to be true at the very large timescales; however, large timescale data were not collected for Task 3 behaviour because this was not of direct interest to this project. The overall similarity in behaviour was expected due to the chemical similarity of the polymers.

4.7 Analytical Procedure and FEA

4.7.1 Procedure Pipeline

Using images of the crack tip during loading, the J-integral, as well as K_1 and K_{11}, were found. To achieve this, the images were processed with the method and Matlab code used by Barhli *et al*. [44]. In this method, the displacement field around the crack tip was extracted from images of the specimen taken during loading using DIC. In principle, assuming that the materials are elastic and the moduli are known, these data should be sufficient to calculate the J-integral, K_1 and K_{11}.

Within this method, the displacement field around the crack tip was inputted into Abaqus 2021 alongside the relevant material properties. This displacement field was extracted from experimental images using DIC and inputted into Abaqus using Matlab. However, it has been found that if the DIC displacement field was inputted directly into Abaqus, the outputs would be inaccurate [44]. DIC is poor at accurately capturing displacement fields around a free surface and in regions of high stress gradients, both of which are present around a crack tip. To account for this, the displacement field immediately surrounding the crack tip was initially ignored, and the remaining field was inputted into an Abaqus and, before the J-integral, K_1 and K_{11} were calculated, an FEA simulation was run. This simulation returned an equilibrium displacement field around the crack tip that is consistent with the geometry,

material properties and the deformation field of the surrounding material. From this displacement field, Abaqus calculates the J-integral, K_1 and K_{11}. For a more detailed description of this method, see Ref [44].

4.7.2 Dynamic Influence

The method described above used the displacement field at each frame as the input into Abaqus and used a static analysis of the J-integral. For simplicity, this analysis was still used for the dynamic version of this wedge experiment, so it is necessary to understand the limitations of this approach. To understand this, an FEA simulation of the wedge experiment was created and loaded statically and dynamically. The displacement outputs of these simulations were used to artificially deform images which were then processed using DIC and the previously described analysis. As well as determining the influence of stress waves on the overall results, further comparisons can be made into the robustness of the above procedure experimental noise, which can be artificially imposed onto images and to the DIC processing settings.

The experiment was created using a 2D homogenous model of dimensions 100 x 16 mm with a 25 mm crack midway up the short edge. A vertical boundary condition of 2 m s^{-1} was applied to the short edge of the top section, Figure 4. The simulation was created in Abaqus/Explicit using the parameters defined in Table 2. The simulation was run with an elastic material model with realistic material density, then repeated using the same material model but with artificially low density. This low density increases the wave speed of the material in the simulation, so the loading becomes effectively quasi-static. For simplicity, no failure criterion was input into the model because this model was not used as an absolute comparison to the experimental results.

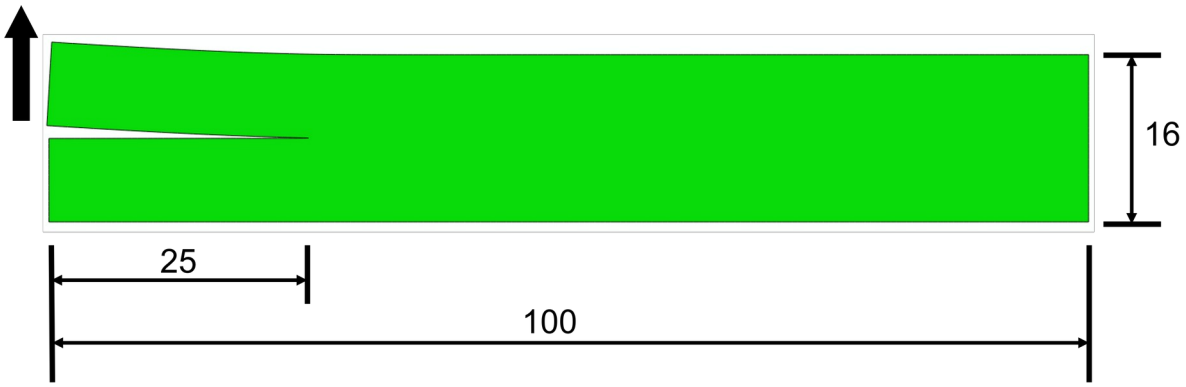


Figure 4 - Schematic of FEA wedge experiment where all dimensions are in mm. The deformation has been greatly exaggerated.

The displacement field from these simulations was used to artificially deform images taken from real experiments to give representative speckle fields. Data from the dynamic and static simulations were then processed in one of the following three ways.

- The displacement field from the simulation was directly processed using the previously mentioned procedure pipeline.
- The displacement fields were used to produce artificially deformed images, which were then processed as above using representative DIC processing conditions.
- The artificially deformed images were distorted using 2 % Gaussian noise, which was chosen to mimic measured camera noise. Images were then processed as above.

From these, comparisons between static and dynamic simulations could be made alongside the influence of DIC processing settings and camera noise.

	Alumina Representative	Alumina Artificially low density
Density	3000 kg m^{-3}	3 kg m^{-3}
Stiffness	275 GPa	
Poisson's Ratio	0.25	
Mesh Density	0.5 mm	
Element Type	Triangular S3	

Table 2 - Material properties and mesh parameters used for the wedge experiment FEA simulation.

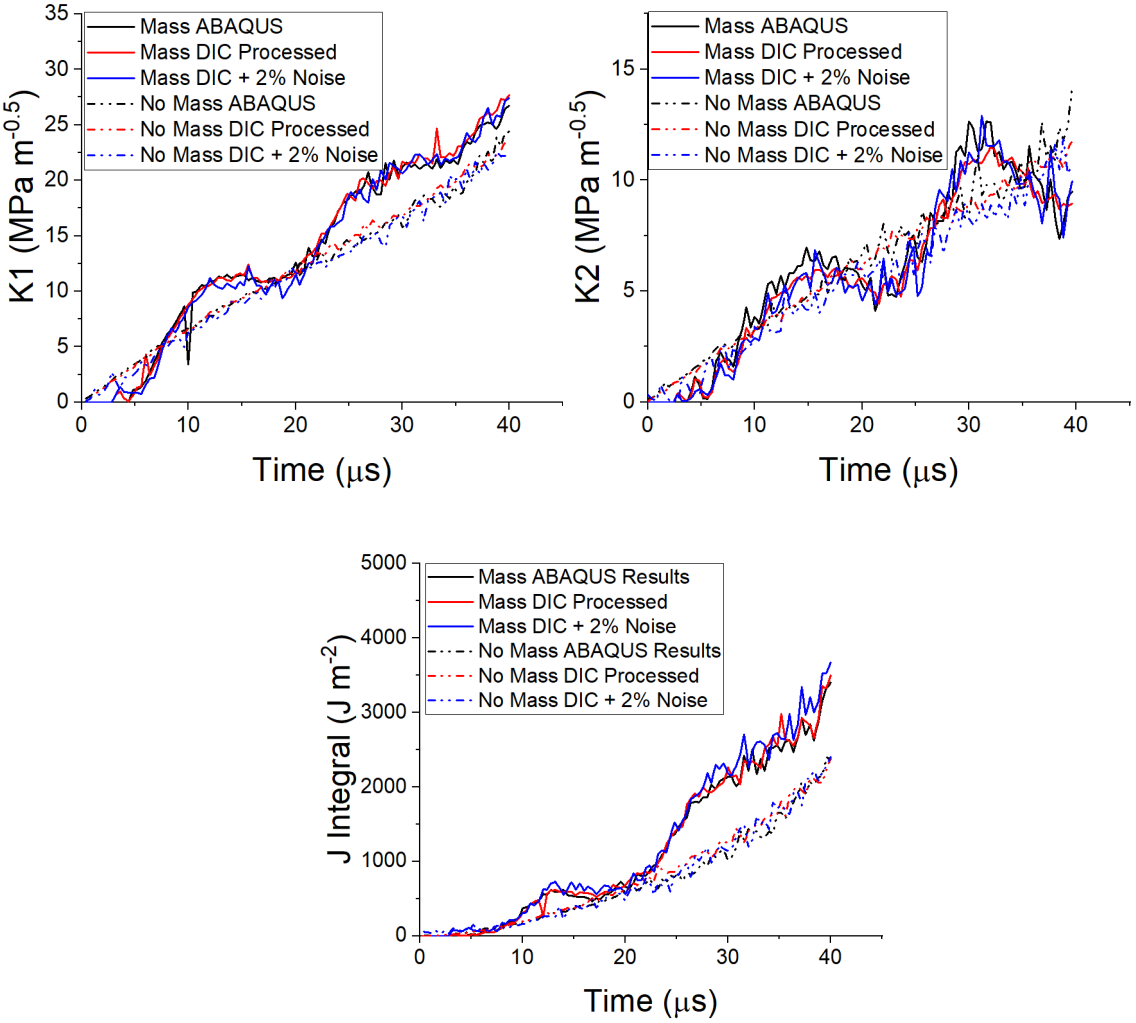


Figure 5 - FEA output results comparing the effects of inertia, DIC processing settings and image noise on the J-integral, K_1 and K_{11}.

The variation in J-integral, K_1 and K_{11}, with and without the influence of mass, are presented in Figure 5. For the dashed lines, which represented the low-mass analysis, K_1 and K_{11} increased linearly with loading, resulting in a quadratic increase in the J-integral. When inertial effects were accounted for, solid lines, the influence of wave oscillations can be seen in the periodic oscillations present in the results of each of the three outputs, and as a bulk offset. For $K_{1,}$ there was a 15 % increase in gradient upon loading and a periodic oscillation of ±3 MPa $m^{-0.5}$ compared to the static analysis. For $K_{11,}$ there is a periodic oscillation of ±1.3 MPa $m^{-0.5}$ and no change in gradient. The dynamic analysis produces a greater J-integral than the static analysis, and the peaks and troughs coincide with those observed in K_1 and K_{11}. Further, these data also demonstrated that the DIC settings are appropriate, and the representative noise had a negligible influence on the results.

Additionally, the contributions of kinetic and strain energies to the overall energy in the simulations are shown in Figure 6. Because the static analysis of the J-integral does not incorporate any kinetic energy terms, it is necessary to understand the contribution of this kinetic energy to the overall energy in the system. From Figure 6, it is shown that these kinetic energy contributions are significant early in the experiment and oscillate between about 0.1 and 1 J m^{-1}; because the strain energy increases, the kinetic energy becomes increasingly less significant as the time increases. As a consequence of these simulations, the authors are confident that, for this experimental set up, any calculated parameters will be representative of the dynamic properties of the interface and that effective comparisons can be made between the materials and loading rates of interest, which are the made focuses of this study.

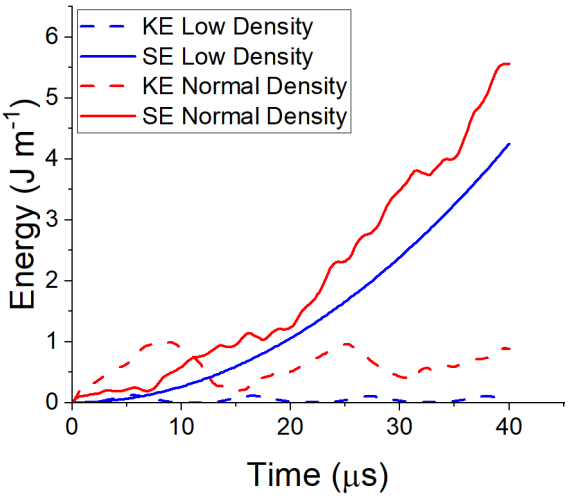


Figure 6 - Kinetic and strain energy contributions to total energy in the simulated wedge experiment using alumina with representative (3000 kg m^{-3}) and artificially low (3 kg m^{-3}) densities.

4.8 Results and Discussion

4.8.1 Analytical Procedure

Having verified the analytical procedure using FEA, the experimental data was processed. Here, a detailed example of the analytical procedure is shown for a specimen of Task 3 loaded dynamically.

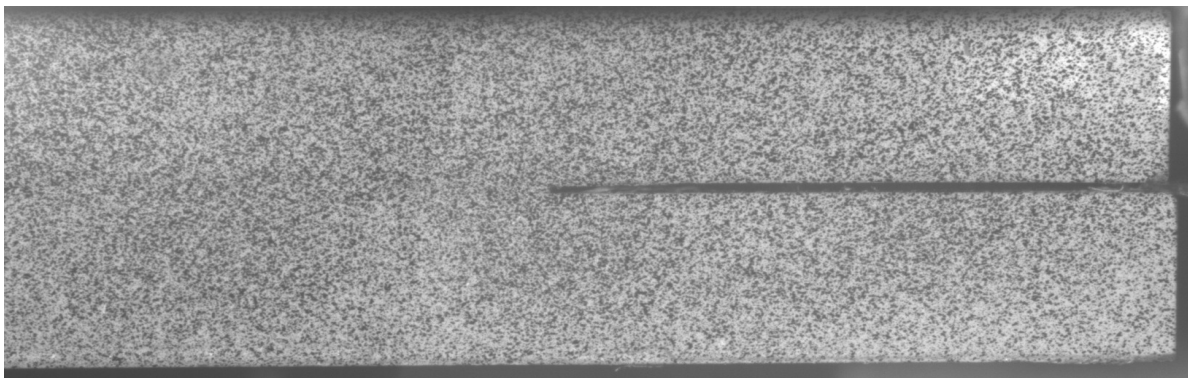


Figure 7 - Typical experimental image under quasi-static loading.

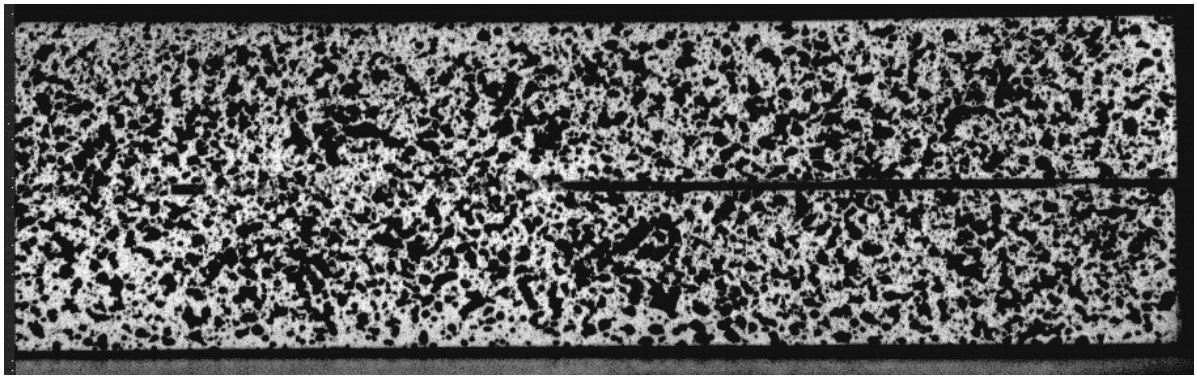


Figure 8 – Typical experimental image under dynamic loading.

Figure 7 and Figure 8 show example specimen images for the quasi-static and dynamic loading, respectively. The speckle pattern differs between experiments due to the differences in camera resolution, requiring larger speckles for the lower resolution high-speed camera to limit the effects of aliasing. These images were processed in MatchID using the DIC processing settings in Table 2, and the displacement field was extracted.

This displacement field was then inputted into Abaqus via Matlab code provided by Barhli [44] and analysed using the procedure described in section 4.7.1. A required input to this code is knowledge of the crack tip position. To define this position, a separation threshold was used, i.e. once the interface reached a critical separation, it was deemed to have failed, and this was the position of the crack tip. Under dynamic conditions, this critical separation threshold was defined to be 2 % strain for Task 3 and 3 % for Task 11, corresponding to approximately 0.01 mm and 0.015 mm, respectively. Under quasi-static conditions, due to the increase in ductility of the interface, this was increased to 3 % for Task 3 and 5 % for Task 11, approximately 0.015 mm and 0.025 mm, respectively. These thresholds were chosen as they aligned with a visual inspection of crack growth and evidence provided by the correlation coefficient parameter in DIC. This parameter measures the degree of

similarity between small subsets of the two images and is equal to 1 if the two regions are identical. A crack has a distinct influence on the correlation coefficient because it splits the subset in two, causing the similarity to drop. Therefore, this value can be used as a reliable method of crack detection, which helps to reduce the amount of user-input. In this study, the threshold for crack detection was chosen to be at the point where the correlation coefficient was distinct from the background noise. An example correlation coefficient map is shown in Figure 9.

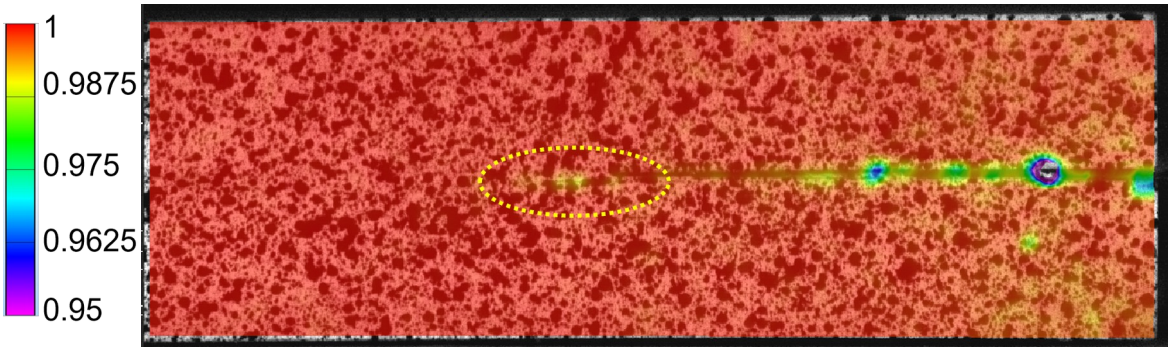


Figure 9 - Correlation coefficient map for dynamically loaded wedge specimen. The highlighted region provides evidence for the onset of fracture.

Using the above thresholds and the displacement map provided by DIC, the separation between the two ceramic faces was calculated along the length of the interface, and these have been plotted in Figure 10. For simplicity, only every 10th frame has been presented. For each frame, a fourth-order polynomial was fitted to the separation along the interface, and then the separation threshold criterion was applied. The points less than this threshold have been highlighted in red, and the furthest point defines the crack tip.

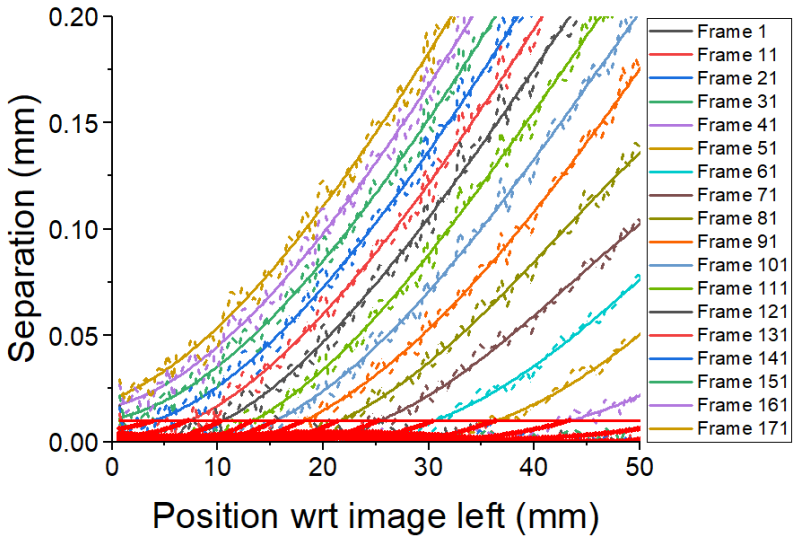


Figure 10 - interface separation as a function of position for each image. The image origin was on the left of each image. The dashed lines are the separation data, and the solid lines are a fourth-order polynomial fit to these data. Points highlighted in red are the positions at which crack failure has occurred.

This was calculated for each frame, and the crack tip position with time is presented in Figure 11. Crack growth was only recorded when the crack tip position calculated with the threshold separation criterion increased beyond the initial predefined crack length of 25 mm. From Figure 11, it was observed that, for the high-speed camera used, every 10th frame was significantly noisier than the surrounding frames, and this presented as periodic peaks in crack position, highlighted in red. These points were ignored, and the average of the surrounding points was used instead. The crack position was now used as an input into the analytical method described to calculate K_1, K_{11} and the J-integral at each frame.

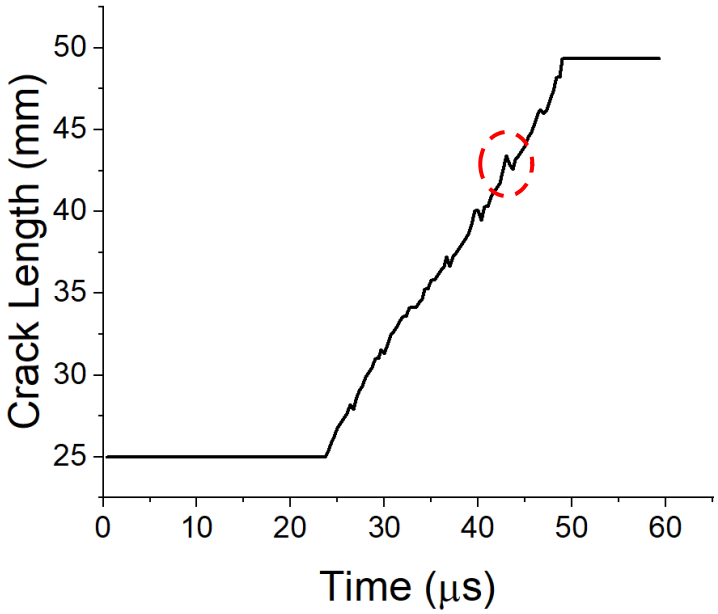


Figure 11 - Typical crack position as a function of time for Task 3 Primer specimens. Crack length increases from 25 mm until frame exit. The red circle highlights the influence of periodic noise in the camera every 10th frame.

4.8.2 Quasi-static Results

Using the procedure described previously in this paper, K_1, K_{11} and the J-integral were calculated from experiments performed under quasi-static loading for each polymer and bonding condition; these results are presented in Figure 12 - Figure 15. In these figures, the evolution of the fracture parameters was evaluated against crack length and time. Typically, these parameters reached a critical threshold, after which they stabilised as crack propagation occurred. This was believed to be due to the crack's initial bluntness, which meant that a higher stress intensity was required to initiate propagation than to continue it. On the rightmost of each figure, the mean and standard deviation of these critical values have been presented, and these results have been tabulated in Table 3.

For K_1, Figure 12, specimens bonded with Task 11 exhibited a greater stress intensity factor than Task 3 on average, although there was a greater spread in the data. When comparing both polymers to their low temperature equivalents, the low temperature significantly

reduced the bond strength for Task 3 and appeared to also do this for Task 11; however, there was a significantly greater spread in the material response. For both polymers, there was limited influence of adding a primer pre-treatment for ambient and sub-ambient conditions.

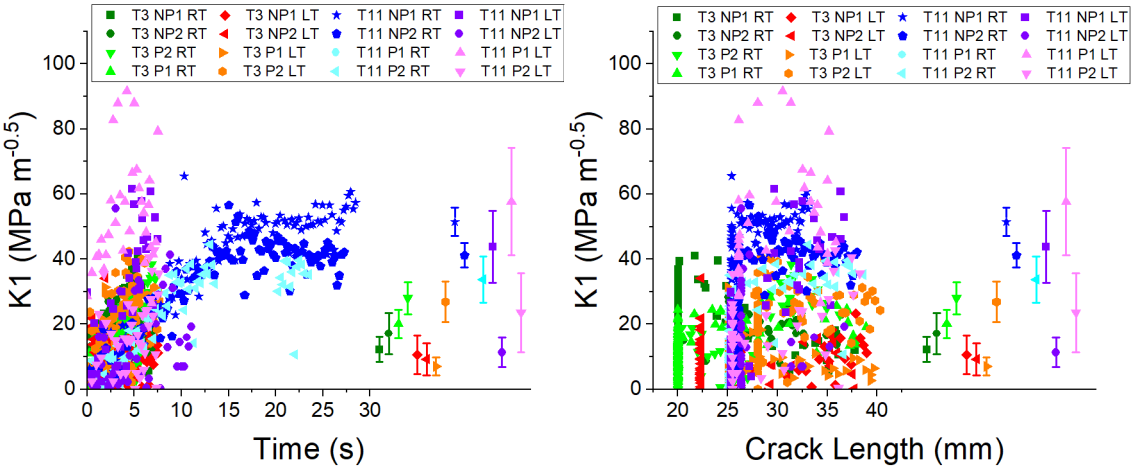


Figure 12 – K_1 vs time or crack length for quasi-static wedge experiment. Error bars on the right denote the mean ± one standard deviation. P represents primer surface pre-treatment and NP represents non-primer. Two experiments were performed for each specimen type, labelled as 1 and 2.

For all loading conditions for Task 3, there is very little loading in the mode 2 direction compared to mode 1, Figure 13. Although, this wasn't the case for Task 11, where substantial mode 2 loading can be observed, particularly at room temperature. However, this was likely to be artificially high because Task 11 at room temperature is relatively ductile compared to Task 3, so shearing between the two ceramic strips was observed. As mentioned previously, the code used to process these data assumed a crack in a homogenous material with no bonded interface. This assumption is valid for thin and stiff interfaces although breaks down for ductile bonding, as observed here. The consequence of this is significant ductility processed with the material properties of ceramics, thus, a vast overcalculation of the K_{11} stress intensity factor was processed. It is observed that the low

temperature processing of these data for Task 11, the K_{11} stress intensity factor is significantly reduced because the polymer is less ductile, and K_{11} would be closer to the true value.

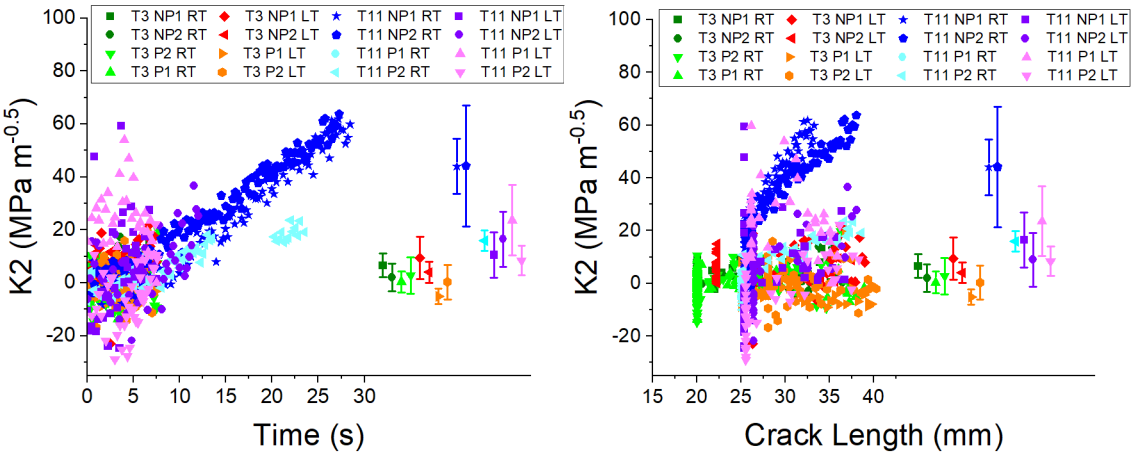


Figure 13 – K_{11} vs time or crack length for quasi-static wedge experiment. Error bars on the right denote the mean ± one standard deviation. P represents primer surface pre-treatment and NP represents non-primer.

As a consequence of an artificially high K_{11} for Task 11, the J-integral for this polymer was inflated because of the relation between K_{11} and the J-integral. To account for this, a separated J-integral could be processed in which the distinct mechanical properties are accounted for; however, this was beyond the current scope of this research. For Task 3, the J-integral at room temperature was greater than that observed at low temperature. This was thought to be a consequence of a reduction in ductility of the polymer, hence reducing the bonding ability of the polymer, which reduced the energy absorption capabilities of the interface. A further influence was thought to be due to a difference in thermal expansion between the polymer and ceramic, which would have created thermal strains across the ceramic-polymer interface and likely weakened the interface. Further, the addition of the

primer pre-treatment appears to further weaken the interface at ambient and sub-ambient conditions for Task 3.

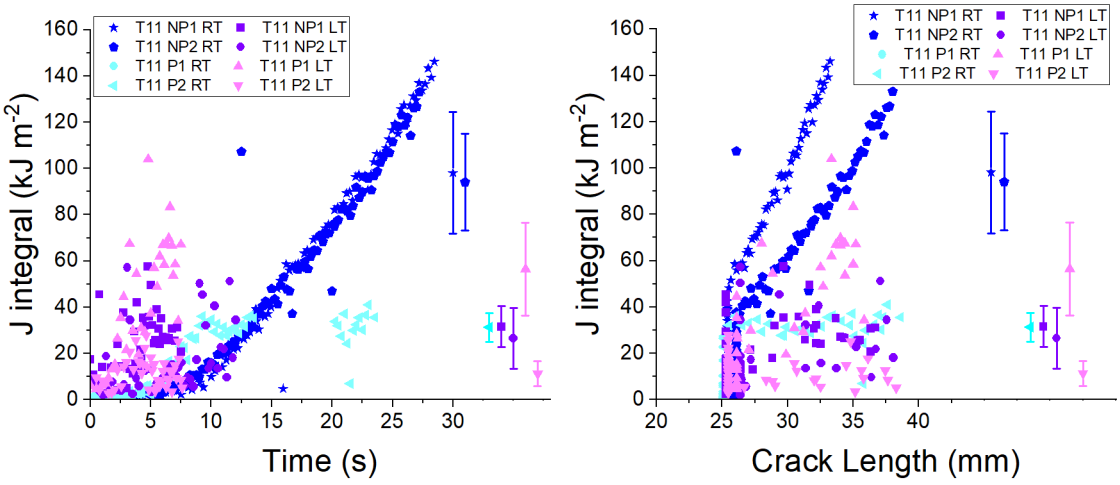


Figure 14 – J Integral vs time or crack length for quasi-static wedge experiment for Task 11. Error bars on the right denote the mean ± one standard deviation. P represents primer surface pre-treatment and NP represents non-primer.

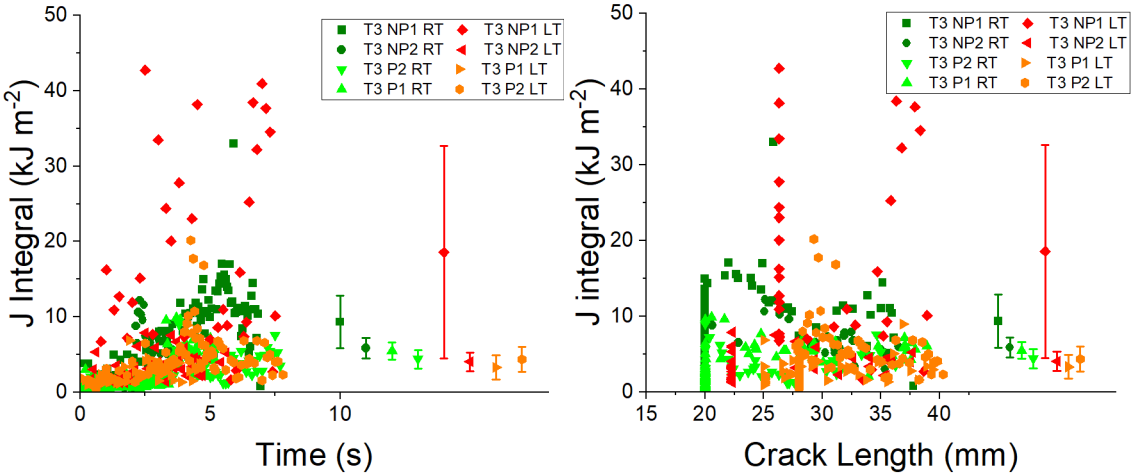


Figure 15 - J Integral vs time or crack length for quasi-static wedge experiment for Task 3. Error bars on the right denote the mean ± one standard deviation. P represents primer surface pre-treatment and NP represents non-primer.

			J integral		K_1		K_{11}	
			Mean	Standard Deviation	Mean	Standard Deviation	Mean	Standard Deviation
Task 3	Room Temperature	Primer 1	5500	1100	20.1	4.4	0.43	4.0
		Primer 2	4400	1200	28.0	5.0	2.8	6.9
		Non-Primer 1	9330	3500	12.3	3.9	6.65	4.5
		Non-Primer 2	5870	1400	17.1	6.4	2.08	5.2
	Low Temperature	Primer 1	3330	1600	7.08	2.73	5.13	2.8
		Primer 2	4350	1700	26.9	6.2	0.341	6.5
		Non-Primer 1	18600	14000	10.6	6.0	9.42	7.9
		Non-Primer 2	4040	1300	9.27	4.99	4.0	3.9
Task 11	Room Temperature	Primer 1						
		Primer 2	31200	6200	33.8	7.1	15.9	3.9
		Non-Primer 1	98100	26000	51.5	4.3	44.0	11
		Non-Primer 2	94000	21000	41.2	3.7	44.1	23
	Low Temperature	Primer 1	56400	20000	57.7	16.5	23.6	13
		Primer 2	11200	5400	23.6	12.1	8.46	5.5
		Non-Primer 1	31600	8800	43.8	11.1	16.5	10
		Non-Primer 2	26500	13000	11.4	4.6	8.97	10

Table 3 - Mean and standard deviation for the critical J-integral, K_1 and K_{11} for quasi-static wedge experiments.

4.8.3 Dynamic Results

The values of the J-integral, K_1 and K_{11} calculated from dynamic experiments are shown in Figure 16 - Figure 18. These results show the variation in J-integral, K_1 and K_{11} against crack length and time for each polymer (Task 3 and Task 11) and in the presence or absence of a primer. The points and error bars on the right of each graph denote the mean, and standard deviation of the results after crack growth has begun: these values have been tabulated in

Error: Reference source not found. All specimens were observed to fail interfacially. Note the time origin here does not coincide with the origin from previous FEA simulations under dynamic loading conditions.

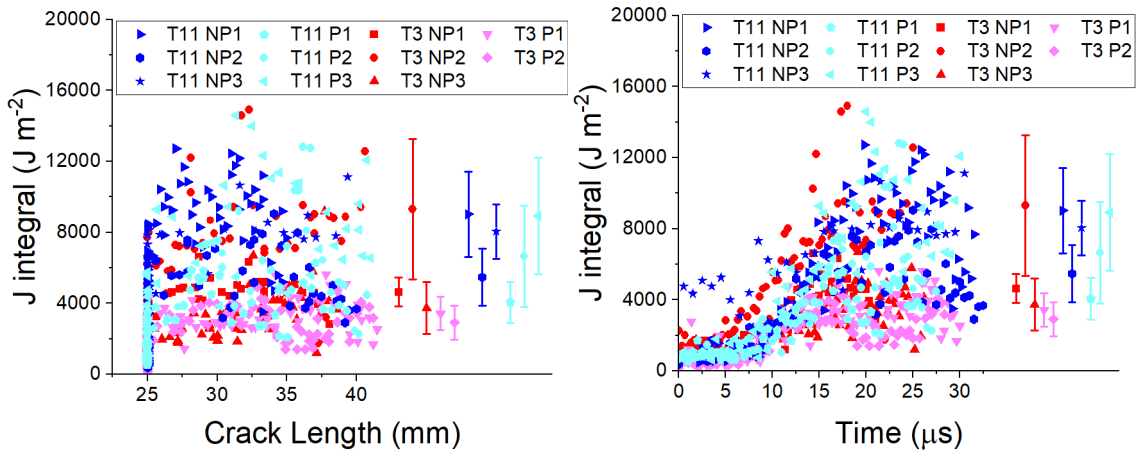


Figure 16 - J integral vs crack length and time for the dynamic wedge experiment. Error bars on the right denote the mean ± one standard deviation. P represents primer surface pre-treatment and NP represents non-primer.

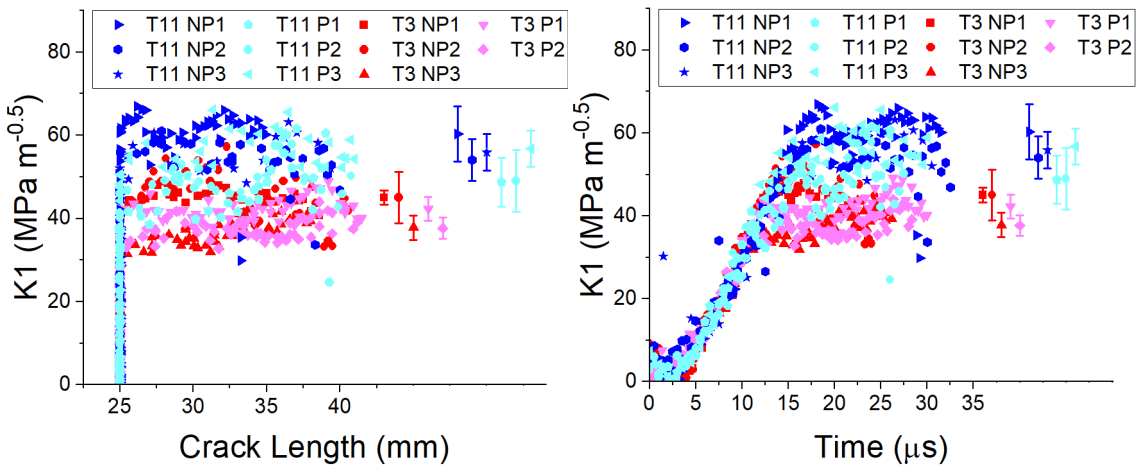


Figure 17 - K1 vs crack length and time for the dynamic wedge experiment. Error bars on the right denote the mean ± one standard deviation. P represents primer surface pre-treatment and NP represents non-primer.

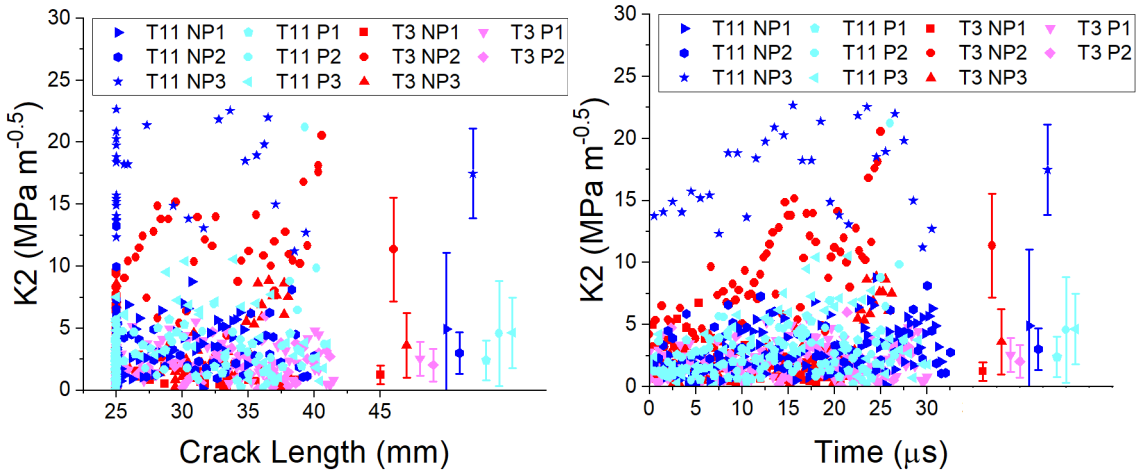


Figure 18 – K_{11} vs crack length and time for the dynamic wedge experiment. Error bars on the right denote the mean ± one standard deviation. P represents primer surface pre-treatment and NP represents non-primer.

		J integral		K_1		K_{11}	
		Mean	Standard Deviation	Mean	Standard Deviation	Mean	Standard Deviation
Task 3	Primer 1	3420	950	42.3	2.9	2.6	1.4
	Primer 2	2910	970	37.7	2.5	2.0	1.3
	Non-Primer 1	4640	810	45.1	1.8	1.25	0.75
	Non-Primer 2	9310	960	45.0	6.1	11.4	4.2
	Non-Primer 3	3740	1500	37.8	3.0	3.6	2.6

Task 11	Primer 1	4050	1200	48.8	5.9	2.4	1.6
	Primer 2	6640	2900	49.0	7.4	4.6	4.2
	Primer 3	8920	3300	56.8	4.3	4.7	2.8
	Non-Primer 1	9030	2400	60.3	6.7	4.9	6.2
	Non-Primer 2	5460	1600	54.1	5.1	3.0	1.7
	Non-Primer 3	8040	1500	55.9	4.4	17.5	3.6

Table 4 - Critical J-integral, K_1 and K_{11} results for the dynamic wedge experiment.

For all results, the J integral and K_1 were seen to increase as the crack was loaded and, once crack growth occurred, these results reached their critical value. Similarly to the quasi-static experiment, an overshoot was sometimes observed before reaching this steady state value. This was thought to be due to the initial crack tip being blunter than that of a propagating crack.

From Figure 16 - Figure 18, there does appear to be a significant difference from the influence of the polymer as the specimens bonded with Task 11 displayed a greater J-integral and K_1 than Task 3. Additionally, it appears unlikely that there is any significant influence from the presence or absence of a primer surface pre-treatment. If any difference was present, it was smaller than the intra-specimen variation.

The J-integral is related to the sum of the squares of K_1 and K_{11} and for the loading here, it can be seen that the greatest contribution came from K_1 and very little from K_{11}. Interestingly, this was different from that observed in the FEA simulations in which K_{11}, whilst the smaller contributor, was of the order of half of K_1. Experimentally, the relative error in K_{11} was far greater than K_1, which was believed to have caused the significant noise observed in the J-integral.

4.9 Discussion

Comparing the dynamic and quasi-static wedge behaviour results, the relative error in the critical J integral and stress intensity factors is significantly smaller in the dynamic compared to the quasi-static case. It is believed this is due to the crack behaviour during failure. Under dynamic loading conditions, stable crack growth was present and therefore defining the crack tip position with a separation threshold criterion produces J-integral and stress intensity factors which are representative of the critical value. It was thought that for the quasi-static experiment, the crack tip jumped in discrete influences and there was greater uncertainty in the crack tip location. This behaviour can be seen in Figure 19 where, after the initial crack tip was loaded, the stress intensity factor reduces until the crack tip is reloaded again and propagates.

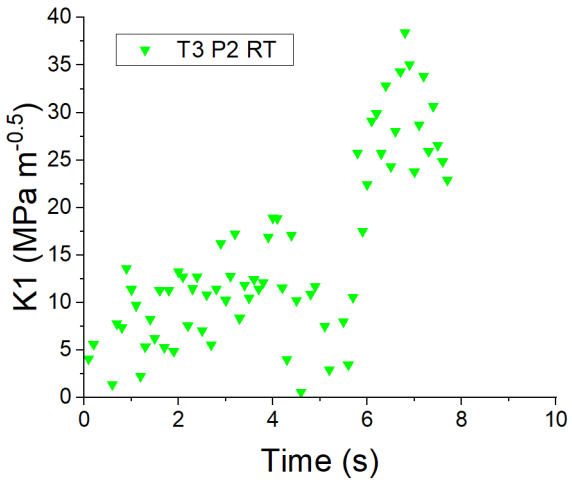


Figure 19 - K1 stress intensity factor for Task 3 non-primer at room temperature.

For the J-integral for Task 3, Table 5, the dynamic version of this experiment produced a smaller J-integral than its quasi-static counterpart at the same temperature. Interestingly, this was very similar to that calculated using sub-ambient environmental conditions under quasi-static loading, which aimed to simulate the dynamic behaviour. However, for K_1, Table

6, the stress intensity factor is significantly greater in the dynamic experiment compared to the quasi-static at ambient and sub-ambient temperatures. This raises an interesting comparison where a high J-integral does not correlate with a high K_1 despite a similar K_{11} and there being a relation between these parameters. This phenomenon could have arisen when the mean of these results is determined because the mean J-integral, K_1 and K_{11} do not follow the same distribution as the individual data points. Therefore, if we assume K_1 and K_{11} possess independent distributions, we can determine the expected parameters to follow the relationship,

$$E(J) = E(K_1)^2 + var(K_1) + E(K_{11})^2 + var(K_{11}). \quad (3)$$

Therefore, the expected value of the results will be influenced by the variance of the original distribution. For the results discussed here, the K_{11} parameter is small with a comparatively large variance. Therefore, this significant variance will influence the results of the K_1. So, for the comparison between the quasi-static and dynamic results for Task 3, it was thought that the quasi-static results could have been artificially low because they were influenced by the variance found in these data.

For Task 11, the J-integral and K_{11} values were likely inaccurate for the quasi-static experiments due to the issues associated with a relatively ductile material and a non-separated J-integral calculation. Therefore, a limited comparison can be made between the quasi-static and dynamic rates of loading for these two parameters. However, comparing the polymers, the dynamic properties of Task 11, log(t)~-5, and the quasi-static properties of Task 3, log(t)~1, are similar, Figure 3. The J-integral for quasi-static Task 3 and dynamic Task 11, produce similar values, particularly for the non-primer specimens. For K_1, the dynamic experiment produced the greatest value compared to the room temperature, which agrees

with expectation because the polymer was significantly stiffer at these loading rates and, provided it remained bonded, was able to withstand greater stress before failure. At quasi-static sub-ambient temperatures, mimicking the dynamic behaviour, K_1 increased compared to ambient temperature and was closer to the dynamic experiment.

Table 5 - Average J integral for all loading conditions.

J Integral	T3 Primer	T3 Non-Primer	T11 Primer	T11 Non-Primer
Quasi-static	4950	7600	31,200	96,000
Dynamic	3170	4190	6540	7510
Low Temperature	3840	4040	33,800	29,000

Table 6 - Average K_1 for all loading conditions.

K_1	T3 Primer	T3 Non Primer	T11 Primer	T11 Non-Primer
Quasi-static	24.1	14.7	33.8	46.4
Dynamic	40	42.6	51.5	56.8
Low Temperature	17.0	9.94	40.7	27.6

Table 7 - Average K_{11} for all loading conditions.

K_{11}	T3 Primer	T3 Non Primer	T11 Primer	T11 Non-Primer
Quasi-static	1.62	4.37	-15.9	-44.1
Dynamic	2.3	5.42	3.9	8.47
Low Temperature	2.74	6.71	16	12.7

4.10 Conclusions

The aim of this study was to characterise a polyurethane-alumina interface at a variety of loading rates and temperatures and to investigate the use of time-temperature superposition to determine the dynamic properties of the interface. Wedge experiments were conducted on bonded specimens and, using DIC, the displacement field around the crack tip was extracted and inputted into an Abaqus simulation which was then able to calculate the J-integral as well as K_1 and K_{11}. Two polyurethanes were investigated: 'Task 3'

which was operating below its glass transition temperature and ‘Task 11’ which was at the glass transition.

For Task 3, the stiffer polymer, it was found that determining the J-integral from dynamic experiments produced similar results to that found using quasi-static experiments at low temperatures, which supported using time-temperature superposition to investigate the dynamic properties of the interface. However, the K_1 values were different between these loading conditions, although it was believed this was as a consequence of far greater variation in the quasi-static results.

For Task 11, it was difficult to make a significant comparison between the dynamic and sub-ambient loading due to the increased ductility of the polymer under quasi-static conditions, leading to artificially high K_{11} and J-integral values. Although interestingly, the polymer properties of Task 11 under dynamic loading conditions, log(t)~-5, are similar to that of Task 3 under quasi-static loading, log(t)~1, and these generated very similar J-integral values.

From these observations, it was believed that time-temperature superposition could be used to give an estimate of the dynamic properties of the interface. However, care should be taken because it was noted that the significant difference in thermal contraction between the alumina and polymer would cause residual thermal strains over the interface, likely weakening the interface more than expected. Further, for more complex interfaces, such as those pre-treated with a primer, at sub-ambient conditions caused excessive weakening of the interface than otherwise predicted.

4.11 Acknowledgements

The authors would like to thank Dstl for their financial and intellectual support during this work under contract number DSTLX1000128371. Additionally, thanks must be extended to Prof. James Marrow, Dr. Igor Dyson and Nick Hawkins for their experimental and analytical assistance as well as Neil Warland and Andy Bateman for specimen manufacture.

For the purpose of Open Access, the author has applied a CC BY public copyright license to any Author Accepted Manuscript (AAM) version arising from this submission.

4.12 References

[1] R. P. Reed, “The Economic effects of fracture in the United States. Washington, D.C.,” *U.S. Dept. of Commerce, National Bureau of Standards*, 1983.

[2] S. L. Raykhere, P. Kumar, R. K. Singh, and V. Parameswaran, “Dynamic shear strength of adhesive joints made of metallic and composite adherents,” *Mater Des*, vol. 31, no. 4, pp. 2102–2109, Apr. 2010, doi: 10.1016/j.matdes.2009.10.043.

[3] P. Kumar, S. Tiwari, and R. K. Singh, “Characterization of toughened bonded interface against fracture and impact loads,” *Int J Adhes Adhes*, vol. 25, no. 6, pp. 527–533, Dec. 2005, doi: 10.1016/j.ijadhadh.2005.01.007.

[4] M. Lißner, E. Alabort, B. Erice, H. Cui, and N. Petrinic, “A rate dependent experimental and numerical analysis of adhesive joints under different loading directions,” *European Physical Journal: Special Topics*, vol. 227, no. 1–2, pp. 85–97, Sep. 2018, doi: 10.1140/epjst/e2018-00070-x.

[5] M. Lißner *et al.*, “Multi-material adhesively bonded structures: Characterisation and modelling of their rate-dependent performance,” *Compos B Eng*, vol. 195, p. 108077, 2020.

[6] G. R. Irwin, “Onset of fast crack propagation in high strength steel and aluminum alloys,” Naval Research Lab Washington DC, 1956.

[7] G. R. Irwin, “Analysis of stresses and strains near the end of a crack traversing a plate,” 1957.

[8] H. M. Westergaard, “Bearing pressures and cracks: Bearing pressures through a slightly waved surface or through a nearly flat part of a cylinder, and related problems of cracks,” 1939.

[9] G. P. Cherepanov, “The propagation of cracks in a continuous medium,” *Journal of Applied Mathematics and Mechanics*, vol. 31, no. 3, pp. 503–512, 1967.

[10] J. R. Rice, “A path independent integral and the approximate analysis of strain concentration by notches and cracks,” 1968.

[11] C. E. Inglis, “Stresses in a plate due to the presence of cracks and sharp corners,” *Trans Inst Naval Archit*, vol. 55, pp. 219–241, 1913.

[12] A. A. Griffith, “VI. The phenomena of rupture and flow in solids,” *Philosophical transactions of the royal society of london. Series A, containing papers of a mathematical or physical character*, vol. 221, no. 582–593, pp. 163–198, 1921.

[13] F. Z. Li, C. F. Shih, and A. Needleman, “A comparison of methods for calculating energy release rates,” *Eng Fract Mech*, vol. 21, no. 2, pp. 405–421, 1985.

[14] A. D903-98, “Standard test method for peel or stripping strength of adhesive bonds,” *ASTM International*, 2017.

[15] O. I. de Normalización, *Adhesives: Determination of the Mode 1 Adhesive Fracture Energy of Structural Adhesive Joints Using Double Cantilever Beam and Tapered Double Cantilever Beam Specimens*. ISO, 2009.

[16] A. Standard, “D7905/D7905M−14,” *Standard Test Method for Determination of the Mode II Interlaminar Fracture Toughness of Unidirectional Fiber-Reinforced Polymer Matrix Composites*, p. 20, 2014.

[17] F. Kadioglu and R. D. Adams, “Flexible adhesives for automotive application under impact loading,” *Int J Adhes Adhes*, vol. 56, pp. 73–78, 2015.

[18] J. P. Casas-Rodriguez, I. A. Ashcroft, and V. v Silberschmidt, “Damage evolution in adhesive joints subjected to impact fatigue,” *J Sound Vib*, vol. 308, no. 3–5, pp. 467–478, 2007.

[19] A. Beevers and M. D. Ellis, “Impact behaviour of bonded mild steel lap joints,” *Int J Adhes Adhes*, vol. 4, no. 1, pp. 13–16, 1984.

[20] U. K. Vaidya, A. R. S. Gautam, M. Hosur, and P. Dutta, “Experimental–numerical studies of transverse impact response of adhesively bonded lap joints in composite structures,” *Int J Adhes Adhes*, vol. 26, no. 3, pp. 184–198, 2006.

[21] Z. A. Aga and E. Woldesenbet, “Bond thickness effect on impact response and damage of adhesively-bonded graphite/epoxy composites,” *J Adhes Sci Technol*, vol. 21, no. 1, pp. 21–34, 2007.

[22] C. Galliot, J. Rousseau, and G. Verchery, “Drop weight tensile impact testing of adhesively bonded carbon/epoxy laminate joints,” *Int J Adhes Adhes*, vol. 35, pp. 68–75, 2012.

[23] T. Yokoyama and H. Shimizu, “Evaluation of impact shear strength of adhesive joints with the split Hopkinson bar,” *JSME International Journal Series A Solid Mechanics and Material Engineering*, vol. 41, no. 4, pp. 503–509, 1998.

[24] T. Yokoyama, “Experimental determination of impact tensile properties of adhesive butt joints with the split Hopkinson bar,” *J Strain Anal Eng Des*, vol. 38, no. 3, pp. 233–245, 2003.

[25] J. Neumayer, P. Kuhn, H. Koerber, and R. Hinterhölzl, “Experimental determination of the tensile and shear behaviour of adhesives under impact loading,” *J Adhes*, vol. 92, no. 7–9, pp. 503–516, 2016.

[26] H. Zhao *et al.*, “Dynamic characteristics of adhesive bonded high strength steel joints,” *Science and Technology of Welding and Joining*, vol. 15, no. 6, pp. 486–490, 2010.

[27] S. Sassi, M. Tarfaoui, and H. ben Yahia, “An investigation of in-plane dynamic behavior of adhesively-bonded composite joints under dynamic compression at high strain rate,” *Compos Struct*, vol. 191, pp. 168–179, 2018.

[28] H. Paul, N. Ledford, M. Sauer, M. May, and M. Okamura, “Assessment of test methods for thick and thin layer adhesive joints under high rates of loading,” *Int J Adhes Adhes*, vol. 83, pp. 123–129, 2018.

[29] P. Rüthnick, N. Ledford, M. Imbert, and M. May, “Mechanical behavior of multi-material single-lap joints under high rates of loading using a Split Hopkinson Tension Bar,” *Metals (Basel)*, vol. 12, no. 7, p. 1082, 2022.

[30] S. Sassi, M. Tarfaoui, and H. ben Yahia, “In-situ heat dissipation monitoring in adhesively bonded composite joints under dynamic compression loading using SHPB,” *Compos B Eng*, vol. 154, pp. 64–76, 2018.

[31] T. Yokoyama and K. Nakai, “Determination of the impact tensile strength of structural adhesive butt joints with a modified split Hopkinson pressure bar,” *Int J Adhes Adhes*, vol. 56, pp. 13–23, 2015.

[32] M. Lißner, E. Alabort, B. Erice, H. Cui, B. R. K. Blackman, and N. Petrinic, “On the dynamic response of adhesively bonded structures,” *Int J Impact Eng*, vol. 138, p. 103479, 2020.

[33] S. N. Atluri, “Path-Independent Integrals in Finite Elasticity and Inelasticity, with Body Forces, Inertia, and Arbitrary Crack-Face Conditions.”

[34] T. Nishiokat and S. N. Atlurii, “Path-Independent Integrals, Energy Release Rates, and General Solutions of Near-Tip Fields in Mixed-Mode Dynamic Fracture Mechanics.”

[35] T. Nishioka, S. Shen, and J. Yu, “Dynamic J integral, separated dynamic J integral and component separation method for dynamic interfacial cracks in piezoelectric bimaterials,” 2003.

[36] M. L. Williams, R. F. Landel, and J. D. Ferry, “The temperature dependence of relaxation mechanisms in amorphous polymers and other glass-forming liquids,” *J Am Chem Soc*, vol. 77, no. 14, pp. 3701–3707, 1955.

[37] A. S. Wineman and K. R. Rajagopal, *Mechanical response of polymers*. Cambridge: Cambridge University Press, 2000.

[38] “Bentley Advanced Materials,” *https://www.benam.co.uk/products/plastic/task*.

[39] “Morgan Ceramics,” *https://www.morgantechnicalceramics.com/en-gb/*.

[40] “Sika,” *https://gbr.sika.com/en/industry/marine/leisure-boats-andyachts/interior-sealing/sika-primer-206-gp.html*.

[41] A. Harris, B. Vaughan, J. Yeomans, P. Smith, and S. Burnage, “Ballistic testing of surface-treated alumina and silicon carbide with improved adhesive bond strength,” *Int J Appl Ceram Technol*, vol. 14, no. 3, pp. 323–330, May 2017, doi: 10.1111/ijac.12668.

[42] A. J. Harris, B. Vaughan, J. A. Yeomans, P. A. Smith, and S. T. Burnage, “Surface preparation of silicon carbide for improved adhesive bond strength in armour applications,” *J Eur Ceram Soc*, vol. 33, no. 15–16, pp. 2925–2934, Dec. 2013, doi: 10.1016/j.jeurceramsoc.2013.05.026.

[43] M. L. Williams, R. F. Landel, and J. D. Ferry, “Temperature Dependence of Relaxation Mechanisms The Temperature Dependence of Relaxation Mechanisms in Amorphous Polymers and Other Glass-forming Liquids,” 1955. [Online]. Available: https://pubs.acs.org/sharingguidelines

[44] S. M. Barhli, M. Mostafavi, A. F. Cinar, D. Hollis, and T. J. Marrow, “J-Integral Calculation by Finite Element Processing of Measured Full-Field Surface Displacements,” *Exp Mech*, vol. 57, no. 6, pp. 997–1009, Jul. 2017, doi: 10.1007/s11340-017-0275-1.

5 Quasi-1D Model Armour under Impact and Quasi-static Loading

This chapter comprises an introduction, then a paper submitted for publication to the International Journal of Impact Engineering.

5.1 Chapter Introduction

This chapter draws the previous data and collective understanding of the constitutive materials and interfaces together in the form of model armour specimens. Polymer backed ceramic strips are loaded quasi-statically, at ambient and sub-ambient conditions, and under impact; the capabilities of the specimens to remove energy from the projectile were investigated. It was discovered that, under quasi-static loading, the backing and interface had significant influence over the mode of failure and could correspond to an increase in approximately 3x that of the reference. Under impact, whilst it was found a significant proportion of the incidence kinetic energy was transferred to the kinetic energy of the fragment, the backing and interface were observed to influence the fracture pathway. This could be influential for more representative materials, geometries and armour backings.

5.2 Abstract

Ballistic impact is a highly complex environment, the understanding of which is compounded by the advanced materials used for ceramic-polymer composite armours. In this study, the influence of surface preparation and polymer backing properties on the energy absorptive capabilities and ballistic performance of simplified model armours was approached via a methodical investigation using simplified materials and geometries. Quasi-1D (beam) specimens consisting of polyurethane-backed alumina were loaded under three-point bend quasi-statically and at impact speeds. The specimen geometries allowed for the fracture pathways to be observed. To produce the specimens, two polyurethanes with different glass transition temperatures were cured onto alumina strips, eliminating the requirement for a dedicated adhesive and thus simplifying the interfacial dynamics. Further modifications were made by applying a primer surface treatment, by using unbonded polyurethane and adhered polyurethane, and by replacing the polyurethane with glass-reinforced polycarbonate. The beam specimens were loaded quasi-statically at 0.05 mm s^{-1} at ambient and sub-ambient temperatures, and at 50-300 m s^{-1} at ambient temperatures. The quasi-static specimens were found to fail by one of two failure modes with approximately a 3x energy absorption difference; the failure was highly dependent upon the interface and polymer characteristics. Under impact, a significant proportion of the energy absorption was provided by the kinetic energy of the fragments. Although, the polymer backing and interfacial properties were found to influence fracture paths during loading. FEA simulations were used to model the behaviours using characterisation data from a previous study; these were found to predict the experimental response well.

5.3 Introduction

Composite structures are often used for defence against high energy projectiles. Personnel armours typically consist of a hard ceramic strike face and a more ductile polymer backing [1]–[3]. When the composite armours are impacted, stress waves propagate through the ceramic material. On reaching the interface between the strike and backing plates, due to the impedance mismatch, reflected and transmitted waves are generated [4]. These are highly dependent upon the interface between the ceramic and polymer and significantly influences the overall performance of the armour [5]–[11]; however, these processes are not well understood and conflicting results are not uncommon in the literature. Furthermore, interfaces within the two base materials can heavily affect the overall armour response. For example, Yadav *et al.* found that for monolithic ceramic armours, separating the ceramic into 3 layers showed an increase in performance, whilst an increase to 6 layers reduced it [12]; Akella reported that increasing the number of layers can weaken performance against a single impact, but improves the multi-hit capacity of the armour [13]. It has been suggested that in fact that there are 30 – 150 layers within a typical composite armour, including internal surfaces, air gaps and inter-ply interfaces within the polymer, which is often manufactured from bonded fibres of ultra-high molecular weight polyethylene (UHMWPE) [14]; however, given the high speed of stress waves (c. 10 mm/μs in ceramic, or 1-2 mm/μs across the polymer) the equilibrium time for stress waves within these layers will be very short.

The literature, therefore, emphasises the inherent complexity present in ballistics research. Hence, a study involving simplified materials, bonding and geometry can give insights into the properties that would otherwise be difficult to obtain. In the study reported in this

paper, simple homogenous materials were used and the requirement for a layer of adhesive at the interface was removed entirely to simplify the ceramic-polymer interaction. Quasi-1D (beam) specimens consisting of alumina backed with a polyurethane that was directly cured onto the rear alumina face were loaded under quasi-static and ballistic loading. Due to the approximate plane stress nature of this geometry, the fracture pattern of the material could be observed on the material surface. Further, FEA simulations were conducted using previously determined interfacial properties to predict the quasi-static and ballistic behaviour.

Within this study, two polyurethanes with different glass transition temperatures were investigated: one above (55 °C), and one just below (15 °C), room temperature. This allows an investigation into stiffness and strain rate sensitivity: there is a rapid change in stiffness as the polymer passes through its glass transition. This change in stiffness arises from the ability, or lack thereof, of the polymer chains to move in response to an applied load; see, e.g., [15] for a detailed description. The position of the glass transition is influential because polymers loaded under impact can undergo a deformation rate-induced glass transition in which the polymer behaviour moves from rubbery to glassy, which significantly changes the energy dissipation characteristics [16]–[18]. There is also an opportunity to compare the rate and temperature dependence of the material behaviour to obtain a fuller picture of the nature of the armour response: separating structural from material changes. The use of chemically similar polymers helps make this comparison by reducing changes resulting from chemical interactions at the interface, which have been shown to strongly influence ballistic performance [10], [11]. Further comparisons were drawn between these two polyurethanes using the presence or absence of a primer surface pre-treatment before adhesion.

Additionally, the response of the model armours was compared against glass filled polycarbonate, which is significantly stiffer than polyurethane.

5.4 Materials and Specimen Preparation

5.4.1 Materials

Polymer backed ceramics were manufactured using Sintox^{TM} FF Alumina plates with a typical Al_2O_3 content of 95 %, sourced from Morgan Ceramics [19]. For the polymer, two polyurethanes were obtained from Bentley Advanced materials [20]. These are commercially known as 'Task 3' and 'Task 11', where Task 3 has a glass transition around 55 °C, and Task 11 around 15 °C (see Appendix). A detailed characterisation of the polymer is given in Chapter 3, and relevant properties are described in Section 5.6. No adhesive was used to bond the polymers; the baseline materials were allowed to cure in direct contact with the ceramic to form a bond, thus simplifying the interfacial dynamics. Further specimens were produced using a primer, Sika 206 G+P, to modify the interface properties.

Additional investigations were conducted using polymer backings consisting of 30 % glass-fibre reinforced polycarbonate sourced from Ensinger [21], with a reported glass transition temperature of 147 °C. Dynamic mechanical analysis (DMA) experiments were performed (see Appendix), which show that this polymer has a modulus of around 3 GPa at room temperature and is relatively rate insensitive, with no significant transitions over the rates and temperatures of interest. To adhere this polymer to the alumina beams, Dowsil 6-1104 was used.

5.4.2 Specimen Preparation

The baseline specimens consisted of thin alumina strips with the polyurethanes cured directly in contact with the rear face of the ceramic, Figure 1. To produce these specimens,

alumina strips of dimension 100 × 8 × 5 mm were cut using a diamond saw from a 100 mm square plate. Before bonding the polymer, the surface was thoroughly cleaned using isopropyl alcohol, then water, and left to air dry. To create interfacial variation, for half of the specimens a thin layer of primer was applied to the ceramic surface using a lint free cosmetic sponge.

The polyurethanes used in this project were acquired as 2-part polymers and were degassed before and after mixing and once more when poured onto the ceramic strips, which were held in a mould. The polyurethanes were allowed to cure at ambient temperature for 24 hours before a final 4-hour heat treatment in a furnace at 65 °C to ensure the polymers had fully cured. After curing, the top of the polymer was cut flat using a CNC mill, creating a level polymer backing with approximate dimensions of 60 x 10 x 5 mm. Digital image correlation (DIC) was used to track the displacement field on the specimen surfaces; to enable this, a black and white speckle pattern was painted on the specimens using an airbrush. This speckle pattern was imaged during loading, and commercial DIC software, MatchID [22], was used to calculate the resulting displacements.

Further specimens were produced using glass-fibre reinforced polycarbonate bonded to the ceramic using Dowsil 6-1104. For these specimens, once the adhesive was applied, the specimens were held in a press for 72 hours until fully cured.

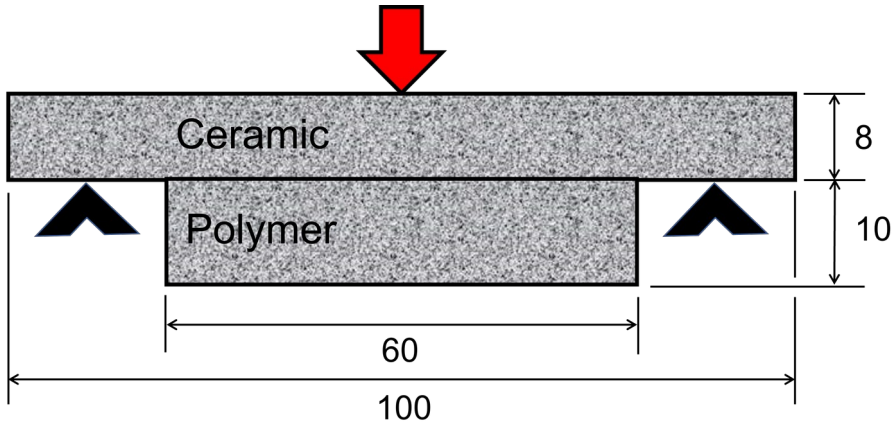


Figure 1 - Beam bend specimen schematic. All dimensions are in mm and specimens were 5 mm thick. The red arrow denotes the applied force.

5.5 Experimental Overview

5.5.1 Quasi-static Beam Bend

Beam bend specimens were tested in 3-point bend at 0.05 mm/s at ambient and sub-ambient temperatures as presented in Table 1. The sub-ambient temperatures were selected using time-temperature superposition to achieve two separate conditions: -49 °C for Task 3 and Task 11 to simulate impact loading by replicating the polymer stiffness expected on timescales of approximately 1 µs; -36 °C for Task 11 to mimic the stiffness of Task 3 at room temperature. Specimens were imaged with a Point Grey GS3-U3-41C6M-C camera allowing DIC analysis to accurately determine the central point deflection as well as observation of the resulting fracture patterns. The DIC parameters and camera settings can be found in the Appendix.

Specimen Type	Backing	Bonding Condition	Test Temperature (°C)
1	None	-	
2	Task 3	Direct Curing – Primer and non-primer pre-treatment	20 and -49
3	Task 11	Direct Curing – Primer and non-primer pre-treatment	20, -36 and -49

Table 1 - Quasi-static specimen type and environmental testing conditions.

5.5.2 Impact Beam Bend

A single stage compressed nitrogen gas gun was used to investigate the performance of the specimens under impact, Figure 2. Specimen variation was introduced as presented in Table 2. As well as the directly cured PU backings, specimen types 2 and 3, additional experiments were conducted investigating a very low strength interface in which the backing was weakly bonded to the polymer using a small amount of commercially available paper adhesive, Pritt-Stick®, on specimen types 4 and 5. This allowed separation of the effect of interfacial strength from that of the backing's inertia. Further experiments were conducted using the silicone based adhesive Dowsil 6-1104 to delay interfacial fracture for Task 3 and the significantly stiffer glass filled polycarbonate, specimen types 6 and 7.

The specimens were set up as shown in Figure 2 and were impacted using an EN16 steel projectile of 8 mm diameter and 30 mm length. The projectile had a cylindrically rounded tip of 4 mm radius, Figure 3. A Photron Fastcam SA-Z high speed camera was used to record images of the impact at a rate of 100,000 fps; these images were used to obtain the specimen deformation and the speed of the projectile. A light gate was used to trigger the camera and determine the projectile speed before impact.

Specimen Type	Backing	Bonding Condition
1	None	-
2	Task 3	Direct Curing – Primer and non-primer pre-treatment
3	Task 11	Direct Curing – Primer and non-primer pre-treatment
4	Task 3	Bonded – Low Strength – Pritt-Stick®
5	Task 11	Bonded – Low Strength – Pritt-Stick®
6	Task 3	Bonded – Dowsil 6-1104
7	Glass filled PC	Bonded – Dowsil 6-1104

Table 2- Experimental specimen variation for impact beam bend experiment.

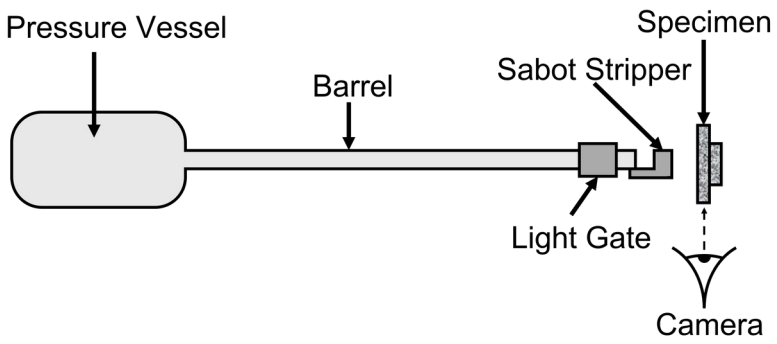


Figure 2 – Schematic of the gas gun used to investigate the impact behaviour of specimens under beam bend.

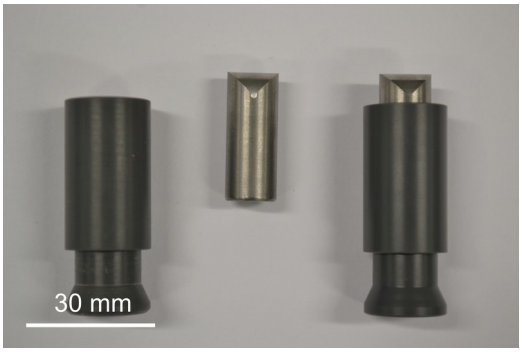


Figure 3 – Projectile and sabot used for impact beam bend.

5.6 Polymer Properties

5.6.1 Stiffness

Extensive mechanical characterisation of the polymers was performed, Chapter 3. Of particular relevance here is the DMA characterisation of the small strain viscoelastic response. DMA specimens were loaded using a stress-relaxation testing procedure in a three-point bend configuration. Specimens were loaded slowly to 0.1 % strain and held for 10 minutes, during which time the force was measured. The specimens were then allowed to recover, unloaded, for a further 20 minutes. This was repeated from -85 to +55 °C in 5 °C

intervals. The principal of time-temperature superposition [23] was used to generate the 20 °C mastercurves shown in Figure 4.

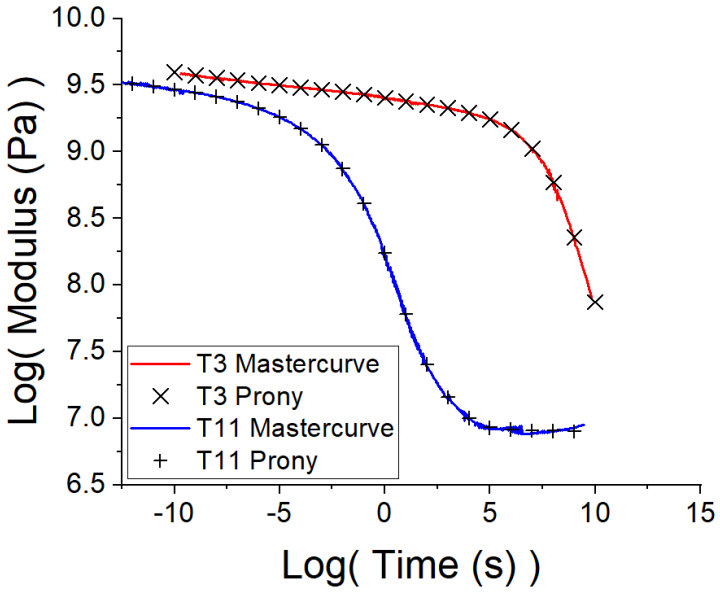


Figure 4 - Three-point bend DMA stiffness mastercurve for Task 3 and Task 11.

These results show that, in the range of interest for both polymers, the only transition is the glass transition, Figure 4. The glass transition temperature was also confirmed using DSC, in which both materials were heated from -90 ° to 120 °C at a heating rate of 3 °C min^{-1}; the glass transition temperature was found to be at approximately 50 °C for Task 3 and 15 °C for Task 11. The full DSC results are presented in the Appendix.

From the DMA results, Figure 4, it was observed that Task 3 was always stiffer than Task 11. In particular, under quasi-static loading, for which log(t)≈1, Task 3 was approximately two orders of magnitude stiffer than Task 11 and substantially less strain rate sensitive. Under impact loading conditions, log(t)≈-6, the polymer stiffnesses converge and have similar sensitivity to strain rate. Thus, the use of two polymers allows an investigation into the effects of the glass transition on the response. Additionally, it was noted that the stiffness of the polymers converges at short timescales, which was expected due to their chemical

similarity. It is also expected that the stiffnesses would converge at very long timescales; however, data were not obtained as this is not of direct interest to the current research.

5.6.2 Modelling

A Prony series was used to model the polymers. A Prony series consists of a number of spring-dashpot pairs in parallel, each with different stiffness and relaxation time and each known as a branch, Figure 5.

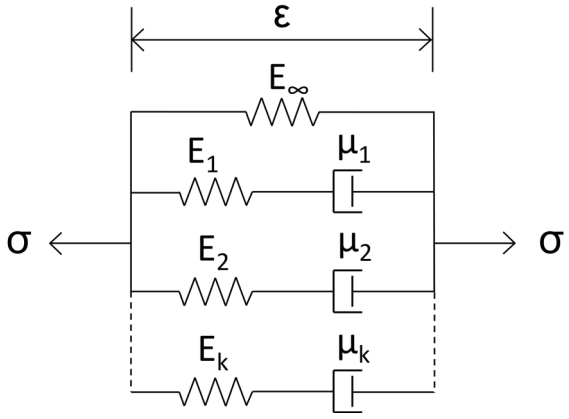


Figure 5 - Schematic representation of a Prony series.

To determine the constitutive behaviour for this Prony series representation, a force balance along each branch should be taken and then a Laplace transform with the particular initial conditions applied, [24], [25]. For a step strain input, ε_0, the stress relaxation behaviour can be represented by

$$\frac{\sigma(t)}{\varepsilon_0} = G(t) = G_\infty + \sum_{n=1}^{k} G_n e^{\frac{-t}{\tau_n}} \qquad (1)$$

where, $\tau_n = \frac{\mu_n}{E_n}$ (2)

Here, G_n is a constant found from model parameters [24] and E_n and μ_n are the spring stiffness and dashpot viscosities, respectively, for each branch. The complexity increases for more general loading cases because the relaxation of the model will begin as soon as the loading starts. Therefore, for a general case

$$\sigma(t) = \varepsilon ¿ \quad (3)$$

To define the Prony series representation of these polymers, equation (1) was fitted to the DMA mastercurves using the curve fitting toolbox in Matlab®. The number of branches was defined such that the characteristic time constant of each branch, defined by equation (2), was spaced by one decade. For Task 3 and Task 11, a 22-branch and 24-branch Prony series were fitted respectively. The predicted moduli at each loading decade are overlain on the mastercurve in Figure 4, and the Prony series parameters used are presented in the Appendix.

5.7 Results and Discussion

5.7.1 Quasi-static Beam Bend

5.7.1.1 Unbacked Ceramic

The variation in strength of the unbacked ceramic was initially measured by loading six specimens quasi-statically in three-point bend to produce the force displacement relationships in Figure 6. To account for variations in specimen size, the force was then normalised with respect to the second moment of area and modulus of the ceramic; the results are shown to collapse on the same loading line, Figure 7.

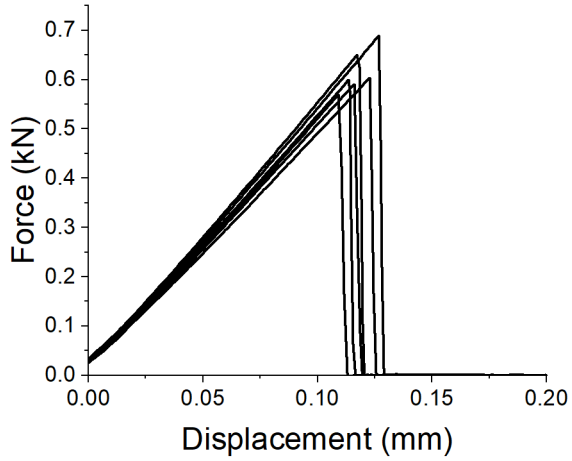


Figure 6 - Force vs. displacement for unbacked ceramic.

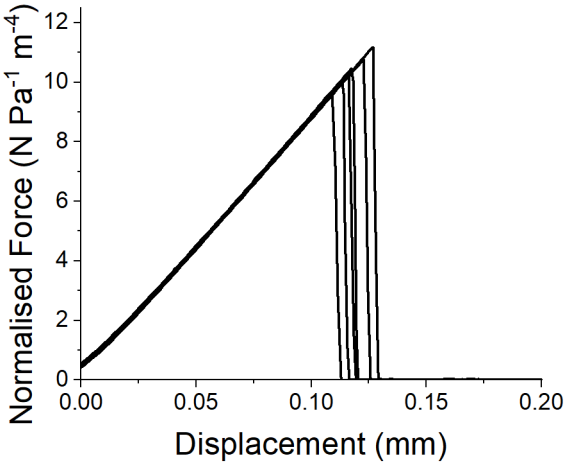


Figure 7 - Force vs. displacement for unbacked ceramic normalised by Young's Modulus and second moment of area of each specimen to account for geometric effects.

The breaking stress in the ceramic was calculated for each specimen using the simple beam bend relation

$$\sigma = \frac{M\, y_{max}}{I} \qquad (4)$$

Where M was the bending moment at the centre of the beam, y_{max} is the maximum distance from the neutral axis (i.e. the depth of the beam) and I is the second moment of area. A Weibull distribution was fitted to these results [26], by calculating the probability of failure, P_f, for each specimen and plotting against strength, Figure 8. The Weibull modulus was determined to be 17.1, which is high for a ceramic and demonstrates this material has a relatively reliable breaking stress.

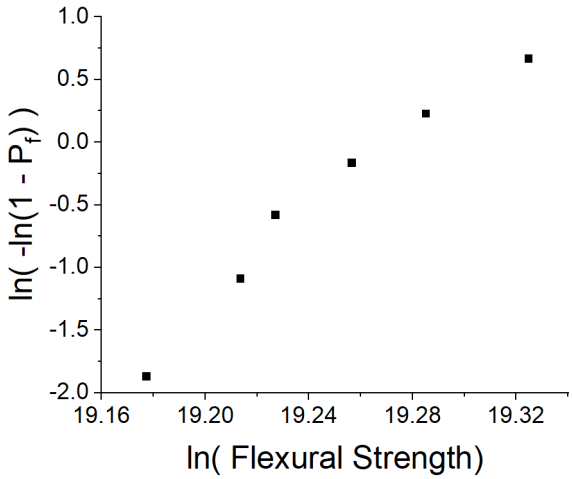
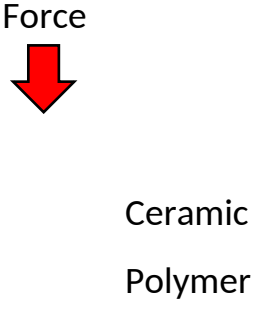


Figure 8 - Weibull plot for unbacked ceramic loaded under three-point bend.

5.7.1.2 Backed Ceramic – Failure modes

The Task 3 and Task 11 backings were moulded to the ceramic specimens as previously described with and without a primer surface pre-treatment. It was observed that all specimens failed via two distinct modes schematically displayed in Figure 9, and these gave the characteristic force-displacement curves presented in Figure 10.



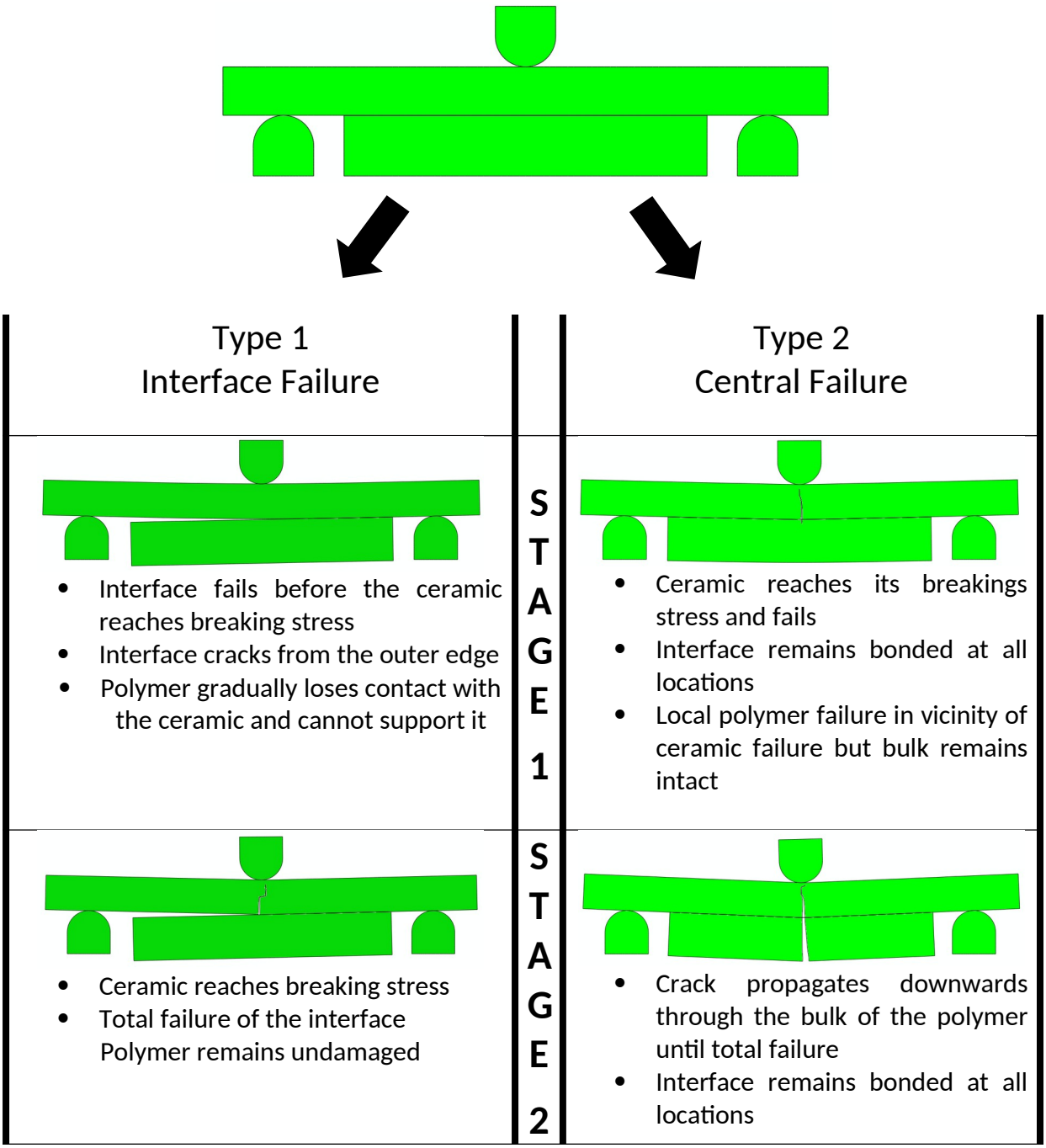


Figure 9 - Schematics of Type 1 and Type 2 failure.

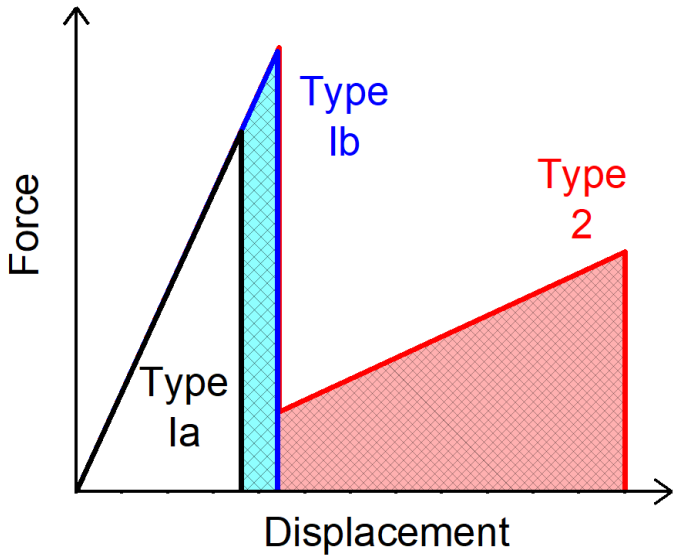


Figure 10 - Typical Force-displacement curves for Type 1 (Interfacial failure) and Type 2 (central failure). The shaded areas represent the additional load carrying capacity from each failure type.

Type 1 - Interface Failure

The first failure mode was termed interface failure. A characteristic of this failure was that the interface was observed to fail before either of the constitutive materials. A crack was observed to propagate from the outer edge of the ceramic-polymer bond and, thus, the ceramic gradually lost adhesion from and support of the polymer backing. Following this, once the ceramic reached its failure stress, the ceramic crack and the interfacial crack combined and the whole structure lost load carry capacity. This produced the typical force-displacement curve, Figure 10, in which there was a single peak at the moment of ceramic failure.

This failure could be split into two further sub-divisions depending on how far the initial interfacial crack propagated along the specimen at the moment of ceramic failure. If the crack had propagated to the centre of the specimen, the ceramic behaved as if it were

unbacked. This failure was denoted failure type *1a* and these specimens were effectively indistinguishable from the unbacked ceramics.

In other cases, denoted type *1b*, the ceramic failed before the interfacial crack reached the centre, such that it was still partially supported by the polymer. This increased the breaking stress in the ceramic, and also moved the failure away from the centre of the ceramic to the location of the interface crack tip. Because this location has a lower bending moment for any given force, the force required to fail the ceramic is increased, allowing the structure to survive to greater loads and displacements, see blue line in Figure 10. After the ultimate failure of the ceramic, the ceramic crack and debonded interface still combined, resulting in the total failure of the specimen. This phenomenon, the polymer backing allowing the ceramic to withstand greater breaking stresses, has been previously observed under simulated ballistic impact [27]. When this failure was observed to occur, the energy absorption was observed to increase by approximately 1.5 – 1.8 times that of the unbacked ceramic.

Type 2 – Central Failure

The key characteristic for a type 2 failure was that no interfacial failure was observed to occur or, if any interfacial failure was present, it was limited to the farthest edges of the ceramic-polymer interface and did not affect the subsequent failure of the materials. The polymer remained fully bonded and was able to support the ceramic to greater breaking stresses, akin to those observed in type 1b. However, after the ceramic failed, the polymer remained bonded to the two halves of the ceramic section, allowing the system to withstand further load and resulting in a second peak in the force-displacement curve, Figure 10, at which the polymer fractured via a second crack propagating from the interface.

This additional loading secondary peak resulted in a substantial increase in energy absorption to approximately 3 times that of the unbacked ceramic.

Experimental Observations

Type 1 and 2 behaviours were captured by observation during the loading, and are illustrated by images of failed specimens in Figure 11 and Figure 12. The failures could be observed visibly, but more accurately by using DIC to detect the crack paths during loading. One output of the DIC systems is a parameter called the correlation coefficient, which provides an indication of the similarity between images and can be used to detect fracture. As a crack propagates across an image, it produces significant local distortion of the image, resulting in a reduced value of the coefficient. Full-field maps of the correlation coefficient for a type 1 and a type 2 failure are presented in Figure 13 and Figure 14. Figure 13, taken moments before total failure, clearly shows a crack along the interface. Once the ceramic fails, the ceramic crack and interfacial crack combine to produce the Type 1 failure in Figure 11. Figure 14 shows an image in the moments after ceramic failure and shows that, despite the ceramic having failed, the polymer remained bonded, which is consistent with the specimen continuing to support load. No failure of the interface was detected in the centre of this specimen. The crack in the polymer propagated downward until total failure of the polymer, producing the specimen in Figure 12.

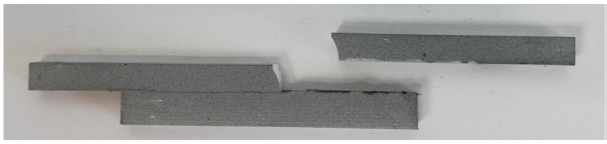


Figure 11 – Type 1- Interfacial failure of a composite bend specimen. Specimens have been painted to allow DIC to be performed.

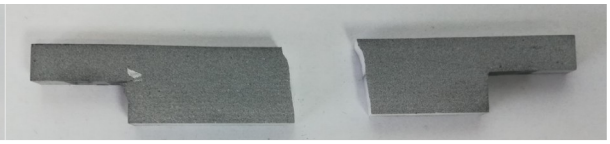


Figure 12 – Type 2 - Central failure of a composite bend specimen. Specimens have been painted to allow DIC to be performed.

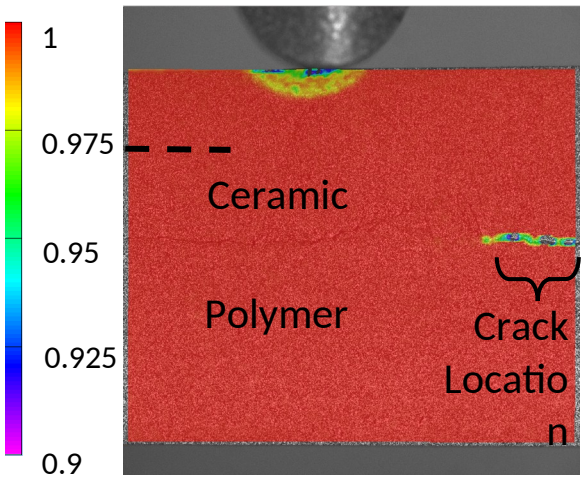


Figure 13 – Type 1 (interfacial failure) of a composite bend specimen using DIC to calculate the correlation coefficient map. The crack has propagated along the interface of the specimen from the right.

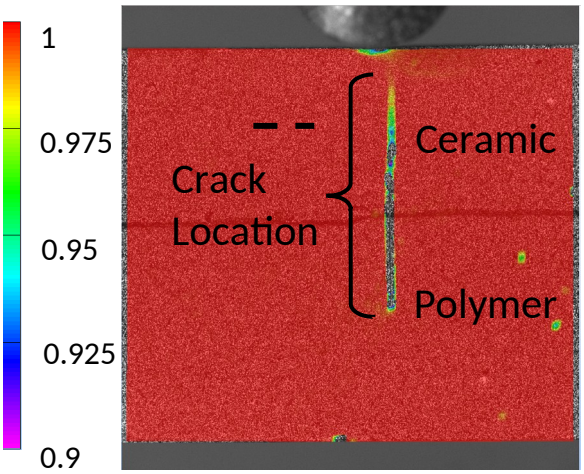


Figure 14 – Early stages of Type 2 (central failure) of a composite bend specimen using DIC to calculate the correlation coefficient map.

5.7.1.3 Backed Ceramic - Results

The normalised force-displacement results are presented in Figure 15 and Figure 16. To account for geometric differences, the force was normalised using the combined second moment of area and stiffness of the ceramic and backing. This was performed using

$$\hat{F} = \frac{F}{E_c I_c + E_p I_p} \tag{5}$$

Where $\hat{F}$ is the normalised force, and *E* and *I* are the modulus and second moment of area respectively for the ceramic and polymer. The second moment of area of the polymer was calculated using the parallel axis theorem assuming that the neutral axis remains in the centre of the ceramic. In fact, the addition of the polymer backing moves the neutral axis, but the differences in stiffness are large and this effect was therefore calculated to be negligible.

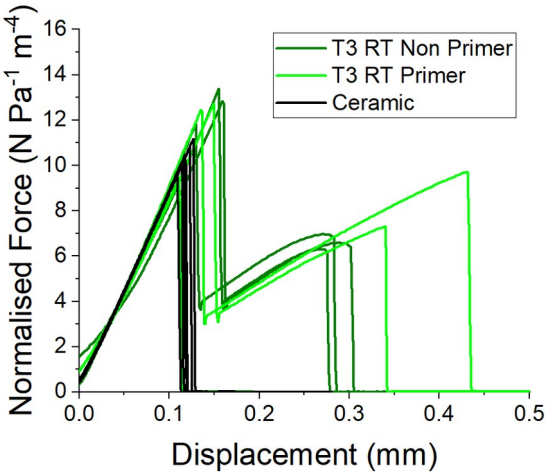


Figure 15A - Task 3 room temperature.

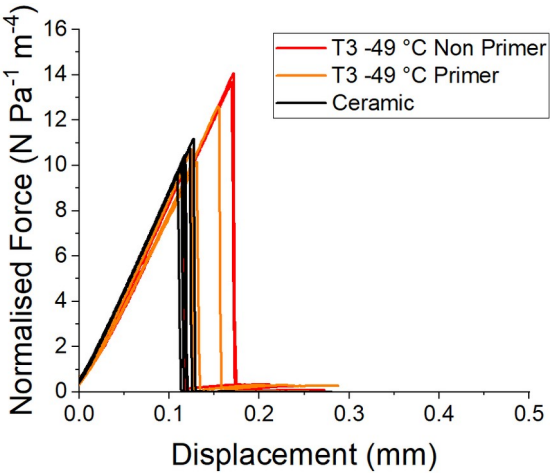


Figure 15B - Task 3 sub-ambient.

Figure 15 –Force vs displacement response for Task 3 under quasi-static loading conditions split into the room temperature and low temperature experiments.

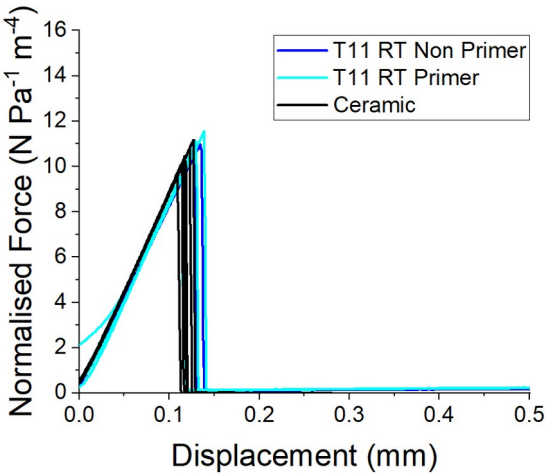


Figure 16A - Task 11 room temperature response. Zoomed into point of ceramic failure.

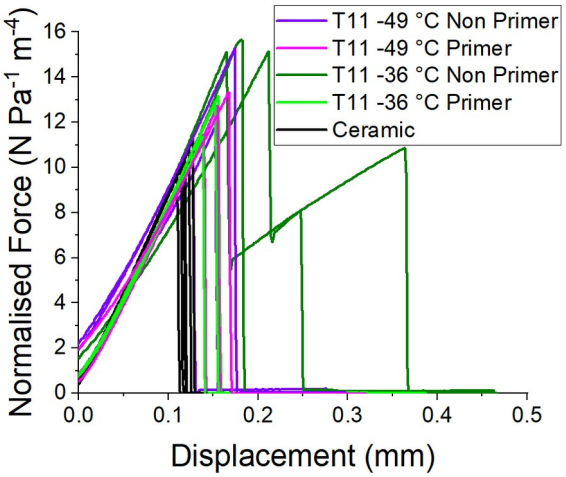


Figure 16B - Task 11 sub-ambient response.

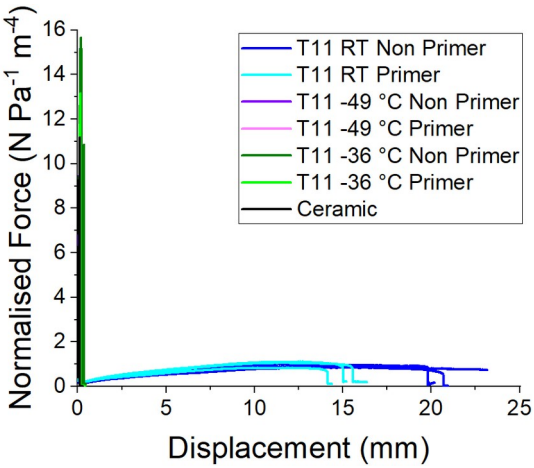


Figure 16C – All Task 11 results for full displacement recorded.

Figure 16 - Force vs displacement response for Task 11 under quasi-static loading conditions. Task 11 -36 °C and Task 3 room temperature share the same colour scheme (green) as these conditions were chosen to mimic each other.

At room temperature for Task 3 (green), Figure 15, both the primer and non-primer surface treatment displayed type 2 failure, resulting in the characteristic double peak response in the force-displacement graph. Further, the maximum breaking force in the ceramic was consistently observed to be greater than that of the unbacked ceramic. For these specimens, the addition of the primer allowed for specimens exhibiting greater ultimate failure displacement over those bonded without this surface pre-treatment. When the temperature was reduced to -49 °C (red/orange), the failure mode became, generally, type 1b, in which the interface was observed to fail before the ultimate failure of the ceramic, but the polymer was still sufficiently bonded to the ceramic to allow the breaking stress of the ceramic to increase over the unbacked ceramic. At these temperatures, the surface prepared in the absence of a primer, was generally observed to increase the ultimate failure displacement of the specimens over those specimens bonded with the primer. It was thought that the increased complexity of the interface from the presence of the primer at sub-ambient temperatures caused a general weakening of the interface.

For Task 11, at room temperature Type 2 failure was observed to occur, although due to the ductility of this polymer this was the extreme of this classification of behaviour. Whilst there was relatively little increase in the ceramic breaking stress, there was a significant increase in ultimate failure displacement as neither the interface nor polymer failed for a considerable time. Under this loading, the primer surface treatment was observed to reduce the ultimate failure displacement considerably. Once unloaded, all deformation of the polymer was fully recoverable. When the temperature was reduced to -49 °C (purple/pink), Type 1b failure now occurred. The breaking stress was found to have been increased over that of the unbacked ceramics, and the influence of the primer/non-primer surface treatment on the breaking stress was similar. At -36 °C, where the temperature was

selected to mimic the polymer response of Task 3 at room temperature, there was a re-emergence of the Type 2 failure mode very similar to that exhibited by Task 3, Figure 17, which suggests this behaviour can be controlled through polymer stiffness as well as the interfacial strength. Interestingly, those specimens bonded with a primer pre-treatment all failed in the Type 1b failure mode. This suggests the difference between Type 1 and Type 2 fails is a relatively fine threshold and differences such as the use of a primer pre-treatment or not can have significant effects on the overall specimen response. This subsequently would have a significant influence on the overall energy absorbing capacity of the specimen.

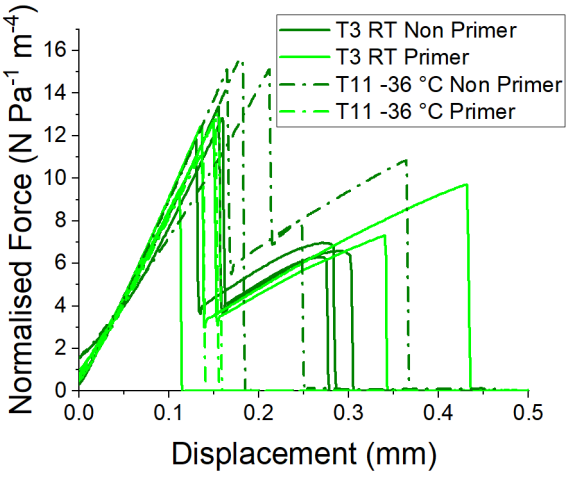


Figure 17 - Comparison between Task 3 and low temperature Task 11. The temperature was chosen to give the similar polymer stiffness between the polymers.

The breaking stress in the ceramic at the point of failure, calculated using beam bend theory, is displayed in Figure 18 and Figure 19, and the energy absorbed during loading, calculated as the area under the force-displacement curve, is presented in Figure 20 and Figure 21. In these graphs, black diamonds represent Type 1 failure and stars represent Type 2. Whilst there was relatively little influence of the failure mode type on the breaking stress, it had a significant influence on the energy absorption capability of the specimens and

significantly more energy was absorbed when the specimens failed in the Type 2 failure mode compared to Type 1. These results are tabulated in Table 3. When failure Type 1b was present, there was an approximate increase in energy absorption by a factor of 1.5 – 1.8 over that of the unbacked ceramics. When specimens failed under Type 2, the increase was on the order of a factor of 3, aside from the ductile Task 11 under ambient conditions, which absorbed approximately 20 times as much energy as the unbacked ceramic. Therefore, if the threshold between Type 1 and 2 behaviour could be better understood and controlled the increase in energy absorption capability could be significant.

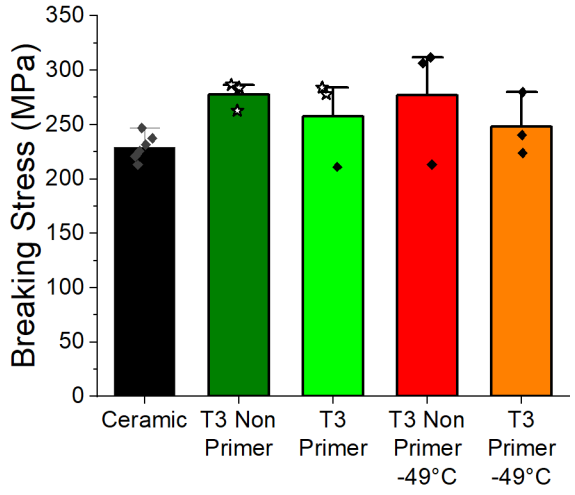


Figure 18 - Breaking stress in the ceramic for ceramic bend specimens backed with Task 3. Diamonds denote Type 1 failure and stars, Type 2.

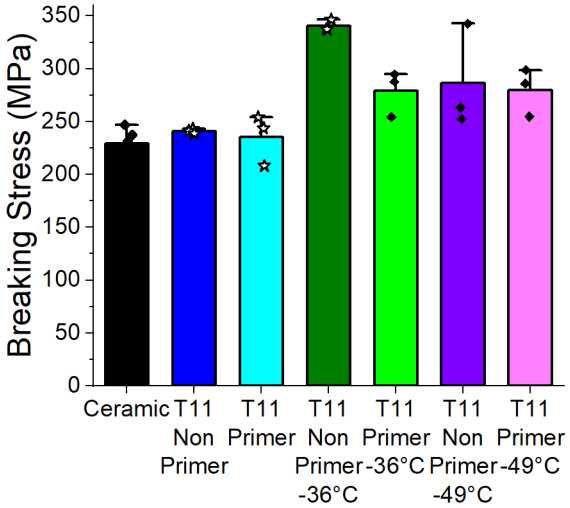


Figure 19 - Breaking stress in the ceramic for ceramic bend specimens backed with Task 11. Diamonds denote Type 1 failure and stars, Type 2.

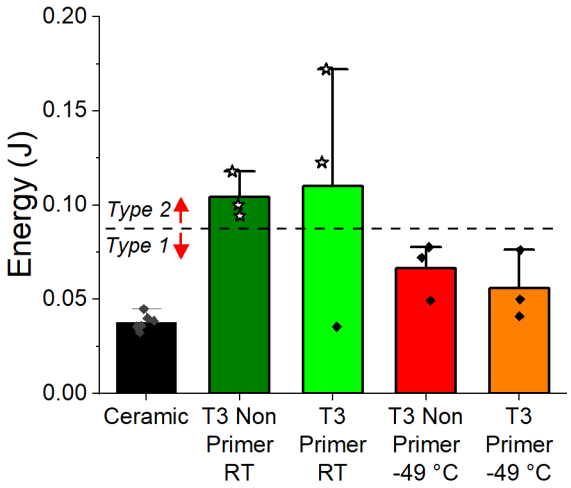


Figure 20 - Energy absorbed during loading for Task 3. Diamonds denote Type 1 failure and stars, Type 2.

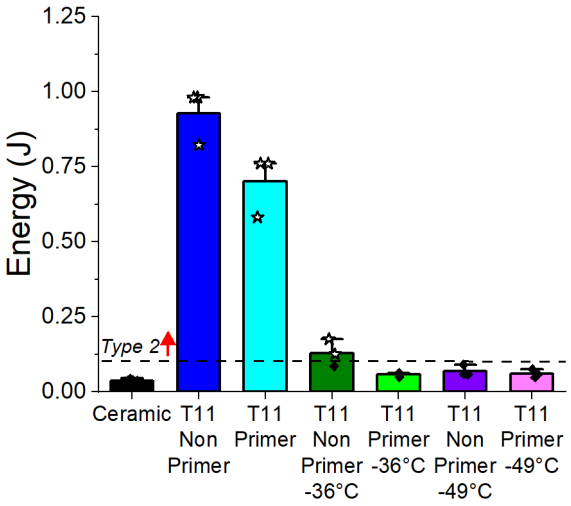


Figure 21 - Energy absorbed during loading for Task 11. Diamonds denote Type 1 failure and stars, Type 2.

			Mean energy absorbed (J)	Improvement factor vs. unbacked ceramic	Failure mode type
Ceramic			0.038	-	-
Task 11	RT	Non Primer	0.93	24.5	Type 2
		Primer	0.70	18.5	Type 2
	-36 °C	Non Primer	0.13	3.4	2× Type 2, 1× Type 1
		Primer	0.06	1.6	Type 1
	-49 °C	Non Primer	0.06	1.6	Type 1
		Primer	0.070	1.8	Type 1
Task 3	RT	Non Primer	0.10	2.8	Type 2
		Primer	0.11	2.9	2× Type 2, 1× Type 1
	-49 °C	Non Primer	0.066	1.8	Type 1
		Primer	0.056	1.5	Type 1

Table 3 - Energy absorbed for each loading condition.

One final consideration was the influence of thermal contraction on the specimens. Because there is approximately an order of magnitude difference in the coefficient of thermal expansion for alumina (~1.3 x10^{-5} K^{-1}) and polyurethane (~2 x10^{-4} K^{-1}), upon contraction thermal strains were likely to develop over the interface. To determine this influence,

speckled specimens were cooled from ambient temperature to -60 °C and images were taken every second during the cooling process. DIC was performed on the resulting images to extract the displacement fields, Figure 22 and Figure 23. It was found that there was significant thermal strain across the PU-alumina interface, which resulted in thermally-induced interfacial failure. Here, failure was defined as the first point of detection of a discontinuity in the vertical displacement field at the edge of the interface. Specimens backed with Task 3 were observed to fail at approximately -10 °C for both the primer and non-primer specimens; those backed with Task 11 failed at approximately -40 °C for the primer and non-primer, respectively, but the primer was generally found to debond 2-3 °C earlier. This shows that the use of time-temperature superposition here would likely cause a different specimen behaviour than the dynamic loading it was aiming to simulate. However, the conclusions above on the energy absorption capabilities of the specimen due to the failure modes and their sensitivity to stiffness and interfacial performance are still valid.

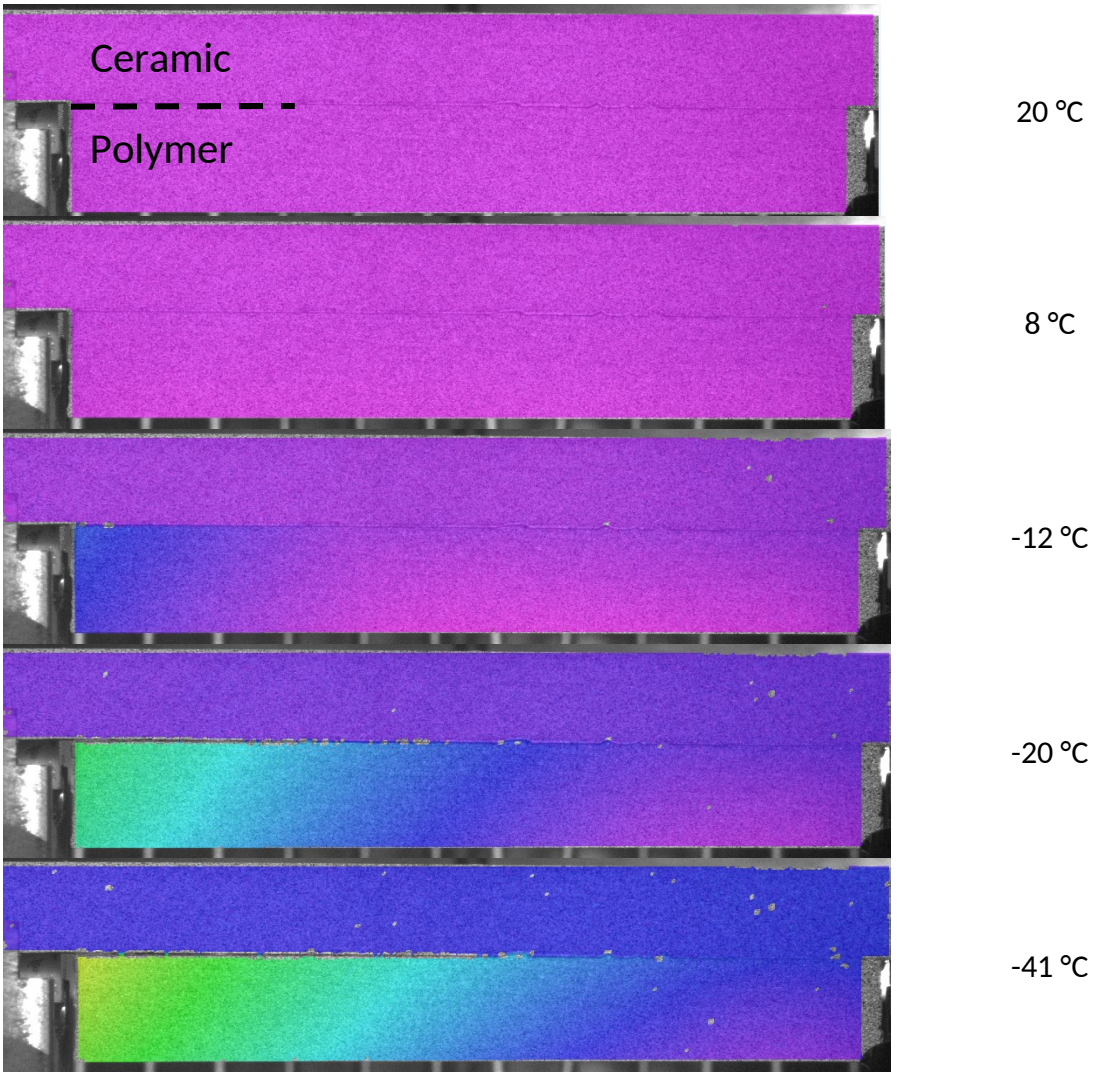


Figure 22 – DIC vertical displacement map for Task 3 backed alumina for select images for the primer backed specimens. Failure from thermal contraction was observed.

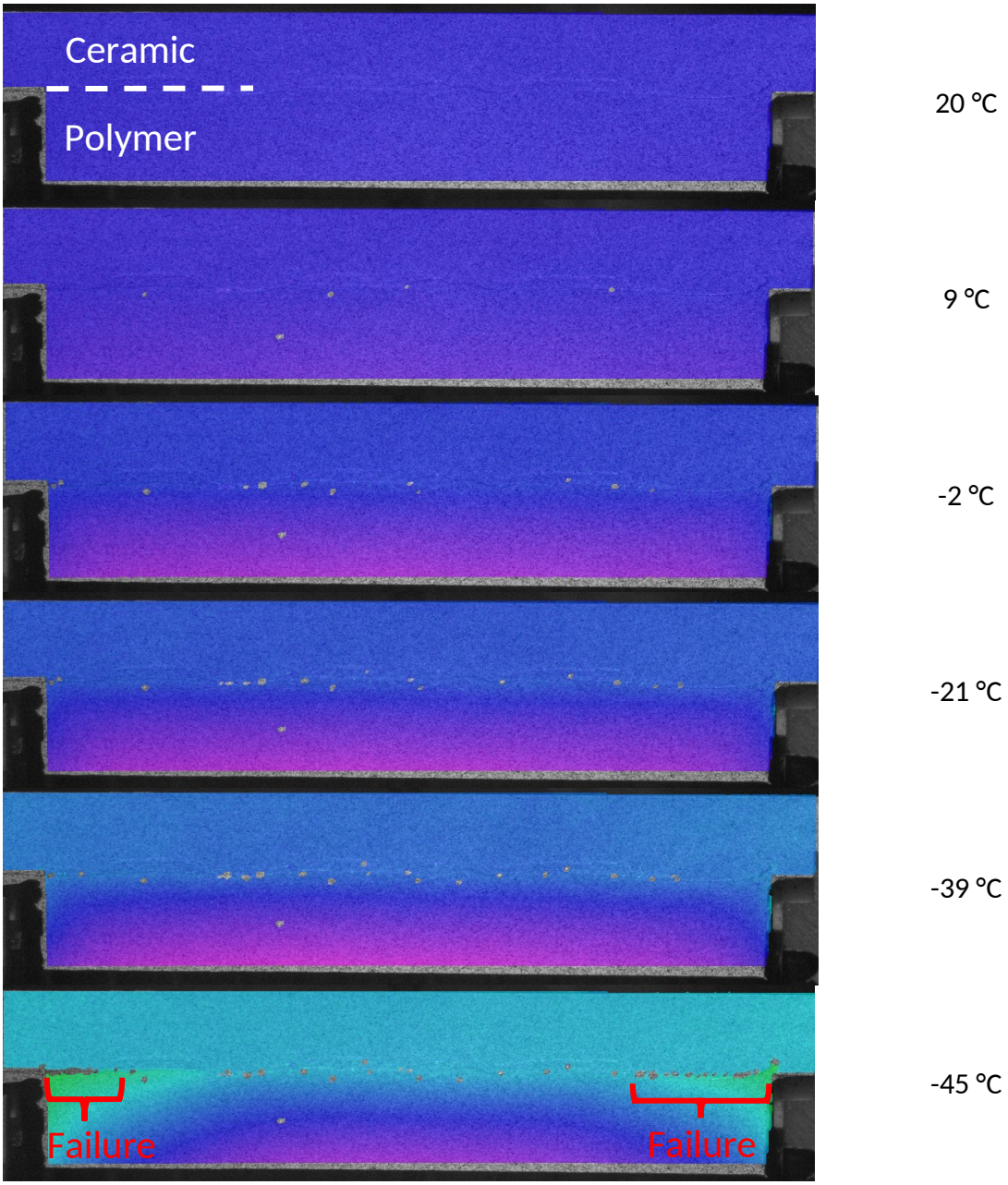


Figure 23 - DIC vertical displacement map for Task 11 backed alumina for select images for the primer backed specimens. Failure from thermal contraction was observed.

5.7.2 Impact Beam Bend

5.7.2.1 Task 3 and 11 - Primer vs Non-Primer

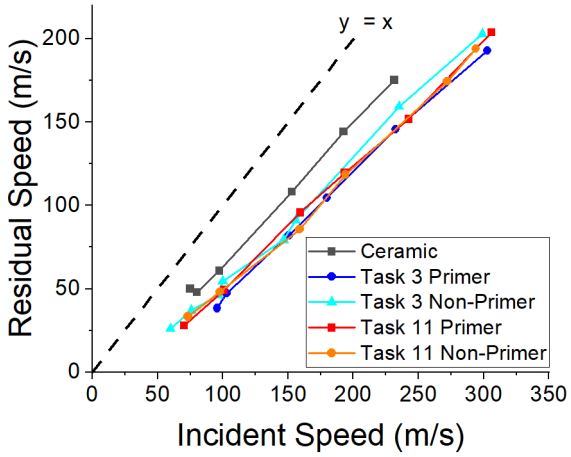


Figure 24 - Incident vs. residual speed during impact for Task 3 and Task 11 with and without a primer pre-treatment. The line of y = x is shown for reference.

Results for impact beam bend experiments for Task 3 and Task 11 are presented in Figure 24, in the form of incident vs residual speed. The speeds were calculated from tracking the projectile through images, determining the number of pixels traversed in a known time and converting this to speed using the known pixel to mm conversion. All the results displayed a relatively linear relationship between the incident and residual speed across the range of speeds tested as would broadly be predicted by the Lambert-Jonas relation above the ballistic limit [28], [29]. In general, the addition of the polymer backing produces approximately a 30 % reduction in absolute speed over the unbacked ceramic specimens.

Comparing the primer and non-primer pre-treatments, for Task 3 there was an improvement of approximately 10 % from the addition of the primer pre-treatment but minimal improvement for the Task 11 polymer. The mechanism for this performance improvement was believed to be observed in the failure, Figure 25 and Figure 26. From observation of fracture pathways, cracks originating from the point of impact spread in a conical pattern typical of ballistic impact [4]. Once these cracks reach the polymer interface,

they either pass directly across the boundary into the polymer or propagate along the interface. Generally, it was observed that the interfaces pre-treated with a primer inhibited crack growth along the interface. Instead, cracks grow more slowly into the polymer, which allows the polymer to support the ceramic for longer and absorbs more energy for the same amount of crack elongation. This was opposed to debonding and cracking directly along the interface which was generally observed in the Task 3 specimens without a primer pre-treatment. Further, polymers typically have a greater fracture energy compared to ceramics so any increased polymer fracture observed here would lead to greater energy absorption. This behaviour has been highlighted in red in Figure 25 compared to Figure 26. This behaviour is akin to the previously observed Type 2 failure mode under quasi-static loading. This observed phenomenon highlights the benefits of this geometric experimental set up as such observations would be obscured in plate impact.

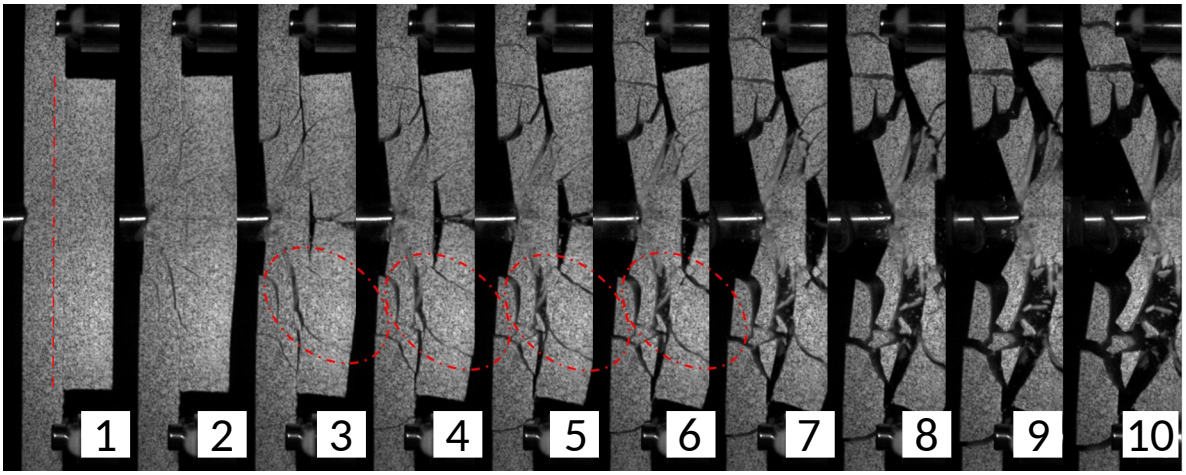


Figure 25 - Task 3 beam bend impact at 100 m s^{-1} with a primer surface pre-treatment. The polymer-ceramic boundary is shown in image 1 with the ceramic as the strike face. The region circles in red shows crack propogation across the interface into the polymer. Image 1 is at the moment of impact and subsequent images are shown every 20 µs.

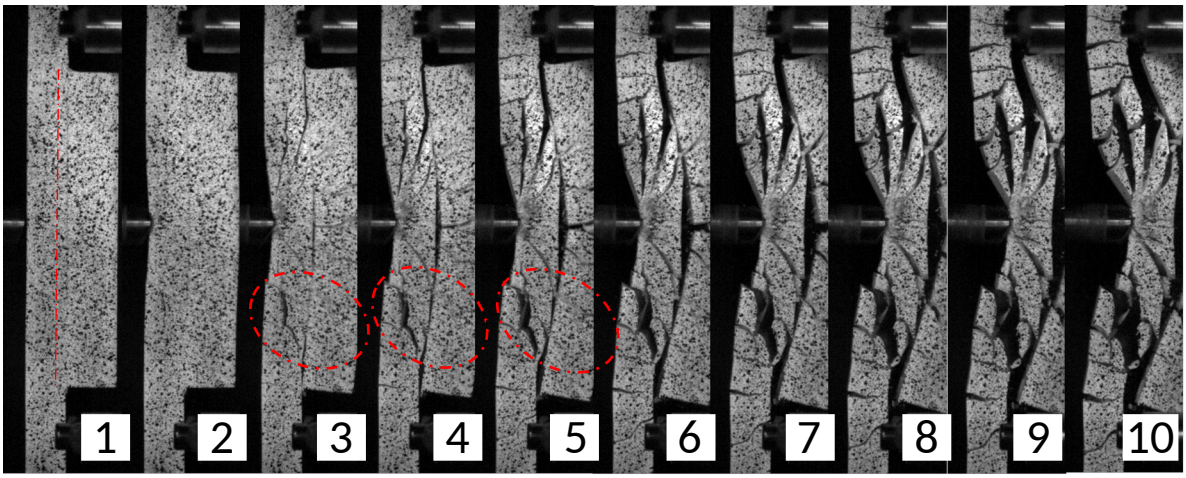


Figure 26 - Task 3 beam bend impact at 100 m s^{-1} without a primer surface pre-treatment. The polymer-ceramic boundary is shown in image 1 with the ceramic as the strike face. Image 1 is at the moment of impact and subsequent images are shown every 20 µs.

For Task 11, no measurable difference in performance was recorded between specimens with and without a primer pre-treatment. This was thought to be because, for each surface preparation type, there was no observed difference in failure mode, Figure 27 and Figure 28. Once the cracks, propagating through the ceramics from the point of impact, reached the interface, the ductility of the polymer was such that no cracks could propagate into the polymer and instead chose to propagate along the interface. The energy release rate of

these interfaces under dynamic loading were found to be similar, Chapter 4, and so any energy absorption differences due to interfacial fracture would be small.

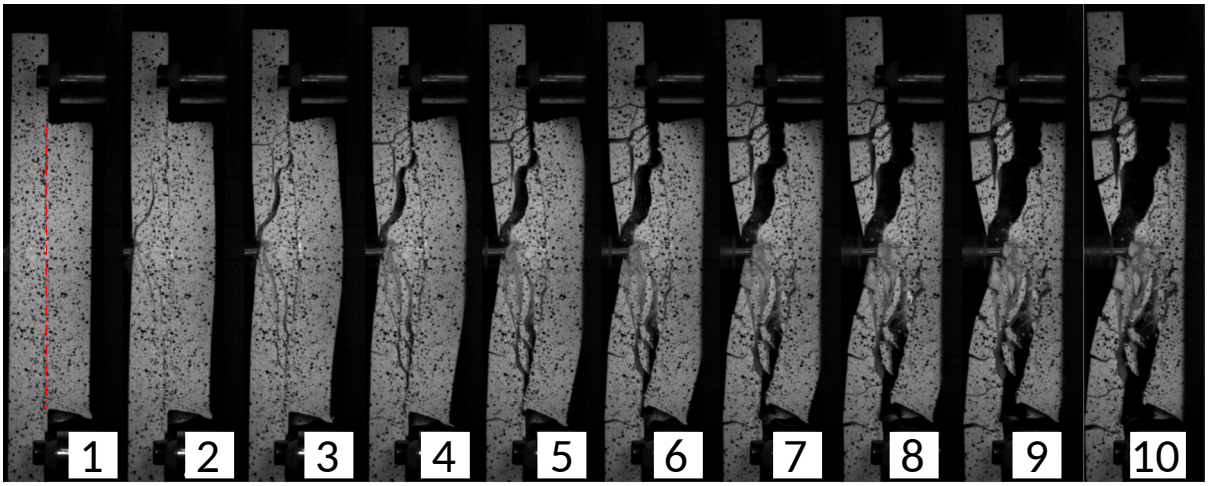


Figure 27 - Task 11 beam bend impact at 100 m s^{-1} with a primer surface pre-treatment. The polymer-ceramic boundary is shown in image 1 with the ceramic as the strike face. Image 1 is at the point of impact and subsequent images are shown every 20 µs.

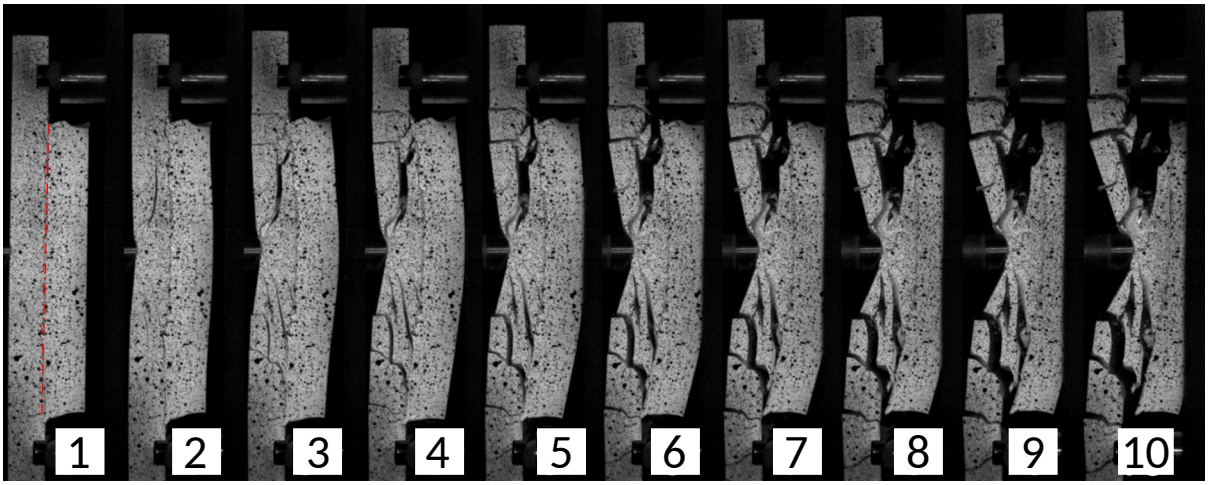


Figure 28 - Task 11 beam bend impact at 100 m s^{-1} without a primer surface pre-treatment. The polymer-ceramic boundary is shown in image 1 with the ceramic as the strike face. Image 1 is at the point of impact and subsequent images are shown every 20 µs.

Inertial effects are significant in dynamic experiments; therefore, to allow a fair comparison to be made, the velocities can be replotted and normalised with respect to the total masses of the specimens, Figure 29. Here it is shown that the mass normalised performance from

the addition of the backing produced an improvement of ballistic performance on the order of 15 % compared to the equivalent mass of ceramic.

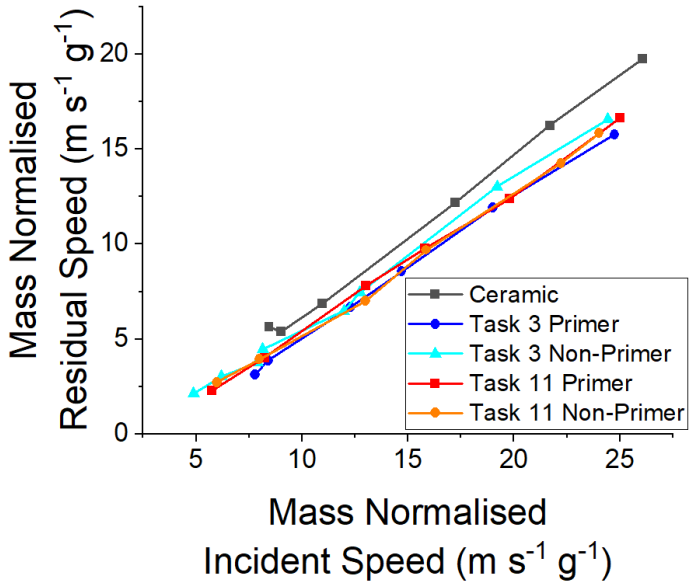


Figure 29 - Mass normalised incident vs residual speed for Task 3 and Task 11 for primer and non-primer pre-treatment.

5.7.2.2 Further Specimen Types

Strengthless Interface

Considering the differences in behaviour, it is interesting that the overall impact performance of specimens made using the two polymers was similar. It was hypothesised that a significant portion of the incident kinetic energy was being converted to kinetic energy of the fragments and not absorbed by material deformation. Therefore, to separate the difference between the interfacial and inertial effects, a further experiment was conducted in which polyurethane backings were cured separately and then lightly adhered

to the alumina using Pritt-stick®. The consequence of this was a specimen in which the polymer was present behind the ceramic, but with almost zero interfacial strength.

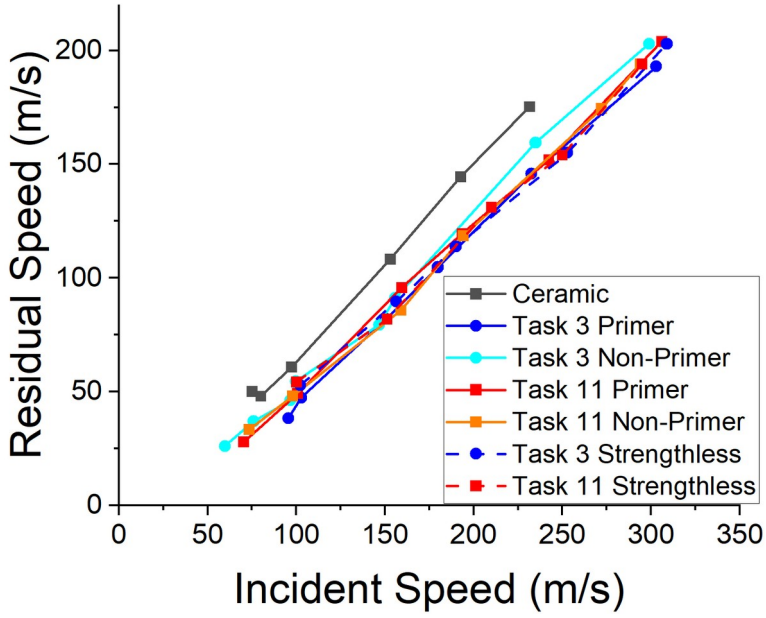


Figure 30 - Task 11 and Task 3 residual vs incident velocities under primer and non-primer surface pre-treatments and strengthless interfaces.

Figure 30 shows that the removal of interfacial strength has little effect on the overall armour performance. For Task 11 and Task 3, the strengthless condition produced very similar results to those above. This suggests that for these polymers and loading conditions, the transfer of kinetic energy to the material fragments is the significant energy absorption mechanism. Although the interface was previously observed to cause differences in the fracture pathways, for this experimental geometry, it was not a significant energy absorption mechanism but could be for more complex geometries and if the armour was used in front of a more representative material instead of free standing, e.g. ballistic gel. Such investigations were beyond the scope of this work.

Glass-fibre reinforced polycarbonate and Dowsil 6-1104

A final investigation was conducted into the influence of a stiffer polymer on the overall armour response. Glass fibre reinforced polycarbonate was bonded to the alumina using Dowsil 6-1104 and compared to Task 3 bonded with this adhesive. This is a silicone-based adhesive and is more ductile than the interface generated by the direct curing method but would allow the polymer to be bonded to the ceramic for a longer duration.

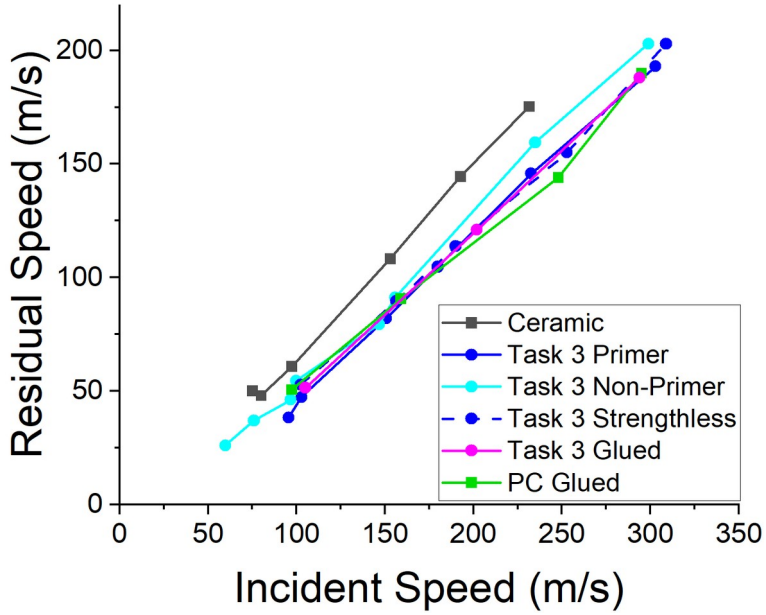


Figure 31 - Task 3 and PC residual vs incident velocities under primer, non-primer, strengthless and bonded interfacial conditions. The results from Task 11 have been removed for clarity.

From the results obtained, Figure 31, it appeared that using the material stiffness and interface ductility investigated here made little difference to the energy absorption. This was perhaps expected from observation of the fracture paths, Figure 32 and Figure 33. These specimens fail in a manner similar to that previously found with Task 11, Figure 27, where

no cracks passed from the ceramic into the polymer backing and all propagated along the interface and so the energy absorption of this was similar.

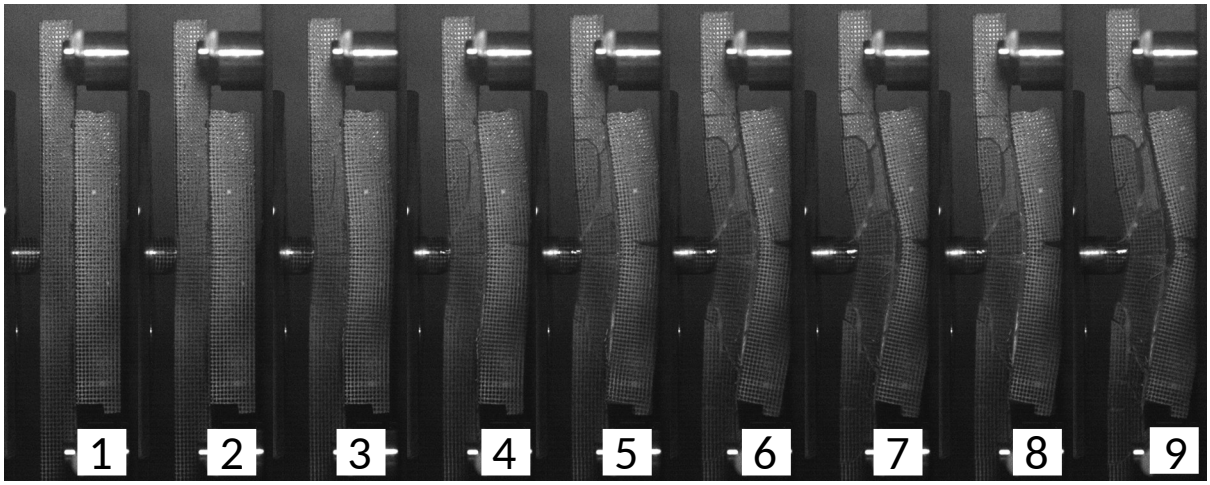


Figure 32 - Task 3 bonded with Dowsil 6-1104. Impact was at 100 m s^{-1} and each image is separated by 10 µs.

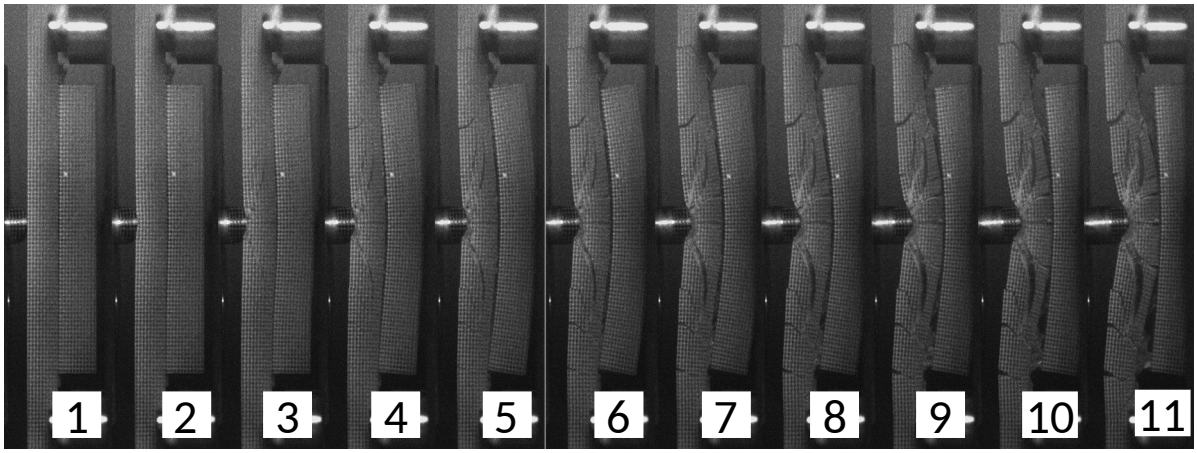


Figure 33 - GFPC bonded with Dowsil 6-1104. Impact was at 100 m s^{-1} and each image is separated by 10 µs.

5.8 FEA Results

FEA simulations were performed in Abaqus 2021 to determine whether the observed behaviour of the specimens can be recreated using materials and interfacial properties that have been separately characterised. Under quasi-static loading, the results only simulated the beam bend response at room temperature as well as -49 °C for Task 3 and -36 °C for Task 11. The results for -49 °C for Task 11 were not simulated because no interfacial characterisation from a separate study, Chapter 4, was performed at this temperature.

A 2D static general model was used with an XFEM fracture definition to model the quasi-static behaviour. A 3D dynamic explicit model was used to capture the impact behaviour of the specimen.

5.8.1 Material Models

5.8.1.1 Steel

The projectiles and specimen supports were manufactured out of EN16 steel and an elastic material model was used to represent their behaviour. The simulation parameters are presented in Table 4, with the material properties obtained from the material datasheet.

Stiffness (GPa)	205
Poisson's Ratio	0.29
Density (kg m^{-3})	7870
Element Type (Quasi-static/Impact)	CPS4R/C3D8R
Element Size (mm)	0.5

Table 4 - Simulation parameters to model the response of steel.

5.8.1.2 Alumina

To model the brittle failure response of the ceramic, an elastic material model was used which allowed XFEM crack growth under tensile stress. The model was calibrated against experimental data to reproduce the observed stiffness and breaking stress, Figure 34. Damage was set to initiate at defined stress and, once this damage had initiated, a very short failure displacement was defined to allow for the brittle nature of the ceramic. The remaining material parameters, the density and Poisson's ratio, were found in the material datasheet. These simulation parameters are presented in Table 5.

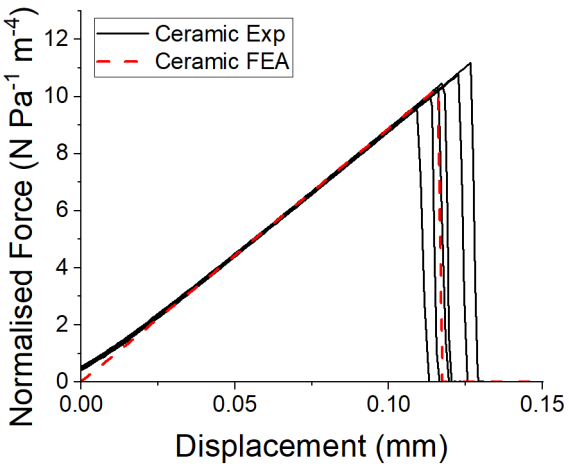


Figure 34 - Ceramic experiment vs FEA under quasi-static beam bend.

Stiffness (GPa)	270
Poisson's Ratio	0.21
Density (kg m^{-3})	3140
Failure Stress (MPa)	207
Post damage displacement (m)	1 x10^{-5}
Element Type (Quasi-static /Impact)	CPS4R/C3D8R
Element Size (mm) (Quasi-static /Impact)	0.5/0.2

Table 5 – Simulation parameters to model the response of alumina.

5.8.1.3 Interface

Quasi-static response

To simulate the interfacial behaviour of the interface, a traction separation law (TSL) was used to populate cohesive elements in Abaqus 2021. To be able to model a propagating crack, this model makes use of the relation,

$$\sigma(\Delta)=\frac{dJ}{d\Delta} \tag{6}$$

where Δ is the opening displacement at the crack tip, σ is the traction normal to the crack and J represents the J-integral, which is a measure of the energy availability to propagate the crack [30], [31]. Therefore, if the evolution of the J-integral with tip opening displacement is known, then the behaviour of the crack can be modelled from the gradient of this relationship [32]. An idealised J-integral vs tip opening relation would start from zero, where the crack is fully closed, before rising to a critical steady state value where the crack is propagating, see [33] for a detailed description. Therefore, the gradient of this curve would rise to a peak before reducing, and this can be approximately represented by the relationship in Figure 11. The behaviour of the element beyond δ^*, where the onset of damage begins, can take a variety of shapes; however, for this study, a linear damage evolution model was chosen.

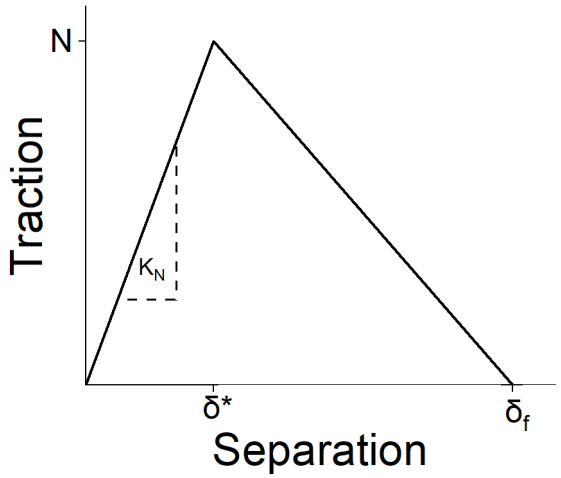


Figure 35 - Example TSL response.

The experimental response of the interfaces of interest to this study have been characterised in a previous study, Chapter 4. In this study, ceramic strips were bonded together using the polyurethanes of interest and a wedge driven between the two surfaces. The crack tip was imaged and the J-integral and tip opening displacement was determined for every timestep. This experimental relationship was determined, differentiated, and plotted as solid lines in Figure 36. This was fitted to the linear TSL representation, displayed as dashed lines in the figure, with the numerical definitions presented in Table 6. The cohesive elements from Task 11 were found to withstand greater forces in general than those from Task 3; however, this was thought to be an overestimation of reality due to the calculation of the J-integral for this polymer due to its increased ductility. For a full investigation of this consult, Chapter 4.

Note, these experiments were performed at temperatures different to that previously discussed in this paper because these experiments were guided by a different set of DMA results, which produced a different set of shift factors. These were used to model the material response closest to the experimental conditions. For Task 11 this was -36 °C, and therefore the material properties of the polymer were defined at these conditions.

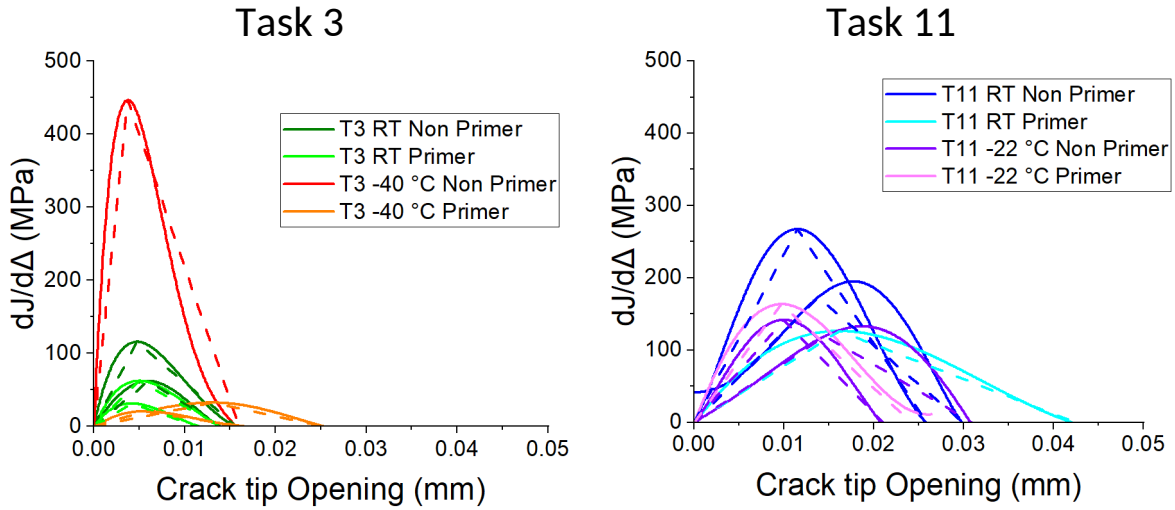


Figure 36 - Cohesive representation and TSL modelling of the PU-alumina interface for Task 3 and Task 11. The solid lines represent the experimental results and the dashed, the linear TSL fit.

			K_N (Pa m^{-1})	N (MPa)	δ_f (µm)
Task 3	RT	Non Primer 1	3.13×10^{13}	116	15.7
		Non Primer 2	1.03×10^{13}	62.0	14
		Primer 1	1.26×10^{13}	62.3	14
		Primer 2	7.6×10^{12}	31.2	11.6
	-40	Non Primer 1	1.21×10^{14}	447	16
		Primer 1	3.68×10^{12}	20.6	16.6
		Primer 2	2.5×10^{12}	32.5	25.4
Task 11	RT	Non Primer 1	2.32×10^{13}	267	25.9
		Non Primer 2	1.25×10^{13}	173	29.9
		Primer 1	7.79×10^{12}	126	42.7
	-22	Non Primer 1	8.19×10^{12}	120	30.9
		Non Primer 2	1.42×10^{13}	142	21
		Primer 1	1.68×10^{13}	163	24.2

Table 6 - TSL parameter definitions.

Impact

Under dynamic explicit loading conditions, the accuracy of cohesive elements is known to be limited. Therefore, only the extremes of loading were investigated: modelling the interface as fully stuck and fully free. This was achieved within the interface definition by allowing it to separate, or not, under loading.

5.8.1.4 Polymer

Quasi-static response

The behaviour of the polymer was approximated from tensile tests on the materials. Similar to the ceramic material model, XFEM fracture was enabled with a short damage evolution displacement being defined to capture the brittle nature of this deformation. All polymers exhibited this behaviour, apart from Task 11 whose response was captured using an Ogden model. The values of these parameters are displayed in Table 7. The material density was found from the provided datasheets. The Poisson's ratio, v, of these polymers was found through ultrasound experiments and the relation between the longitudinal, c_l, to the shear, c_s, wave speed defined as

$$v = \frac{c_l^2 - 2c_s^2}{2\left(c_l^2 - c_s^2\right)} \tag{7}$$

	Task 3		Task 11	
	Room Temp	-49 °C model	Room Temp	-36 °C model
Stiffness (GPa)	2.3	3.2	0.64	2.3
Poisson's Ratio	0.49	0.49	0.49	0.49
Density	1120	1120	1120	1120
Failure Stress (MPa)	25	35	-	30
Post damage displacement (m)	1×10^{-5}	1×10^{-5}	-	1×10^{-5}
Ogden model	-	-	$\alpha = 10.9$ $\mu = 3.3$ MPa	-
Element Type	CPS4R	CPS4R	CPS4R	CPS4R
Element Size (mm)	0.5	0.5	0.5	0.5

Table 7 – Simulation parameters to model the response of Task 3 and Task 11 for a static general simulation.

Impact response

The model of the polymer under impact loading shared similarities with the quasi-static model. However, the key difference was the polymers were now modelled using the Prony series as previously defined in Section 5.6.2 and the exact parameters are presented in the Appendix. No failure model was implemented in the impact simulation.

Stiffness (GPa)	Prony Model *See Appendix
Poisson's Ratio	0.49
Density	1120
Element Type	C3D8R
Element Size (mm)	0.2

Table 8 - Simulation parameters to model the response of Task 3 and Task 11 for a dynamic explicit simulation.

5.8.2 Quasi-static FEA response

The results of the quasi-static simulations were compared against experimental results. For Task 3, the room temperature simulations were found to reliably predict the Type 2 failure mode, Figure 38, producing the double peak behaviour of the beam bend specimens, Figure 37, but found there was little difference from the addition of the primer pre-treatment. At sub ambient conditions there were more significant differences between the simulated and experimental results because the simulated continued to predict Type 2 (central) failure whilst it was observed that Type 1 (interface) failure occurred. This low temperature discrepancy was likely due to the previously discussed issues of thermally induced strains developing across the interface leading to, experimentally, a weaker interface than in the model. Therefore, the simulation could be used to predict an idealised case at low temperatures where no thermally induced strains are present.

Further, as was previously discussed in this paper, experimentally, the difference between Type 1 (interfacial) failure and Type 2 (central) failure can be influenced by relatively small changes in polymer stiffness and interfacial properties. Therefore, because this simulation has been shown to reliably capture specimen response, it provides an opportunity to investigate the thresholds of the failure modes observed, although such a study would be beyond the scope of this research.

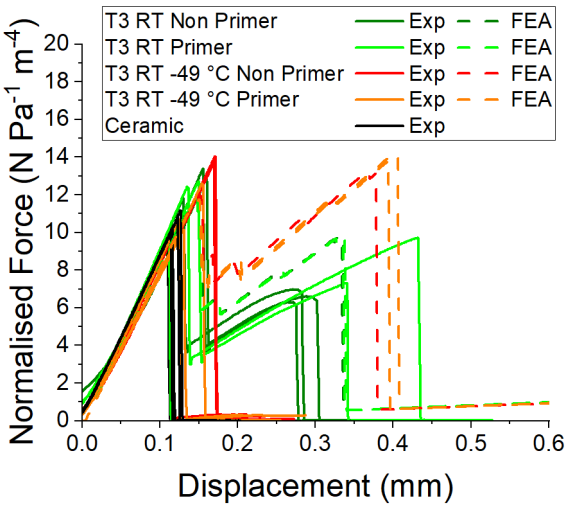


Figure 37 - Quasi-static beam bend experimental vs FEA results for Task 3.

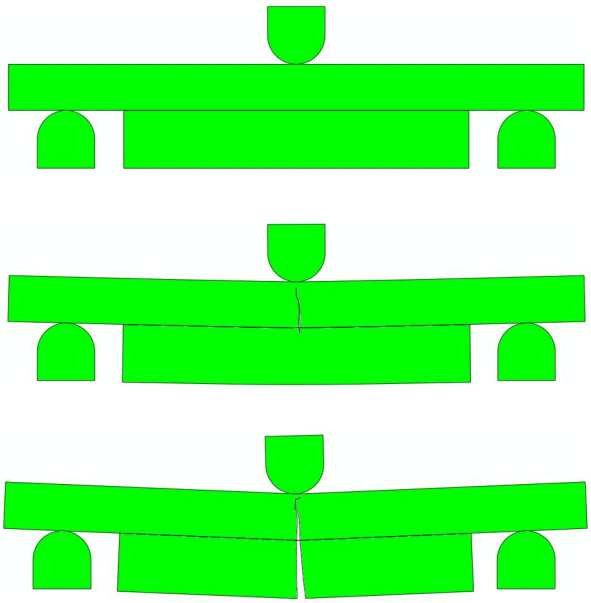


Figure 38 - Typical simulated failure mode for beam bend loading for alumina backed with Task 3 at ambient and sub-ambient conditions.

For Task 11, the model captured the failure load well where there was no major double peak behaviour at ambient temperatures, Figure 39, and this was reflected in the failure mode, Figure 40. As was observed experimentally, the backing did little to increase the failure stress of the ceramic and then, post ceramic failure, remained bonded for a

significant duration. Although, in the simulation, the load sustained by the polymer post ceramic failure was greater than that sustained experimentally. This was thought to be due to local interfacial failure around the centre of the interface, which was not captured in the simulation. This then allowed the backing to sustain greater load than was experimentally observed. Under sub-ambient loading, the double peak behaviour was present, and this is captured accurately by the simulated result. Under these conditions, the simulation results observed that the breaking stress of the ceramic remained unchanged and, once failed, the trough of the double peak loading matched that observed experimentally and captured the post-failure behaviour of the polymer well.

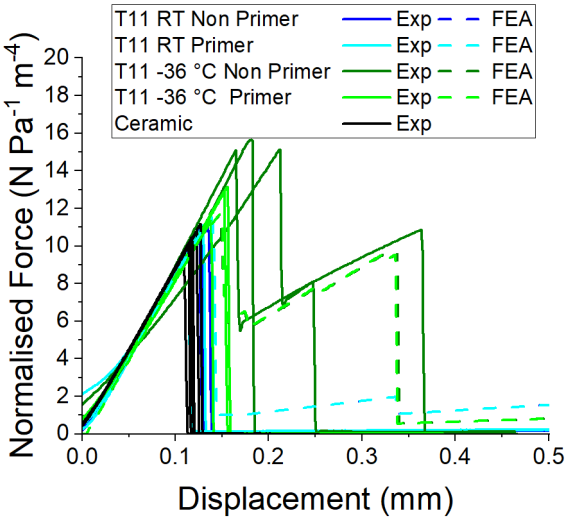


Figure 39 - Quasi-static beam bend experimental vs FEA results for Task 11.

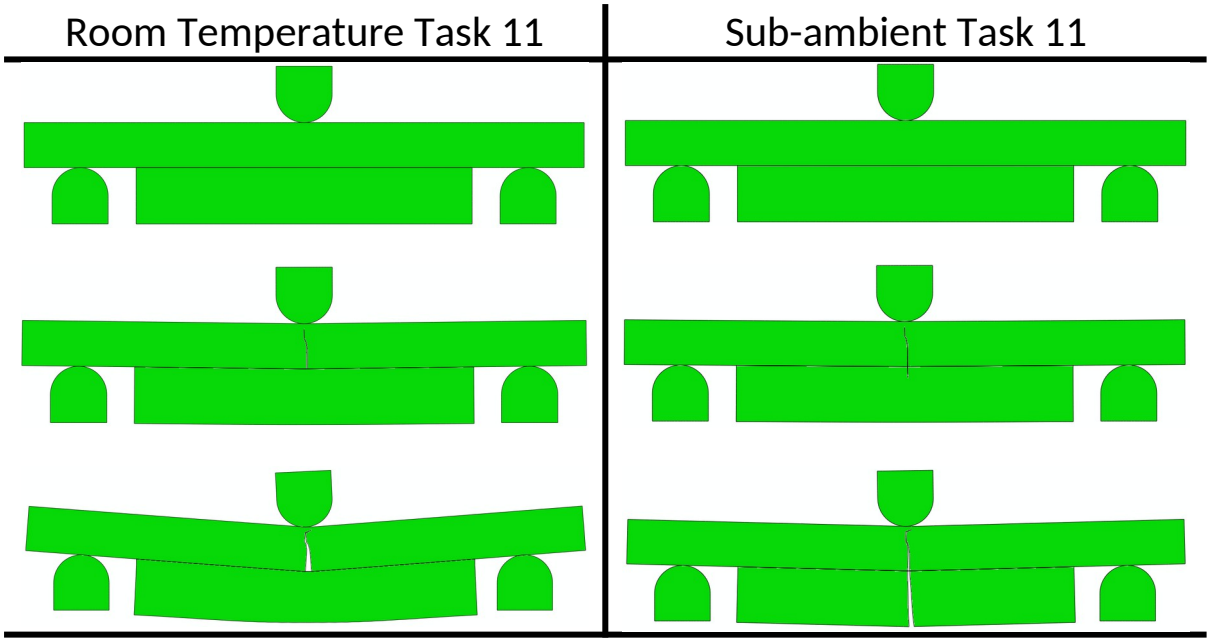


Figure 40 - Failure modes of Task 11 at ambient and sub-ambient conditions.

5.8.3 Impact FEA Comparison

Impact was simulated over the range of impact speeds of interest to this project, Figure 41. The simulation reliably predicted the residual speed after impact for each specimen type. Whilst the performance of the different polymer backings was similar, the simulation predicted that the stiffer Task 3 polymer, acting below its glass transition temperature, was able to reduce the speed of the projectile more than Task 11. This is interesting because, despite the Task 11 polymer undergoing an impact induced glass transition which would be highly energy dispersive, the stiffness of Task 3 ultimately allowed for greater energy absorption from the projectile. This implied the overall stiffness of the backing polymer was more influential than any further energy absorptive abilities from the glass transition.

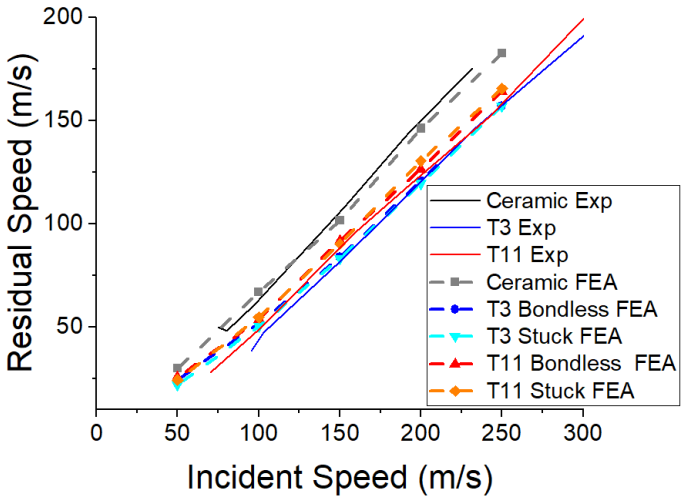


Figure 41 - Incident vs residual speeds comparing experiment (solid) to simulation (dashed) for impact beam bend.

The nature of the bonding between the backing polymer and ceramic (fully stuck or strengthless) was found to have only a small influence on the residual velocity of the projectile. It should be noted that, whilst failure occurred within the Task 3 polymer experimentally, there was no failure mechanism defined for the polymer within the simulation. Despite this fundamental difference between the observed and simulated behaviour, the comparison between the simulation and experiment for Task 3 was no worse than that observed for Task 11 where this fracture-free behaviour was observed.

From this experimental set up, a significant portion of the incident kinetic energy remained as kinetic energy of the fragments and residual projectile velocity; however, the backing was found to be influential on the overall performance. Further, whilst the interface was observed to have limited influence on the overall performance, the interface was observed to influence fracture path dynamics and control the failure modes of the material which could be influential for further experimental set ups using plate impact and ballistic gel.

5.9 Conclusions

The energy absorptive capabilities of polyurethane-backed alumina specimens loaded under quasi-static and impact three-point bend were investigated using quasi-1D (beam) specimens that allowed fracture paths to be observed that would otherwise have been obscured in typical ballistic impact experiments on plates.

Under quasi-static three-point bend, all specimens failed in one of two failure modes, denoted Type 1 or Type 2. In Type 1, the ceramic-polymer interface began to fail under the applied bending stress before the breaking stress of the ceramics, thus the ceramic was left unsupported and ultimately failed. For Type 2, no interface failure was detected during loading and, after the ceramic ultimately failed, the polymer backing did not and remained bonded to the two halves of the ceramic. In this configuration, the structure was able to continuously withstand substantial load. It was found the difference between Type 1 and 2 failure was dependent upon both the interfacial and polymer properties because it was possible, with the manipulation of temperature, to control the type of failure exhibited. This was important because Type 2 failure presented up to 3x the energy absorption of Type 1. Therefore, the temperature manipulation required could be used to govern the correct polymer for the application because the temperature change required could be used to determine the ideal position of the glass transition temperature and hence predict the most suitable polymer for the task. Further, because FEA simulations were found to reliably predict this response and failure, these provide an opportunity to investigate the threshold between Type 1 and Type 2 behaviour and can be used to predict the polymer properties that would be most suitable for the loading and environmental conditions of the required proposed task.

Under impact, the polymer backing and interfacial properties were found to be influential on performance but the strongest energy absorption mechanism was the kinetic energy of the material fragments. Whilst this mechanism was relatively similar for the specimen types of interest to this project, the quasi-1D nature of this experimental design allowed for these significant differences in fracture path dynamics to be directly observable. These dynamics were observed to be influenced by the behaviour of the interface, so whilst this did not produce significant differences in model armour performance as measured by projectile speeds, it is expected that the effect could be influential for more complex experimental geometries, ballistic impacts on plates, or when loaded in conjunction with ballistic gel backings. FEA simulations calibrated using independently obtained material parameters were used to successfully predict armour behaviour under impact. In these simulations, of the two polyurethanes used the stiffer polymer was found to be superior, despite the second polymer undergoing an impact induced glass transition which would be expected to have been highly energy dispersive.

The principle of time temperature superposition was used by manipulation of the temperature to simulate the impact behaviour of the polymer to link the quasi-static to the dynamic results. However, these results were limited due to the influence of thermally induced strains present over the material boundary, causing premature failure of the interface.

5.10 Acknowledgements

The authors would like to thank Dstl for their financial and intellectual support during this work under contract number DSTLX1000128371. Additionally, thanks must be extended to Igor Dyson and Nick Hawkins for their experimental and analytical assistance as well as Neil Warland and Andy Bateman for specimen manufacture.

For the purpose of Open Access, the author has applied a CC BY public copyright license to any Author Accepted Manuscript (AAM) version arising from this submission.

5.11 Appendix

5.11.1 DSC Data

Differential scanning calorimetry (DSC) was conducted on fully cured specimens of Task 3 and Task 11. The specimens were approximately 10 mg in weight and were heated from -90 to 120 °C at a rate of 3 °C per minute. The glass transition points were found to be at approximately 15 °C and 50 °C for Task 11 and Task 3 respectively, Figure 31.

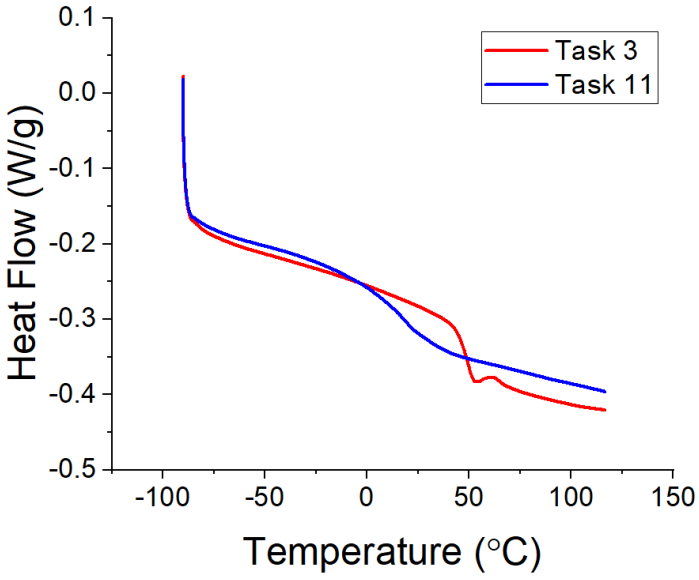


Figure 42 - DSC results for Task 3 and Task 11.

5.11.2 GFPC DMA data

DMA experiments were conducted on prismatic specimens of glass-fibre reinforced polycarbonate of dimensions 17.5 x 12.1 x 3.5 mm. Specimens were tested in a dual cantilever configuration from -60 to 120 °C in 2 °C increments. An oscillatory testing procedure was implemented and specimens were loaded to an amplitude of 0.1 % strain at frequencies of 0.1, 0.316, 1, 3.16, 10 Hz. The principal of time-temperature superposition was used to create the mastercurve presented in Figure 43 using the shift factors in Figure 44.

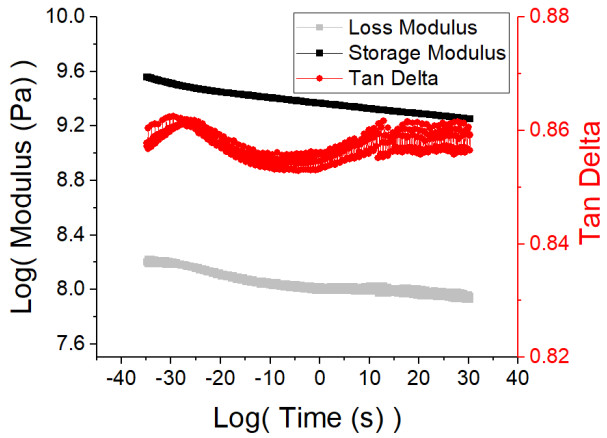


Figure 43 - Mastercurve of GFPC created using oscillatory single cantilever DMA.

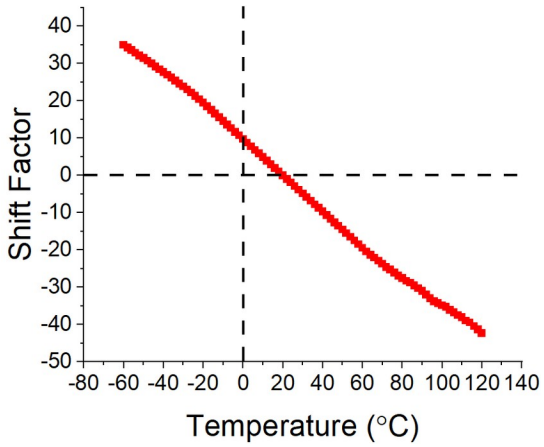


Figure 44 - Shift factors used to generate the mastercurve for GFPC.

5.11.3 DIC parameters

	Point Grey GS3-U3-41C6M-C
Camera Noise	0.9 %
Frame Rate	25 fps
Exposure Time	0.02 s
Field of View	2048 x 1200
DIC Software	MatchID.2021.2
Spatial Resolution	0.02 pixels
Subset Size	17 pixels
Step Size	5 pixels
Pixel Size	0.017 mm
Correlation Method	ZNSSD
Image Prefilter	Gaussian, Kernel 5
Interpolation	Bicubic Spline
Shape Function	Quadratic

Table 9 - Camera properties and DIC processing settings.

5.11.4 Task 3 and Task 11 Prony series parameters

Density = 1120 kg/m^3

Poissons ratio = 0.49

Task 3			Task 11		
E_0	$6.34x10^9$ (Pa)	(instantaneous)	E_0	$4.06x10^9$ (Pa)	(instantaneous)
log(τ (s))	g_i	k_i	log(τ (s))	g_i	k_i
-14	0.027024	0.027024	-14	0.099517	0.099517
-13	0.069250	0.069250	-13	0.018718	0.018718
-12	0.120835	0.120835	-12	0.062411	0.062411
-11	0.125524	0.125524	-11	0.023109	0.023109
-10	0.047087	0.047087	-10	0.049524	0.049524
-9	0.031334	0.031334	-9	0.03617	0.03617
-8	0.021768	0.021768	-8	0.034692	0.034692
-7	0.023346	0.023346	-7	0.049993	0.049993
-6	0.024357	0.024357	-6	0.055586	0.055586
-5	0.015738	0.015738	-5	0.064899	0.064899
-4	0.019053	0.019053	-4	0.075297	0.075297
-3	0.018074	0.018074	-3	0.083994	0.083994
-2	0.018484	0.018484	-2	0.092791	0.092791
-1	0.017316	0.017316	-1	0.09826	0.09826
0	0.027450	0.027450	0	0.077958	0.077958
1	0.021815	0.021815	1	0.051643	0.051643
2	0.018705	0.018705	2	0.015981	0.015981
3	0.023883	0.023883	3	0.004859	0.004859
4	0.026377	0.026377	4	0.001534	0.001534
5	0.032628	0.032628	5	0.000939	0.000939
6	0.050860	0.050860	6	2.56E-05	2.56E-05
7	0.069407	0.069407	7	0.000113	0.000113
8	0.082257	0.082257	8	3.27E-06	3.27E-06
9	0.048129	0.048129	9	1.48E-06	1.48E-06
10	0.011567	0.011567	10	1.2E-05	1.2E-05
11	0.002510	0.002510	11	3.15E-05	3.15E-05
			12	0.000527	0.000527
			13	7.43E-12	7.43E-12
			14	0.000666	0.000666
			15	0.000337	0.000337

Table 10 – Prony series values for Task 3 and Task 11 at 20 °C.

5.12 References

[1] I. G. Crouch, “Body armour – New materials, new systems,” *Defence Technology*, vol. 15, no. 3. China Ordnance Society, pp. 241–253, Jun. 01, 2019. doi: 10.1016/j.dt.2019.02.002.

[2] N. v. David, X. L. Gao, and J. Q. Zheng, “Ballistic resistant body armor: Contemporary and prospective materials and related protection mechanisms,” *Applied Mechanics Reviews*, vol. 62, no. 5. pp. 1–20, Sep. 2009. doi: 10.1115/1.3124644.

[3] K. Akella and N. K. Naik, “Composite armour—A review,” *J Indian Inst Sci*, vol. 95, no. 3, pp. 297–312, 2015.

[4] P. J. Hazell, *Armour: materials, theory, and design*. CRC press, 2022.

[5] W. Seifert, E. Strassburger, S. Grefen, and S. Schaare, “Experimental study about the influence of adhesive stiffness to the bonding strengths of adhesives for ceramic/metal targets,” *Defence Technology*, vol. 12, no. 2, pp. 188–200, Apr. 2016, doi: 10.1016/J.DT.2015.12.002.

[6] R. Zaera, S. Sánchez-Sáez, J. L. Pérez-Castellanos, and C. Navarro, “Modelling of the adhesive layer in mixed ceramic/metal armours subjected to impact,” *Compos Part A Appl Sci Manuf*, vol. 31, no. 8, pp. 823–833, Aug. 2000, doi: 10.1016/S1359-835X(00)00027-0.

[7] J. López-Puente, A. Arias, R. Zaera, and C. Navarro, “The effect of the thickness of the adhesive layer on the ballistic limit of ceramic/metal armours. An experimental and numerical study,” *Int J Impact Eng*, vol. 32, no. 1–4, pp. 321–336, Dec. 2005, doi: 10.1016/J.IJIMPENG.2005.07.014.

[8] A. Prakash, J. Rajasankar, N. Anandavalli, M. Verma, and N. R. Iyer, “Influence of adhesive thickness on high velocity impact performance of ceramic/metal composite targets,” *Int J Adhes Adhes*, vol. 41, pp. 186–197, Mar. 2013, doi: 10.1016/J.IJADHADH.2012.11.008.

[9] M. Übeyli, R. O. Yıldırım, and B. Ögel, “Investigation on the ballistic behavior of Al2O3/Al2024 laminated composites,” *J Mater Process Technol*, vol. 196, no. 1–3, pp. 356–364, Jan. 2008, doi: 10.1016/J.JMATPROTEC.2007.05.050.

[10] A. Harris, B. Vaughan, J. Yeomans, P. Smith, and S. Burnage, “Ballistic testing of surface-treated alumina and silicon carbide with improved adhesive bond strength,” *Int J Appl Ceram Technol*, vol. 14, no. 3, pp. 323–330, May 2017, doi: 10.1111/ijac.12668.

[11] A. J. Harris, B. Vaughan, J. A. Yeomans, P. A. Smith, and S. T. Burnage, “Surface preparation of silicon carbide for improved adhesive bond strength in armour applications,” *J Eur Ceram Soc*, vol. 33, no. 15–16, pp. 2925–2934, Dec. 2013, doi: 10.1016/j.jeurceramsoc.2013.05.026.

[12] S. Yadav and G. Ravichandran, “Penetration resistance of laminated ceramic/polymer structures,” *Int J Impact Eng*, vol. 28, no. 5, pp. 557–574, 2003.

[13] K. Akella, “Studies for improved damage tolerance of ceramics against ballistic impact using layers,” *Procedia Eng*, vol. 173, pp. 244–250, 2017.

[14] I. G. Crouch, “Critical interfaces in body armour systems,” *Defence Technology*, vol. 17, no. 6. China Ordnance Industry Corporation, pp. 1887–1894, Dec. 01, 2021. doi: 10.1016/j.dt.2020.11.006.

[15] C. M. Roland, *Viscoelastic behavior of rubbery materials*. OUP Oxford, 2011.

[16] R. B. Bogoslovov, C. M. Roland, and R. M. Gamache, “Impact-induced glass transition in elastomeric coatings,” *Appl Phys Lett*, vol. 90, no. 22, 2007, doi: 10.1063/1.2745212.

[17] C. M. Roland, D. Fragiadakis, and R. M. Gamache, “Elastomer-steel laminate armor,” *Compos Struct*, vol. 92, no. 5, pp. 1059–1064, Apr. 2010, doi: 10.1016/j.compstruct.2009.09.057.

[18] P. Si, Y. Liu, J. Yan, F. Bai, and F. Huang, “Ballistic Performance of Polyurea-Reinforced Ceramic/Metal Armor Subjected to Projectile Impact,” *Materials*, vol. 15, no. 11, Jun. 2022, doi: 10.3390/ma15113918.

[19] “Morgan Ceramics,” *https://www.morgantechnicalceramics.com/en-gb/*.

[20] “Bentley Advanced Materials,” *https://www.benam.co.uk/products/plastic/task*.

[21] “Ensinger Plastics,” *https://www.ensingerplastics.com/en-gb/shapes/products/tecanat-gf30-natural*.

[22] “MatchID,” *https://www.matchid.eu/*.

[23] M. L. Williams, R. F. Landel, and J. D. Ferry, “Temperature Dependence of Relaxation Mechanisms The Temperature Dependence of Relaxation Mechanisms in Amorphous Polymers and Other Glass-forming Liquids,” 1955.

[24] A. S. Wineman and K. R. Rajagopal, *Mechanical response of polymers*. Cambridge: Cambridge University Press, 2000.

[25] S. Deng, M. Hou, and L. Ye, “Temperature-dependent elastic moduli of epoxies measured by DMA and their correlations to mechanical testing data,” *Polym Test*, vol. 26, no. 6, pp. 803–813, Sep. 2007, doi: 10.1016/j.polymertesting.2007.05.003.

[26] W. Weibull, “A Statistical Distribution Function of Wide Applicability,” *Journal of Applied Mechanics-Transactions of the ASME*, vol. 18, no. 3, pp. 293–297, 1951.

[27] A. Serjouei, G. Gour, X. Zhang, S. Idapalapati, and G. E. B. Tan, “On improving ballistic limit of bi-layer ceramic–metal armor,” *Int J Impact Eng*, vol. 105, pp. 54–67, Jul. 2017, doi: 10.1016/j.ijimpeng.2016.09.015.

[28] G. H. Jonas and J. A. Zukas, “Mechanics of penetration: analysis and experiment,” *Int J Eng Sci*, vol. 16, no. 11, pp. 879–903, 1978.

[29] G. Ben-Dor, A. Dubinsky, and T. Elperin, “On the Lambert–Jonas approximation for ballistic impact,” *Mech Res Commun*, vol. 29, no. 2, pp. 137–139, 2002, doi: https://doi.org/10.1016/S0093-6413(02)00246-X.

[30] G. P. Cherepanov, “The propagation of cracks in a continuous medium,” *Journal of Applied Mathematics and Mechanics*, vol. 31, no. 3, pp. 503–512, 1967.

[31] J. R. Rice, “A path independent integral and the approximate analysis of strain concentration by notches and cracks,” 1968.

[32] F. Sun and B. R. K. Blackman, “A DIC method to determine the Mode I energy release rate G, the J-integral and the traction-separation law simultaneously for adhesive joints,” *Eng Fract Mech*, vol. 234, p. 107097, 2020.

[33] T. L. Anderson, *Fracture mechanics: fundamentals and applications*. CRC press, 2017.

6 Conclusions

6.1 Thesis Aims and Overview

This thesis successfully investigated a novel method for determining the performance of model armours. This methodology was implemented under quasi-static and impact loading and was able to provide insight into the energy absorptive mechanisms for each set of loading rates and these were reproducible using FEA simulation. Therefore, with refinement, this method could aid the screening of numerous potential armour materials and adhesives in a cheaper and quicker method than conducting full ballistic tests for each. It was shown this method does have its limitations which must be considered as the simplicity of specimens and the quasi-1D nature of impact are important because these differ from the reality of ballistic impact. However, this comes with the advantage of the ability to visually determine the fracture pattern generated.

This method was successfully supported by the wedge test investigated in this thesis. It was suggested that the dynamic behaviour of the interface could be investigated by using time-temperature superposition under quasi-static loading. This is a significant benefit because this avoids the complexity of conducting dynamic interface experiments and calculating the dynamic J-integral. However, it was shown the influence of noise can limit the accuracy of the calculated K_1 and K_{11} values, so careful consideration is required when experimentally determining these parameters.

These results were supported by a thermomechanical characterisation of all the polymers used in this project which were successfully modelled using a Prony series. This material model can model the material response under dynamic and quasi-static loading well as well as successfully capture the stress relaxation behaviour on these timescales. Limitations to

the model arose once non-linear processes were recorded, and modifications to account for this behaviour were proposed.

6.2 Accomplishments and Future Work

6.2.1 Polymer characterisation and stress relaxation

6.2.1.1 Accomplishments

The two polymers of interest to this project were successfully characterised at varying rates and temperatures under monotonic loading and, from the results of DMA experiments, a Prony series material model was fitted. This material model was initially verified to reliably predict the stress relaxation behaviour of both polymers under quasi-static loading for a range of temperatures. Of particular note was the ability of the model to capture this relaxation through the polymer's glass transition temperature, where the sensitivity of the polymer modulus to temperature was greatest. The limitations of the model were probed by increasing the strain before relaxation. The model successfully captured this behaviour unless any irrecoverable deformation was present.

The relaxation of the polymers was investigated under dynamic loading conditions. The use of dashpot boundary conditions to model dynamic relaxation, first pioneered by Cloete, was expanded and its use was explored as a function of loading strain. The observed behaviour was successfully captured by the model in most cases, although the strain was underpredicted in one polymer. As the strain before relaxation was increased, it was generally found that the model retained the ability to capture the behaviour during the first phase of relaxation but diverged later, when it is believed that non-linear viscoelasticity became prevalent. An extension to the material model was proposed.

The characterisation data extracted from these polymers have contributed to the wider polymer database. These data have been made available to the wider community with the hope that it could be used in future studies and are also used to underpin modelling work later in this thesis.

6.2.1.2 Future Work

The methodical study of these polymers' behaviour under monotonic loading and stress relaxation for quasi-static and dynamic timescales has provided valuable insight into its response, which was used throughout this thesis. Various limitations to the model were observed; namely, this model deviated with the onset of non-linear viscoelastic processes: modifications were proposed. To extend this study, the full formulation of this model could be investigated by fitting this extended model to a series of large strain experiments at a range of strain rates, thus creating a model able to capture the irrecoverable strain behaviour. This work could be extended further by investigating the behaviour of additional polymers and determining how the models used in this study perform.

6.2.2 Quasi-static and Dynamic Properties of the Ceramic-Polymer Interface

6.2.2.1 Accomplishments

This chapter investigated interfaces manufactured using two distinct polyurethanes and primer surface modifications under quasi-static and dynamic loading conditions. The stress intensity factors, and J-integral were calculated under loading. The analytical pipeline was adapted from Marrow and Barhli. To validate the approach, FEA simulations were conducted, and the results were used to artificially deform experimental images. These

simulations were further used to understand the influence of the dynamic effects of loading on the analytical output.

Dynamic fracture experiments using the dynamic J-integral are exceedingly challenging to perform experimentally due to the necessity of determining a smoothed velocity field local to the crack caused by the loss of path independency of the dynamic J-integral. The use of time-temperature superposition was implemented to predict the dynamic fracture behaviour from sub-ambient quasi-static experiments. Whilst further study is required, these results are encouraging.

6.2.2.2 Future Work

For the environmental conditions in which the polymer was more ductile, excessive shearing of the interface was observed, which artificially increased the results. The analysis could be furthered using the separated J-integral.

As previously discussed in this thesis, the dynamic experiment was analysed using the static J-integral due to the significantly increased difficulty associated with the dynamic J-integral. However, an extension to this research could be to determine the dynamic J-integral, thus allowing a direct comparison to that calculated using the TTS principle.

6.2.3 Quasi-static and Impact Performance of Quasi-1D Model Armour

6.2.3.1 Accomplishments

A novel experimental procedure and geometry were successfully implemented to investigate the influence of polymer backing and interfacial characteristics on model armour response. The quasi-1D geometry chosen for this investigation allowed the fracture

pathways, typically hidden by the material geometry, to be directly observed. The resulting reduction in velocity was calculated and compared against these observed fracture pathways. These results were compared against FEA simulations of the impact event, and good alignment was observed.

Under quasi-static three-point bend, the results presented a wide array of energy absorption capabilities and the mechanism responsible was identified. Two types of failure were identified and linked to the polymer stiffness and interfacial strength. These were shown to be linked via temperature manipulation and therefore could be used to further refine the most suitable adhesive to be used with an optimally located glass transition temperature. These results were successfully reproduced with FEA simulation and hence FEA could be used to further refine the most suitable adhesive polymer for a particular application.

The FE models were populated using data taken from the previous characterisation of the constitutive materials and interfaces involved in this research. Using these data, various material models such as a Prony series, an Ogden model, and cohesive interface elements were successfully populated.

6.2.3.2 Future Work

Under impact, it was observed that a large proportion of the projectile's incident kinetic energy was transferred to the armour fragments' kinetic energy. Whilst this methodology allows the fracture pattern of the ceramic to be directly observed, this significant energy transfer limited the experiment's sensitivity to the influence of any interface and backing variation. A worthy extension could be to first, investigate whether the observations made

regarding the influence of the interface on the observed fracture patterns continue to occur at higher impact speeds. This is because the range of speeds investigated in this thesis (up to 300 m s^{-1}) are relatively low compared to representative projectile velocities. Secondly, this methodology could be repeated using representative armour materials and bonding. This increased interfacial strength and backing stiffness could be more significant energy absorption mechanisms and reduce the proportion of incident energy transferred to the kinetic energy of the fragments.

Further, the experimental set-up should be modified to incorporate the use of a planar backing which supports the model armour because, in reality, the armour would not be pinned in a three-point bend configuration. Additionally, the model armour should be enhanced to plate geometry to allow an investigation to be performed using this representative geometry. This will then allow a link between the quasi-1D beam and ballistic plate to be understood so that the behaviour of the materials investigated using the method described in this thesis can be linked to their representative armour behaviour.

The FE simulation under quasi-static loading successfully captured the range of failure modes observed experimentally. Further, it was observed that there was a relatively narrow threshold of the polymer and interfacial condition, which dictated which failure type would be present, and this would subsequently greatly influence the energy the structure could absorb. The FE simulation could be utilised to explore the boundaries of this behaviour.

6.3 Concluding Remarks

This thesis investigated the issue of ballistic impact on body armour through a combination of experimental and simulation techniques under quasi-static and impact loading. Whilst this study, as research typically does, asks more questions than it answered, good progress towards the issue has been made.

With more research and refinement, a wide array of potential armour materials could be screened relatively quickly and cheaply using the methodology presented in this study. However, it is important that the link between the quasi-1D and plate impact is sufficiently understood. This method will allow greater understanding of the ceramic-polymer interaction because the fracture pathways under impact can be visually observed. If these fracture pathways can be suitably controlled, there could be implications for the multi-hit capabilities of the armour because interfacial cracking could be limited. Further, using the time-temperature superposition principle with the wedge experiment, the dynamic properties of the bonded interface could be investigated using temperature without the requirement for complex, dynamic experiments and the dynamic J-integral.

With additional development, the quasi-static behaviour of the composite beam bend and the interaction between backing and interface can be better understood. For structures such as this, there appeared to be a fine threshold in failure modes where significant differences in energy absorption were present. Greater understanding of this failure will allow polymers with the most suitable glass transition temperature to be selected so that, upon failure, the structure has absorbed the most energy possible. These ideas and understanding could then be extended to more complex structures.